Università degli Studi di Torino
Scuola di Dottorato in Scienza ed Alta Tecnologia
Indirizzo di Fisica ed Astrofisica

Measurement of spin effects in the Drell-Yan process at the COMPASS experiment

Candidate: Dott. Riccardo Longo

Tutor: Dr. Michela Chiosso
Scientific Supervisor: Dr. Bakur Parsamyan

To my Grandfather,
Luigi Lento.
Every time I get lost,
He's my compass.

Abstract

COMPASS (COmmon Muon Proton Apparatus for Structure and Spectroscopy) is a high-energy physics experiment located at the North Area of SPS (M2 beamline) at CERN. One of its main objectives is the study of transverse spin structure of the nucleon trough measurement of target spin (in)dependent azimuthal asymmetries in Semi-Inclusive Deep Inelastic Scattering (SIDIS) and Drell-Yan (DY) processes with transversely polarised targets.

In the past, all the azimuthal asymmetries arising in the cross-section of unpolarised-hadron production in polarised-lepton SIDIS off a transversely polarised nucleon have been studied at COMPASS. Within the QCD improved parton model approach, these asymmetries are interpreted in terms of convolutions of quark transverse-momentum-dependent (TMD) parton distribution functions (PDFs) and fragmentation functions (FF).

Similarly, the cross-section for DY lepton-pair production in collisions of pions off a transversely polarised nucleon also comprises transverse-target-polarization-(in)dependent azimuthal asymmetries. In the case of Drell-Yan, the asymmetries can be interpreted in terms of convolutions of two TMD PDFs, one of the target nucleon and the second of the beam hadron.

Currently, the COMPASS experiment is the only facility exploring the transverse spin structure of the nucleon with two alternative experimental approaches, using mostly the same setup and a similar transversely polarised proton target. This opens the unique opportunity of comparable hard scales when studying the TMD PDFs obtained from SIDIS and DY and addressing the QCD prediction for the sign-change of Sivers and Boer-Mulders TMD PDF.

In 2016 COMPASS published the results for the SIDIS TSAs extracted in four Q^2 ranges corresponding to the regions of the dimuon mass $\sqrt{Q^2}$ used in the analyses of the COMPASS Drell-Yan data. These results allow, together with the ones resulting from the analysis of the DY data presented in this thesis, for a direct comparison of the nucleon transverse-momentum-dependent parton distribution functions extracted from these two alternative measurements.

This thesis is focused on the analysis of the Drell-Yan data collected by COMPASS during the 2015 data taking, with a pion beam on a transversely polarised

NH3 target. Particular attention is given to the TSAs arising in the Drell-Yan cross section. The first extraction of these TSAs, directly linked to Sivers, Transversity and Pretzelosity TMD PDFs of the nucleon, is presented in detail. Also the case of weighted TSAs is treated in this work. In both the cases, the asymmetries are compared with their SIDIS analogues results obtained by COMPASS so far. The second part of the thesis is devoted to the extraction of unpolarised asymmetries appearing in the Drell-Yan cross-section. These asymmetries have attracted particular attention in the recent past, being related to the Lam-Tung sum rule relation. To perform unpolarised analysis extensive Monte Carlo studies are mandatory, to disentangle physics effects from acceptance effects due to the experimental apparatus. The implementation of the DY physics programme in the new COMPASS Monte Carlo toolkit, TGEANT, is also discussed in this work.

Acknowledgements

I would like to express my appreciation and warm thanks to my tutor, Dr. Michela Chiosso, for encouraging my path in research and for allowing me to grow as a research scientist. I am grateful for her trust and support.

My deepest gratitude goes to Dr. Bakur Parsamyan, for his patience, motivation, and his immense expertise. For his constant guidance in my research work, for his precious help and for always being there, even when things got hard. There was no night, weekend or holiday that prevented him to give me his valuable advices and suggestions. I would like to let you know that it was a great honour for me to have the opportunity to work with you.

I gratefully acknowledge Dr. Nicole D'Hose and Dr. Catarina Marques Quintans for their comments on my results and their wise advices.

I thank all the members of the COMPASS Collaboration but in particular a few people who contributed to the work presented in this thesis. My first thoughts go to Dr. Christopher Regali (aka El Rallo) and Dr. Tobias Szameitat (aka TD0G), with whom I collaborated since my early steps as PhD, and spent my best moments during these years in COMPASS. We built a strong friendship that linked us beyond the work in the Collaboration. A special thank goes to my friend Dr. Marcia Quaresma, for the constant support and enjoyable times and discussions we had during my whole experience in COMPASS. Thanks to my dear friend and colleague Dr. Artem Ivanov, with whom I shared office and experiences for three years before he left to return in Russia. A warm thanks to my fellow students, Jan Matousek and Yu-Shiang Lian, with whom I gladly worked on some of the analyses presented in this thesis. I would like also to thank Dr. Yann Bedfer for many useful advices and suggestions, in particular during my early steps in COMPASS as a PhD student. Last but not least, thanks to all the other members of the Drell-Yan group for many interesting and useful discussions.

This work also benefited from many fruitful discussions I had with all the members of the COMPASS group of Torino. I would like to acknowledge first Prof. Daniele Panzieri, for his wise leadership of the group and for his constant encouragement and understanding. A grateful thought to Dr. Angelo Maggiora, who supervised me during my summer student at CERN, always transmitting his

Table of contents

Introduction

More than 100 years ago, Rutherford's pioneering experiment revealed the structure of atomic matter, pointing out the existence of small and massive nuclei at the core of the atoms and leading the way to the era of the experimental scattering techniques. Making use of different probes and rising the energy, a sequence of scattering experiments has increasingly enlarged the knowledge about the fundamental blocks of the matter, protons and neutrons, and their internal structure. Many other new particles were also discovered, pushing forward the development of a theory capable of handling and unifying all these discoveries in a consistent way.

In 1964 Gell-Mann and Zweig formulated their "quark" model [1] [2] suggesting quarks (or, in Zweig's interpretation "aces") as new fundamental components of the hadrons. In the proposed model the nucleons are composed of three quarks, elementary objects with fractional electrical charge and spin 1/2. Later, the quark-model was complemented by the so-called "parton-model" established by Richard Feynman which explained the results obtained in late 60's by Deep Inelastic Scattering (DIS) experiments showing that nucleons contain point-like particles. Feynman proposed that the scattering takes place at large number of 'partons', free point-like spin 1/2 particles inside the nucleon[3]. The two models were unified in 70's, when the Quantum Chromodynamics (QCD), the theory of strong interactions was discovered by Gell-Mann and Fritzsch. Within QCD the nucleon is made up of three valence quarks surrounded by the so-called sea-quarks (quark-antiquark pairs) and a gluon cloud, where the gluons play the role of force-carriers between quarks.

The quark-gluon structure of the nucleons was progressively unveiled by the DIS measurements with high-energy leptons scattering off nucleon targets, opening new frontiers for experimental studies and theoretical developments. Among them, a breakthrough was represented by the data published by the European Muon Collaboration (EMC) in 1988, showing that the axial charge of the proton is much smaller than what was expected from the Ellis-Jaffe sum-rule [4] and only a marginal fraction of the proton spin can be attributed to the spin of the valence

quarks. Since in the naive parton model the quantum numbers of the nucleon are given by the three valence quarks, the resulting nucleon spin is given by the composition of their spins and led to the well-known value of 1/2. Accounting also for relativistic effects, the parton model expectation was that 60% of the total proton spin is carried by the valence quarks. The measurement of EMC was drawing a different picture, where the quark spin contribution was quantified to be surprisingly small, $\Delta\Sigma = (12\pm9_{stat} \pm14_{syst})\%$ [5], raising the so-called *proton spin-crisis*. Triggered by the EMC findings, several new and more precise experiments performed a series of dedicated measurements which have by now corrected the quark spin contribution to approximately 30% ($\Delta\Sigma = 0.32 \pm 0.02_{stat} \pm 0.04_{syst} \pm 0.05_{evol}$, [6]).

The *spin-crisis* had a strong impact on the theoretical understanding of the composition of the nucleon spin. To achieve a more realistic description of the nucleon spin, in addition to the quarks spin sum, $\Delta\Sigma$, also possible contributions from the gluons spin, ΔG, and from the orbital angular momentum carried by nucleon quark and gluon constituents, L_q and L_g, had to be considered:

$$\frac{1}{2} = \frac{1}{2}\Delta\Sigma + \Delta G + L_q + L_g$$

Currently available experimental results on the gluon polarisation are affected by large uncertainties. Nevertheless, there is an evidence that the value is small and positive [7]. The obtained result is not sufficient to resolve the nucleon spin puzzle, but gluon polarisation still may have a significant contribution to the nucleon spin. The remaining part of the nucleon spin is assumed to come from L_q and L_g contributions, which have not been measured so far. The orbital angular motion studies complement the simple collinear picture by the effects in the plane transverse to the direction of motion and give access to the complete three-dimensional structure of the nucleon. A set of observables in deeply virtual Compton scattering (DVCS) and azimuthal asymmetries in lepton-nucleon and hadron-hadron scatterings are used to understand the role of the orbital angular momentum in the nucleon. After decades of intensive experimental and theoretical studies a lot of understanding has been achieved concerning the longitudinal structure of a fast-moving proton, the Bjorken-x dependence of the parton distribution functions and of the helicity distributions, but very little is known about the transverse structure.

The interest to the transverse effects originates from 1975, when significant azimuthal asymmetries were measured in $p^\uparrow+p$ collisions at the CERN PS [8]. From the theory side, the importance of the intrinsic transverse motion of the quarks inside the nucleon and its connection with azimuthal effects were pointed

out in the late 70's [9, 10]. In particular, it was demonstrated that non-zero intrinsic momentum of the quarks induces $\cos\phi$ asymmetries in SIDIS, while in Drell-Yan processes it could be the origin of large transverse momentum and similar azimuthal effects. In the following years, along with the pQCD parton model framework, a set of Transverse Momentum Dependent Parton Distribution Functions (TMD PDFs), Fragmentation Functions (FFs) and their factorisation scheme has been formulated [11, 12]. The TMD PDFs and FFs are QCD objects parametrising different spin and intrinsic transverse momentum correlation states of quarks bounded in the nucleon and (un)polarised quark fragmentation mechanisms, respectively. Model-independent expressions counting all possible azimuthal modulations arising in the SIDIS and Drell-Yan cross-sections, as well as their TMD-interpretation, have been first introduced during the 1990s [13, 14]. The measurements of these physics observables, carried out by different experimental facilities in the last decades, opened the way to global phenomenological fits and extractions of TMD PDFs and FFs.

In the *twist-2* approximation (leading order in an expansion in Q^{-1}) of QCD parton model, the internal spin-structure of a polarised nucleon is described by a set of eight TMD PDFs. One of the key features of the TMD PDFs is their predicted process independence. Within the concept of generalised universality of TMD PDFs, nucleon parton distribution functions accessed via measurements of azimuthal asymmetries in SIDIS and Drell-Yan are expected to be process-independent. Therefore, the extraction of (un)polarised azimuthal asymmetries arising in SIDIS and Drell-Yan measurements have absolute importance for a general understanding of spin physics and validation of the QCD. Study of the spin structure of the nucleon via the measurement of azimuthal spin effects arising in SIDIS and Drell-Yan is one of the most important aspects of the broad physics programme of the COMPASS experiment at CERN [15, 16].

The COMPASS spectrometer is in operation in the SPS M2 beam line in CERN North Area since 2002. During the so-called phase-I (between 2002 and 2012) the major part of data-taking time was dedicated to SIDIS measurements with different polarised targets. In 2012 the experiment entered the phase-II and in 2015 it became the first-ever fixed target experiment collecting polarised Drell-Yan data; it is by now the only experiment possessing the unprecedented opportunity to explore the transverse spin structure of the nucleon via two alternative mechanisms, by measuring the azimuthal asymmetries in SIDIS and Drell-Yan at similar hard scales. The ultimate goal is to test the universality and other key-features of TMDs, as the predicted sign-change of time-reversal odd Sivers and Boer-Mulders TMD PDFs between SIDIS and DY [17].

By the time of this work the analysis of the SIDIS data collected during the phase-I was already accomplished. COMPASS has published a large amount of SIDIS-results which are being widely used in global phenomenological fits and play a crucial role in the modelling of the spin structure of the nucleon and related phenomena. This thesis is focused on the analysis of the Drell-Yan data collected by COMPASS during the 2015 data taking. One of the aims of the presented research is to provide the Drell-Yan counterpart of the SIDIS results on target transverse spin-dependent asymmetries (TSAs) extracted by COMPASS [18]. The first extraction of Drell-Yan target transverse spin-dependent azimuthal asymmetries in the so-called *high mass* range from COMPASS 2015 data is presented in this thesis. The results include a comparison with analogous SIDIS asymmetries and with existing theoretical predictions for Sivers TMD PDF, to address the sign-change prediction. Another way to address the TMD PDFs through Drell-Yan asymmetries is the extraction of the q_T-weighted TSAs with q_T being the transverse component of the photon virtuality in the Drell-Yan reaction. In this way, instead of convolution integrals, the asymmetries are represented in terms of products of two TMD PDFs. Thus, further inputs on the Sivers sign change have been obtained in this work comparing Drell-Yan q_T weighted asymmetries with the SIDIS p_T^h weighted ones. In addition, unpolarised Drell-Yan studies for the *high mass* range, namely the preliminary extraction of λ, μ, ν terms from the 2015 NH_3 data and the subsequent test of the Lam-Tung sum rule [19], are discussed in detail in the last part of the thesis. To access the unpolarised observables, a highly reliable Monte Carlo (MC) description of the experimental setup is mandatory in order to correctly take into account the azimuthal effects introduced by the apparatus itself. For this purpose thorough MC description of the COMPASS setup as used for the Drell-Yan physics programme was implemented in the new MC framework, TGEANT [20, 21], developed for COMPASS phase-II. A general overview of these and other technical developments is also enclosed in the thesis.

Outline of the thesis

The thesis is organized as follows: in Chapter 1 the theoretical introduction is given together with a review of relevant SIDIS and Drell-Yan experimental results obtained in the last decades by different collaborations. In Chapter 2 the COMPASS experimental apparatus is described in detail, with particular attention on the peculiarities of the setup used in 2015 for the Drell-Yan data taking. Chapter 3 is devoted to the Monte Carlo, reviewing the architecture of

TGEANT software and the major improvements implemented for the simulation of Drell-Yan reactions at COMPASS. The analysis framework for extraction of the TSAs arising in the pion-induced Drell-Yan cross-section and various systematic tests are described in Chapter 4, while Chapter 5 reviews the analysis and extraction of the q_T weighted TSAs. Finally, Chapter 6 is dedicated to the preliminary unpolarised analysis of the data collected with the NH_3 target in 2015. An overall summary of the main aspects and highlights of the present work is given in Chapter 7.

Chapter 1

Experimental and Theoretical overview

This chapter reviews theoretical concepts and experimental results relevant for this thesis. After introducing the Deep Inelastic Scattering (DIS) framework, different experimental tools to study the internal structure of the nucleon, such as the study of Semi-Inclusive DIS (SIDIS) and Drell-Yan processes, are described. The theoretical introduction is followed by the experimental counter-part, including highlights from various spin-physics programmes that play a key role in the understanding of the internal dynamics of the nucleon.

1.1 Deep inelastic scattering

Historically the first experimental method used to probe the content of protons and nucleons was the deep inelastic scattering of leptons off nucleons

$$\ell(k,\lambda) + N(P,S) \rightarrow \ell'(k') + X. \tag{1.1}$$

In Quantum Electro Dynamics (QED), in the leading order in α, the DIS process is described by the exchange of a virtual photon between lepton and nucleon. Also the exchange of a Z_0-boson is possible, but this configuration is suppressed at typical fixed target experiment energy scales, much smaller compared to the Z_0 mass (*i.e.* for COMPASS $\sqrt{s} \sim 17.4$ GeV vs $m_{Z_0} \sim 92$ GeV).

If the scattered lepton $\ell'(k')$ is the only particle observed in the final state, the process is called *inclusive*. Usually, it is simply denoted as DIS. On the contrary, if one or more hadrons originating from the fragmentation of the target nucleon $N(P,S)$ are also detected in the final state, the process is called *Semi Inclusive*. In the following, the latter case will be referred to as SIDIS. The case in which all the particles in the final state are detected is being referred to as *exclusive* measurement.

In a DIS measurement, the four-momenta of the lepton in the initial and final state ($k = (E, \vec{k})$ and $k' = (E', \vec{k}')$, respectively) are measured. In a fixed target experiment the four momentum of the target is, $P = (M, \vec{0})$. The interaction is described by the exchange of a virtual photon with four momentum q, as illustrated in the Feynman diagram in Fig 1.1.
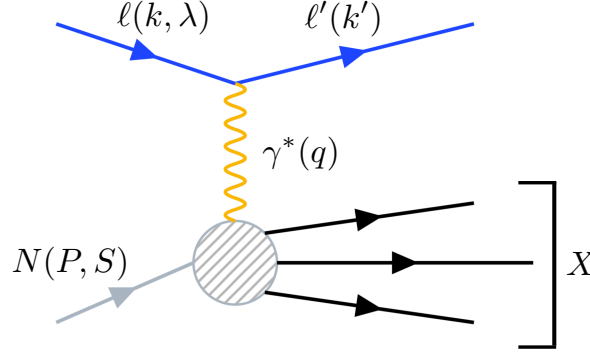
Fig. 1.1 Feynman diagram of the Deep Inelastic Scattering process, $\ell(k, \lambda) + N(P, S) \rightarrow \ell'(k') + X$.

A standard set of Lorentz-invariant DIS variables is defined as follows:

$$Q^2 = -q^2 = -(k - k')^2, \qquad \nu = \frac{P \cdot q}{M}, \qquad x = \frac{Q^2}{2P \cdot q}$$

$$y = \frac{P \cdot q}{P \cdot k}, \qquad W = (P + q)^2 \tag{1.2}$$

where the negative four-momentum transfer, Q^2, represents the hard scale of the reaction, ν is the energy of the virtual photon and y is the fraction of the beam momentum carried by the virtual photon; x is the dimensionless Bjorken scaling variable which can vary in the range $[0; 1]$ and is interpreted as the nucleon momentum fraction carried by the struck quark. Finally, W is the squared center-of-mass energy of the photon-nucleon system. The DIS regime in fixed target experiments is characterised by $W \gg M^2$ and $Q^2 > 1$ (GeV/c^2)^2. To fully parametrise DIS reactions, one can choose a two independent variables among the five aforementioned invariants (*e.g.* x and Q^2).

1.2 DIS cross section

The differential cross section for inclusive DIS is given by the product of the leptonic, $L_{\mu\nu}$, and hadronic tensors, $W_{\mu\nu}$ [22]

$$\frac{d^2\sigma}{d\Omega dE'} = \frac{\alpha^2}{Q^4} \frac{E'}{ME} L^{\mu\nu} W_{\mu\nu} \tag{1.3}$$

In this expression, only the photon exchange is taken into account and α represents the electromagnetic fine-structure constant. $L_{\mu\nu}$ describes the exchange of the photon between the lepton and the struck quark and can be computed within QED framework. The hadronic tensor $W_{\mu\nu}$ describes the absorption of the virtual photon by the nucleon. It includes the effects due to the complex structure of the nucleon, which cannot be calculated using the Quantum Chromodynamics (QCD) because of non perturbative contributions in the strong interaction. Usually both tensors are written splitting them into a symmetric and an antisymmetric part

$$L_{\mu\nu} = L_{\mu\nu}^S + iL_{\mu\nu}^A$$
$$W_{\mu\nu} = W_{\mu\nu}^S + iW_{\mu\nu}^A$$

(1.4)

The symmetric terms describe the spin-independent part of the scattering, while the asymmetric terms depend on the spin of the incoming lepton ($L_{\mu\nu}^A$) and of the target nucleon ($W_{\mu\nu}^A$).

Although it is not possible to calculate the hadronic tensor, a general expression can be written including four dimensionless objects, the so-called *structure functions*: $F_1(x,Q^2)$ and $F_2(x,Q^2)$, describing the spin-independent structure of the nucleon, and $g_1(x,Q^2)$ and $g_2(x,Q^2)$, containing information about the spin structure of the nucleon. The polarised DIS differential cross section can be expressed, in terms of these functions, as

$$\frac{d^2\sigma}{dxdy} = \frac{8\pi\alpha^2}{Q^2}\left[\frac{y}{2}F_1(x,Q^2) + \frac{1}{2xy}\left(1 - y - \frac{y^2\gamma^2}{4}\right)F_2(x,Q^2)\right.$$

(1.5)

$$\left. + c_1g_1(x,Q^2) + c_2g_2(x,Q^2)\right]$$

(1.6)

where c_1 and c_2 are constants which depend on y, $\gamma = Q^2/\nu^2$, and on the nucleon polarisation.

1.3   Structure functions and parton model

The measurements of $F_1(x,Q^2)$ and $F_2(x,Q^2)$ have shown that they are mostly Q^2 independent objects, as predicted by J.Bjorken in 1968 [23]. This behaviour, known as Bjorken-scaling, was first observed in DIS experiments performed at SLAC [24, 25] and interpreted as evidence of the point-like substructure of the nucleons.

The first findings of SLAC were confirmed with new measurements on deuteron targets [26]. The quest of interpretation of these results triggered the development

of the Parton Model (PM) by Feynman and Bjorken [3, 27]. The PM was formulated in a fast moving reference frame, where the nucleon has a large longitudinal momentum ($P_z \rightarrow \infty$). Therefore, all the partons contained in the nucleon are supposed to move collinearly and all the masses and the transverse momenta can be neglected. Under these assumptions, the interaction between lepton and nucleon can be described as an incoherent sum of interactions between the lepton and each single parton.

The so-called Quark Parton Model (QPM) originated combining the already existing quark model, formulated by Gell-Mann and Zweig [1, 2], with the parton model of Feynman and Bjorken. In the naive QPM, the partons are associated to the quarks and each nucleon is composed of three of quarks[1] that define all the quantum numbers of the nucleon. Moreover, quark-antiquark pairs are also present in the nucleon and referred to as sea-quarks.

To interpret the aforementioned structure functions within the QPM, the Parton Distribution Functions (PDFs) $q(x)$ have been introduced. They represent the number of quarks of a given flavour[2] carrying a momentum fraction $\in [x, x + \mathrm{d}x]$. Using the PDFs, the spin-independent structure functions can be expressed as

$$
\begin{aligned}
F_1(x) &= \frac{1}{2} \sum_q e_q^2 (q(x) + \bar{q}(x)) \\
F_2(x) &= x \sum_q e_q^2 (q(x) + \bar{q}(x))
\end{aligned}
\tag{1.7}
$$

where e_q represents the charge of a quark of a given flavour q. The structure function $F_1(x)$ describes the number density of quarks, while $F_2(x)$ their momentum distribution. A confirmation of the quarks being spin-1/2 particles was obtained verifying the Callan-Gross relation [28] relating $F_1(x)$ and $F_2(x)$

$$
F_2(x) = 2x F_1(x)
\tag{1.8}
$$

which holds only for particles with spin 1/2.

Within the QPM, also the spin-dependent structure functions can be calculated. They are expressed by the quark helicity distributions $\Delta q(x)$ and $\Delta \bar{q}(x)$. Defining q^+ (q^-) the number densities of quarks with spin parallel (antiparallel) to that of the nucleon, the PDFs $q(x)$ (or also $f(x)$ in another common notation) can be

---

[1] uud for the proton, udd for the neutron.
[2] Up, Down, Charm, Strange, Bottom, Top.

expressed as

$$q(x) = q^+(x) + q^-(x)$$
$$\bar{q}(x) = \bar{q}^+(x) + \bar{q}^-(x)$$

(1.9)

while the helicity distributions can be written as

$$\Delta q(x) = q^+(x) - q^-(x)$$
$$\Delta \bar{q}(x) = \bar{q}^+(x) - \bar{q}^-(x)$$

(1.10)

Therefore, $\Delta q(x)$ and $\Delta \bar{q}(x)$ carry information about the quark spin contribution to the spin of the nucleon. Starting from them, the spin-dependent structure functions $g_1(x)$ and $g_2(x)$ can be written as

$$g_1(x) = \frac{1}{2} \sum_q e_q^2 \Delta q(x)$$
$$g_2(x) = 0$$

(1.11)

Here $g_1(x)$ is directly linked to quark helicity distributions, describing the spin distribution of the quarks inside the nucleon. As visible in Eq. 1.11, the $g_2(x)$ function has no interpretation in the quark parton model. In QCD, it can be interpreted as higher order effect in $1/Q$ [29].

1.4   QCD improved parton model

A vigorous effort was made by several experiments to measure $F_1(x, Q^2)$ and $F_2(x, Q^2)$ structure-functions in a wide range of x and Q^2, actively improving the precision of the early measurements at SLAC [30–34]. The world data on the structure-function $F_2(x, Q^2)$ as a function of Q^2 in different ranges of x are shown in Fig. 1.2. A dependence on Q^2 was already observed by the early SLAC experiments and was confirmed by many other experimental facilities. At low x values, the structure function tends to increase with Q^2, whereas at high values of x a decrease can be observed. The scaling predicted by Bjorken was found to hold around $x \sim 0.2$, requiring extensions of the model to account for these binding effects, that can be described introducing the exchange of vector bosons, the gluons, and other effects described by QCD. The QCD describes the interaction of quarks within a non-Abelian gauge theory relying on the SU(3) group. Quarks can interact via exchange of gluons and vector bosons that transmit the colour field and couple to the charge of the strong force, the colour. In the model, three colours (red, blue and green) exist together with the corresponding anti-colour.
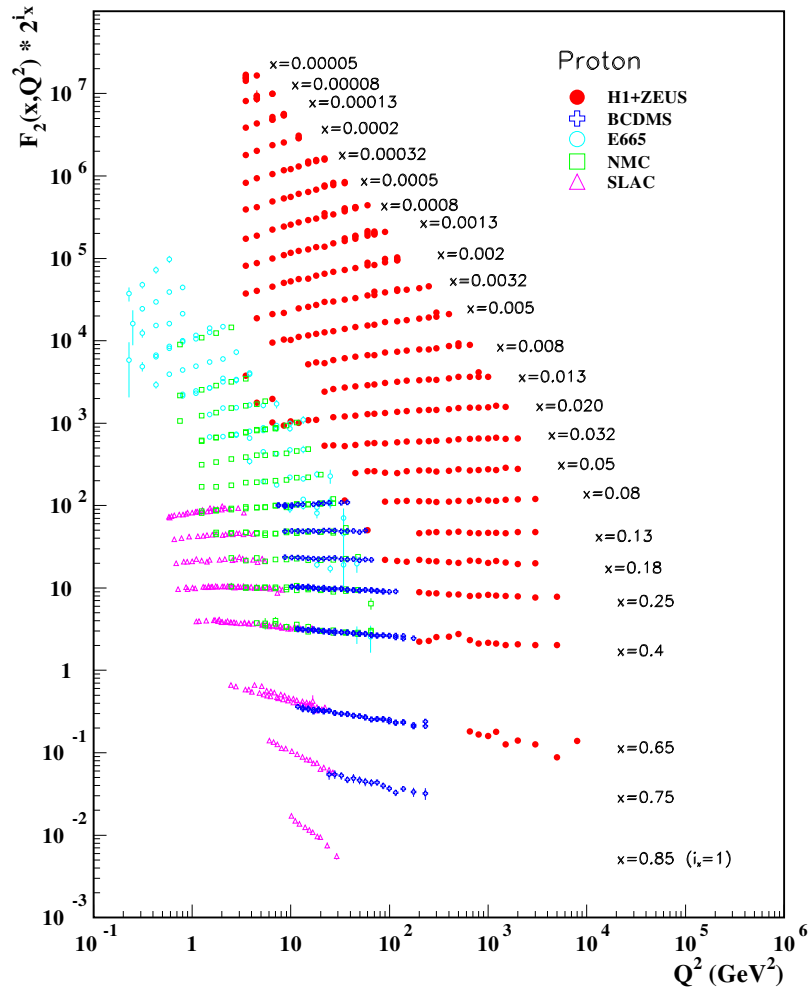
Fig. 1.2 The structure function $F_2(x, Q^2)$ measured by various fixed target experiments using electron (SLAC [30]) or muon beams (BCDMS [31], E665 [32], NMC [33]), and at collider experiments (H1 and ZEUS [34]). The results are shown with an offset function of the Bjorken-x bin. Picture taken from [35].

Opposite to QED, where the photons are not charged, the force carriers of QCD also carry colour. This feature leads to a spread of colour, resulting in a substantial dependence of the strong coupling constant α_s on the photon virtuality [36].

High virtualities correspond to small distances and small coupling α_s, resulting in a free-particle-like behaviour of the quarks. The same is also assumed in the naive QPM and is known as *asymptotic freedom*. In this regime, the small values of the coupling constant allow performing the computations applying a perturbative approach. The opposite was found at small Q^2, where α_s becomes large preventing any perturbative interpretation. Given the strong coupling, quarks and gluons are confined in their colourless housing, the hadrons. Hence, this regime is called *confinement*.

In the QCD improved parton model, the evolution with Q^2 of the PDFs can be described analytically using the Dokshitzer-Gribov-Lipatov-Altarelli-Parisi (DGLAP) equations [37–39].

1.5   The Experimental progress

The surprising findings at SLAC [24, 25] triggered strong interest of many experimental collaborations and inspired new measurements aimed to explore the nucleon spin structure. The new physics programmes were mainly devoted to polarised DIS and proton-proton scattering experiments.

The first synchrotron making use of high energy polarised proton beams was the ZGS[3] at the Argonne National Laboratory (ANL) in 1973. The experiments operating at ANL observed large Single Spin Asymmetries (SSAs) arising in polarised proton-proton collisions [40, 41].

After first pioneering measurements, a broad spin program was launched at SLAC including different measurements dedicated to the understanding of the nucleon structure and focused on high statistics measurements of the inclusive asymmetries. The first measurements of the proton spin structure were performed by the experiments E80 [42, 43] and E130 [44, 45], followed by a series of high precision experiments (E142 [46], E143 [47], E154 PhysRevLett.79.26 and E155 [48]).

In parallel with SLAC, the investigation of the nucleon spin structure started to be a hot topic also at CERN. Firstly, the European Muon Collaboration (EMC) found very puzzling results suggesting that valence quarks have only a small contribution to the proton spin [5, 49], which was in keen contrast with the expectations of the naive QPM. In the '90s, the Spin Muon Collaboration (SMC) continued the EMC research line and performed the first determination of various quark spin distributions via measurements of spin asymmetries in Semi-Inclusive DIS (SIDIS) reactions. At the same time, the Fermi National Laboratory (FermiLab) started to use a polarised proton beam at 200 GeV/c on a proton target to study p-p reactions. All the experiments mentioned above have nowadays completed their data takings and the subsequent analysis of collected data, providing a boost in the knowledge of the nucleon structure but leaving a certain number of open issues to be further explored by new experimental programmes.

In 1995 a new experiment named HERMES was put in operation at the Deutsches Elektronen-Synchrotron (DESY). It was employing an innovative technique for the polarised gas-targets using pure nuclear-polarised atoms of

---

[3]Zero Gradient Synchrotron.

hydrogen or deuterium. This practice allows for measurements with highly po-larised nucleons and eliminates one of the sources of systematics, the uncertainty in the determination of the so-called dilution factor[4]. Making (SI)DIS measure-ments using electron and positron beams scattering off different targets (H, D, ^{3}He), HERMES has brought a vast spectrum of interesting results, significantly increasing the knowledge on the nucleon spin structure. These include many publications on proton, neutron and deuteron structure functions and their quark flavour dependence.

A few years later, in 2002, the COMPASS experiment at CERN has started its data taking. The broad physics programme of the so-called Phase-I ended-up in 2012 and included several years of (SI)DIS measurements that lead to significant improvements in the understanding of the spin-dependent structure functions of the deuteron [50] and of the proton [51] as well as different flavour contributions [52].

Approaching the new millennium, two more facilities joined the effort to investigate the nucleon structure: JLab and RHIC. The former started to take data in 1999 with three dedicated experiments (identified by the experimental hall names): HALL A, scattering a e^- beam off a ^{3}He target [53], HALL B [5], making use of NH_3 and ND_3 targets [54], and HALL C. A new hall, named HALL D, has been recently added.

RHIC, the Relativistic Heavy Ion Collider realised at the Brookhaven National Laboratory (BNL), started the data taking in 2002, being the first collider able to handle polarised proton collisions. Three over four experiments at RHIC have been dedicated to the polarisation-related studies: BRAHMS, studying the transversely polarised proton collisions (physics programme declared over in 2006), PHENIX and STAR, that are currently taking data with longitudinally and transversely polarised proton beams.

1.5.1   Experimental results related to the spin-dependent structure function g_1

All the mentioned experiments contributed, in different ways, to improve the knowledge of the spin structure of the nucleon. Despite this, at the beginning of the '90s, the proton spin puzzle was still far to be solved entirely. Although the data was globally in good agreement between different measurements, a lot of questions remained unanswered. What is the nature of the proton spin? How is it built up from the spins and the angular momenta of its constituents? Why is the

---

[4]See Sec. 4.8

[5]Also known as Continuous Electron Beam Accelerator Facility (CEBAF) Large Angle Spectrometer (CLAS).

quark contribution to the proton spin so small? These are just a few open questions that were addressed by the measurements performed at different facilities.

In this section, the key-results related to the spin-dependent structure functions achieved in the last decades are presented. Several measurements were performed aiming to extract the $g_1(x, Q^2)$ spin-dependent structure function. The world data available so far for $g_1^p(x, Q^2)$, coming from different facilities, are shown in Fig. 1.3, as a function of Q^2 and for various mean values of x. A general consistency among all the proton data sets collected by different experiments can be observed. The light quarks contribution to the proton spin can be reconstructed
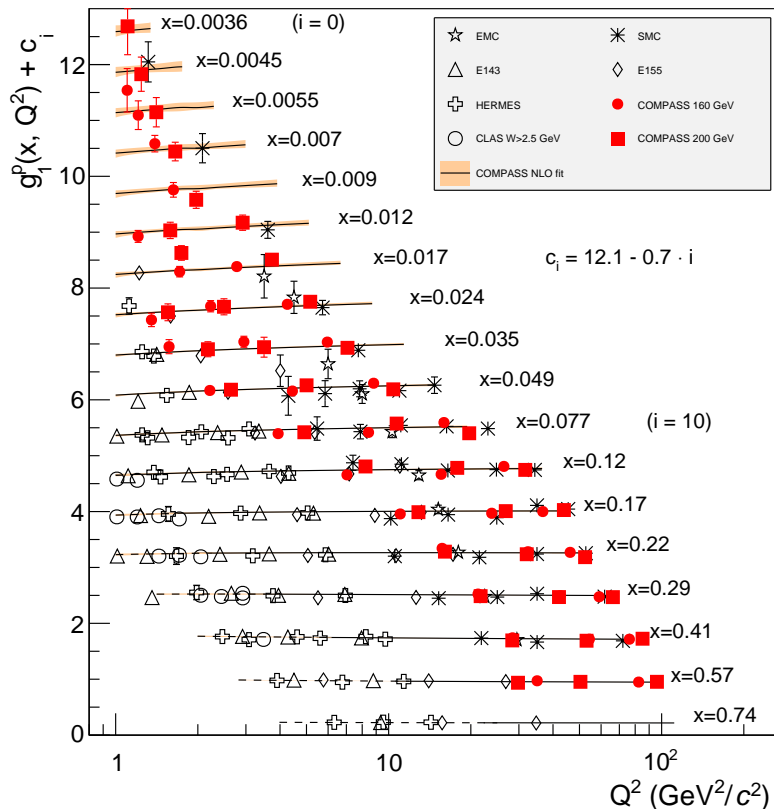
Fig. 1.3 World data on the spin-dependent structure function $g_1(x, Q^2)$ of the proton, as a function of Q^2 for various values of x. The data is coming from EMC [49], SMC [55], E143 [47], E155 [56], HERMES [57] and CLAS[54]. In addition, the COMPASS data are also displayed using red markers (full circles: 160 GeV, full squares: 200 GeV). The lines represent the Q^2 dependence for each value of x, as determined from a NLO QCD fit described in Ref. [58]. The dashed ranges represent the region with $W^2 < 10$ $(GeV/c^2)^2$. Plot taken from Ref. [58]

via semi-inclusive measurements of fast pions and kaons produced in the current fragmentation region in polarised DIS reactions. Extracting asymmetries arising in such reactions it was possible to access convolutions of quark polarised distribution functions with the Fragmentation Function (FF) describing the mechanism of

hadron production from the struck quark. The contributions were disentangled using FFs extracted from global analysis of relevant experimental data on hadron productions [59]. The SMC [60, 61] and HERMES [62–64] experiments were at the forefront in this field, measuring the first moment for valence quark and light-sea polarisation. The information was then enriched by a second generation of data collected with more precision by HERMES [65] and lately also by COMPASS [52]. A summary of the first moment for valence quark and light sea-polarisation extracted by these experiments is listed in Tab. 1.1. COMPASS and HERMES were able also to determine the sum of strange and anti-strange polarisations $\Delta s(x)$. Obtained results are compared in Fig. 1.4.

The production of $W^{\pm}$ bosons in longitudinally polarised proton-proton collisions represents another complementary way to access the valence and sea quark helicity distributions at a high scale, $Q \sim M_W$, without the need of FF as in SIDIS. RHIC W-boson production program goes exactly in this direction. A parity-violating asymmetry for W^+ production in $p+p$ collisions at $\sqrt{s} = 500\text{-}510$ GeV, consistent with predictions based on anti-quark helicity distributions extracted from SIDIS, was observed by PHENIX [66] and STAR [67].
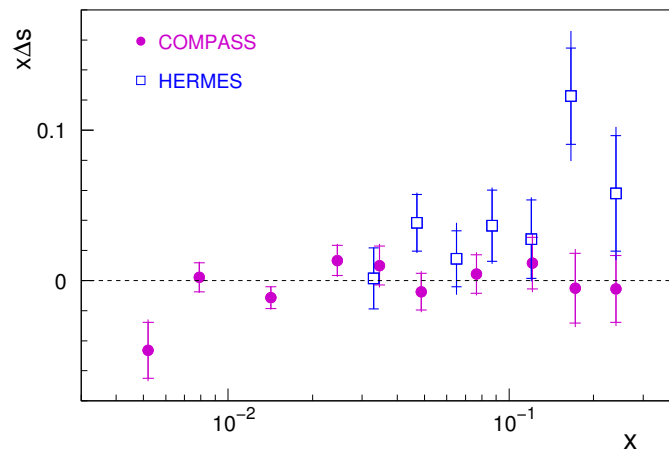
Fig. 1.4 Results for the strangeness polarisation $x\Delta s(x)$ from COMPASS [52] and HERMES [65], shown as function of x. The values are obtained in a leading order analysis of asymmetries measured in SIDIS and using FF resulting from a global data fit performed by the DeFlorian-Stratmann-Sassot (DSS) group [59]. The inner error bar shows the statistical uncertainty, while the full bar represents the quadratic sum of statistical and systematic errors. The integrated first moments are $\Delta s(x) = 0.037 \pm 0.019 \pm 0.027$ for HERMES ($0.02 < x < 0.6$) and $\Delta s(x) = \text{-}0.02 \pm 0.02 \pm 0.02$ for COMPASS ($0.004 < x < 0.7$).

The experimental efforts were focused also on the determination of gluon contribution to the target spin. The FNAL E581/704 collaboration was the first to measure the gluon polarisation, using a 200 GeV polarised proton beam impinging on a polarised proton target. Within their limited sensitivity, they found small ef-

Experiment	x range	Q^2 (GeV/c^2)^2	Δu_v	Δd_v	$\Delta \bar{u}$	$\Delta \bar{d}$
SMC	0.003 - 0.7	10	$0.73 \pm 0.10 \pm 0.07$	$-0.47 \pm 0.14 \pm 0.08$	$0.01 \pm 0.04 \pm 0.03$	$0.01 \pm 0.04 \pm 0.03$
HERMES	0.023 - 0.6	2.5	$0.60 \pm 0.07 \pm 0.04$	$-0.17 \pm 0.07 \pm 0.05$	$0.00 \pm 0.04 \pm 0.02$	$-0.05 \pm 0.03 \pm 0.01$
COMPASS	0.006 - 0.7	10	$0.67 \pm 0.03 \pm 0.03$	$-0.28 \pm 0.06 \pm 0.03$	$0.02 \pm 0.02 \pm 0.01$	$-0.05 \pm 0.03 \pm 0.02$

Table 1.1 First moment of valence quark and light-sea polarisation measured from SMC, HERMES and COMPASS. The extracted sea polarisation are compatible with zero. The x range and the Q^2 of each extraction are also quoted. The integrated sea value was evaluated from data up to $x = 0.3$ and, in case of SMC, assuming the polarised sea to be isospin symmetric.

Experiment	$< x_g >$	Hard scale (GeV/c)^2	$\Delta g/g$
HERMES (high p_T) [70]	0.17	~ 2	$0.41 \pm 0.18 \pm 0.03$
HERMES (inclusive hadrons) [73]	0.22	1.35	$0.049 \pm 0.034 \pm 0.010^{+0.125}_{-0.099}$
SMC (high p_T) [69]	0.07	3	$-0.20 \pm 0.28 \pm 0.10$
COMPASS ($Q^2 < 1$) [71]	0.085	3	$0.016 \pm 0.058 \pm 0.054$
COMPASS ($Q^2 > 1$) [74]	0.09	3	$0.125 \pm 0.060 \pm 0.063$
COMPASS (Open charm, LO) [75]	0.11	13	$-0.06 \pm 0.21 \pm 0.08$
COMPASS (Open charm, NLO) [75]	0.20	13	$-0.13 \pm 0.15 \pm 0.15$

Table 1.2 First moment of valence quark and light-sea polarisation measured from SMC, HERMES and COMPASS. The extracted sea polarisations are compatible with zero. The x ranges and corresponding Q^2 values are also quoted. The integrated sea value was evaluated from data up to $x = 0.3$ and, in case of SMC, assuming the polarised sea to be isospin symmetric.

fects suggesting $\Delta g/g$ to be not so large in the region $0.05 < x_g < 0.35$ [68]. Later on, SMC [69] and HERMES [70] also attempted to access the gluon polarisation reconstructing high p_T hadrons originated in DIS reactions. The same approach was also applied by COMPASS [71], that in parallel used also the semi-inclusive measurements of charmed mesons [72] to investigate the photon-gluon fusion mechanism. All these measurements of $\Delta g/g$ in fixed target experiments are summarised in Tab. 1.2 and shown in Fig. 1.5.

1.6 Description of the nucleon structure

A comprehensive understanding of the structure of the nucleon, in terms of quarks and gluons, remains nowadays one of the most challenging task in particle physics. Within the QPM, a fast moving nucleon is described as a collection of quasi-free quarks, antiquarks and gluons. The longitudinal momentum of these particles can be described in terms of parton densities. These ideas are implemented in the
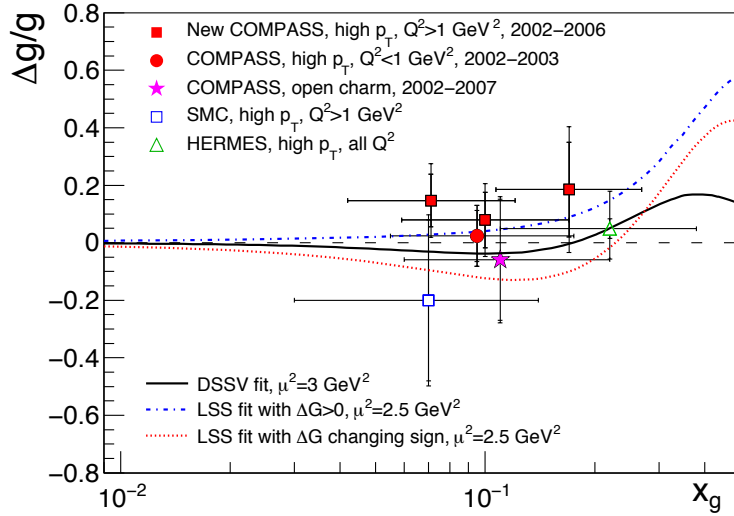
Fig. 1.5 Gluon polarisation $\Delta g/g$ from leading order analyses of semi-inclusive hadron production measurements in DIS process as function of the probed gluon momentum fraction x_g. The NLO fits from de Florian *et al.* [76] and Leader *et al.* [77] are also displayed. The inner error bar represents the statistical error, while the full one consists in the quadratic sum of statistical and systematic uncertainties.

collinear factorisation formalism which, in several cases, fails to describe obtained experimental results, suggesting that the conventional parton densities quantify correctly the nucleon structure just in one single space dimension and that possible transverse motion of partons inside the nucleon also needs to be considered.
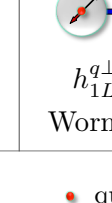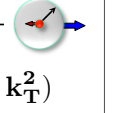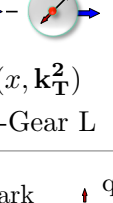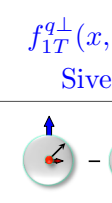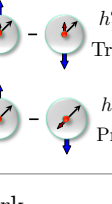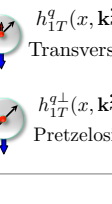
While extending the nucleon spin structure description considering the plane transverse to the direction of motion of the parent nucleon, two complementary aspects should be taken into account. Firstly, the non-zero intrinsic transverse momentum of the partons in the nucleon which should have an impact on the transverse momenta of the produced hadron in SIDIS and secondly the spatial distribution of the partons (the distance from the transverse 'centre' of the nucleon) which can be studied in Deeply Virtual Compton Scattering processes. In the former case, the spin and quark transverse motion correlations are encoded in the Transverse-Momentum-Dependent (TMD) Parton Distribution Functions (PDFs), while in the latter, the so-called Generalised Parton Distributions (GPDs) are introduced.

In both cases, the length or momentum scales are typical of the non-perturbative approach. This feature contrasts with the dimensionless longitudinal momentum fractions on which all the PDFs depend. Therefore, the TMDs and GPDs represent a more direct way to study non-perturbative phenomena, as the confinement. Transverse momentum and position of the partons are interrelated by the uncertainty principle and cannot be determined simultaneously. However, related

phenomena can be unified within the concept of the so-called Wigner distributions. For more details and theoretical aspects of TMDs, GPDs and Wigner distributions the reader is referred to Ref. [78].

1.7 Transverse Momentum Dependent Parton Distribution Functions

The TMD PDFs are QCD objects describing the correlations between the intrinsic transverse momentum of the partons, their spin and the spin of the parent nucleon. In QCD, there are eight twist-2 (leading-twist) quark TMD PDFs [13, 79, 80]. All twist-2 quark TMD PDFs are listed in Fig. 1.6 where they are ordered according to their relation with the polarisation of the parent nucleon and with the polarization of the quark.

		Nucleon Polarisation		
		U	**L**	**T**
Quark Polarisation	**U**	$f_1^q(x, \mathbf{k_T^2})$ Number Density		$f_{1T}^{q\perp}(x, \mathbf{k_T^2})$ Sivers
	L		$g_1^q(x, \mathbf{k_T^2})$ Helicity	$g_{1T}^{q\perp}(x, \mathbf{k_T^2})$ Worm-Gear T
	T	$h_1^{q\perp}(x, \mathbf{k_T^2})$ Boer-Mulders	$h_{1L}^{q\perp}(x, \mathbf{k_T^2})$ Worm-Gear L	$h_{1T}^{q}(x, \mathbf{k_T^2})$ Transversity / $h_{1T}^{q\perp}(x, \mathbf{k_T^2})$ Pretzelosity

Nucleon ⬆ Nucleon spin • quark ⭡ quark spin ╱ $\mathbf{k_T}$

Fig. 1.6 Twist-two TMD PDFs classified according to the polarisation of the nucleon (columns) and quarks (rows). U, L and T stands for Unpolarised, Longitudinally polarised and Transversely polarised. The $h_1^{q\perp}(x, \mathbf{k_T^2})$ and $f_{1T}^{q\perp}(x, \mathbf{k_T^2})$ distributions are called naive time reversal-odd TMD PDFs.

Three functions, namely the unpolarised parton distribution $f_1^q(x, \mathbf{k_T^2})$, the helicity distribution $g_1^q(x, \mathbf{k_T^2})$ and the transversity distribution $h_{1T}^q(x, \mathbf{k_T^2})$ survive

integration over the transverse momentum. The other five TMD PDFs vanish when integrated over k_T, hence they exist just in the TMD approach. The three TMDs denoted by h describe distributions of transversely polarised quarks. They are chiral-odd and thus can be accessed only in the form of convolutions with other chiral-odd partners. The TMD PDFs can be accessed by measuring spin (in)dependent asymmetries arising in lepton-nucleon and hadron-hadron scattering processes. In the former case, these asymmetries are proportional to convolutions of TMD PDFs and FFs of the target hadron and the struck quark, respectively, while in hadron-hadron scattering they are linked to convolutions of the TMDs of the two hadrons participating in the reaction. Within the concept of generalised universality of TMD PDFs, nucleon TMD PDFs accessed in both these ways are expected to be process-independent.

Sivers and Boer-Mulders TMDs have been a matter of particular interest in the last decades because of their oddity under time reversal. Due to this feature, such correlations were believed to be forbidden until 2002, when it was shown that the effects associated to these two functions could be non-zero in QCD-processes with initial- or final-state interactions [81, 82]. The former case may occur in Drell-Yan (DY) reactions [83], while the latter in SIDIS. The initial colour interactions taking place in DY and the final state interactions in SIDIS lead to a process-dependent sign difference in the Sivers and Boer-Mulders distribution while measuring them via the two different processes [17]:

$$f_{1T}^{q\perp}(x,\mathbf{k_T^2})|_{SIDIS} = -f_{1T}^{q\perp}(x,\mathbf{k_T^2})|_{DY} \tag{1.12}$$

$$h_1^{q\perp}(x,\mathbf{k_T^2})|_{SIDIS} = -h_1^{q\perp}(x,\mathbf{k_T^2})|_{DY} \tag{1.13}$$

On the other hand time-reversal even TMD PDFs, like the transversity and the pretzelosity functions, are expected to be genuinely universal (process independent). The experimental test of these fundamental predictions is one of the major challenges in hadron physics. While the SIDIS phenomena were extensively studied by various experimental collaborations in the '90s and the '00s, measuring sizable asymmetries at the level of about 5-10 % for proton and neutron targets, the polarised Drell-Yan measurements were still missing. Therefore, the interest of the spin-community on the topic has rapidly grown, giving rise to various experimental programmes aiming to perform polarised Drell-Yan measurements and to test the predicted sign-change of Sivers and Boer-Mulders functions, and the pQCD generalised universality concept for the TMD PDFs.

1.8 Semi-Inclusive Deep Inelastic Scattering

Several physics programmes, started in the last decades, were devoted to the study of the internal spin structure of the nucleon via Semi-Inclusive DIS (see Fig. 1.7) for the diagram) measurements. In comparison to the *inclusive* DIS measurements, in addition to the scattered lepton also at least one hadron is registered in the final state

$$\ell(k,\lambda) + N(P,S) \rightarrow \ell'(k') + h(p) + X \tag{1.14}$$

Because of the confinement property of QCD, the interacting quark and the target remnants promptly fragment into hadrons. This part of the process is parametrised via Fragmentation Functions (FFs). They describe how the color-carrying quarks and gluons transform into color-neutral particles such as hadrons or photons. Fragmentation processes involve low Q^2 (long distance) reactions and thus appear as non-perturbative ingredients in QCD factorisation theorems.
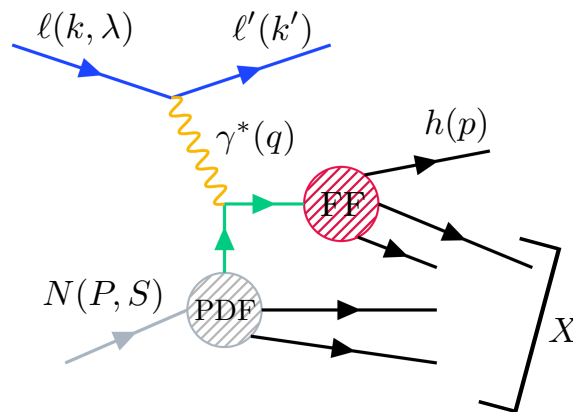
Fig. 1.7 Feynman diagram of the Semi-Inclusive Deep Inelastic Scattering process, $\ell(k,\lambda) + N(P,S) \rightarrow \ell'(k') + h(p) + X$.

The best studied FF is the unpolarised fragmentation function D_q^h. It describes the fragmentation of an unpolarised parton of type q into an unpolarised hadron of type h, where the hadron carries the fraction z of the parton momentum The unpolarised FF D_q^h is chiral-even and T-even.

The Collins FF $H_1^{q\perp}$ describes the correlation between transverse momentum gained during the fragmentation and the transverse polarisation of the struck quark. It is chiral-odd and T-odd. The SIDIS process is described by set of DIS (x, y, Q^2)and SIDIS-specific kinematic variables (momentum fraction z, transverse momentum of the produced hadron p_T). The SIDIS kinematic variable z is defined

as follows:

$$z = \frac{P \cdot p}{P \cdot q} \qquad (1.15)$$

where $q = k - k'$ denotes the four-momentum of the exchanged virtual photon and p is the four momentum of the produced hadron.

1.8.1   SIDIS cross-section

In this Thesis the SIDIS process and the corresponding cross section are discussed within the one-photon exchange approximation and neglecting the lepton mass. In Fig. 1.8 a schematic view of the adopted reference frame (the so-called γ^*N target rest frame) and definitions of the relevant azimuthal angles are shown. The γ^*N frame is a right-handed coordinate system defined by the virtual photon direction (z-axis), lepton transverse (w.r.t the z-axis) momentum direction (x-axis), and respective normal vector (y-axis). Symbols l, l' and q represent the four-momenta of the incident and outgoing leptons and virtual photon (γ^*), respectively, while vectors $\mathbf{p}$ and $\mathbf{p}_T$ denote the momentum and the transverse momentum of the produced hadron h. The angle ϕ_h (ϕ_S) define the azimuthal orientation of the hadron momentum (target polarisation vector) with respect to the lepton scattering plane calculated about the virtual-photon momentum direction. In the introduced framework, S_T is the transverse component of the target polarisation vector $\mathbf{S}$.

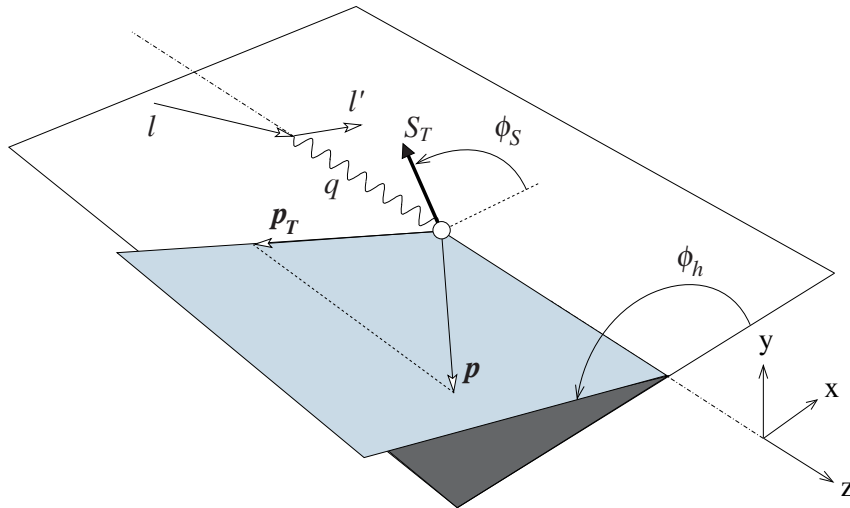
Fig. 1.8 Definition of ϕ_S and ϕ_h angles in the γ^*N target rest frame.

Adopting the aforementioned notations and considerations, the general expression for the cross section of unpolarised-hadron production in polarised-lepton

SIDIS off a transversely polarised nucleon can be written in the following model-independent way [79, 84]:

$$
\frac{d\sigma}{dx\,dy\,dz\,p_T\,dp_T\,d\phi_h\,d\phi_S} = 2\left[\frac{\alpha}{xyQ^2} \frac{y^2}{2(1-\varepsilon)}\left(1+\frac{\gamma^2}{2x}\right)\right](F_{UU,T}+\varepsilon F_{UU,L})
$$

$$
\times \Bigg\{ 1 + \varepsilon A_{UU}^{\cos 2\phi_h}\cos(2\phi_h) + \sqrt{2\varepsilon(1+\varepsilon)}A_{UU}^{\cos\phi_h}\cos\phi_h + \lambda\sqrt{2\varepsilon(1-\varepsilon)}A_{LU}^{\sin\phi_h}\sin\phi_h
$$

$$
+ S_T\Big[A_{UT}^{\sin(\phi_h-\phi_S)}\sin(\phi_h-\phi_S) + \varepsilon\Big(A_{UT}^{\sin(\phi_h+\phi_S)}\sin(\phi_h+\phi_S) + A_{UT}^{\sin(3\phi_h-\phi_S)}\sin(3\phi_h-\phi_S)\Big) \qquad (1.16)
$$

$$
+ \sqrt{2\varepsilon(1+\varepsilon)}\Big(A_{UT}^{\sin\phi_S}\sin\phi_S + A_{UT}^{\sin(2\phi_h-\phi_S)}\sin(2\phi_h-\phi_S)\Big)\Big]
$$

$$
+ S_T\lambda\Big[\sqrt{(1-\varepsilon^2)}A_{LT}^{\cos(\phi_h-\phi_S)}\cos(\phi_h-\phi_S)
$$

$$
+ \sqrt{2\varepsilon(1-\varepsilon)}\Big(A_{LT}^{\cos\phi_S}\cos\phi_S + A_{LT}^{\cos(2\phi_h-\phi_S)}\cos(2\phi_h-\phi_S)\Big)\Big]\Bigg\},
$$

where $\varepsilon = \frac{(1-y-\frac{1}{4}\gamma^2 y^2)}{(1-y+\frac{1}{2}y^2+\frac{1}{4}\gamma^2 y^2)}$ is the ratio of longitudinal and transverse photon fluxes, λ represents the longitudinal polarisation of the beam and $\gamma = 2Mx/Q$. Eq. 1.16 comprises three unpolarised and eight transverse-target-polarisation-dependent modulations in ϕ_h and ϕ_S angles. Each modulation gives rise to a $A_{BT}^{w_i(\phi_h,\phi_S)}$ Unpolarised or Transverse-Spin-dependent Asymmetry (UA and TSA, respectively) defined as the ratio of the corresponding structure function $F_{BT}^{w_i(\phi_h,\phi_S)}$ to the unpolarised one $F_{UU} = F_{UU,T} + \varepsilon F_{UU,L}$. Here the superscript, $w_i(\phi_h,\varphi_S)$, indicates the associated modulation, while subscripts denote beam (B) and target (T) polarisation states, respectively ("U" stands for unpolarised, "L" for longitudinal polarisation and "T" for transverse polarisation). In total, eleven asymmetries appear in Eq. 1.16. Among the eight TSAs, the five depending only on S_T are called Single-Spin Asymmetries (SSA), while the three depending both on S_T and λ are known as Double-Spin Asymmetries (DSA). The UAs do not depend on the target polarisation. Only one out of three UAs depends on λ.

1.8.2   QCD parton model interpretation of the SIDIS asymmetries

Within the QCD parton model, the five asymmetries marked in red in Eq. 1.16 (1 UA and 4 TSAs) have a pure *twist-two* interpretation in terms of convolutions of TMD PDFs and FFs. The $A_{UT}^{\sin(\phi_h-\phi_S)}$ (Sivers) and $A_{UT}^{\sin(\phi_h+\phi_S)}$ (Collins) TSAs are the most studied ones. The corresponding structure functions are interpreted as convolutions of Sivers PDF with the ordinary fragmentation function (D_q^h) and transversity PDF with Collins FF ($H_1^{q\perp}$), respectively. The $A_{UT}^{\sin(3\phi_h-\phi_S)}$ asymmetry

allows to access the pretzelosity PDF convoluted with Collins FF, while $A_{LT}^{\cos(\phi_h - \phi_S)}$ is related to the Worm-Gear-T PDF (also know as Kotzinian-Mulders TMD PDF). Measuring the UA $A_{UU}^{\cos(2\phi_h)}$ one can access the Boer-Mulders TMD PDF convoluted with $H_1^{q\perp}$. Note that this asymmetry receives contribution also from the so-called Cahn effect [10], related to the intrinsic transverse motion of the quarks in the target nucleon. The Boer-Mulders effect contributes at *twist-two* level to the $\cos(2\phi_h)$ amplitude, whereas the Cahn contribution enters at twist-4 level (with a $1/Q^2$ suppression) [85]. A summary on the interpretation of LO UAs and TSAs in terms of convolutions of PDFs and FFs is presented in Tab. 1.3.

Table 1.3 QPM interpretation of Leading Order UAs and TSAs in terms of convolutions of PDFs and FFs.

LO UA/TSA	*twist-2*: **PDF** $\otimes$ **FF**
$A_{UU}^{\cos(2\phi_h)}$	$h_1^{\perp q} \otimes H_{1q}^{\perp h}$
$A_{UT}^{\sin(\phi_h - \phi_S)}$	$f_{1T}^{\perp q} \otimes D_{1q}^h$
$A_{UT}^{\sin(\phi_h + \phi_S - \pi)}$	$h_1^q \otimes H_{1q}^{\perp h}$
$A_{UT}^{\sin(3\phi_h - \phi_S)}$	$h_{1T}^{\perp q} \otimes H_{1q}^{\perp h}$
$A_{LT}^{\cos(\phi_h - \phi_S)}$	$g_{1T}^q \otimes D_{1q}^h$

The other 6 asymmetries present in Eq. 1.16 and marked in blue (2 UAs and 4 TSAs) are at sub-leading order in Q^{-1}, and involve a mixture of *twist-2* and, induced by largely unexplored quark-gluon correlations, *twist-3* parton distribution and fragmentation functions. However, by applying the widely adopted simplification known as Wandzura-Wilczek approximation (WWA) [86], the interpretation of these higher twist objects can be brought to the *twist-2* level [79, 84]. The TMD interpretation of sub-leading UAs and TSAs is summarised in Tab. 1.4.

1.9 A selection of results from SIDIS measurements

Various SIDIS spin-phenomena have been widely studied at the COMPASS, HERMES and JLab experiments. All the modulations mentioned above have been measured in different facilities bringing intriguing results that were crucial to draw the path of theoretical and phenomenological developments. In the following, particular attention is given to the published results on Boer-Mulders, Collins and Sivers effects. Preliminary COMPASS results on the pretzelosity TMD PDF related asymmetry are also briefly discussed. An overview of the global results available so far for LO UAs and TSAs is given in Tab. 1.5.

Table 1.4 Interpretation of sub-leading UAs and TSAs in terms of convolutions of PDFs and FFs. The third column shows the *twist-2* approximation obtained applying the Wandzura-Wilczek approximation.

sub-leading **UA/TSA**	*twist-3* **PDF** $\otimes$ **FF**	**WWA** *twist-2*: **PDF** $\otimes$ **FF**
$A_{UU}^{\cos(\phi_h)}$	$xh^q \otimes H_{1q}^{\perp h}, \, xf^{\perp q} \otimes D_{1q}^h$	$f_1^q \otimes D_{1q}^h, \, h_1^{\perp q} \otimes H_{1q}^{\perp h}$
$A_{LU}^{\sin(\phi_h)}$	$xe^q \otimes H_{1q}^{\perp h}, \, xg^{\perp q} \otimes D_{1q}^h$	$f_1^q \otimes H_{1q}^{\perp h}, \, h_1^{\perp q} \otimes D_{1q}^h$
$A_{UT}^{\sin(\phi_S)}$	$xf_T^q \otimes D_{1q}^h, \, xh_T^q \otimes H_{1q}^{\perp h}, \, xh_T^{\perp q} \otimes H_{1q}^{\perp h}$	$f_{1T}^{\perp q} \otimes D_{1q}^h, \, h_1^q \otimes H_{1q}^{\perp h}$
$A_{UT}^{\sin(2\phi_h - \phi_S)}$	$xf_T^{\perp q} \otimes D_{1q}^h, \, xh_T^q \otimes H_{1q}^{\perp h}, \, xh_T^{\perp q} \otimes H_{1q}^{\perp h}$	$f_{1T}^{\perp q} \otimes D_{1q}^h, \, h_1^q \otimes H_{1q}^{\perp h}$
$A_{LT}^{\cos(\phi_S)}$	$xg_T^q \otimes D_{1q}^h, \, xe_T^q \otimes H_{1q}^{\perp h}, \, xe_T^{\perp q} \otimes H_{1q}^{\perp h}$	$g_{1T}^q \otimes D_{1q}^h$
$A_{LT}^{\cos(2\phi_h - \phi_S)}$	$xg_T^{\perp q} \otimes D_{1q}^h, \, xe_T^q \otimes H_{1q}^{\perp h}, \, xe_T^{\perp q} \otimes H_{1q}^{\perp h}$	$g_{1T}^q \otimes D_{1q}^h$

Table 1.5 Experimental results related to *twist-two* TMD PDFs in SIDIS with different polarisations of the beam (U,L,T) and of the target (U, T).

UA/TSA	TMD PDF	Experiment	$\sqrt{s}$ (GeV)	Target	Observed hadron types
$A_{UT}^{\sin(\phi_h + \phi_S)}$	Transversity	COMPASS	18	^{6}LiD	$h^\pm, \pi^\pm, K^\pm, K^0$ [87, 88]
				NH$_3$	$h^\pm$ [89, 90], $\pi^\pm, K^\pm$ [91]
		HERMES	7.4	H	$\pi^\pm, \pi^0, K^\pm$ [92, 93]
		JLab - Hall A	3.5	^{3}He	$\pi^\pm$ [94]
$A_{UT}^{\sin(\phi_h - \phi_S)}$	Sivers	COMPASS	18	^{6}LiD	$h^\pm, \pi^\pm, K^\pm, K^0$ [87, 88]
				NH$_3$	$h^\pm$ [90, 95], $\pi^\pm, K^\pm$ [91]
		HERMES	7.4	H	$\pi^\pm, \pi^0, K^\pm$ [92, 96]
		JLab - Hall A	3.5	^{3}He	$\pi^\pm$ [94]
$A_{UU}^{\cos(2\phi_h)}$	Boer-Mulders	COMPASS	18	^{6}LiD	$h^\pm$ [97]
		HERMES	7.4	H	$\pi^\pm, K^\pm$ [98]
		JLab - Hall A	3.5	^{3}He	π^+ [94]
$A_{UT}^{\sin(3\phi_h - \phi_S)}$	Pretzelosity	COMPASS	18	^{6}LiD	$h^\pm$ [99]
				NH$_3$	$h^\pm$ [100]
		HERMES	7.4	H	$\pi^\pm, K^\pm$ [101]
		JLab - E06-010	2.1	^{3}He	$\pi^\pm$ [102]
$A_{LT}^{\cos(\phi_h - \phi_S)}$	Worm-Gear T	COMPASS	18	^{6}LiD	$h^\pm$ [99]
				NH$_3$	$h^\pm$ [100]
		HERMES	7.4	H	$\pi^\pm, \pi^0, K^\pm$ [103]
		JLab - Hall A	3.5	^{3}He	$\pi^\pm$ [104]

1.9.1   Experimental SIDIS results related to the Boer-Mulders TMD PDF

The Boer-Mulders TMD PDF [80], describes the correlation between transversely polarised quarks inside an unpolarised nucleon and their intrinsic transverse momentum. As discussed in Sec. 1.7, it is a T-odd function. However, the Boer-Mulders TMD PDF is also a chiral-odd object, and thus it can be probed only in a conjunction with a second chiral-odd function (the Collins FF in the SIDIS case). In past two decades measurements of the Boer-Mulders TMD PDF related amplitudes appearing in Eq. 1.16 ($A_{UU}^{\cos(2\phi_h)}$) have been performed by HERMES [98] (see Fig. 1.9), COMPASS [97] (see Fig. 1.10) and CLAS [105].   The
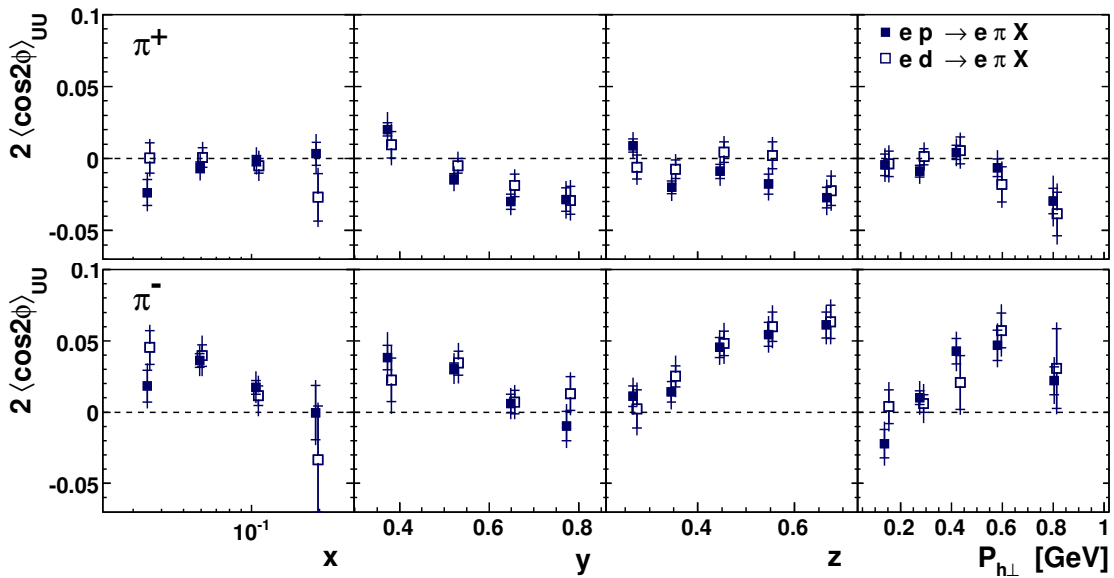

Fig. 1.9 HERMES results [98] for $A_{UU}^{\cos(2\phi_h)}$ amplitudes for π^+ (upper row) and π^- (lower row). Closed and open squares represent amplitudes extracted from hydrogen and deuterium targets, respectively. The inner bar represents the statistical uncertainty, while the outer bar the total uncertainty.

interpretation of the results for $A_{UU}^{\cos(2\phi_h)}$ is complicated by the contribution of the *twist-four* Cahn effect, which accounts for the non-collinear kinematics of quarks in the elementary subprocess $\ell q \to \ell' q$ and has been estimated to be sizable even in the COMPASS kinematic range [106, 107]. The proton and deuteron HERMES results for $A_{UU}^{\cos(2\phi_h)}$ were found to be in agreement, which might indicate that the Boer-Mulders TMD PDFs of u and d quarks are very similar.

In past years, several phenomenological extractions of Boer-Mulders TMD PDF from global fits of existing SIDIS and Drell-Yan (see next sections) experimental data have been performed. The presence of Cahn and other higher-twist contributions to the $A_{UU}^{\cos(2\phi_h)}$ asymmetry, as well as poor knowledge of transverse
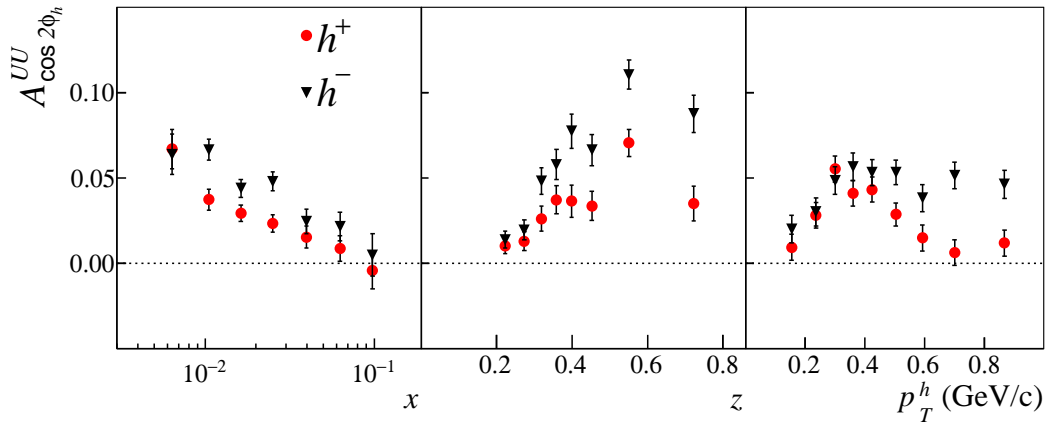
Fig. 1.10 COMPASS results [97] for $A_{UU}^{\cos(2\phi_h)}$ amplitudes for positive (red circles) and negative (**black** triangles) hadrons, extracted from data collected with deuterium target. The results are displayed as functions of x, z and p_T . The error bars represent the statistical uncertainties.

momentum and flavour dependence of PDFs and FFs, leads to large uncertainties on the Boer-Mulders TMD PDF and non-conclusive results.

1.9.2 Experimental SIDIS results related to the Pretzelosity TMD PDF

The pretzelosity TMD PDF related $A_{UT}^{\sin(3\phi_h-\phi_S)}$ asymmetry was measured at HER-MES [101], COMPASS [99, 100] (see Fig. 1.11) and JLab-E06-010 [102] facilities. The pretzelosity TMD PDF $h_{1T}^{q\perp}(x, \mathbf{k_T^2})$ [108] describes the "non-sphericity" of the spin distribution of quarks in a transversely polarised nucleon. Given its chiral-odd nature, the pretzelosity can be accessed only in a combination with another chiral-odd object, the Collins fragmentation function in SIDIS case. Therefore, for the extraction of $h_{1T}^{q\perp}(x, \mathbf{k_T^2})$ from experimental data a precise knowledge of $H_1^{q\perp}$ is mandatory. The $A_{UT}^{\sin(3\phi_h-\phi_s)}$ is expected to scale according to $\sim p_T^3$ and thus is suppressed by $\sim p_T^2$ with respect to the $\sim p_T$-scaled Collins, Sivers ampli-tudes [79]. In COMPASS kinematics average $\sim p_T$ is about 0.3 GeV/c which leads to a strong suppression of the effect. In Fig. 1.11 COMPASS preliminary results for the $A_{UT}^{\sin(3\phi_h-\phi_S)}$ asymmetry are presented together with the phenomenological fit curves from Ref. [108]. The fit was performed using preliminary COMPASS, HERMES, and JLAB experimental data on proton, and effective deuteron and neutron targets and existing parameterizations for the Collins fragmentation func-tion. Extracted pretzelosty TMD PDFs are shown in Fig. 1.12. The asymmetry was found to be small and compatible with zero within the uncertainties which led to large uncertainty-bands of the extracted TMD PDF. Nevertheless, the resulting

distributions show tendency for up-quark pretzelosity TMD PDF to be positive while for down-quark to be negative.
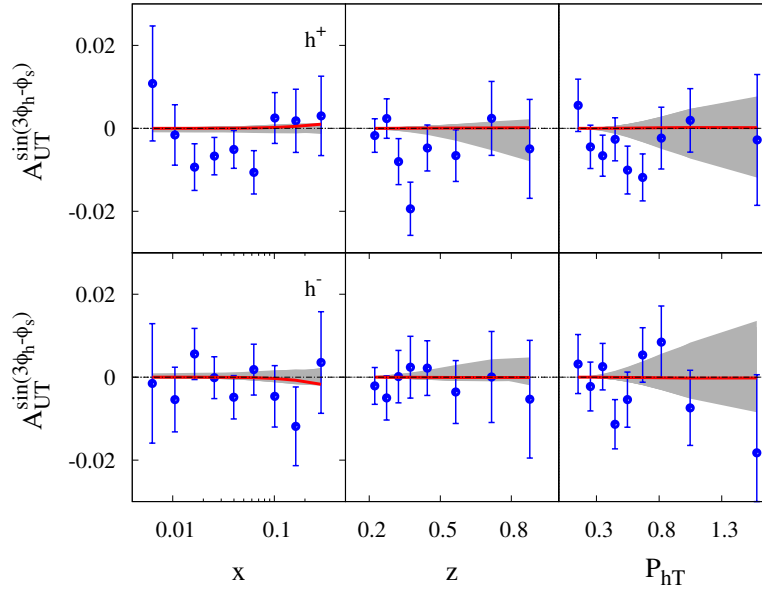

Fig. 1.11 $A_{UT}^{\sin(3\phi_h-\phi_S)}$ measured by COMPASS [100] on NH_3 target in bins of x, z and p_T. The solid line corresponds to the best fit from [108] and the shadowed region corresponds to the uncertainty corridor.
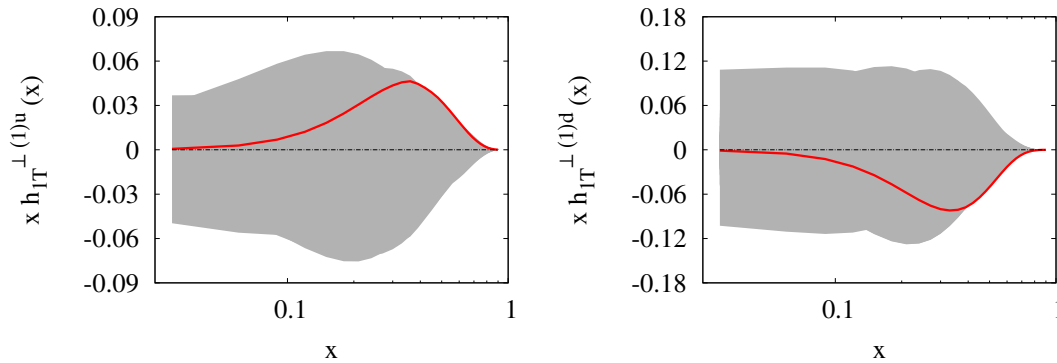

Fig. 1.12 First moment of the pretzelosity distribution extracted from a global fit of preliminary COMPASS, HERMES and JLab data [108] for up (a) and down (b) quarks at $Q^2 = 2.4 \ (GeV/c^2)^2$ The solid line corresponds to the best fit and the shadowed region corresponds to the error corridor.

1.9.3 Experimental SIDIS results related to the Transversity TMD PDF

The transversity distribution h_1^q [109] describes the transverse polarisation of quarks within a transversely polarised nucleon. It represents the only source of information on the nucleon tensor charge, which is related to the first moment of the transversity TMD PDF. The h_1^q is a chiral-odd quantity, thus it cannot be

studied in inclusive DIS reactions. It was widely explored in the recent past in SIDIS reactions where it can be accessed in a convolution with Collins FF. The corresponding azimuthal asymmetry, $A_{UT}^{\sin(\phi_h+\phi_S)}$, is often referred to as Collins effect.

The COMPASS [91] [89, 95], HERMES [92, 93] and JLab Hall A [94] have measured the Collins TSA in various experimental conditions (polarised proton, deuteron and neutron targets, different beam energies). In Fig. 1.13 the COMPASS and HERMES results for Collins effect for charged π production on protons are compared.
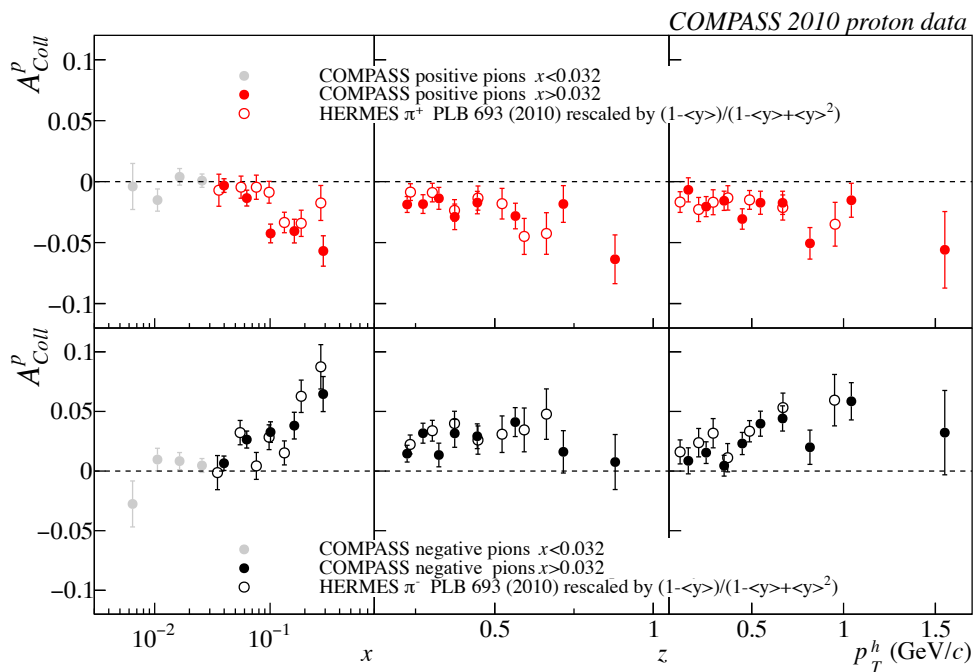

Fig. 1.13 The Collins asymmetries for π^+ (top) and π^- (bottom) measured by COMPASS with proton (NH$_3$) target [91] as a function of x, z and p_T^h, requiring $x > 0.032$. The asymmetries are compared to HERMES proton (H) results, corrected by the corresponding depolarisation factor. In the left column, COMPASS results for $x < 0.032$ are also displayed using shaded dots.

Even if the experiments were working at different Q^2 (the Q^2 at COMPASS is as much as two to three times larger compared to that of HERMES), the results are in statistical agreement. It may be interpreted as an important information on the properties of the Transversity TMD PDF, suggesting a weak dependence of h_1^q on the hard scale. Nevertheless, the comparison between results coming from different facilities operating with different beams and energy cannot be conclusive. The results for π^+ and π^- at small x are compatible with zero, while in the valence region the signal increases with opposite signature in the two cases. Also, a mirror symmetry between π^+ and π^- results can be noticed. Taking into account these
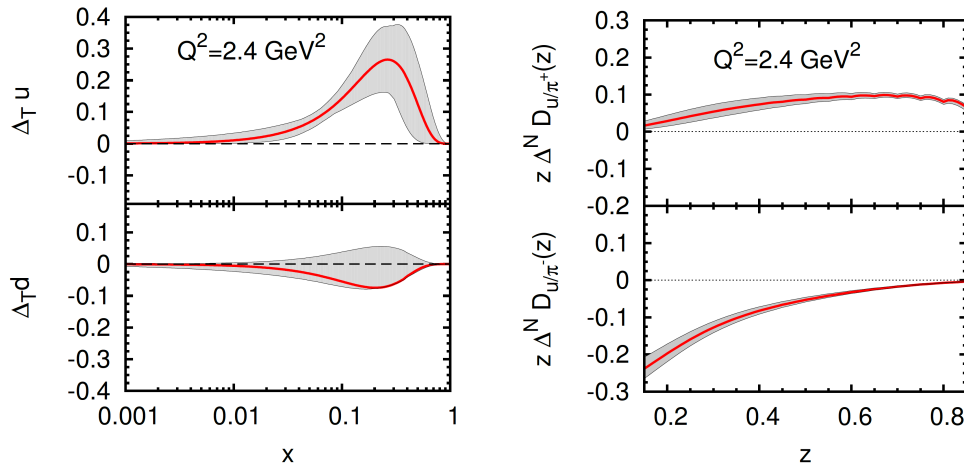
Fig. 1.14 Results from Ref. [110] for the valence u and d quark transversity TMD PDF (left panel) and for the favoured and un-favoured Collins functions (right panel). In both the cases, the extraction is done at $Q^2 = 2.4 \text{ GeV}/c^2$ and the shaded bands represent the uncertainty of the fit.

two observations, one can conclude that the favoured and un-favoured Collins FF are opposite in sign but have a similar magnitude.

A fundamental ingredient for the extraction of h_1^q is the knowledge of $H_1^{q\perp}$ accessible from the analysis of data coming from $e^+ e^-$ colliders such as BELLE and BABAR [111, 112]. A global analysis of COMPASS, HERMES and BELLE results allowed extractions of Transversity TMD PDF and Collins FF. The latest extraction of the transversity function for u and d quarks, performed by Anselmino et al. [110] (see Fig. 1.14), shows that h_1^u is significantly different from zero, while the h_1^d PDF tends to be opposite in sign even if affected by large uncertainties due to lack of precise deuteron data on Collins effect. The favoured and unfavoured Collins FFs are found to be large, with similar magnitudes but opposite signs.

1.9.4 Experimental SIDIS results related to the Sivers TMD PDF

The Sivers TMD PDF [113], $f_{1T}^q(x, \mathbf{k_T^2})$, was first brought up to explain the large transverse single-spin asymmetries observed in the 1970s [40, 41] and 1980s [114]. It allows to describe correlations between the intrinsic transverse momentum k_T of the unpolarised struck quark and the transverse spin S_T of the target nucleon and is sensitive to the angular momentum of the partons inside the nucleon.

Over the years, the Sivers asymmetry has been measured by HERMES [92, 96] and COMPASS [91, 95] for both positive and negative hadrons, making use of deuteron (COMPASS only) and proton targets. The results published by the two experiments in the commonly accessible range of the Bjorken-x variable are superimposed in Fig. 1.15.
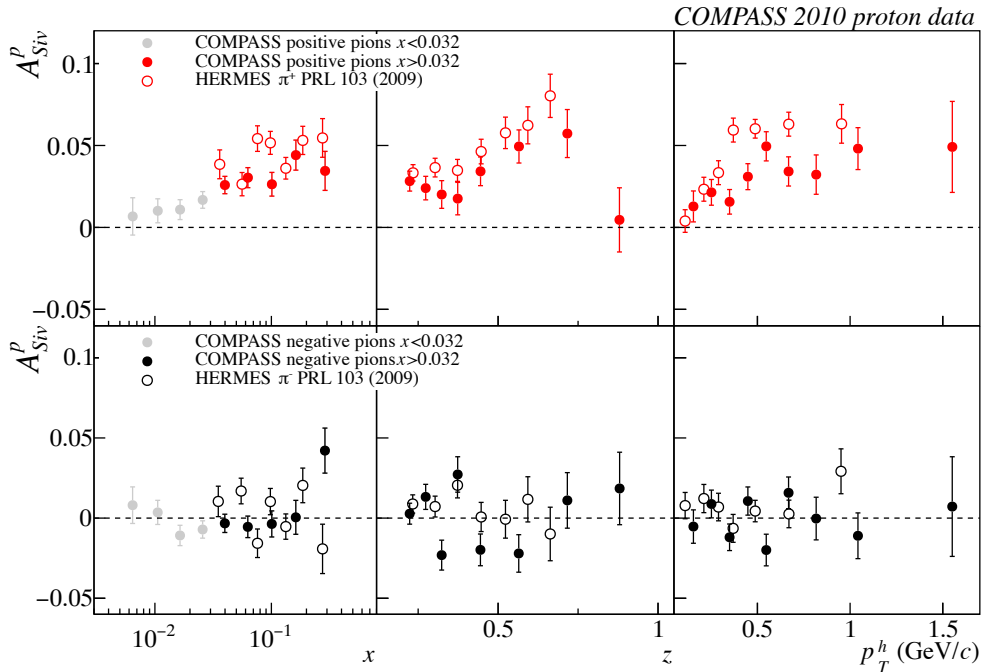
Fig. 1.15 The Sivers asymmetries for π^+ (top) and π^- (bottom) measured by COMPASS with proton (NH$_3$) target [91] as a function of x, z and p_T^h, for $x > 0.032$ range. The asymmetries are compared to HERMES proton (H) results, rescaled by the corresponding depolarisation factor. In the left column, COMPASS results for $x < 0.032$ are also displayed using shaded dots.

In contrast to the Collins case, the Sivers TSA at HERMES was found to be somewhat larger compared to that measured at COMPASS. Here it is important to mention that, at a given x value, COMPASS was operating at mean Q^2 values 2 - 3 times larger with respect to HERMES. This observation brings the discussion to one of the hottest topics in the field of spin-physics arisen in the last years: the study of TMD evolution of various PDFs and FFs and related asymmetries. Thus, the observed behaviour of Sivers effect can be used to adjust the description of the Q^2-dependence of TMDs (see next section for more details). The Sivers asymmetry was also measured with a neutron target by JLab - Hall A experiment [94] in the DIS region and found to be below 5%.

1.9.5 TMD factorisation and evolution

Factorisation theorems [115] provide the link between theoretical concepts and phenomenology, and give great predictive power to the perturbative QCD (pQCD). The PDFs and FFs play a key-role in relating the pQCD-formalism to the parton model concepts. While the standard collinear factorisation works reasonably well for inclusive processes, the more sophisticated TMD factorisation formalism

becomes essential for processes where the intrinsic transverse momentum of partons starts to be important.

The TMD factorisation holds in the limit $Q^2 \to \infty$, neglecting the power corrections of p_T/Q. Therefore TMD factorisation framework can be applied only in kinematic regions of transverse momentum[6] much smaller than the hard scale, $p_T \ll Q$.

Consequently, different mechanisms will dominate the physics in different p_T regions. At high p_T, $\sim Q$, SSAs can be computed in pQCD applying the collinear factorisation theorem, whereas at small $p_T \ll Q$ the TMD factorisation scheme applies and the SSAs depend on the associated TMD functions. If $p_T \gg \Lambda_{QCD}$, the transverse momentum dependence can be computed using pQCD framework. In between of these regimes, one can define an intermediate kinematic region ($\Lambda_{QCD} \ll p_T \ll Q$), where the results obtained extrapolating the collinear approach are supposed to match those obtained applying the TMD factorisation scheme (see [116] and references therein).

Within the TMD factorization framework, collinear gluon radiations are factorised into TMD PDFs. Similar to the integrated parton distribution functions, these contributions can be resummed to all orders by solving the associated evolution equations, (the so-called TMD or Collins-Soper-Sterman resummation [117]). As a result, choosing the factorisation scale around the hard momentum scale $\mu_F = Q$, the differential cross section simplifies to a convolution of soft factor–subtracted TMD distributions. Different approaches to subtract the soft factor and regulate the associated light-cone singularity introduce scheme dependence in the TMD definition and factorization. However, after solving the evolution equations, the scheme dependence can be factorized into perturbative calculable coefficients, which can be compared with different schemes.

Applying the TMD evolution, a given TMD PDF being a function of x and $\mathbf{k_T^2}$ becomes also scale-dependent (*e.g.* the Sivers function, $f_{1T}^q(x, \mathbf{k_T^2}, \mu_F)$). The inclusion of TMD evolution effects was a breakthrough in the phenomenological TMD related studies. Recently the study of unpolarised TMDs and of the Sivers function has been subject of a series of papers [118–123] where a TMD factorisation framework has been worked out for the treatment of SIDIS data and the extraction of polarised TMDs. An example, taken from Ref. [120], is shown in Fig. 1.16.

---

[6]The discussion sticks to the SIDIS case, but can be extended to Drell-Yan replacing p_T with q_T (see Fig. 1.21 for the definition of q_T).

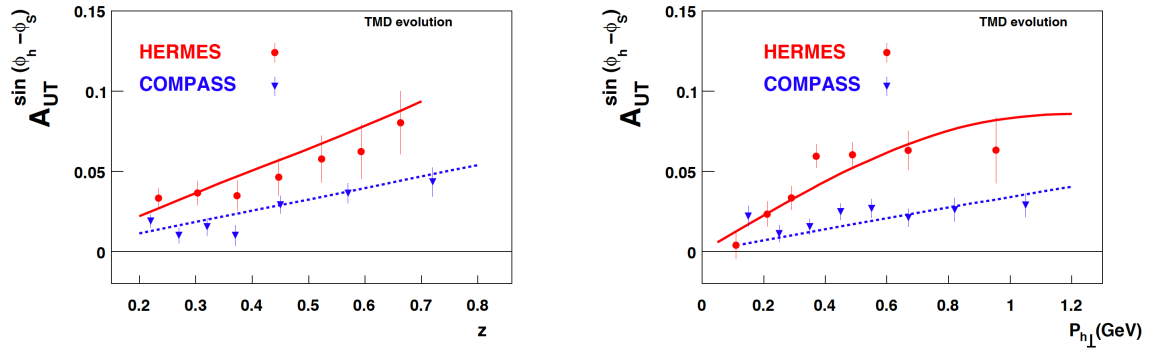Fig. 1.16 The Sivers asymmetry for positive hadrons is shown as extracted from HERMES [96] (red points) and COMPASS [91] (blue points) proton data as a function of z (left panel) and as a function of p_T (right panel). The red solid curves represent the result of the fit of plotted HERMES data ($< Q^2 >= 2.4$ (Gev/c^2)^2) performed in Ref. [124]. The blue dashed curves are based on the parametrization extracted from this fit, but evolved to the COMPASS scale ($< Q^2 >= 3.8$ (Gev/c^2)^2) using the TMD-evolution scheme from Ref. [120].

1.9.6 Weighted transverse spin asymmetries in SIDIS

In the previous sections it was discussed that the spin (in)dependent azimuthal asymmetries give access to convolutions of TMD PDFs and corresponding FFs. The convolutions can be evaluated analytically only making assumptions on their transverse momentum dependence. For instance, the so-called *Gaussian ansatz* can be adopted [125–127]. This may introduce model dependence in the extracted PDFs, that can vary depending on the PDF.

To bypass this problem it was proposed to measure the p_T-weighted asymmetries, which allow to solve the convolution integrals over transverse momenta in a model-independent way, without making assumptions on the transverse momentum dependence of PDFs and FFs [80, 128, 129].

The p_T-weighted Sivers asymmetry is of a particular interest. It is proportional to the product of the first transverse moment of the Sivers function $f_{1T}^{q\perp(1)}$ and the fragmentation function $D_1(z)$ and can be presented as

$$A_{UT}^{\sin(\phi_h - \phi_S)\omega}(x,z) = 2 \frac{\sum_q e_q^2 x f_{1T}^{q\perp(1)}(x) \cdot D_1^q(z)}{\sum_q e_q^2 x f_{1T}^q(x) \cdot D_1^q(z)} \qquad (1.17)$$

where

$$f_{1T}^{q\perp(1)}(x) = \int d^2 k_T \frac{k_T^2}{2M^2} f_{1T}^{q\perp}(x, k_T^2) \qquad (1.18)$$

with M the nucleon mass and k_T the intrinsic transverse momentum of the quark q. For more than ten years, the only results available for the p_T-weighted asymmetries

were the ones from HERMES [130]. Even if still preliminary, they have been used to constrain SIDIS fits and estimate the q_T-weighted Sivers asymmetry expected in DY experiments [131] (see Fig. 1.17).
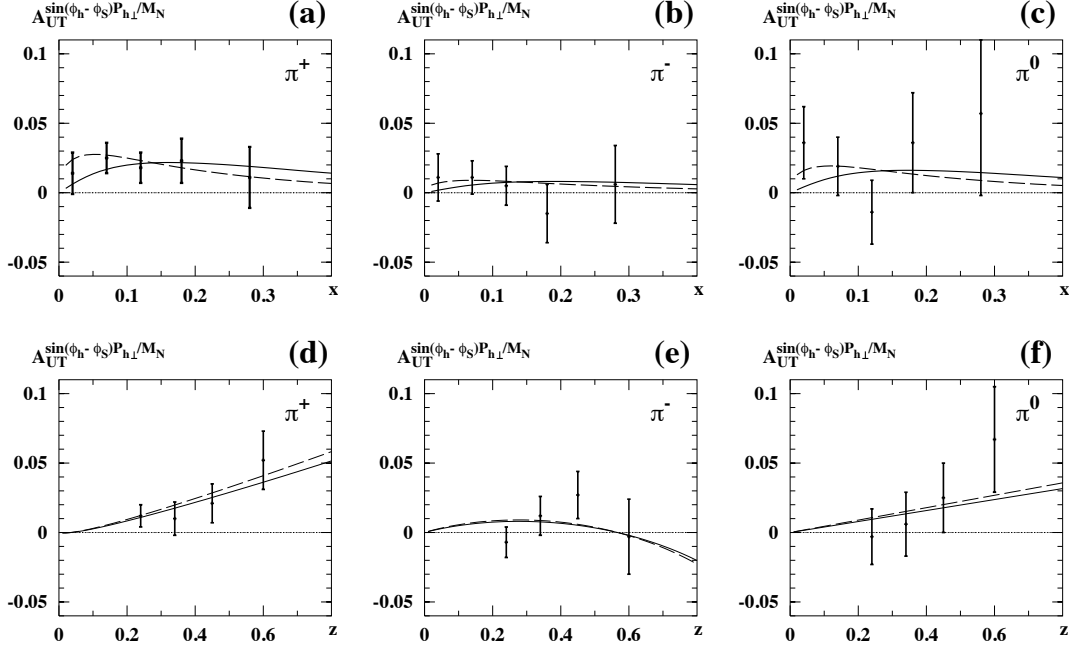

Fig. 1.17 The azimuthal SSA $A_{UT}^{\sin(\phi_h-\phi_S)\frac{P_T}{M}}$ measured by HERMES[130] as function of x (top row) and z (bottom row). Information about the fit can be found in Ref. [131].

Recently, the p_T-weighted Sivers asymmetry was extracted also by COMPASS [132], using two weightings

$$\omega = \frac{p_T}{zM} \qquad , \qquad \omega' = \frac{p_T}{M} \tag{1.19}$$

The weighted Sivers extracted using ω is shown in Fig. 1.18, compared with the unweighted results published in [95]. Assuming u quark dominance[7], the results for positive hadrons are clearly different from zero (in particular at large x) and represent the first direct measurement of the $f_{1T}^{u\perp(1)}(x)/f_1^u(x)$ ratio.

The extraction using ω' as weight was performed to study the z dependence of the weighted Sivers asymmetry and to check the validity of the Gaussian model for the k_T-decadence. Obtained results, shown in Fig. 1.19, are in qualitative agreement with the expectations.

---

[7]Assuming u quark dominance for positive hadrons produced on a proton target, the fragmentation function in Eq. 1.17 can be omitted and the asymmetry simplifies to $A_{UT}^{\sin(\phi_h-\phi_S)\omega}(x,z) \simeq 2\frac{f_{1T}^{u\perp(1)}(x)}{f_1^u(x)}$
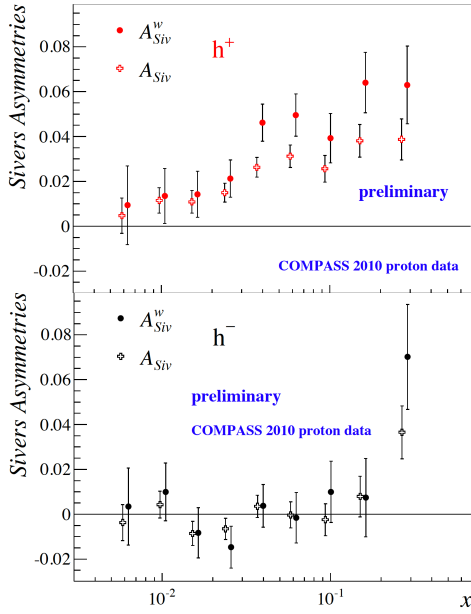
Fig. 1.18 $A_{UT}^{\sin(\phi_h-\phi_S)\frac{p_T}{zM}}$ (full points) in bins of x for positive (top panel) and negative (bottom panel) hadrons. The open crosses represent the standard Sivers asymmetries $A^{\sin(\phi_h-\phi_S)}$ from Ref.[95].
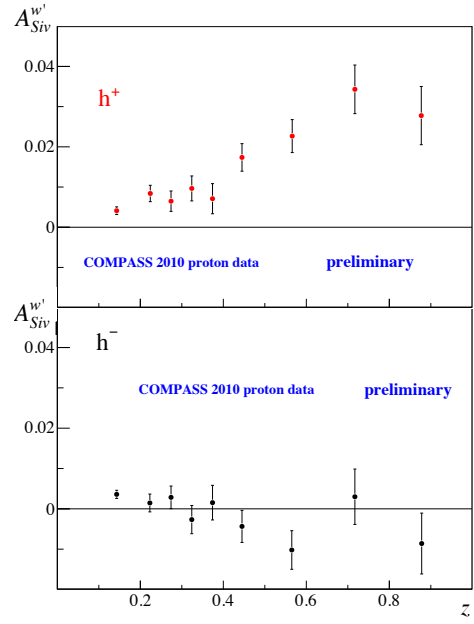
Fig. 1.19 $A_{UT}^{\sin(\phi_h-\phi_S)\frac{p_T}{M}}$ weighted Sivers asymmetries in bins of z for positive (top panel) and negative (bottom panel) hadrons.

1.10 Drell-Yan process

The TMD structure of the nucleon can be studied also in hadron-hadron collisions and here a particular attention is given to Drell-Yan (DY) processes, where a massive lepton-antilepton pair is produced in a quark anti-quark annihilation via the decay of an intermediate vector boson (virtual photon, γ^*, or Z_0). The QED formulation of the DY process framework was suggested in 1970 by Sidney Drell and Tung-Mow Yan [83]. Independently from them, the same mechanism for lepton-antilepton production in hadron-hadron collisions was considered also by Matveev, Muradian and Tavkhelidze already in 1969 [133]. Experimentally this process was observed for the first time at the Alternating Gradient Synchrotron (AGS) at Brookhaven National Laboratory [134], where muon pairs in the mass range $1 < M_{\mu\mu}/(GeV/c^2) < 6.7$ have been observed in collisions of high energy (22 - 29.5 GeV) protons with uranium nuclei.

The Drell-Yan reaction, for two initial hadrons h_1 and h_2 with polarisations S_{h_1} and S_{h_2}, respectively, can be written as follows:

$$H_{h_1}(P_{h_1}, S_{h_1}) + H_{h_2}(P_{h_2}, S_{h_2}) \rightarrow \gamma^*(q) + X \rightarrow \ell^-(l) + \ell^+(l') + X \qquad (1.20)$$

The full description of the dilepton production process in the collision of two polarised spin $\frac{1}{2}$ hadrons can be found in Ref. [135]. In the following, the discussion will be limited to the COMPASS case, considering the reaction with an unpolarised negative pion beam (H_π) impinging on a transversely polarised target (H_N) with muon-antimuon pair ($\mu^-\mu^+$) detected in the final state. In these conditions, the Eq. 1.20 can be re-written as:

$$H_\pi(P_\pi) + H_N(P_N, S) \to \gamma^*(q) + X \to \mu^-(l) + \mu^+(l') + X \qquad (1.21)$$

The corresponding Feynman diagram for a pion-induced Drell-Yan reaction with dimuon pair in the final state is shown in Fig. 1.20. To describe various char-
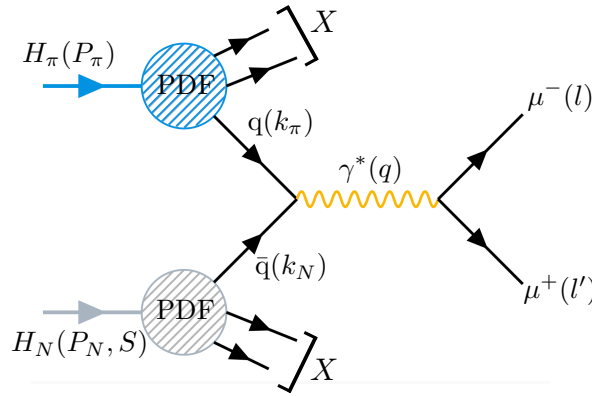
Fig. 1.20 Feynman diagram for pion-induced Drell-Yan process at COMPASS.

acteristics of the process, a standard set of Drell-Yan kinematic variables is defined [135, 136]. They are summarised in Tab. 1.6.

Table 1.6 Drell-Yan kinematic variables.

Varible(s)	Description
$P_\pi, P_N,$	4-momenta of the pion, and of the target nucleon
$l, l', q = l + l',$	4-momenta of the lepton, the antilepton and of the virtual photon
$S_T,$	transverse component of the target polarization in TF
$Q^2 = q^2,$	photon virtuality
$M_{\mu\mu} \sim \sqrt{Q},$	invariant mass of the dimuon
$q_T,$	transverse component of the virtual photon momentum
$x_\pi = q^2/(2P_\pi \cdot q),$	pion Bjorken variable (often referred to as x_1)
$x_N = q^2/(2P_N \cdot q),$	nucleon Bjorken variable (often referred to as x_2)
$x_F = x_\pi - x_N,$	Feynman variable

1.10.1 The Drell-Yan cross section

The DY cross section can be expressed in terms of the target spin and the polar and azimuthal angles of the outgoing dimuon defined in the target rest (TF) and the Collins Soper (CS) coordinate systems [135, 136], presented in Fig. 1.21.
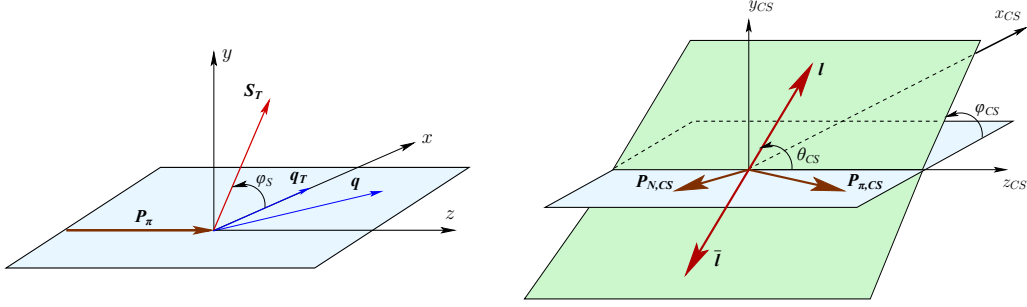

Fig. 1.21 Reference systems. Left panel: target rest frame. Note that z-axis (x-axis) is chosen along the beam momentum (along q_T). Right panel: the Collins-Soper frame. It is the rest frame of the virtual photon obtained from the TF frame by boosting first along the z-axis and then along the x-axis so that both longitudinal and transverse components of the momentum of the virtual photon vanish.

When the polarizations of the produced leptons are summed over, the cross-section of pion-nucleon Drell-Yan lepton-pair production off a transversely polarised nucleon can be written as [135, 136]:

$$
\begin{aligned}
\frac{\mathrm{d}\sigma}{\mathrm{d}q^4\mathrm{d}\Omega} \;=\; & \frac{\alpha^2}{Fq^2}\hat{\sigma}_U \\
& \times \Bigg\{ 1 + A_U^1\cos^2\theta_{CS} + \sin 2\theta_{CS}A_U^{\cos\varphi_{CS}}\cos\varphi_{CS} + \sin^2\theta_{CS}A_U^{\cos 2\varphi_{CS}}\cos 2\varphi_{CS} \\
& \quad + S_T\Big[(A_T^{\sin\varphi_S} + \cos^2\theta_{CS}\tilde{A}_T^{\sin\varphi_S})\sin\varphi_S \\
& \quad + \sin 2\theta_{CS}\Big(A_T^{\sin(\varphi_{CS}+\varphi_S)}\sin(\varphi_{CS}+\varphi_S) + A_T^{\sin(\varphi_{CS}-\varphi_S)}\sin(\varphi_{CS}-\varphi_S) \Big) \\
& \quad + \sin^2\theta_{CS}\Big(A_T^{\sin(2\varphi_{CS}+\varphi_S)}\sin(2\varphi_{CS}+\varphi_S) + A_T^{\sin(2\varphi_{CS}-\varphi_S)}\sin(2\varphi_{CS}-\varphi_S) \Big) \Big] \Bigg\},
\end{aligned}
$$

(1.22)

Here $\hat{\sigma}_U = (F_U^1 + F_U^2)$, with F_U^1, F_U^2 being the polarisation and azimuth-independent structure functions. The subscript $(U)T$ denotes transverse polarisation (in)dependence of the corresponding asymmetry. In total, Eq. 1.22 contains three UAs and five TSAs. The asymmetries are defined as ratios of corresponding structure functions to the sum of the unpolarised ones ($\hat{\sigma}_U$) and are given as the amplitudes of the respective modulations in the azimuthal (polar) angle of the lepton momentum in the Collins-Soper frame, φ_{CS} (θ_{CS}), and azimuthal angle of the target spin vector in the target rest frame, φ_S [135, 136]. The three UAs in Eq. 1.22, often referred

in the literature as:

$$\lambda = A_U^1, \quad \mu = A_U^{\cos\varphi_{CS}}, \quad \nu = 2A_U^{\cos 2\varphi_{CS}} \tag{1.23}$$

will be discussed more in detail in the following (see Sec. 1.12). One UA and two out five TSAs entering in Eq. 1.22 can be described by contributions from only *twist-2* TMD PDFs. These are the $A_U^{\cos 2\varphi_{CS}}$, $A_T^{\sin(2\varphi_{CS}-\varphi_S)}$ and $A_T^{\sin(2\varphi_{CS}+\varphi_S)}$ terms. The $A_U^1 = (F_U^1 - F_U^2)/(F_U^1 + F_U^2)$ asymmetry in addition to the *twist-2* structure function F_U^1 contains a higher-twist (HT) object F_U^2. At leading order of pQCD, within the *twist-2* approximation, $F_U^2 = 0$ and therefore $A_U^1 = 1$. Similarly, $A_T^{\sin\varphi_S} = (F_{UT}^1 + F_{UT}^2)/(F_U^1 + F_U^2)$ and $\tilde{A}^{\sin\varphi_S} = (F_{UT}^1 - F_{UT}^2)/(F_U^1 + F_U^2)$ asymmetries, along with twist-2 F_{UT}^1, contain F_{UT}^2 structure function which vanishes at LO, thus leading to $A_T^{\sin\varphi_S} = \tilde{A}^{\sin\varphi_S}$. Regarding $A_U^{\cos\varphi_{CS}}$, $A_T^{\sin(\varphi_S-\varphi_{CS})}$, $A_T^{\sin(\varphi_S+\varphi_{CS})}$ asymmetries, they are purely 'higher-twist' objects. Assuming $A_T^{\sin\varphi_S} \approx \tilde{A}^{\sin\varphi_S}$ and introducing the so-called depolarisation factors, defined as

$$D_{[f(\theta_{CS})]} = \frac{f(\theta_{CS})}{(1 + A_U^1 \cos^2\theta_{CS})} \tag{1.24}$$

one can re-write Eq. 1.22 in the following way:

$$
\begin{aligned}
\frac{d\sigma}{dq^4 d\Omega} =\ & \frac{\alpha^2}{Fq^2}\hat{\sigma}'_U \\
& \times \Bigg\{ 1 + D_{[\sin 2\theta_{CS}]} A_U^{\cos\varphi_{CS}} \cos\varphi_{CS} + D_{[\sin^2\theta_{CS}]} A_U^{\cos 2\varphi_{CS}} \cos 2\varphi_{CS} \\
& + S_T \Big[D_{[1+\cos^2\theta_{CS}]} A_T^{\sin\varphi_S} \sin\varphi_S \\
& + D_{[\sin 2\theta_{CS}]} \left(A_T^{\sin(\varphi_{CS}+\varphi_S)} \sin(\varphi_{CS}+\varphi_S) + A_T^{\sin(\varphi_{CS}-\varphi_S)} \sin(\varphi_{CS}-\varphi_S) \right) \\
& + D_{[\sin^2\theta_{CS}]} \sin^2\theta_{CS} \left(A_T^{\sin(2\varphi_{CS}+\varphi_S)} \sin(2\varphi_{CS}+\varphi_S) + A_T^{\sin(2\varphi_{CS}-\varphi_S)} \sin(2\varphi_{CS}-\varphi_S) \right) \Big] \Bigg\},
\end{aligned}
\tag{1.25}
$$

where

$$\hat{\sigma}'_U = \left(F_U^1 + F_U^2 \right)\left(1 + A_U^1 \cos^2\theta_{CS} \right) \tag{1.26}$$

1.10.2   Interpretation of the Drell-Yan asymmetries

In Eq. 1.25 the four marked in red asymmetries (1 UA and 3 TSAs) have a LO (*twist-2*) interpretation within the QCD parton model framework. $A_U^{\cos 2\varphi_{CS}}$ UA is related to the Boer-Mulders ($h_1^{q\perp}$) TMD PDFs of the proton, while the three TSAs

$A_T^{\sin\varphi_S}$, $A_T^{(2\varphi_{CS}+\varphi_S)}$ and $A_T^{(2\varphi_{CS}-\varphi_S)}$ are related to Sivers ($f_{1T}^{q\perp}$), pretzelosity ($h_1^{q\perp}$) and transversity (h_1^q) TMD PDFs of the proton, respectively [135, 136]. In contrast to the SIDIS case, in pion-induced Drell-Yan dimuon production no fragmentation process is involved and the TMD PDFs of the nucleon enter in the asymmetries in a form of a convolution with a specific pion TMD PDF. The measurement of the Sivers asymmetry gives access to the proton PDF convoluted with the unpolarised pion PDF, while $A_T^{\sin(2\varphi_{CS}-\varphi_S)}$ and $A_T^{\sin(2\varphi_{CS}+\varphi_S)}$ TSAs are related with pion Boer-Mulders TMD PDF convoluted with the transversity and the pretzelosity nucleon TMD PDFs, respectively. The unpolarised $A_U^{\cos 2\varphi_{CS}}$ asymmetry allows to probe the convolution of pion and nucleon Boer-Mulders TMD PDFs. The three asymmetries marked in blue in Eq. 1.25 are *higher-twist* objects and cannot be interpreted within the *twist-2* approach of the LO QCD parton model.

1.11 COMPASS SIDIS - Drell-Yan bridge

As illustrated in the previous sections, within the concept of generalized universality of TMD PDFs, nucleon parton distributions functions accessed via UAs and TSAs measurements in SIDIS and Drell-Yan are expected to be process-independent. The two T-odd TMD PDFs (Sivers and Boer-Mulders functions) are predicted to have opposite sign when measured in SIDIS or DY and thus are only conditionally universal.

In 2015, COMPASS was the first fixed-target experiment to collect polarised Drell-Yan data, using a 190 GeV/c π^- beam scattering off a transversely polarised NH$_3$ target. It became the only experiment providing complementary access to the TMD PDFs via two mechanisms by measuring azimuthal asymmetries in both SIDIS and Drell-Yan processes, while making use of mostly the same experimental setup and exploring comparable kinematic phase spaces [18]. The TMD PDFs of the proton accessible via (un)polarised azimuthal asymmetries measured by COMPASS in SIDIS and DY reactions are summarised in Tab. 1.7.

While the SIDIS measurements are essentially background free, for various Drell-Yan studies being carried out at COMPASS it is convenient to disentangle four dimuon mass, $M_{\mu\mu} = \sqrt{Q^2}$, ranges:

I) $1 < M_{\mu\mu}/(\text{GeV}/c^2) < 2:$ *Low Mass Range*

II) $2 < M_{\mu\mu}/(\text{GeV}/c^2) < 2.5:$ *Intermediate Mass Range*

III) $2.5 < M_{\mu\mu}/(\text{GeV}/c^2) < 4:$ *Charmonia mass range*

IV) $4 < M_{\mu\mu}/(\text{GeV}/c^2) < 9:$ *High Mass range*

SIDIS $\ell^{\rightarrow} N^{\uparrow}$	TMD PDF	Drell-Yan $\pi N^{\uparrow}$ (LO)
$A_{UU}^{\cos 2\phi_h}, A_{UU}^{\cos \phi_h}$	$h_1^{\perp q}$	$A_U^{\cos 2\varphi_{CS}}$
$A_{UT}^{\sin(\phi_h-\phi_s)}, A_{UT}^{\sin \phi_s}, A_{UT}^{\sin(2\phi_h-\phi_s)}$	$f_{1T}^{\perp q}$	$A_T^{\sin \varphi_S}$
$A_{UT}^{\sin(\phi_h+\phi_s-\pi)}, A_{UT}^{\sin \phi_s}$	h_1^q	$A_T^{\sin(2\varphi_{CS}-\varphi_S)}$
$A_{UT}^{\sin(3\phi_h-\phi_s)}, A_{UT}^{\sin(2\phi_h-\phi_s)}$	$h_{1T}^{\perp q}$	$A_T^{\sin(2\varphi_{CS}+\varphi_S)}$

Table 1.7 Nucleon TMD PDFs accessed via SIDIS and Drell-Yan UAs and TSAs.

Various physics contributions to the invariant mass spectrum are disentangled in Fig. 4.5 (see Sec. 4.4). The *Low Mass Range* is not suited for physics studies, since there the combinatorial background and other concurrent physics processes (e.g. Open Charm decays) dominate over the DY channel in the mass spectrum. The *Intermediate Mass Range* represents a challenging range for physics studies: there the DY cross-section is high but the background contributions are still strong, such that the signal-to-background ratio is far to be favourable. In the *Charmonia Mass Range* COMPASS can study the Sivers asymmetry in J/ψ range. Existing models assuming $q\bar{q}$ dominance for J/ψ-production at COMPASS, predict quite large signal for the COMPASS kinematics [137] (see Fig. 1.22). Extraction of the asymmetries from the J/ψ-range is one of the ongoing COMPASS analyses, however it is not considered in this work.
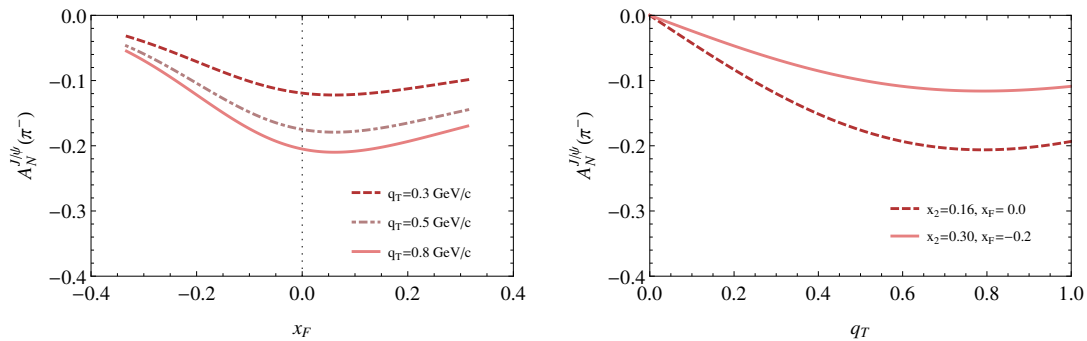
Fig. 1.22 Predictions for $A_T^{\sin \varphi_S}$ (reads $A_N^{J/\Psi}$ on the plots) in the J/ψ mas region, taken from Ref. [137]. The left plot shows the predicted asymmetry as a function of x_F computed for different mean values of q_T, while, on the right plot q_T-dependence is shown for different mean values of x_F. All presented predictions are accounting for the sign-change of Sivers TMD PDF between SIDIS and Drell-Yan.

Among the four aforementioned $M_{\mu\mu}$ regions, the so-called *High Mass Range* (HM) is particularly suited for studies of the predicted sign change of the Sivers

TMD PDF when comparing SIDIS and DY results. First, this range best fulfils the requirement of TMD factorisation that the transverse momentum of the dimuon in DY (or of the hadron in SIDIS) has to be much smaller than the hard scale $M_{\mu\mu}$ (Q). Second, in this range both SIDIS and DY cross sections for a proton target are dominated by the contribution of u-quark nucleon TMD PDFs in the valence region, where the extracted Sivers TMD PDF is expected to reach its maximum [138, 139].
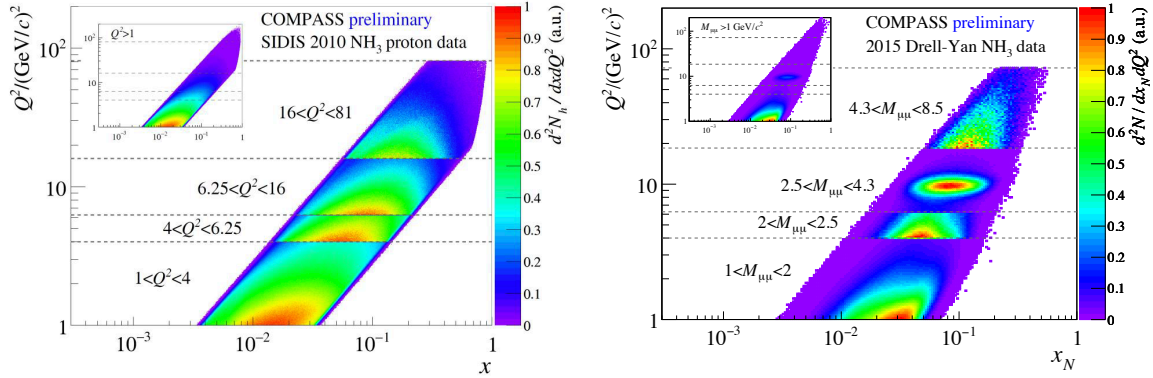
Fig. 1.23 Left: charged hadron SIDIS 2010 two-dimensional (Q^2, x) distribution for $z > 0.1$. Right: dimuon pairs DY 2015 two-dimensional (Q^2, x_N). In both plots sub-Q^2 ranges, correspond to four DY Q^2 ranges. They are normalised to their number of entries and the insert shows the integrated distribution.
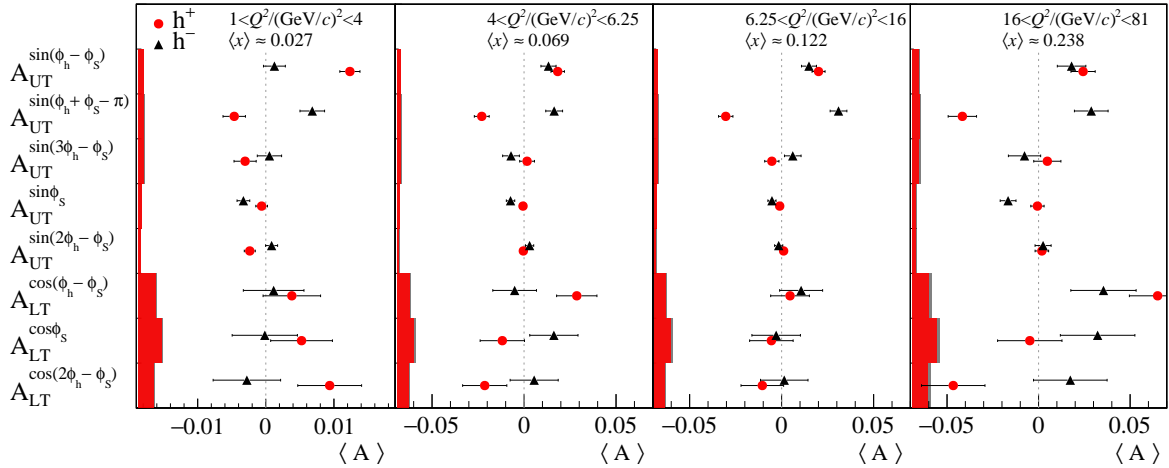
Fig. 1.24 Mean SIDIS TSAs measured by COMPASS in the four DY Q^2-ranges. The error bars represent statistical uncertainties. Systematic uncertainties are shown by the full bands next to the vertical axes [18].

Third, in this region the background contaminations are estimated to be negligible[8], as can be seen in Fig. 4.5.

---

[8]The background estimation is presented in detail in Chap. 4.4.

In order to provide useful input for a future direct comparison of the nucleon TMD PDFs obtained from SIDIS data with those obtained from DY data, COMPASS performed a dedicated analysis extracting all eight SIDIS transverse-spin-dependent azimuthal asymmetries in the four regions of the Q^2 defined for the DY analysis [18]. The data in SIDIS 2010 and DY 2015 runs have been collected using similar NH_3 targets, beam energies[9] and spectrometer setup. This is directly reflected in the two (Q^2, x_N) phase-spaces explored. As shown by Fig. 1.23 they result to be comparable.
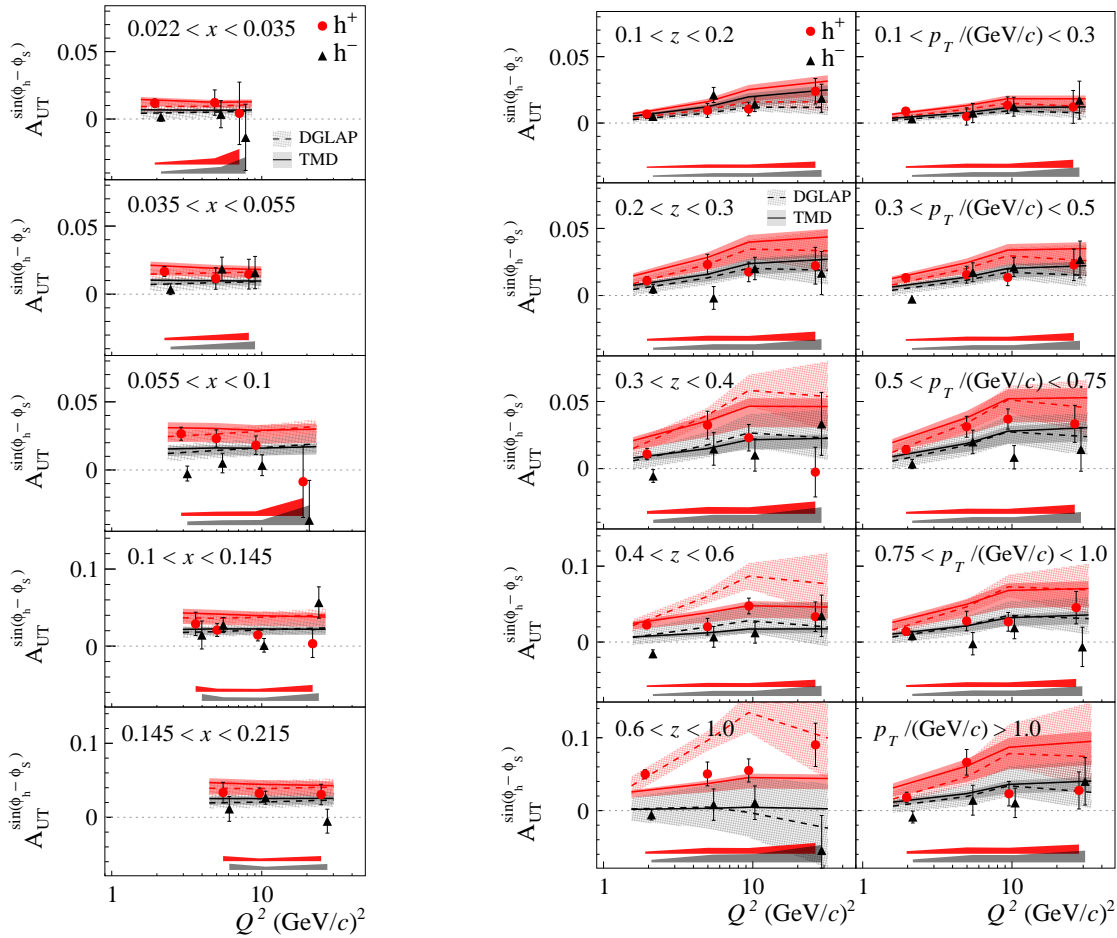
Fig. 1.25 The Q^2-dependence of the COMPASS Sivers asymmetry for positive and negative hadrons in five selected bins of x (left panel) and in bins of z and p_T (right panel) [18]. The abscissa positions of the points for negative hadrons is staggered to the right for better visibility. The solid (dashed) curves represent the calculations based on TMD (DGLAP) evolution for the Sivers TSAs [140, 141].

In the analysis presented in [18] the TSAs are extracted for the first time using a two-dimensional representations in (Q^2, x), (Q^2, z), and (Q^2, p_T). The results for mean TSAs are shown in Fig. 1.24. For h^+, a positive Sivers TSA is observed in

all four Q^2-ranges. Statistically significant results are observed also for the Collins asymmetry, which for positive hadrons is found to be negative in all Q^2-ranges. The pretzelosity related effect is found to be small and fully compatible with zero in the HM range for both h^+ and h^-. This represents the SIDIS side of the COMPASS TMD picture, which can be complemented with the results from the analysis of 2015 DY data presented in this thesis.

COMPASS has also determined the TSAs in each of the four Q^2-ranges as functions of x (eleven bins), z (5 bins) or p_T (5 bins). In addition, the Q^2-dependence of the Sivers asymmetries has been also examined in different kinematic bins, as shown by Fig. 1.25. In the figure are shown also the predictions from collinear (DGLAP) and TMD-evolution approaches, based on the best fit [140] of all published HERMES [96] and COMPASS [88, 95] measurements. The measured Q^2-dependence of the SIDIS Sivers TSA at given x does not allow to quantitatively distinguish between the predictions for Q^2-evolution obtained using TMD and DGLAP schemes when fitting the existing one-dimensional data. The situation may improve making use of multi-dimensional data as the one published in Ref. [18]

1.11.1   Weighted Transverse Spin Asymmetries in DY

The formalism of transverse-momentum-weighted asymmetries in SIDIS (see, Sec. 1.9.6) was adapted for the LO Drell-Yan asymmetries as well [131, 142, 143]. In case of conventional transverse spin asymmetries, the TMD PDFs enter in a form of convolution-integrals in the transverse momentum space. However, when the cross section is weighted with the proper powers of q_T the amplitude turns into a simple product containing specific n-th k_T^2-moments of the TMD PDFs defined as:

$$f^{(n)}(x) = \int d^2\mathbf{k_T} \left(\frac{k_T^2}{2M^2} \right)^n f(x, k_T^2) \tag{1.27}$$

Within this definition the 0-th k_T^2-moments are associated with k_T-integrated PDFs (e.g. $f_1(x) = f_1^{(0)}(x) = \int d^2\mathbf{k_T} f_1(x, k_T^2)$). In this thesis the results of Drell-Yan q_T-weighted TSAs (wTSAs) will be presented. In the following the two initial hadrons are denoted as a and b (in case of COMPASS: $a = \pi^-$ and $b = p$). The wTSAs are defined as,

$$A_X^{Y W_Y}(x_a, x_b) = \frac{\int d^2\mathbf{q_T} W_Y F_X^Y}{\int d^2\mathbf{q_T} F_U^1}, \tag{1.28}$$

where W_Y is the weight corresponding to the azimuthal modulation Y ($Y = \varphi_S$, $2\varphi_{CS} + \varphi_S$, $2\varphi_{CS} - \varphi_S$). The W_Y is chosen in a way that it is suitable to deconvolute corresponding structure function and the integral in the numerator is simplified and easy to interpret. Additional factors are added in some cases added in order to get more compact and refined results. Taking the Sivers example, the wTSA-numerator from Eq. 1.28 is given by the integral of the related structure function $F_T^{\sin \varphi_S}$ over $\mathbf{q_T}$. The integral yields a simple result when it is weighted with q_T/M_b. First, the integral over $\mathbf{q_T}$ is solved,

$$
\begin{aligned}
\int d^2\mathbf{q_T} \frac{q_T}{M_b} F_T^{\sin \varphi_S} &= -\int d^2\mathbf{q_T} \frac{q_T}{M_b} \mathscr{C}\left[\frac{\mathbf{q_T} \cdot \mathbf{k_{bT}}}{q_T M_b} f_{1,a} f_{1T,b}^\perp\right] \\
&= -\sum_q e_q^2 \int d^2\mathbf{k_{aT}} d^2\mathbf{k_{bT}} \frac{(\mathbf{k_{aT}} + \mathbf{k_{bT}}) \cdot \mathbf{k_{bT}}}{N_c M_b^2} \\
&\quad \times \left[f_{1,a}^{\bar{q}}(x_a, k_{aT}^2) f_{1T,b}^{\perp q}(x_b, k_{bT}^2) + (q \leftrightarrow \bar{q})\right].
\end{aligned}
\tag{1.29}
$$

Using the delta function after employing the definition of the n-th moment (for n=1) of a PDF from Eq. 1.27 and taking into account that only the terms even in $\mathbf{k_T}$ can contribute,

$$
\int_{-\infty}^{\infty} d^2\mathbf{k_{aT}}(\mathbf{k_{aT}} \cdot \mathbf{k_{bT}}) f(k_{aT}^2) = 0.
\tag{1.30}
$$

for Eq. 1.29 we finally get:

$$
\int d^2\mathbf{q_T} \frac{q_T}{M_b} F_T^{\sin \varphi_S} = -\frac{2}{N_c} \sum_q e_q^2 \left[f_{1,a}^{\bar{q}}(x_a) f_{1T,b}^{\perp q}(x_b) + (q \leftrightarrow \bar{q})\right]
\tag{1.31}
$$

In this way, the first k_T^2-moment of the Sivers function of the target nucleon times the unpolarised PDF of the beam hadron can be directly accessed from measurement of the dedicated wTSA. The same approach can be applied also to the other wTSAs and involved structure functions. In particular, the structure functions related to transversity and pretzelosity TMDs can be deconvoluted as,

$$
\int d^2\mathbf{q_T} \frac{q_T^3}{2M_a M_b^2} F_T^{\sin(2\varphi_{CS} + \varphi_S)} = -\frac{2}{N_c} \sum_q e_q^2 \left[h_{1,a}^{\perp(1)\bar{q}}(x_a) h_{1T,b}^{\perp(2)q}(x_b) + (q \leftrightarrow \bar{q})\right]
\tag{1.32}
$$

$$
\int d^2\mathbf{q_T} \frac{q_T}{M_a} F_T^{\sin(2\varphi_{CS} - \varphi_S)} = -\frac{2}{N_c} \sum_q e_q^2 \left[h_{1,a}^{\perp(1)\bar{q}}(x_a) h_{1,b}^q(x_b) + (q \leftrightarrow \bar{q})\right].
\tag{1.33}
$$

The wTSA-denominator from Eq. 1.28 contains the unpolarised structure function ans is common for all wTSAs. It can be computed as follows,

$$\int d^2\mathbf{q_T} F_U^1 = \frac{1}{N_c} \sum_q e_q^2 \left[f_1^{\bar{q}}(x_a) f_1^q(x_b) + (q \leftrightarrow \bar{q}) \right] \tag{1.34}$$

Within TMD approach, it is easy to interpret the weighted asymmetries using Eqs. 1.31, 1.32, 1.33, 1.34. For instance, in the case of the Sivers-related asymmetry

$$A_T^{\sin \varphi_S \frac{q_T}{M_b}} = \frac{\int d^2\mathbf{q_T} \frac{q_T}{M_b} F_T^{\sin \varphi_S}}{\int d^2\mathbf{q_T} F_U^1} = 2 \frac{\sum_q e_q^2 \left[f_{1,a}^{\bar{q}}(x_a) f_{1T,b}^{q\perp(1)}(x_b) + (q \leftrightarrow \bar{q}) \right]}{\sum_q e_q^2 \left[f_1^{\bar{q}}(x_a) f_1^q(x_b) + (q \leftrightarrow \bar{q}) \right]} \tag{1.35}$$

which, assuming u quark dominance in the pion-proton DY, can be approximated to

$$A_T^{\sin \varphi_S \frac{q_T}{M_b}} \approx 2 \frac{f_{1T,p}^{\perp(1)u}(x_N)}{f_{1,p}^u(x_N)}, \tag{1.36}$$

Thus, under this assumption, the measurement of the q_T-weighted DY Sivers asymmetry gives direct access to the first moment of the u-quark Sivers function in Drell-Yan and can be used as an alternative way to test the Sivers TMD PDF sign change.

1.12 Lam-Tung sum rule and unpolarised Drell-Yan asymmetries

The three target polarization independent Drell-Yan asymmetries, λ, μ and ν, appearing in Eq. 1.22 attracted particular attention in the last decades. Considering COMPASS case where Drell-Yan dimuon production from quark-antiquark annihilation goes through an intermediate virtual photon (Z_0-production is suppressed), the unpolarised part of the differential cross-section in d^4q and $d\Omega = d\cos\theta d\varphi_{CS}$ can be written as follows [144],

$$\frac{d\sigma}{dqd\Omega} = \frac{\alpha^2}{2\pi N_c Q^2 s^2} \Big(F_U^1 (1 + \cos^2\theta_{CS}) + F_U^2 (1 - \cos^2\theta_{CS}) \tag{1.37}$$

$$+ F_U^{\cos\varphi_{CS}} \sin 2\theta_{CS} \cos\varphi_{CS} + F_U^{\cos 2\varphi_{CS}} \sin^2\theta_{CS} \cos 2\varphi_{CS} \Big)$$

where $N_c = 3$ is the number of colours in QCD and s represents the center of mass squared energy of the reaction. The structure functions F_U^1, F_U^2, $F_U^{\cos\varphi_{CS}}$ and

$F_U^{\cos 2\varphi_{CS}}$ depend on q and are used to parametrise the hadronic tensor as,

$$
\begin{aligned}
W^{\mu\nu} = &-(g^{\mu\nu} - T^\mu T^\nu)(F_U^1 + F_U^{\cos 2\varphi_{CS}}) - 2X^\mu X^\nu F_U^{\cos 2\varphi_{CS}} \\
&+ Z^\mu Z^\nu (F_U^2 - F_U^1 - F_U^{\cos 2\varphi_{CS}}) - (X^\mu Z^\nu + Z^\mu X^\nu) F_U^{\cos \varphi_{CS}}
\end{aligned}
\tag{1.38}
$$

where X, Y, Z and T are a set of orthonormal axes introduced in the Collins-Soper frame. In case of larger hard scales when Z boson contribution is not negligible, additional terms should be added to the cross-section [145]. From Eq. 1.37 one can derive the expression for the normalised decay angular distribution

$$
\begin{aligned}
\frac{\mathrm{d}N}{\mathrm{d}\Omega} = \frac{3}{8\pi} \Bigg(&\frac{F_U^1(1 + \cos^2\theta_{CS}) + F_U^2(1 - \cos^2\theta_{CS})}{2F_U^1 + F_U^2} \\
&+ \frac{F_U^{\cos\varphi_{CS}} \sin 2\theta_{CS} \cos\varphi_{CS} + F_U^{\cos 2\varphi_{CS}} \sin^2\theta_{CS} \cos 2\varphi_{CS}}{2F_U^1 + F_U^2} \Bigg)
\end{aligned}
\tag{1.39}
$$

Introducing λ, μ and ν, defined as

$$
\lambda = \frac{F_U^1 - F_U^2}{F_U^1 + F_U^2} \quad , \quad \mu = \frac{F_U^{\cos\varphi_{CS}}}{F_U^1 + F_U^2} \quad , \quad \nu = 2\frac{F_U^{\cos 2\varphi_{CS}}}{F_U^1 + F_U^2}
\tag{1.40}
$$

one can re-write Eq. 1.39 as

$$
\frac{\mathrm{d}N}{\mathrm{d}\Omega} = \frac{3}{4\pi} \frac{1}{\lambda + 3} \left[1 + \lambda \cos^2\theta_{CS} + \mu \sin 2\theta_{CS} \cos\varphi_{CS} + \frac{\nu}{2} \sin^2\theta_{CS} \cos 2\varphi_{CS} \right]
\tag{1.41}
$$

In the *naive* Drell-Yan model, where the intrinsic k_T of the partons and QCD processes involving gluons are neglected, the expectation is $\lambda = 1, \mu = \nu = 0$ Including intrinsic k_T contribution and QCD effects to $\mathcal{O}(\alpha_s)$ allows $\lambda \neq 1$, $\mu, \nu \neq 0$. Nevertheless the so-called Lam-Tung relation [146]

$$
\lambda + 2\nu = 1
\tag{1.42}
$$

is expected to be largely satisfied. This relation is a direct consequence of the spin-1/2 nature of the quarks and is analogous to the Callan-Gross (Eq 1.8) relation in the DIS case. The Lam-Tung relation is predicted to be insensitive to QCD corrections (unlike the Callan-Gross relation). Derived in Refs [147, 148], next-to-leading order (NLO) corrections to the cross sections relevant for the angular coefficients suggest overall modest $\mathcal{O}(\alpha_s^2)$ effects on λ, μ and ν so that also the Lam-Tung relation, although found to be violated at NLO, still holds to fairly

good approximation. As discussed in the following, recent results from collider experiments have brought different theoretical groups to revisit this point, coming to different conclusions.

The Drell-Yan unpolarised asymmetries were studied by a number of fixed target experiments in the past. During the '80s, the NA10 [149] collaboration at CERN was one of the pioneering DY-experiments. They were measuring pion-induced DY reactions occurring on tungsten target at different beam energies (140, 194 and 286 GeV/c)[10]. The highest statistics was collected with 194 GeV beam. The corresponding results [151] are shown in Fig. 1.26. The coefficient μ was found to be small in the Collins-Soper frame, indicating that the annihilating quarks contribute about equally to the dimuon transverse momentum. A strong dependence on q_T was observed for ν, while λ was measured to be close to one and substantially independent from the kinematics. The Lam-Tung sum-rule and the NA10 data were fairly in agreement, except for the high q_T region where a significant deviation from zero can be observed.

NA10 also studied collisions with a deuterium target [152] using a 286 GeV/c π^- beam. The results are presented in Fig. 1.27, together with the tungsten results obtained with the same energy. The statistics for D data is a factor ten lower with respect to the W case. Nevertheless, the data looks compatible within the statistical uncertainties and no striking deviation is observed.

Unpolarised DY reactions were also studied at the E615 experiment at Fermilab, using a 252 GeV π^- beam scattering off a tungsten target. The results [153], shown in Fig. 1.28, exhibit sizably values of μ and ν in the so-called Gottfried-Jackson reference frame [154]. Since, contrary to the Lam-Tung relation, λ, μ and ν are not expected to be frame-invariant [155], the comparison with NA10 must be done using results obtained in the same reference frame. In about twenty years from NA10 and E615 measurements, another experiment at FNAL (E866, aka NuSea Collaboration) performed DY data-takings with a 800 GeV proton beam impinging on a deuteron target and extracted λ, μ and ν amplitudes. The E866 results [156], shown in Fig. 1.29 together with NA10 and E615 measurements, indicate qualitatively different behaviour of the azimuthal angular distributions between p+d and π^- + W collisions.

An intriguing feature to be noticed is that NA10 and E866 data largely confirm the Lam-Tung sum rule (see Eq. 1.42) while in E615 the relation appears to be violated, suggesting the presence of effects other than pQCD. Different non-perturbative effects have been proposed to explain the data [157–159]. In particular

---

[10]In the '80s also the NA3 collaboration studied dimuon production in collisions of $pi^\pm$, K^-,p and $\bar{p}$ on platinum and hydrogen targets [150]. The limited statistics (15 000 with π^- at 150 GeV/c impinging on a platinum target) did not allow to draw firm conclusions on the unpolarised angular distributions.

it was suggested that the observed behaviour of ν could be explained by the Boer-Mulders effect and corresponding TMD PDF [80].

The magnitude of ν shows intriguing features, when compared between $p+d$ and π^-+W. In the former case, taking into account proton and deuteron valence-quark compositions (*uud* and *uud + ddu*, respectively), the DY process must involve at least one sea-quark. This is not true in pion-induced collisions, where the DY cross-section is dominated by $u\bar{u}$ annihilation. Thus, these results may suggest a smaller Boer-Mulders function for sea quarks compared to valence. This was confirmed by a recent analysis [160] of this data, showing that the sea-quark Boer-Mulders functions are indeed smaller by a factor ~ 5 than the valence-quark Boer-Mulders functions.

E866 collected also $p+p$ data [161], finding a larger ν coefficient at high q_T while comparing with $p+d$ data. Neither the prediction based on Boer-Mulders functions nor the QCD prediction could describe this data over the entire range of q_T. This observation suggested that an analysis combining both effects is required before a reliable extraction of the Boer-Mulders functions could be obtained.
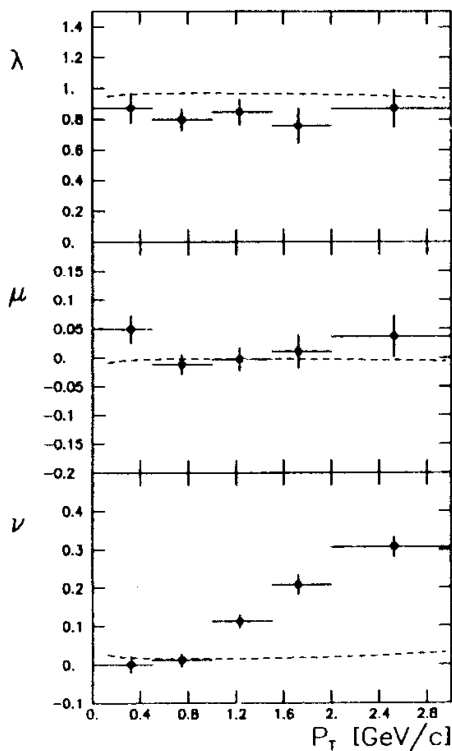
Fig. 1.26 Results for λ, μ and ν UAs extracted as function of p_T, in the Collins-Soper frame, from the analysis of π^- (194 GeV) + W data [152].
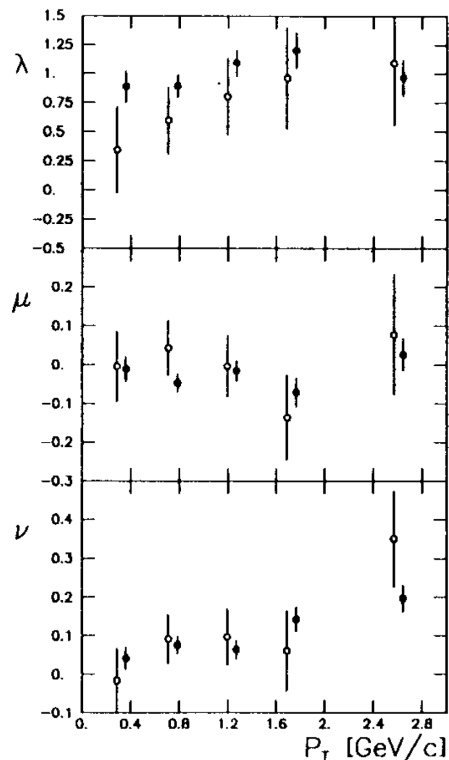
Fig. 1.27 Results for λ, μ and ν UAs extracted as function of p_T, in the Collins-Soper frame, from the analysis of π^- (286 GeV) + W (full circles) and π^- (286 GeV) + D (empty circles) data [152].
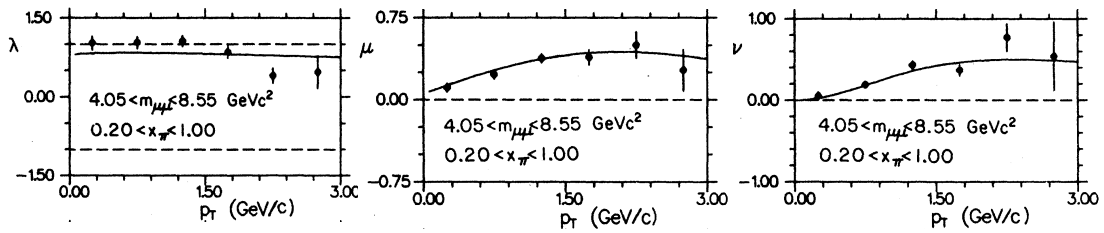
Fig. 1.28 Results for λ, μ and ν UAs extracted as function of p_T, in the Gottfried-Jackson frame, from the analysis of π^- (252 GeV) + W data [153] from E615 experiment.
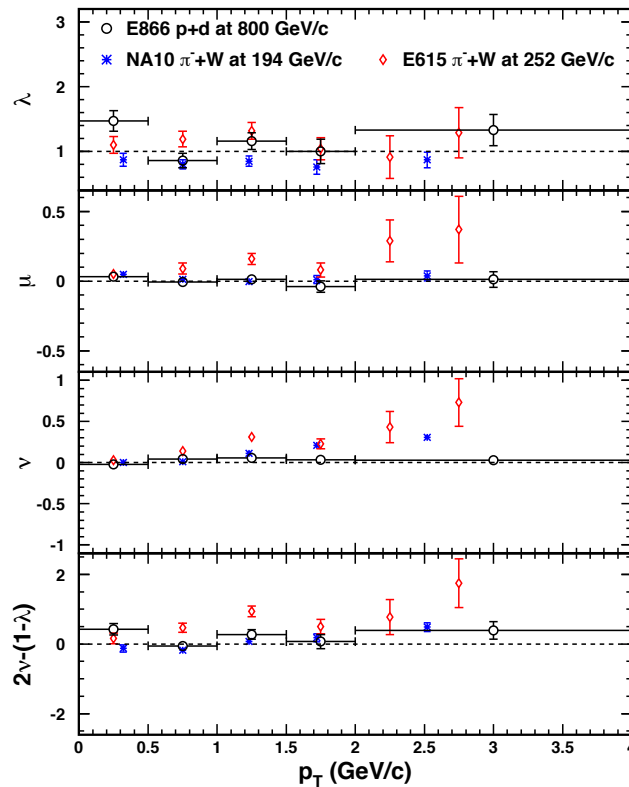
Fig. 1.29 Measurements of λ, μ and ν and Lam-Tung sum rule evaluation carried out by NA10, **E866** and E615 [156]. The parameters are shown in function of q_T (read p_T on the plot) and are evaluated in the Collins-Soper frame. The error bars include the statistical uncertainties only.

A summary of the results obtained from the three aforementioned fixed-target experiments for λ, μ and ν, together with the respective values obtained for the Lam-Tung sum, is presented in Tab. 1.8.

In the last years, the measurement of λ, μ and ν attracted interest of the Tevatron and LHC collider experiments as well[11]. The unpolarised DY-asymmetries

---

[11]While for fixed-target data q_T and Q are limited to few GeV, the measurements carried out at Tevatron and LHC experiments are characterised by $Q \sim m_Z$, where m_Z represents the Z-boson mass, and by much wider ranges of explored qT (almost to 100 GeV at Tevatron and up to 300 GeV at the LHC). The fixed-target regime is dominated by LO $q + \bar{q}$ annihilation and non perturbative effects, whereas in collider-kinematics the cross-sections become dominated by the QCD radiative processes (hard gluon emission)

Experiment	E866		NA10	E615
Beam Energy	800 GeV/c		194 GeV/c	252 GeV/c
Reaction	$p + p$	$p + d$	$\pi^- + W$	$\pi^- + W$
$\langle \lambda \rangle$	0.85 ± 0.10	1.07 ± 0.07	0.83 ± 0.04	1.17 ± 0.06
$\langle \mu \rangle$	-0.026 ± 0.019	0.003 ± 0.013	0.008 ± 0.010	0.09 ± 0.02
$\langle \nu \rangle$	0.040 ± 0.015	0.027 ± 0.010	0.091 ± 0.009	0.169 ± 0.019
$\langle 2\nu - (1 - \lambda) \rangle$	-0.07 ± 0.10	0.12 ± 0.07	0.01 ± 0.04	0.51 ± 0.07

Table 1.8 Mean value of λ, μ, ν parameters and for the Lam-Tung relation for Drell-Yan measurements performed by E866, NA10 and E615.

have been measured by CDF at Tevatron [162] in $p + \bar{p}$ collision and by CMS at LHC in $p + p$ collisions [163]. Also here the published results are quite intriguing, since CDF data are in good agreement with the Lam-Tung sum rule, in contrast with the clear violation observed by CMS. These results have triggered strong attention from various theoretical groups which tried to estimate the NLO corrections to be included in global models capable to describe data in both fixed-target and colliders regimes [144, 145, 164].

Even if the spectrum of collected interesting results is quite wide, the current global understanding is far to be conclusive. In this contest, the data collected by COMPASS on NH_3 and W will serve as an important input for the further studies of unpolarised effects arising in Drell-Yan reactions.

Chapter 2

The COMPASS Experiment

The analyses presented in this thesis are based on data collected by the COMPASS[1] experiment during 2015 data taking. COMPASS [15] is a fixed target experiment operating at CERN North-Area at the end of the M2 beamline of the Super Proton Synchrotron (SPS). The M2 is a 1.13 km long beam line which starts from the T6 primary target and serves just COMPASS, delivering hadron or muon beam depending on the requests of the experiment.

COMPASS is a two-stage spectrometer comprising two dipole magnets, SM1 and SM2. SM1 provides an integrated field of 1 T m and identifies the so-called Large Angle Spectrometer (LAS), mainly dedicated to the detection of small momentum particles scattered at large polar angles. SM2 can dispense an integrated field up to 4.4 T m and is the core of the Small Angle Spectrometer (SAS), mostly dedicated to the detection of high momenta particles emitted with small polar angles. Both the stages are equipped with electromagnetic and hadronic calorimeters, as well as a system dedicated to detection of the muons (muon filter). The two stages structure ensures a large polar (18 mrad $< \theta < 180$ mrad) and momentum acceptance. A sketch of the COMPASS spectrometer, as it was set up during the 2015 data taking, is shown in Fig. 2.1

This chapter contains an overview of all the components contributing to the COMPASS data takings, namely the beam line, the polarised target, the various detectors stations enclosed in the spectrometer and the trigger system. A detailed focus on the experimental setup adopted in 2015 for the first year of polarised Drell-Yan data taking is also included in the last part of the chapter.

---

[1]**CO**mmon **M**uon **P**roton **A**pparatus for **S**tructure and **S**pectroscopy
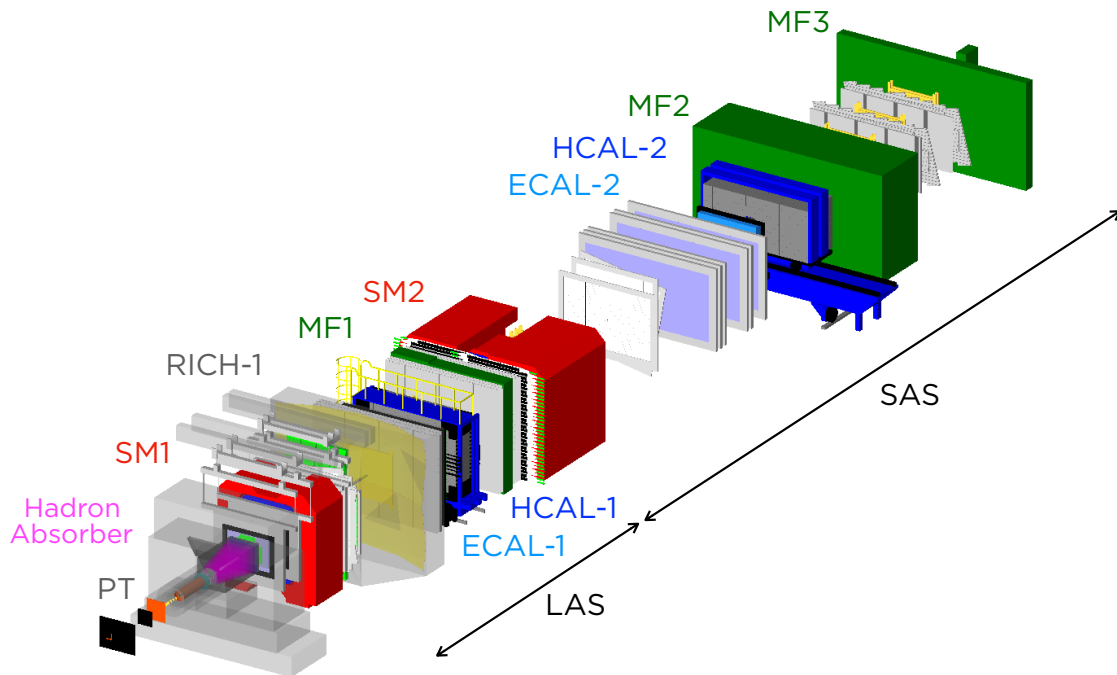
Fig. 2.1 Visualization of the 60 m-long COMPASS spectrometer, obtained from TGEANT (see Chapter 3). This picture shows the Drell-Yan setup used in 2015, discussed in detail in Sec. 2.8

2.1 The Beam

The high-energy particle beam used in the COMPASS experiment is provided via the M2 beam line (schematically represented in Fig. 2.2) from the Super Proton Synchrotron (SPS) accelerator. The CERN SPS M2 beam line can deliver either high-intensity positive muon beams up to 190 GeV/c or high-intensity hadron (mainly pion, positive or negative) beams up to 280 GeV/c. With lower intensities also negative muon beams are available. Also a low-energy and low intensity tertiary electron beam can be delivered, to perform test and calibrations.

2.1.1 Muon Beam

The beam is derived from a high intensity primary proton beam, extracted from the SPS with a momentum of 400 GeV/c and impinging on a Beryllium target (T6) 500 mm thick. Thinner targets can be selected in case a lower flux is desired. The nominal proton flux available for COMPASS on the T6 target is $1.2 \cdot 10^{13}$ protons during 4.8 s long spills within a SPS cycle that may vary in function of other parallel tasks supplied by the facility.

In the reaction of the extracted proton beam with the T6 target, mainly pions are created with a kaon component of about 3.6 % and minor contaminations of

protons and antiprotons ($\sim 0.5\%$). These secondary particles are then selected by an array of quadrupoles and dipoles set to a determined momentum range. A pion beam with a momentum of 172 GeV/c is chosen in order to obtain a tertiary muon beam of 160 GeV/c to be delivered to the COMPASS hall. The muons are originated via weak-decay of pions and kaons in a 600 m long tunnel equipped with alternating focusing and defocusing (FODO) quadrupole magnets, aimed to keep the beam well focused. At the end of the decay line the hadron component is removed by a series of 9 motorised modules of Beryllium, 1.1 m long each (referred as ABS in Fig.2.2). The muon beam is subsequently selected in momentum by a set of five magnetic collimators and then transported to the surface level by a second 250 m long FODO channel. It reaches the ground level $\sim$ 100 m upstream of the COMPASS target, where three consecutive dipole magnets (B6) compose the last vertical bend that arches the beam to the horizontal orientation before entering the experimental hall. The B6 dipoles are surrounded by four quadrupoles and six detector planes (BM01-06). The whole system, called Beam Momentum Station (BMS, Fig. 2.3), is the most upstream part of the COMPASS experimental apparatus. It is used to reconstruct the momentum of each muon beam track with precision $\leq 1\%$ and efficiency of $\sim 93\%$. The final section of the beam line comprises other additional bending and quadrupole magnets to fine-steer the beam on the target.

2.1.2 Hadron beam

Originally, the CERN SPS M2 beam line was built as high-energy and high-intensity muon beam. In the 2000s the facility was upgraded to include a high-intensity hadron beam options, opening new frontiers for the COMPASS physics program. While running in hadron beam configuration, the ABS are moved out and the muons produced by weak decay of pions and kaons are almost completely removed by the second momentum-defining collimator in the second FODO channel. In order to minimize the material budget on the beam path, the BMS is moved out. Therefore, during data taking with hadron beams only the trajectory of the beam particle is measured.

The relative composition of the hadron beam at the COMPASS target depends on the beam momentum and on the beam charge. A summary for typical momenta available at the M2 beam line is reported in Tab. 2.1.

During the 2015 Drell-Yan run a high intensity π^- beam with momentum 190 GeV/c was used. During the 2014 pilot run, special runs with the BMS in the beam line and low beam intensity ($\sim 10^6$) were collected to determine the typical
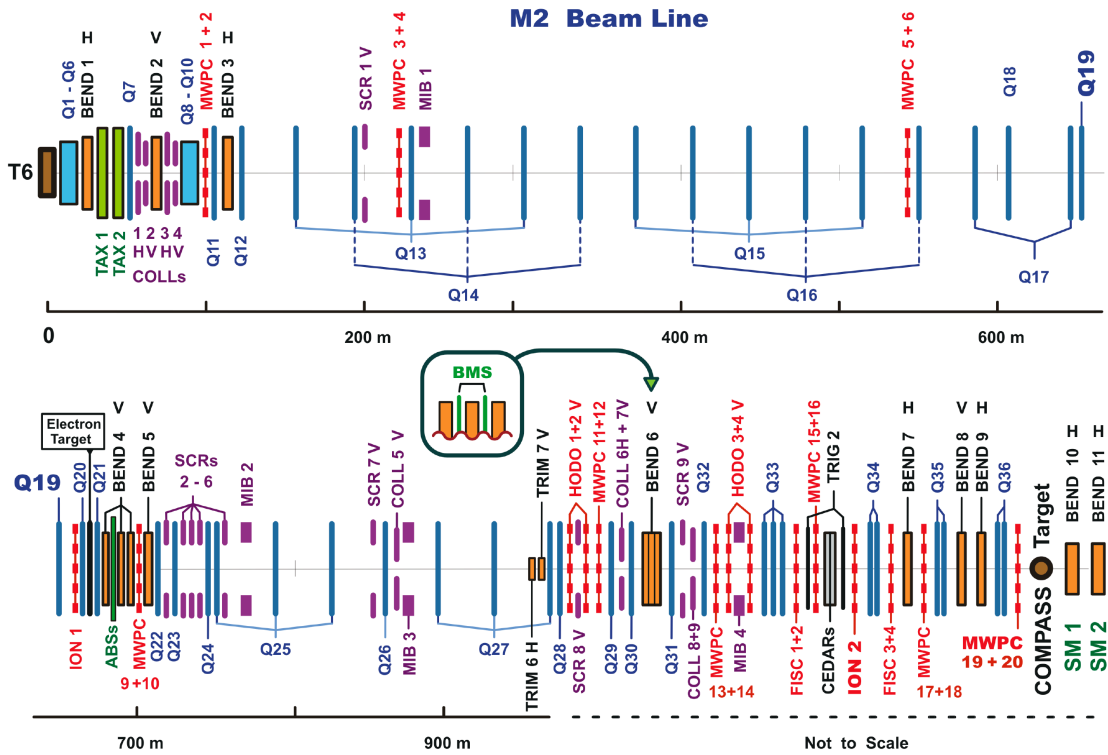
Fig. 2.2 The CERN M2 beam line.
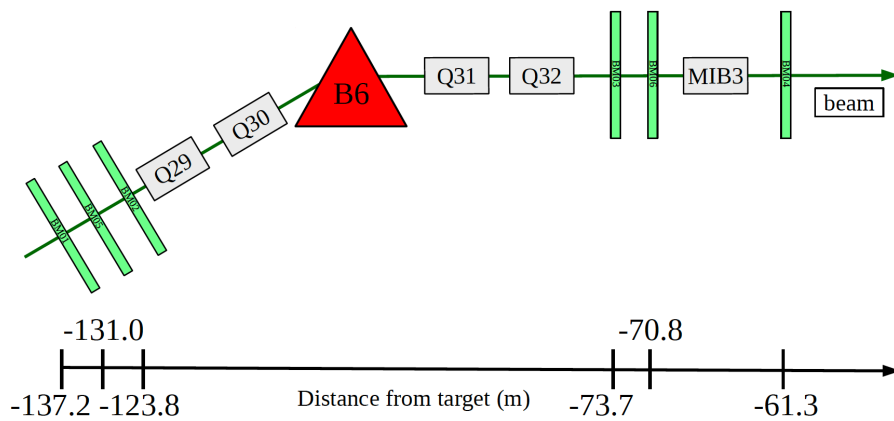
Fig. 2.3 Layout of the Beam Momentum Station for the COMPASS muon beam.

Momentum	Positive beams			Negative beams		
(GeV/c)	π^+	K^+	p	π^-	K^-	$\bar{p}$
100	0.618	0.015	0.367	0.958	0.018	0.024
160	0.360	0.017	0.623	0.966	0.023	0.011
190	0.240	0.014	0.746	0.968	0.024	0.008
200	0.205	0.012	0.783	0.969	0.024	0.007

Table 2.1 The relative composition of the hadron beam at the COMPASS target for some typical momenta. It does not include the $e^{\pm}$ component, which is still present at 100 GeV/c but rapidly decreasing at higher momenta because of the synchrotron radiation. The composition is calculated from measured values [165] with relative uncertainties around 1% for pions and proton and 2-3% for kaons and antiprotons.

momentum distribution of the secondary π^- beam. The result of the measurement is reported in Fig. 2.4 and shows a mean value of 190.9 GeV/c with a standard deviation of 3.2 GeV/c.

2.1.3   The CEDARs

Since the hadron beam delivered to COMPASS has different components, a fast beam particle identification system is needed to disentangle events occurring with different kind of beam particle. For this reason, two CEDAR detectors can be installed 30 m upstream of the target while running in hadronic beam mode. CEDAR detectors are high pressure gas-Cherenkov counters making use of specially designed optics to select desired particle momenta for tagging. The principle of operation is shown in Fig. 2.5. Two particles with the same momentum but with different masses (represented in the figure by red and green lines) radiate Cherenkov photons at different angles, resulting in rings with different radii. The rings of the required particle type are selected with a ring shaped diaphragm located in the focal plane perpendicular to the beam direction. The CEDAR detectors, designed in the late 1970s to provide fast beam particle identification at high rates for particle momenta up to 300 GeVc, have shown large inefficiency at the Drell-Yan beam intensity ($\sim 10^8$ particles/s) making the kaon and anti-proton tagging very difficult. A major upgrade of these detectors, including the electronics, the optical and the thermal systems, was approved in 2016 and is expected to be finished in March 2018, before the starting of the 2018 Drell-Yan run.
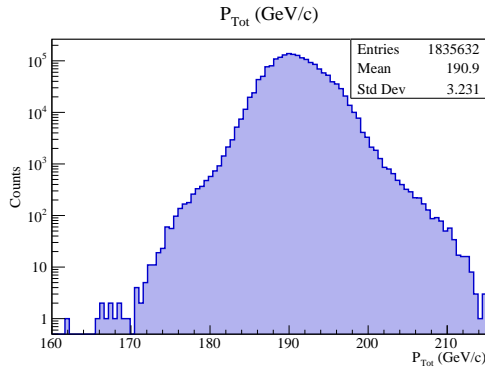
Fig. 2.4 Measured momentum of the π^- beam used for Drell-Yan data taking [166].
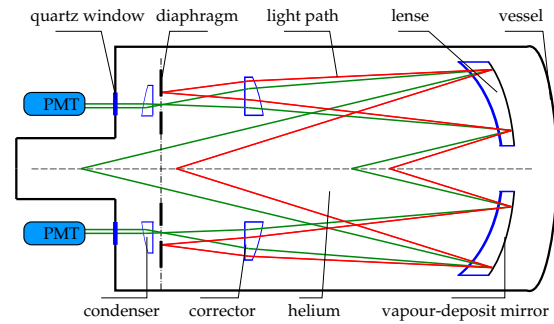
Fig. 2.5 The basic principle of a CEDAR counter.

2.2 The Polarised Target

The polarised target is one of the most complex and fascinating technological devices of the COMPASS experiment. It was designed for the muon programme, trying to match the challenging requirements imposed by the physics case. The aim was to maximize the luminosity in the measurement of the asymmetries arising in cross-sections, taking into account also the need of compensate for the limited muon flux. Furthermore, the measurement of target-spin-dependent azimuthal asymmetries requires a high polarisability of the target material and the possibility to optionally polarise it longitudinally or transversely with respect to the beam axis. Trying to fulfil all these requirements a solid state target with a high density of polarisable nucleons was realized. Until 2006 COMPASS used an isoscalar polarised target material (deuterated lithium, ^{6}LiD), while starting from 2007 data taking a proton target, realized with irradiated NH_3, was adopted. The polarisable solid state material is kept inside two or three cylindrical cells, inserted in a superconducting solenoid magnet capable of delivering a longitudinal magnetic field of 2.5 T. Once the longitudinal polarisation is built up, a dipole field 0.63 T strong is applied in order to pass to the transverse spin mode.

The polarisation is built using the Dynamic Nuclear Polarisation (DNP) technique [167]. The method consists in transferring the electron polarisation to the nucleons using microwave radiations, suitably tuned to a specific frequency to get the proton spin parallel or anti-parallel to the magnetic field. The polarisation is measured during the whole data taking using 10 NMR coils placed on the target holder, which allows a monitoring of the polarisation on a run-by-run basis that can be retrieved afterwards at level of the analysis. Thanks to this quite efficient technique, a polarisation around 90% can be achieved after polarising the target for three days.

Usually COMPASS collects transversely polarised data with neighbouring cells polarised in opposite direction, in order to collect simultaneously data with the two spin configurations. The configuration of the polarisation is reversed periodically and the data are then combined at level of the analysis, to minimize possible errors arising because of differences in the acceptance of the target cells. Working in transverse spin mode, the polarisation cannot be inverted just reversing the dipole field (as it is done in the longitudinal spin mode) because of too many systematic uncertainties originated by the operation. The polarisation is then destroyed and re-built with opposite configuration every two weeks. An intermediate rebuilding step is achieved every week, to compensate for the polarisation decrease along the time. Also the beam tuning takes into account the dipole field, foreseeing the beam to enter with an angle in the horizontal plane to get, after the bending in the dipole, a straight beam coming out of the target and matching the dead zones of the detectors while passing through the spectrometer.

In the asymmetries extraction an important role is being played by the dilution factor f, which accounts for the fraction of polarised material into the target. For the deuterated lithium, since ^{6}Li can be considered, in a reasonable approximation, as a spin-0 ^{4}He nucleus and a deuteron, the dilution factor is of the order of 0.35, taking into account also the He content in the target region. In the case of NH_3, since only the hydrogen protons are polarisable, naively one can expect a dilution factor of 3/17. But beyond this, other effects have to be accounted for, like the dilution coming from radiative effects originated by unpolarised protons and the one introduced by impurities in the target material. More details about this topic, in the specific case of DY 2015 target, will be given in Chap. 4. A sketch of the PT as it was used for 2015 polarised DY data taking is shown in Fig. 2.6.

2.3   Tracking

The tracking system of COMPASS comprises many stations, each composed by a set of planar tracking detectors of a specific type placed at approximately the same z-coordinate along the beam direction. Many different detector technologies with different sizes, granularities and resolutions are in use. Far from the beam in the outer region, large areas of several square meters have to be covered in order to detect low-momentum particles scattered at large angles. Close to the beam in the inner region the particle rates rapidly rise while decreasing distance to the beam axis. Therefore, detectors working in the beam region should be capable to combine a fast response with a good resolution. One can group the tracking detectors in operation at COMPASS in three different typologies:
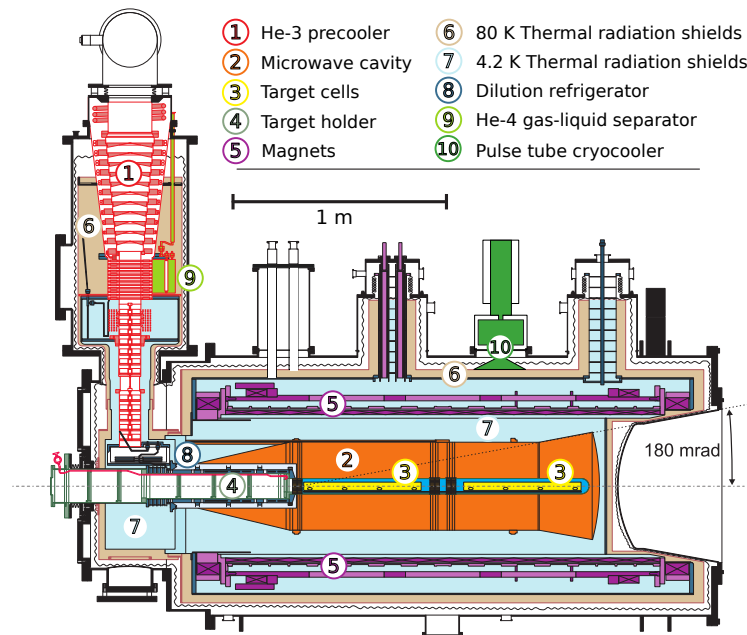
Fig. 2.6 COMPASS Polarised Target as it was during 2015 Drell-Yan data taking.

- **Very Small Area Trackers (VSATs)**, which cover the beam region up to a radial distance of around 3 cm from the beam axis.

- **Small Area Trackers (SATs)**, which are used to measure particles emitted at low angles. However these detectors have central dead zones, or recently, pixelized high flux capable central regions, matching with the coverage area of the VSATs.

- **Large Area Trackers (LATs)**, covering the vast area outermost regions.

The terms X- and Y-plane are adopted in the following to designate the group of channels within a station measuring the horizontal and vertical coordinates, respectively, of the particle penetration point. Similarly, the terms U- and V-plane describe all channels measuring projections onto axes rotated clockwise and anticlockwise, respectively, concerning the x-axis.

2.3.1 Very Small Area trackers

To cope with the very high rate of beam particles in this area (up to $5 \cdot 10^7$ Hz), the VSATs have an excellent time and position resolution. These features ensure a well-performing tracking to measure the beam and other particles trajectories very close to the beam axis, as the scattered muon in the DIS case. The detectors at COMPASS that have such characteristics are the Scintillating Fibres (SciFi)

detectors and the Silicon Microstrips detectors. They complement each other since the formers have an excellent time resolution and the latter own a very good spatial resolution. Together they compose the so-called Beam Telescope (BT) system, which carries on the beam tracking during the data takings.

There are ten SciFi stations in COMPASS with different sizes, varying from 3.9×3.9 cm^2 to 12.3×12.3 cm^2. The diameter of the fibres is 0.5, 0.75 or 1 nm depending on the considered station, corresponding to a spatial resolution of 130, 170 and 210 μm. The time resolution of all the SciFis stations is about 400 ps.

Five stations of Silicon Microstrips detectors are available in COMPASS, with an active area of 5×7 cm^2 and a time resolution of 2.5 ns and a spatial resolution of 10 μm. Three of them are used in the BT, while the other two stations are usually placed downstream of the target, to enforce the vertex reconstruction.

Since the high beam intensity employed in the 2014 and 2015 Drell-Yan measurements cannot be standing by the Silicons, these detectors were not included in the setup. Therefore the BT consisted of just three SciFi stations (FI01, FI03, and FI15) during the DY data takings.

Starting from 2009 a new typology of VSATs was included in the COMPASS setup. With the aim of minimising the material budget from detectors directly exposed to the beam, some of the scintillating fibre detectors that were used in the spectrometer were replaced by thinner trackers based on Gas Electron Multiplier (GEM) foils [168]. The spatial resolution of these pixelized planes was measured to be around 105 μm, coupled with a time resolution around 11 ns.

2.3.2 Small Area Trackers

The SATs at COMPASS cover the region at a radial distance from 5 cm to 40 cm from the beam axis. In this area, the particles rate decreases up to two orders of magnitudes ($\sim 10^5$ Hz) with respect to the innermost region. Therefore, the requirements on the time resolution of the trackers covering this area are less strict, allowing the use of gaseous detectors like Micromesh Gaseous Detectors (Micromegas) and Gas Electron Multipliers (GEMs).

The Micromegas are gaseous detectors composed by a conversion and an amplification region, separated by a metallic micromesh. The particles passing through the detector ionize the gas in the conversion gap, freeing electrons that drift in a moderate field (3.2 kV/cm) toward the amplification region, where a higher field (50 kV/cm) produces an avalanche collected by the strips (see Fig. 2.7). The time resolution is about 9 ns, while the pitch of the strips goes from 360 μm (inner part) up to 420 μm (outer part).
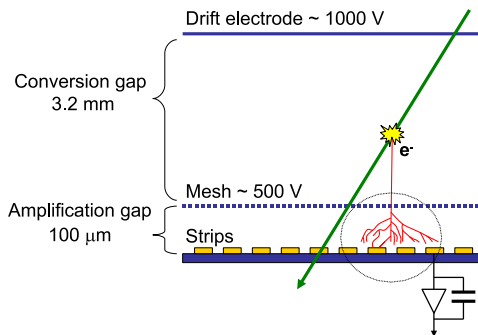
Fig. 2.7 Working principle of a Micromegas detector.
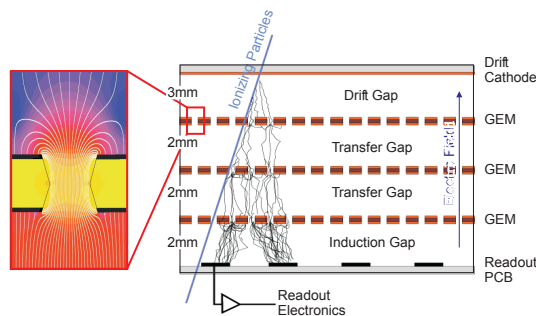
Fig. 2.8 Schematic cross section of a COMPASS GEM detector. The insert on the left shows the electric field configuration for typical GEM voltages.

The COMPASS spectrometer is equipped with three Micromegas stations, each composed of four projection planes with an active area of 40×40 cm^2. All the stations are placed between the target region and SM1 and have a circular dead zone of 5 cm radius. In 2014 all the Micromega planes were upgraded installing a pixelised core in correspondence of the dead zone, to cover the region crossed by particles emitted at very low angles.

The GEMs consist of a 50 μm thin Polyimide foil, clad with Cu on both sides and with $\sim 10^4$/cm^2 micro-holes of 70 μm diameter. Because of a potential difference of several 100 V applied across the foil, a primary electron generates an avalanche into the holes. Suitable electric fields extract then the electrons from the holes on the other side of the foil, guiding them to the next amplification stage or toward the readout anode. As represented in Fig. 2.8, the COMPASS GEM detectors [169] have three amplification stages, stacked on top of each other, and separated by thin spacer grids of 2 mm height.

In the COMPASS experiment, in total eleven stations of GEMs are placed in the setup. Any of them has an active surface of 31×31 cm^2, composed of two orthogonal projections containing 768 strips. For each particle trajectory, one detector consequently records two projections of the track with highly correlated amplitudes, reducing ambiguities significantly. A central region of 5 cm diameter is deactivated while running in normal high-intensity beam condition to avoid a too high occupancy in the median strips.

2.3.3 Large Area Trackers

Large area trackers are covering the outermost regions of the COMPASS acceptance. Thanks to the reduced rate, there also gaseous detector, with not excellent

time resolution, can be installed. Detectors belonging to this group are the Drift Chambers (DCs), the Straw tube detectors (Straws), the Multi-Wire Proportional Chambers (MWPCs), the large area drift chambers (W45) and the RichWall.

Four DC stations surround SM1. Two of them, characterised by a smaller sensitive area (180×127 cm^2), stand between the target region and the magnet, while the other twos are located downstream of it and cover a surface of 240×200 cm^2. In both cases, the size of the detectors was chosen to match the acceptance of SM1 yoke. The most downstream DC station, DC05, is a brand new detector put in operation in 2015 to enforce the tracking in the LAS. The DCs have a deactivated central region, which is 30 cm in diameter. Each DC station comprises two planes per projection, in turn, composed by a set of sensitive wires of 20 μm diameter and potential wires of 10 μm diameter. The distance between wires of the same kind is 7 mm. Two cathode foils enclose the wires in a gas gap of 8 mm, as can be seen in Fig. 2.9. The DCs have a spatial resolution of about 250 μm.

The COMPASS spectrometer also comprises six stations of large area (500×250 cm^2) DCs in the SAS, the so-called W45. Each chamber has four layers, two per different projections. The diameter of the anode wires is 20 μm, while for the cathode wires is 100 μm. The gap between the anode and the cathode is 10 mm, and the separation between subsequent signal wires is made by field wires of 200 μm diameter. The resolution of the W45 stations is about 500 μm.

During the Phase I, the COMPASS setup included three stations of Straw Tube Chambers, covering a broad range in polar angle acceptance ($15 < \theta$ (mrad) < 200). Two stations were placed in the LAS and one in the SAS. Fig. 2.10 shows a schematic view of the COMPASS Straw structure. Each Straw plane is divided into two outer and one inner piece. The Straw tubes have in their center an anode, consisting of a gold-plated tungsten wire, which attracts electrons resulting from ionization. Their diameter depends on the region where they are placed: 6.1 mm for inner part, 9.6 mm for the outer one. The dimensions of the planes are slightly different, depending on the orientation of their wires: for X and Y planes the active area is 350×245 cm^2, while for U and V projections is 323×272 cm^2. The dead zone of each plane is located in the inner part and has a size of 20×20 cm^2. The resolution was estimated to be around 400 μm. Before the beginning of the 2015 DY run, the first Straw station after SM1 was removed from the setup, to be replaced by DC05. Given the small contribution in the tracking, mainly due to the low-efficiency level caused by ageing effects, at the end of 2016 also the Straw station located in SAS was removed from the COMPASS setup.

Fourteen stations of MWPCs are also included in the spectrometer, six in the LAS and eight in the SAS. One can separate them into three different types, A,
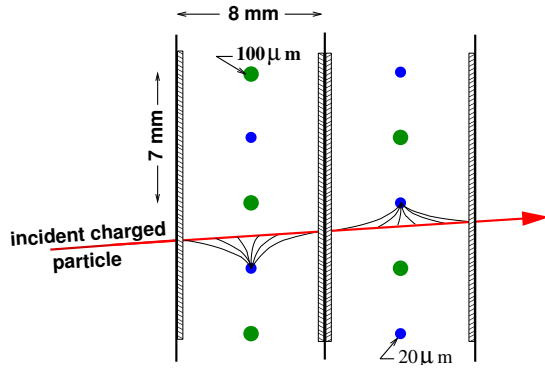
Fig. 2.9 Working principles and geometry of COMPASS Drift Cells.
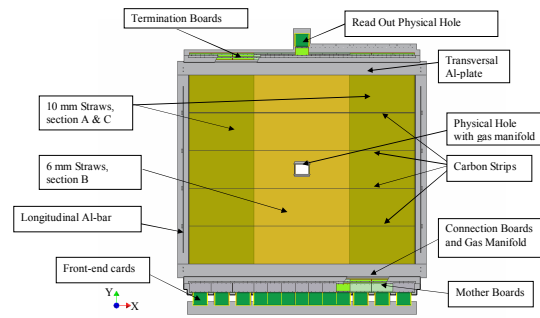
Fig. 2.10 Schematic section of a COMPASS Straw detector.

A*, and B. The seven chambers belonging to the so-called type-A cover an area of 178×120 cm^2 and have three projections, X (vertical wires), U (vertical wires rotated of +10 degrees) and V (vertical wires rotated of -10 degrees). The second MWPC type is the A*, similar to A type with an additional Y projection. There is only one station of this kind in COMPASS, located downstream the RICH. The remaining six chambers of type-B are smaller in size, 178×80 cm^2, and are composed by one X projection coupled with an inclined one (U or V). The dead zones are circular and with a diameter varying from 16 to 22 mm. The typical spatial resolution of these chambers is about 600 μm.

The last detector belonging to LATs is the so-called RichWall. It is positioned between the RICH and ECAL1 and it has an active area of 5.27×3.91 cm^2, with a central hole of 1.02×0.51 cm^2. The detector consists of eight planes of Mini Drift Tubes (MDTs) made up of MDT modules (see Fig. 2.11). An MDT module is formed by an aluminium comb extrusion with eight-cells and a wall thickness of 0.44 mm, covered on the top by a 0.15 mm thick stainless steel foil. Gold-plated tungsten wires of 50 μm diameter are inserted in the centre of the cells. The wire pitch is 10 mm. Each module is encapsulated into a Noryl plastic envelope with a thickness of around 1 mm and it is separated from the neighbours by a plastic spacer. The eight MDT planes are arranged in four pairs of the same kind of projections (X or Y). The two planes within one group are staggered by 2.5 mm.

2.4 Particle Identification

The particle identification (PID) at COMPASS is carried on by four different kinds of detectors. The muon identification is performed by two Muon Wall Systems (MW1 and MW2), one per each stage of the spectrometer. The Ring Imaging Cherenkov (RICH) detector, placed in the LAS, identifies pions, kaons and protons.
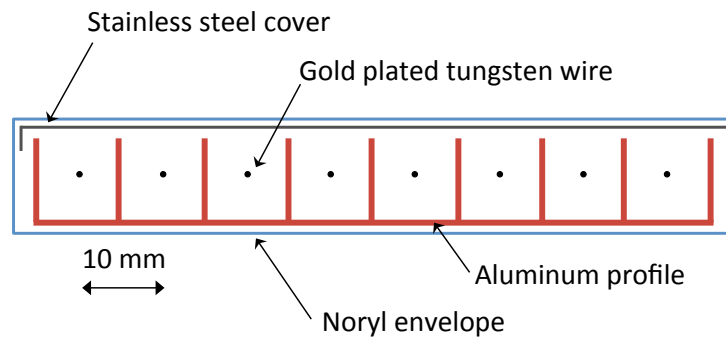
Fig. 2.11 Sketch of a Mini Drift Tube module.

Both LAS and SAS are equipped with two Electromagnetic Calorimeters (ECAL1 and ECAL2) and two Hadronic Calorimeters (HCAL1 and HCAL2). The formers are measuring the energy of photons and electrons, while the latter the energy of hadrons. Although this study does not include hadron type specific measurements, all PID detectors are briefly described in the following for completeness.

The COMPASS RICH detector [170] is located in the LAS, downstream of the SM1 magnet, before the calorimetry stages. It performs hadron identification in the domain between 5 GeV/c and 50 GeV/c. Its large dimensions allow covering a wide acceptance range (up to $\pm$ 250 mrad in the horizontal plane and $\pm$ 180 mrad in the vertical one). The principle of operation of the detector is based on the Cherenkov effect, occurring when a particle is travelling in a dielectric medium (C_4F_{10} in the case of COMPASS) with a velocity larger than the velocity of the light in that medium. The emitted photons are reflected and focused by two mirrors to the photon detectors (PDs), placed outside of the LAS geometrical acceptance. Initially, the photon detection was carried out just by MWPC-CsI detectors. Before the 2006 data taking the MWPC-CsI in the central region have been replaced by Multi-Anode Photo-Multipliers Tubes (MAMPTs), much more suited to cope with the high rate of photons in this area [171]. At the beginning of 2016 other four stations of MWPC-CsI, placed at the top and bottom part of the detector, have been substituted by novel hybrid Micro Pattern Gaseous Detectors, combination of two Thick Gas Electron Multipliers and a MicroMegas stage [172]. An artistic view of the RICH and a summary of the different PDs used along the years can be found in Fig. 2.12. One electromagnetic and one hadronic calorimeter measure the energy of the particles in both the stages of the spectrometer. The ECALs detects photons and electrons via measurement of the light produced by the showering of these particles inside their modules. The intensity of the detected light is directly linked to the energy deposited in the module. ECAL1 is positioned
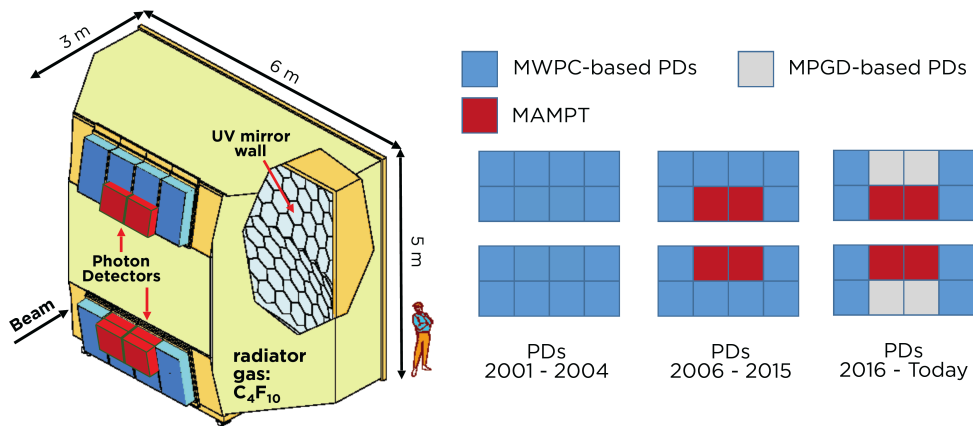
Fig. 2.12 Artistic view of the COMPASS RICH detector (left) and schematic representation of the PDs configuration adopted during different years (right).

between the RICH and HCAL1, and covers an area of 3.97×2.86 m^2 with a central hole of 1.07×0.61 m^2. As it is illustrated in Fig. 2.13, three different kind of modules, GAMS[173], OLGA [174] and MAINZ [175], composes the detector. ECAL2 is installed in the SAS, in front of HCAL2, covering a surface of 2.84×1.83 m^2. It consists of 3068 modules of three different types: GAMS, GAMS-R and Shashlik. They are arranged as in Fig. 2.14.

For 2016-2017 DVCS data taking, a new electromagnetic calorimeter, named ECAL0, was assembled and placed downstream the target. The final setup of this detector has been decided profiting of the experience gained in 2012 DVCS pilot run, when a prototype with smaller dimensions was installed in the spectrometer. This detector was installed in the setup just during DVCS runs, more information about it can be found in [176].

The hadronic calorimeters present in the COMPASS spectrometer are based on a sampling technique. Both are equipped with Shashlik modules that are different from the electromagnetic Shashlik types in size and material. In the HCALs Shashlik modules layers of irons alternate with a scintillating material. The firsts are responsible for the showering of the hadrons, while the seconds measure the light signal originated in the shower, which is proportional to the energy deposit in the module. Each of the two HCALs have a central window which matches in acceptance the hole of the associated ECAL.

The Identification of the muons is performed by two dedicated muon filters (MFs). Because of the weak interaction nature of the muons, each stage of the COMPASS spectrometer has a MF at its end. The design principle of the MFs is the same for LAS (MF1) and SAS (MF2): they consist of a thick absorber layer preceded and followed by trackers station, the so-called Muon Walls. Since the
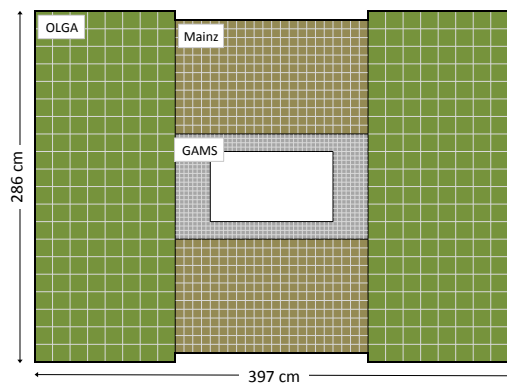
Fig. 2.13 Configuration of ECAL1. The central region is instrumented with GAMS modules. The MAINZ modules cover the surfaces above and below the GAMS area. The outer left and right regions are equipped with OLGA modules.
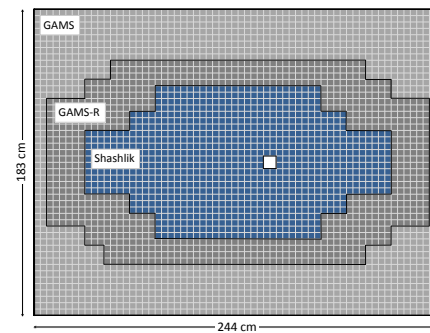
Fig. 2.14 Configuration of ECAL2. The central region is equipped with Shashlik modules. GAMS module are used for the outer region, while the intermediate one is instrumented with GAMS-R. The central hole of 2×2 modules can be seen as a white spot.

absorber is thick enough to stop incoming hadrons, a track can be associated to a muon when it can be reconstructed both upstream and downstream of it. The MF1 consist of two stations of squared drift tubes[2] covering an area of 4.8×4.1 m^2, with a central hole of $1.4 \times$. An iron wall, 60 cm thick, is acting as absorber between the two stations. The MF2 system is built around a concrete absorber 2.4 m thick. Upstream of it, the tracking is carried on by SAS trackers (MWPCs, W45, ST05), while downstream it is up to two stations of steel drift tubes with an active surface of 4.5×2.0 m^2 each.

There is a last absorber, called muon filter 3 (MF3), in front of the H5 hodoscope stations. This filter is made of iron and ensures that the inner trigger is only fired by muons.

2.5   Trigger

Due to limitations regarding the buffer-time and the available disk space, a fast selection of events of interest on hardware level is crucial to optimise data storage in a high rate environment. To fulfil this requirement, the COMPASS trigger is based on the fast signals of hodoscopes, on the energy deposit measurement in the calorimeters, and on a veto system around the incoming beam axis.

In view of the high rates due to the large acceptance of the spectrometer, the hodoscopes of the trigger system are grouped into five subsystems consisting of two hodoscopes stations each, listed in Tab. 2.2. Because of the muon selection,

---

[2]The Muon Walls MDTs are very similar to the Rich Wall ones.
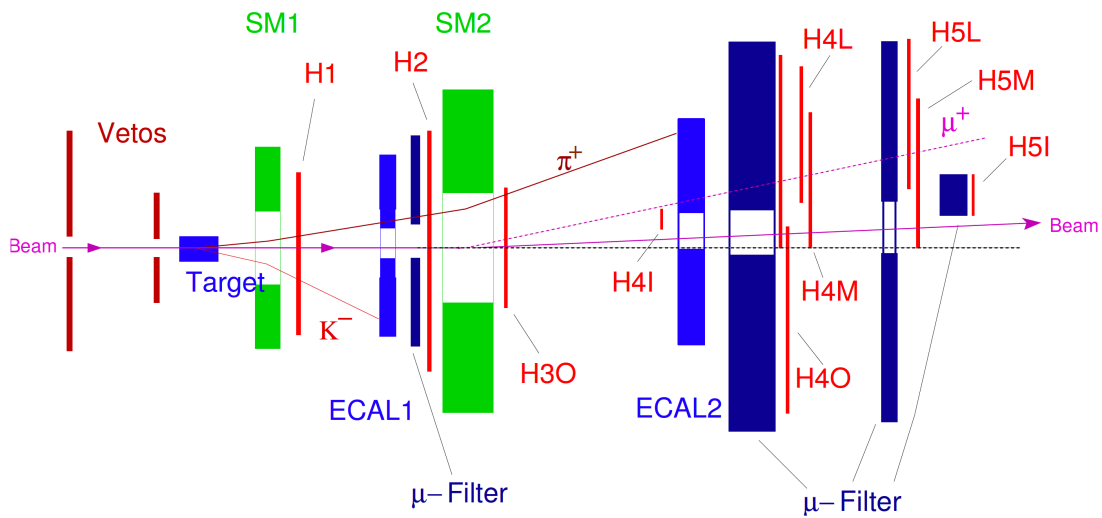
Fig. 2.15 Schematic location of the components relevant for the trigger.

each of these systems has one of the two hodoscopes downstream of an absorber, to reject hadrons and electrons (see Fig. 2.15).

Relying on several station of hodoscopes placed along the spectrometer, the trigger system of COMPASS covers a wide range of phase space, as can be seen in Fig. 2.16.

The trigger for events with a large Q^2 is fired by the scattered muon. These events are mainly triggered by the Outer Trigger (OT) or by the Large Angle Spectrometer Trigger (LAST). These hodoscopes are composed of horizontal slabs, which can measure the vertical position of the muon trajectory. The vertical positions at the two hodoscope stations at different z positions are combined to extrapolate the muon track to the target region in the non-bending plane of the two dipole magnets. The combinations of hits associated with muon tracks originating from the target are then selected on a trigger-matrix basis.

Events at low Q^2 are usually related with muons scattered at low polar angles during the interaction. In this case, because of the large uncertainty on the vertex position, the target pointing method adopted for OT and LAST is not applicable. The triggers operating in this kinematic range (LT, IT and MT) are based on a different approach, the so-called energy-loss trigger, where a scattered muon with a minimal energy-loss in the target is desired. This trigger makes use of vertical hodoscope slabs and a triangular coincidence matrix, which takes into account the angular spread of the scattered muons. The principle of operations of the target pointing and of the energy loss triggers are depicted in Fig. 2.17.

To better measure Semi-Inclusive reactions and perform hadron spectroscopy studies, also calorimeter based triggers (CT) have been implemented. Anyhow,

Name of the system	Hodoscopes	Projections	Size ($x \times y$)
Large Angle Spectrometer Trigger (LAST)	H1	Y	230×192
	H2	Y	500×419.2
Outer Trigger (OT)	H3O	Y	200×100
	H4O	Y	480×225
Middle Trigger (MT)	H4M	X-Y	120×102
	H5M	X-Y	150×120
Inner Trigger (IT)	H4I	X (up - down)	17.3×19.4
	H5I	X (up - down)	35.3×25.95
Ladder Trigger (LT)	H4L	X	128.2×40
	H5L	X	168.2×47.5

Table 2.2 COMPASS trigger systems based on hodoscopes. 'X' or 'Y' distinguishes between the different orientation of the slabs, vertical or horizontal respectively. The latter are not sensitive to magnetic field bending of the particles. The size is given in cm^2.

after constructing the LAST in 2010, the CT was not used any more as physics trigger. Its usage nowadays is mostly related to trigger efficiency determination.

Because of the high muon beam emittance and the halo component of about 25%, many fake triggers fired by muons not interacting in the target can take place. These eventualities can be avoided at COMPASS thanks to a veto system added to the trigger. It consists of three stations of scintillation counters installed upstream of the target, aimed to detect the intense near-beam halo muons.

2.6 Data acquisition and Reconstruction

2.6.1 Data acquisition

The typical trigger rates on spill ranges from 10 kHz to 100 kHz, depending on the physics programme. Thus, despite of the triggering system, the data rate handled at COMPASS remains considerable. To cope with it a pipelined and nearly dead-time free readout scheme has been adopted. An overview of the data flow[3] is given in Fig. 2.18.

The digitisation of analogic signals read-out from the detectors is carried out by ADC or TDC placed directly on the front-end board or directly by GANDALF[4], GeSiCA[5] or CATCH[6] readout cards. The data is then transferred via optical

---

[3]Since the DAQ was significantly improved for COMPASS-II, the description given in this section concerns the new system. Details about the old DAQ, used during the Phase I, can be found in [15].

[4]**G**eneric **A**dvanced **N**umerical **D**evice for **A**nalog and **L**ogic **F**unctions [177].

[5]**Ge**m and **Si**licon **C**ontrol and **A**cquisition

[6]COMPASS **A**ccumulate, **T**ransfer and **C**ontrol **H**ardware.
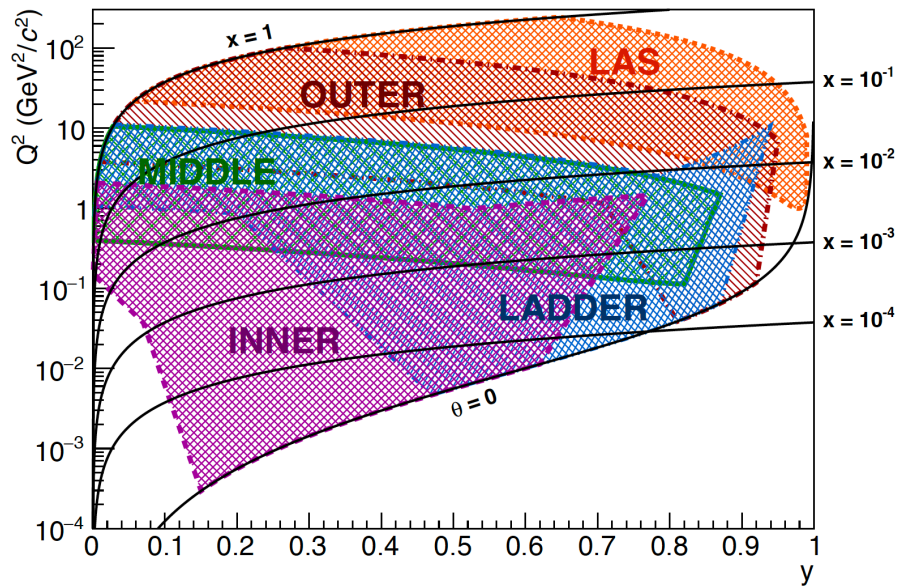
Fig. 2.16 Kinematic acceptance of the COMPASS muon trigger system.
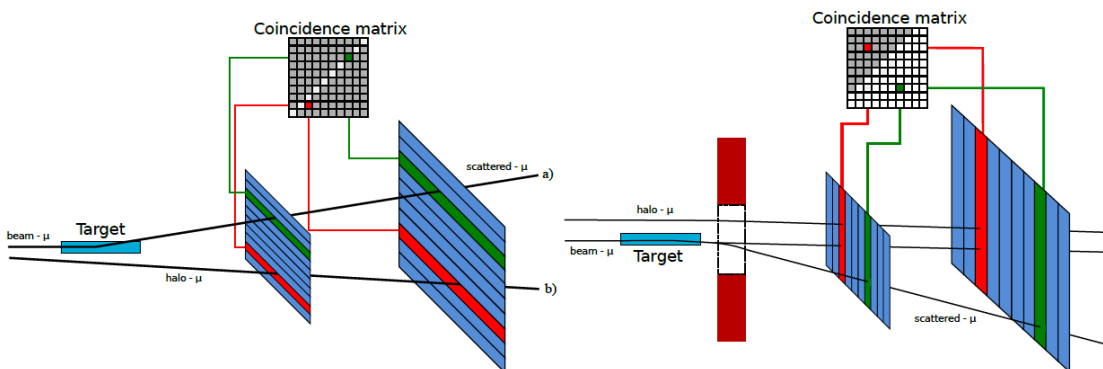
Fig. 2.17 Schematic representation of target pointing (left) and energy loss (right) triggers working principles.
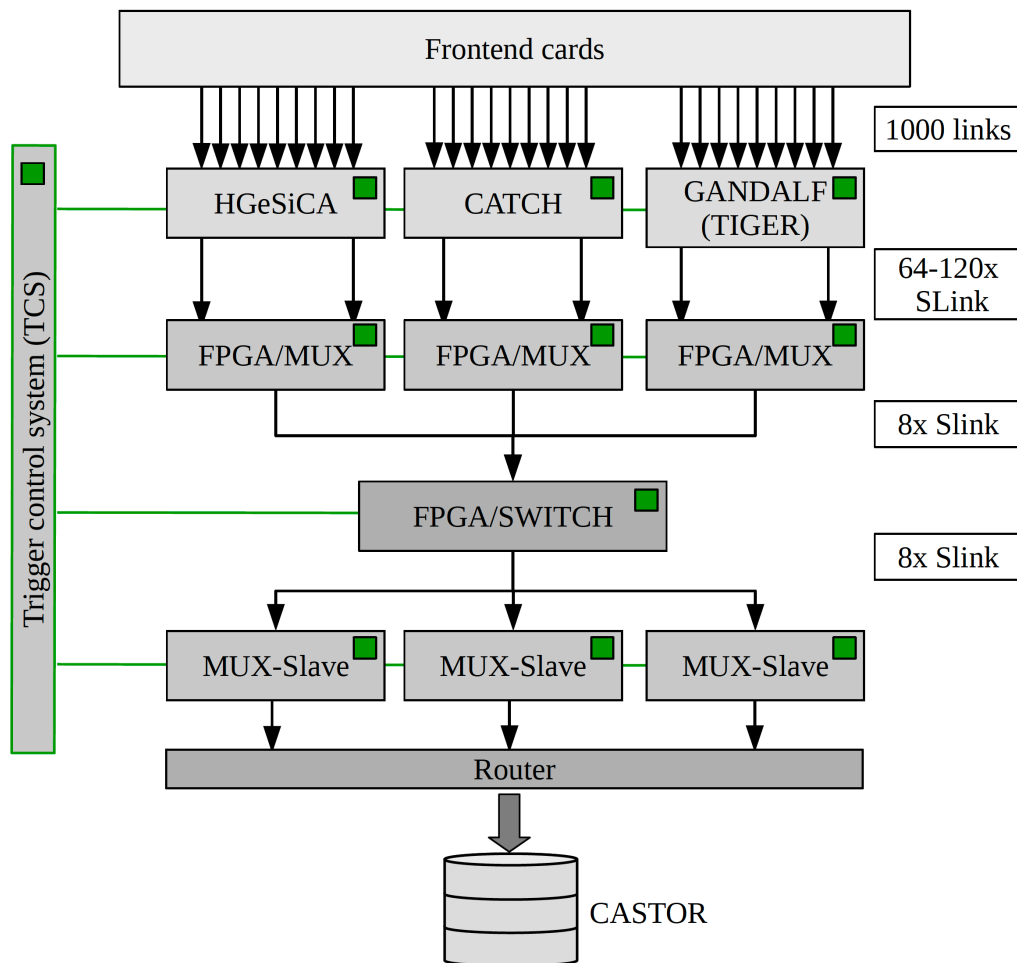
Fig. 2.18 Schematic readout and data acquisition flow at the COMPASS experiment since 2015 [179]. The green boxes mark the components that receive the trigger signal from the TCS.

fibres[7] to FPGA[8] multiplexing cards, where the data is buffered for one spill while merging it into sub-events. These products are then distributed to multiplexer slaves by a FPGA switch [178]. The slaves are online computers that manage the building of the final raw data events and their transfer to CASTOR[9], to be recorded on magnetic tape.

2.7 Event Reconstruction

To be analysed, the raw data events stored on CASTOR must be processed with the COMPASS reconstruction software, CORAL[10], a fully object oriented C++

---

[7]The so-called **S**imple **Link** Interface.

[8]**F**ield **P**rogrammable **G**ate **A**rray.

[9]**CERN A**dvanced **STOR**age.

[10]**COMPASS R**econstruction and **A**na**L**ysis Program.

based package. The complete COMPASS reconstruction work flow is summarized in Fig. 2.19

The first step in the reconstruction is the so-called decoding process, where the raw data, encoded in binary format, are read and translated into calibrated digits. Afterwards, the digits are opportunely clustered in hits assigning to each of them a well-defined space-time information (for some detector as calorimeters also paired with energy deposit).

The hits are the entities used in the tracking and the vertexing procedure. The former makes use of a Kalman Filter algorithm [180], trying first to build tracklets in regions free from strong magnetic fields and then to bridge them together through the magnetic fields using a fast lookup table for the bending in the field (*dicofit*). The outcome of the Kalman procedure, a track with defined charge, momentum and χ^2 from the fit, is then extrapolated to the target where the points of intersection with other tracks are fitted, searching for interaction vertices. When an interaction vertex is reconstructed, it is classified as primary or secondary. In the former case, a beam particle track, defined as a reconstructed track in the region upstream the target, is also associated to the vertex during the fitting procedure.

In the case of Monte Carlo (MC), the data flow is slightly different. The response of the apparatus is simulated at level of CORAL including the smearing due to finite resolutions of the detectors. In this digitization process, real-hits are created from the Monte-Carlo hits. Since the subsequent steps of the work-flow have no information on the nature of the hits fed in the reconstruction chain, it is ensured that no systematic biases are introduced while treating MC instead of real data.

Once the reconstruction procedure is terminated, the information is stored in the resulting files, the so-called mini-Data Summary Trees (mDSTs). These files can be analyzed afterwards using PHAST[11], a C++ based software package that allows to write routines in C++ to select the data event-wise.

2.8 Drell-Yan setup

The Drell-Yan (DY) measurements are one of the pillars of the COMPASS II proposal [136]. The apparatus used in the 2015 DY run includes some modifications with respect to the one used for SIDIS, DVCS and hadron spectroscopy. The distinctive features of the DY setup are briefly discussed in this section.

---

[11]**PH**ysics **A**nalysis **S**oftware **T**ool.
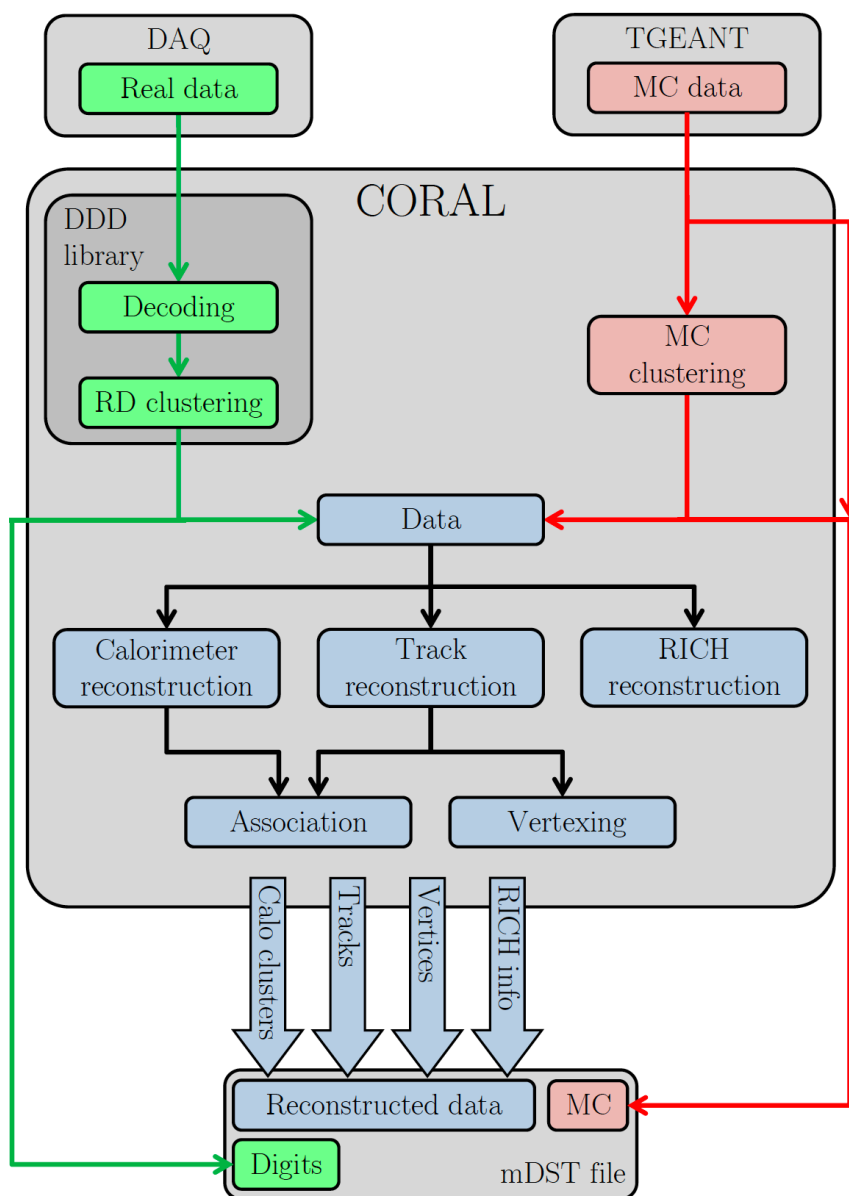
Fig. 2.19 Schematic representation of the data flow in the COMPASS reconstruction software for Real Data (green) and Monte Carlo (red).

2.8.1 Beam Line

Using a high intensity π^- beam ($\sim 10^8$ π^-/s), the BMS must be removed from the beamline to consistently reduce the material budget crossed by the hadron beam before the interaction in the target. Thus, no beam momentum measurement was available during 2014 and 2015 runs. Since in 2015 the dipole field of the PT was turned on, a chicane system, made with bending magnets, was realised upstream of the COMPASS hall to have the beam impinging on the target with an inclination in the horizontal plane. The magnitude of the slope has been estimated by means of MC to have the beam centred on the beam dump placed downstream of the target after passing through the PT dipole field.

2.8.2 Hadron Absorber

A spectrometer configuration with a hadron absorber downstream of the PT was chosen after the DY beam tests performed in 2007 and 2009. Since in the DY measurements just a dilepton pair is searched in the final state, this passive structure aims to stop the massive flux of secondary hadrons originated in the target and the non-interacting π^- beam, to considerably reduce the detectors occupancy in the spectrometer.

Various configurations, comprising different materials and geometries, have been evaluated using MC. The chosen one consists of ten layers, 19 cm long each, realised with alumina (Al_2O_3) tiles inserted in a stainless steel frame. Neighbour layers are interspersed with thin aluminium layers (0.5 cm long). Downstream of the alumina, three layers of stainless steel, 5 cm, 5 cm and 10 cm long respectively, forms the endcap of the absorber. The alumina layers have a 5 cm radius cylindrical hole in their centre. This cavity is the housing of a thin aluminium target (7 cm long) and a tungsten beam dump. Both the former and the latter are employed as nuclear targets to perform also unpolarised DY studies. An additional cone-shaped aluminium piece is placed in front of the structure and plugged into the target solenoid, leaving a 6 cm gap between it and the absorber for the installation of the vertex detector. The cone also has a cylindrical hole of 5 cm radius.

At the beginning of 2015, to reduce the occupancy on the trackers placed just downstream of the absorber (DCs and MicroMegas), two additional Li layers, 0.3 cm thick, have been added in front and on the back of the last stainless steel layer. The endcap was also extended with a polyethylene layer 0.5 cm thick, installed for the same purposes. The structure of the hadron absorber is schematically demonstrated in Fig. 2.20.
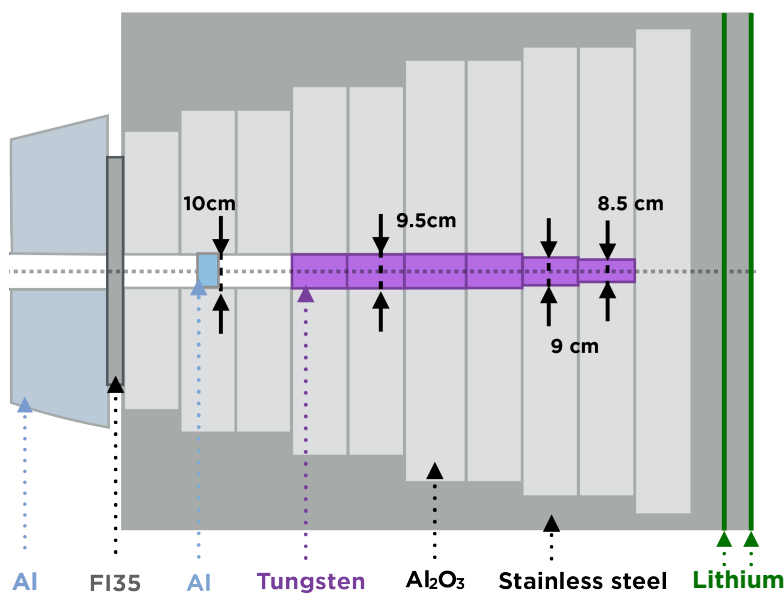
Fig. 2.20 Schematic representation of the Hadron Absorber design.

2.8.3   Polarised Target

After an incident occurred with the solenoid at the end of 2011, the superconducting magnet of the PT was completely refurbished and equipped with a new CERN-standard Magnet Control System (MCS) and Magnet Safety System (MSS). Also the cryogenic system of the PT has been fully renewed. The layout of the target cells was modified taking into account the different peculiarities of the polarised DY measurements with respect to the transversely polarised SIDIS ones. During 2015 DY data-taking the polarised target consisted of two longitudinally aligned cylindrical cells of 55 cm length and 2 cm in radius, divided by a 20 cm gap[12] and placed in a magnetic field of 0.6 T generated by the PT magnet. Similarly to the SIDIS case the cells were polarised vertically in opposite directions. In case of DY measurements the polarisation reversal took place every two weeks. Five nuclear magnetic resonance (NMR) coils, made of stainless steel, were installed in each cell: 3 outer coils were fixed on the outside surface, while the 2 inner ones were placed on the internal walls of the target holder. The NMR coils were responsible for the measurements of the proton polarisation of the target material surrounding them.

---

[12]The vertex resolution in DY is much worse with respect to SIDIS because of the hadron absorber and it would not be enough to separate the events between the cells. Thus, the three cells configuration was not feasible.

2.8.4 Vertex detector

To improve the vertex resolution along the beam direction a SciFi vertex detector was realised and installed in the gap between the nose and the absorber body. The detector consists of three planes of Scintillating fibres stacked one on each other. Each plane measures a different projection (X, V and U). The X plane covers a 22.5×22.5 cm^2 area, while the U and V planes have an active surface of 15×15 cm^2. However, this detector suffers for the high occupancy, and its inclusion in the reconstruction is still under development. All the analysis shown in this thesis are based on data produced without including the vertex detector in the reconstruction.

2.8.5 The dimuon trigger

Looking for a dimuon pair in the final state, a new dimuon trigger system has been implemented in the COMPASS trigger logic chain. Relying on MC studies performed so far, three dimuon trigger system have been setup for the study of DY reactions, namely:

- **LAST 2μ**, triggering with a coincidence of two LAST triggers within 5 ns.

- **OTLAST**, fired by a coincidence of one muon in OT and one muon in LAST within a time window of 10 ns.

- **MTLAST**, fired by a coincidence of one MT trigger with a LAST trigger into 12 ns.

A schematic representation of the trigger logic adopted for DY can be found in Fig. 2.21. The Q^2 vs x_N coverage of the DY triggers for dimuon pairs generated in the range $4.0 < M_{\mu\mu}/(\text{GeV}/c^2) < 9.0$ is illustrated in Fig 2.22.

Some modification hardware-wise was also needed to optimize the trigger for the DY measurements. The hodoscopes were re-designed to be symmetric around the zero of the *x-y* transverse plane. This was not fully achieved, due to limitations of the beam onto which the OT hodoscopes were. The OT hodoscopes were not shifted in position, and a symmetrical hole was introduced, resulting in a similar but not equal acceptance for positive and negative muons. The MT hodoscopes were shifted to cover the hole of the OT hodoscopes.

Only in case of special runs aimed to extract trigger efficiency, the CALO trigger was also turned on, to provide unbiased data acquired without the involvement of the hodoscopes.
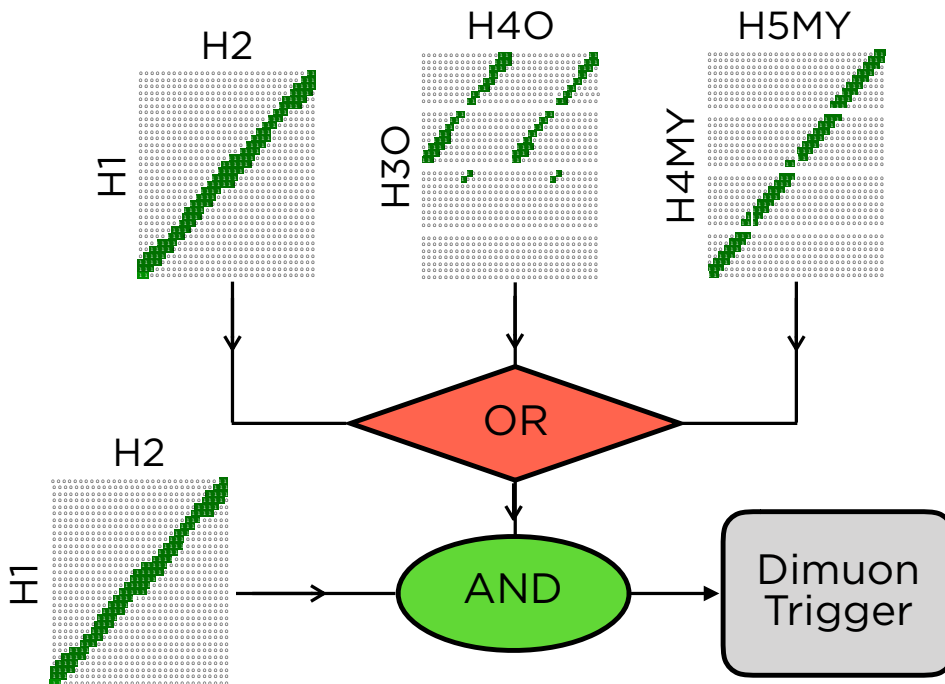
Fig. 2.21 Dimuon trigger logic for the DY run in 2015. Hit combinations in the upstream and downstream planes of a hodoscope system are analyzed for their geometrical correlation using the trigger matrices. Each row and column corresponds to a hodoscope slab in the corresponding station. Entries marked in green in the matrices give a positive outcome of the coincidence, required in a specific time window.
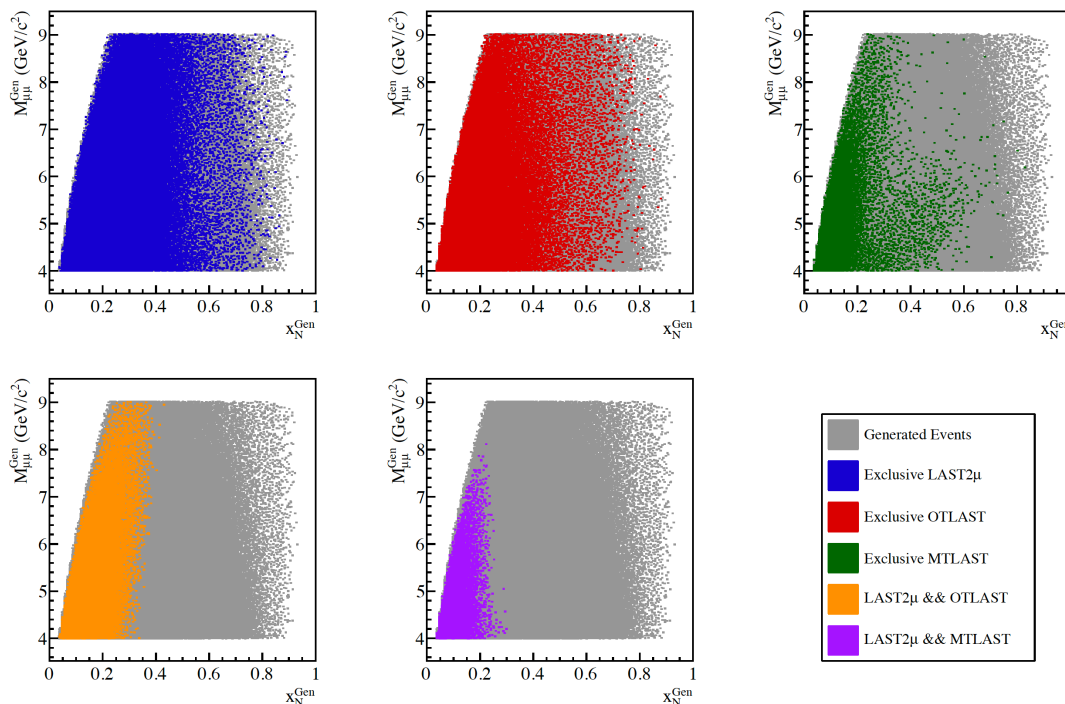
Fig. 2.22 Kinematic acceptance of the COMPASS dimuon trigger system. Both exclusive and inclusive triggers are demonstrated. Events firing both OTLAST and MTLAST are extremely rare and thus neglected in the representation.

Chapter 3

TGEANT Monte Carlo software for Drell-Yan simulations

All the physics programmes belonging to COMPASS-II proposal [136] foresee high precision measurements. The collected physics data are polluted by background and spectrometer acceptance effects. The term *acceptance* includes either the effects due to the geometrical coverage of the experimental apparatus either the effects coming from the reconstruction algorithms. The acceptance is parametrised by means of Monte Carlo (MC) to correct the data before extracting the physics observables. Therefore a new MC software, named TGEANT, was developed and successfully implemented in the COMPASS MC chain.

TGEANT [20] [21] is fully developed in a object-oriented C++ philosophy and it is based on the Geant4 toolkit. Initially, it was thought to simulate DVCS reactions at COMPASS-II, but, given the impressive results achieved, the other physics programmes decided to join the project. In this sense, the Drell-Yan group was a pioneer, joining the TGEANT project in early 2015. In this chapter, a general review of the event simulation is given, together with a description of the various upgrades done to include DY simulations in the software package.

The goal of TGEANT is to simulate the passage of the reaction products through the COMPASS experimental setup, together with the response of the apparatus. The first requirement to achieve this goal is a detailed description of the COMPASS setup as discussed in the following sections, with particular attention to the new geometries implemented for DY.

The MC simulation can be separated into two steps, the event generation and the transport of the reaction products through the experimental apparatus. The first is based on different generators, depending on the physics process to be simulated, while the latter is implemented using Geant[1] 4 toolkit [181][182]. Since COMPASS is a fixed target experiment working with both secondary and

---

[1]**Ge**ometry **an**d **t**racking

tertiary beams, much more complicated in terms of phase space coverage with respect to the monochromatic case, an accurate description of the beam features is also crucial to reproduce the effects observed in the data. This aspect was accurately treated in the TGEANT development, as discussed in the next sections.

To embed TGEANT in the COMPASS MC chain, a brand new interface to the COMPASS reconstruction software, CORAL (see Sec. 2.6), has been implemented. Innovative features, like the implementation of the 2D efficiency maps of the various detectors and trigger systems, have been added at this stage. These aspects will also be reviewed in this chapter.

3.1   Software overview

In addition to TGEANT, the software package comprises four sub-packages: the libEvent, the libSettings, the Graphical User Interface (GUI) and the Toolbox. The first two are libraries needed to handle the data exchange between different packages. The Qt4-based GUI allows the user to easily create and modify TGEANT setup files, while the Toolbox is a special analysis software designed for the TGEANT output files. A flowchart showing the interplay between the different sub-packages is shown in Fig. 3.1.

The simulation is initialised feeding to TGEANT a setup file written in XML[2]. Such a file, read by TGEANT using the libSettings, encodes all the information that the software needs to perform the simulation. Part of the settings written in the setup file regards the position of the detectors in the COMPASS experimental hall. These positions can be imported from a real data detectors.dat, a file obtained analysing alignment runs.

The event loop produces an output written in a gunzip-compressed ASCII file making use of the libEvent. The TGEANT output files can be either analysed using the Toolbox or produced via CORAL, to get MC-mDST. The libSettings handles TGEANT special options for production via CORAL. For CORAL processing, a MC detectors.dat, containing sizes and positions of all the detectors as initialized in the simulation, and a geometry file, describing the material budget present in the experimental hall, are needed. Both of them can be produced via TGEANT.

---

[2]e**X**tensible **M**arkup **L**anguage.
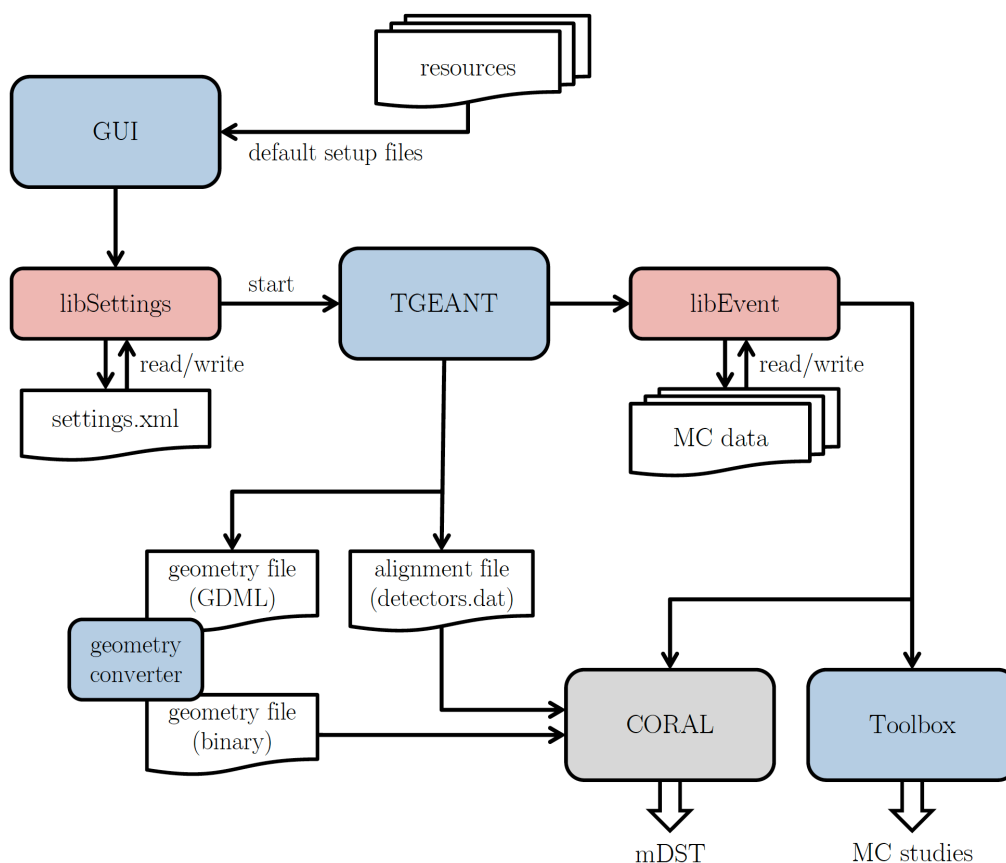
Fig. 3.1 Schematic representation of the interplay between TGEANT sub-packages [21]. The geometry file produced by TGEANT is in GDML format and can be converted in the desired *root* file using the geomPreLoad binary, delivered with the software.

3.2   Event simulation

In Geant4 philosophy, the so-called *primaries* are particles injected in the simulation volume in a given starting position with defined momentum. After this initialisation step, the event loop can start. During an iteration, the primaries are transported through the experimental setup according to the Geant4 algorithms. Interactions of the primaries are the only possible source of new particles during a loop iteration. These occur according to the cross sections of the processes selected by the user in the physics lists. All the interactions with the sensitive detectors are recorded, as well as the information of the various tracks at their starting and ending point. The whole stack of data about the event is written to the output file at the end of each iteration. A schematic view of the TGEANT work-flow can be observed in Fig. 3.3.

In the following, a detailed look at the event loop simulation features in case of the DY simulations will be given. Analogous details on the simulations for the muon programme can be found in [21].

3.2.1   Beam simulation

The beam simulation for the DY programme must take into account several factors to be realistic. As explained in Sec. 2.1 the π^- are obtained via collisions of p extracted from the SPS and shot on a thick Beryllium target, the T6. The phase space characterising the resulting secondary beam is more complicated with respect to a primary beam.

Before the release of TGEANT, the simulation of the beam at COMPASS was quite approximative. A back-propagation, starting from the primary interaction vertex, was needed to have the beam parameters at the entrance of the experimental hall included in the simulation. This approach was foreseeing several steps, as the inversion of the beam particle charge and the spread of the primary vertices to be defined by the user. Despite these efforts, many aspects of the beam complexity could not be taken into account, like the energy loss of the primary π^- before the DY interaction and the multiple scattering.

To remedy these deficiencies, a brand-new philosophy for hadron beams simulation was introduced in TGEANT. The code was modified to start the simulation injecting the beam π^- as *primaries*. The starting coordinate along the beam axis in TGEANT can be selected by the user[3], as well as the beam particle type. The coordinates in the transverse plane are read from a beam-file encoded in binary

---

[3]The *z* coordinate for the injection can be selected in any point of the world volume, even downstream of a group of detectors plane. In this case, no information will be recorded by the stations upstream of the beam injection.

format. Apart from header and footer flags, each beam particle injected in the simulation is described in a TGEANT beam file by:

- x coordinate in the transverse plane, in mm;

- y coordinate in the transverse plane, in mm;

- θ_x slope in the x-z plane, in mrad;

- θ_y slope in the y-z plane, in mrad;

- $|\vec{p}|$ total momentum of the beam particle, in GeV/c;

A graphical representation of θ_x and θ_y in the COMPASS reference system can be found in Fig 3.2. Given the five parameters in the beam file and the type of beam particle selected by the user, the four-momentum of the primary is fully defined.

Usually for DY simulations the beam file is extracted at z = -750 cm, just upstream of the first station of the beam telescope (FI01). In this way the beam particle is propagated starting from the entrance of the experimental hall, suffering energy losses and multiple scattering in all the materials crossed before the DY interaction occurs.

A new approach has also been implemented to spread the position of the primary vertices[4]. Due to inelastic hadronic interactions, the π^- beam flux drops exponentially along the beam axis, with a slope defined by the density and the atomic number of the crossed materials [183]. This feature was reproduced embedding the physics event generator in TGEANT and calling it when the first inelastic interaction of the beam occurs. At this stage, profiting from the step logic of Geant4, the particles that would be originated by the internal generator of Geant are killed, and the beam four-momentum is retrieved to be fed as input to the event generator[5].

The new vertex generation algorithm allows to account correctly for the effects affecting the beam before the DY interaction and to generate the vertex position automatically, without any additional user input. The target materials determine the slope of the exponential decrease characterising the vertex distribution along the beam axis material[6]. The distribution in the transverse plane is mainly influenced

---

[4]In the past, the users spread the vertices by hand, according to the attenuation of the beam provoked by the inelastic interaction with the materials crossed. The events were generated apart, combined with a vertex position and then converted into a format readable by the transport software. Such a procedure, not user-friendly, was requiring several iterations from user's side.

[5]The event generator handling is discussed in the next section.

[6]The automatic tuning of the z-vertex distribution with the target material represents an excellent advantage for DY simulations, where the target composition varies between different years. The results of the measurements performed at the end of 2014 and 2015 runs have been implemented and are automatically initialised choosing the associated *Trigger Plugin*, discussed in Section 3.8
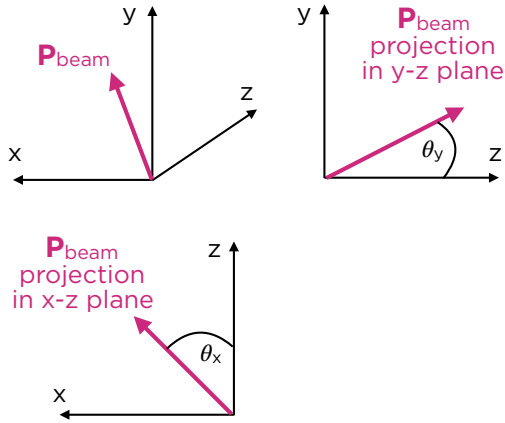
Fig. 3.2 Definition of the beam slopes θ_x and θ_y. The former represents the angle between the beam and the z-axis in the x-z plane, while the latter is defined as the angle between the beam and the z-axis in the y-z plane.
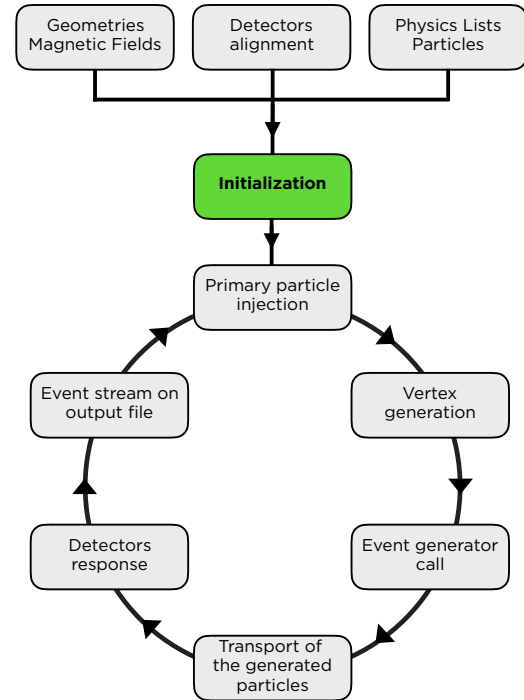
Fig. 3.3 Flow chart of the TGEANT event loop. The loop ends when the number of beam particles injected reaches the number of events required by the user.

by the beam file parametrisation and by the magnetic fields crossed by the beam hadron upstream of the primary vertex. The new vertex generation mechanism for hadron beams is schematically summarised in Fig. 3.4. The magnitude of the effects of the energy loss, the multiple scattering and the magnetic field of the dipole before the DY interaction are shown in function of the z position of the primary vertex in Figs. 3.5 and 3.6.

3.3   Event generators

Several event generators, suited for the different physics programmes of COMPASS, have been embedded in TGEANT. For this purpose, an event generator function was written and added to the physics processes available in the Geant4 physics lists. The Geant4 tracking logic foresees a step length associated with each possible process. The higher the process probability, the shorter the step length associated with it. The shortest step length is selected by the Geant4 tracking algorithm to be applied to the particle next step. To never invoke the event generator process by chance, its step length is set by default to the maximum
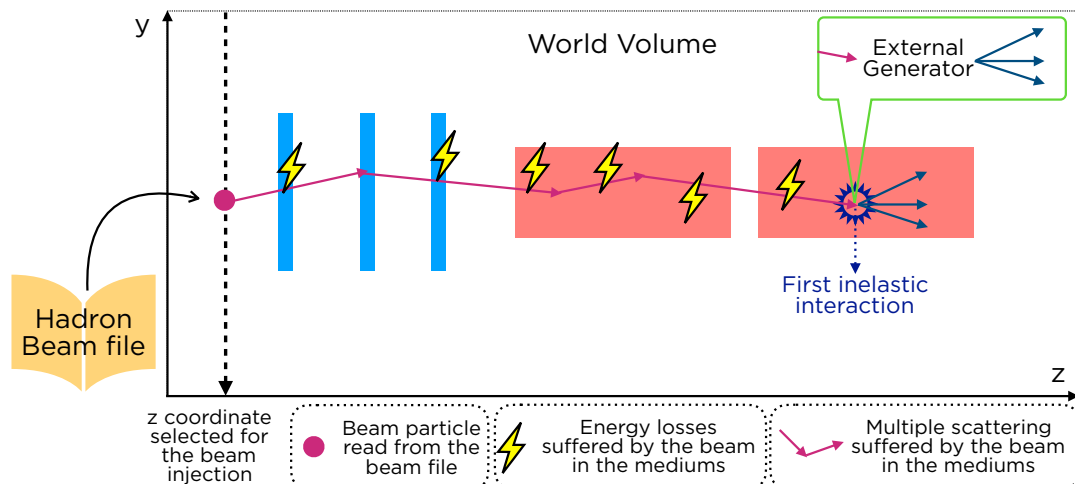
Fig. 3.4 Schematic work-flow of the new vertex generation mechanism for DY. The simplified part of the setup represented is not in scale.
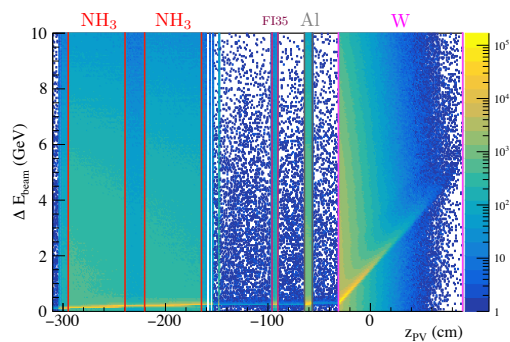
Fig. 3.5 Energy loss suffered by the beam π^- in the materials crossed before the primary interaction, drawn in function the z_{PV} (z coordinate of the primary vertex). The regions corresponding to NH_3 cells, the vertex detector (FI35), the Aluminium (Al) thin target and the tungsten (W) plug are highlighted.
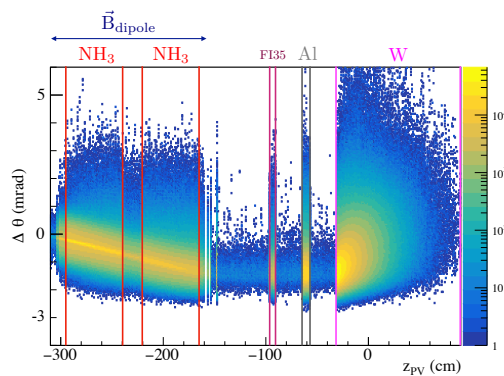
Fig. 3.6 Variation of the polar angle of the beam, computed between the injection point and the primary interaction point, drawn in function of z_{PV} (z coordinate of the primary vertex). The variation is originated by the multiple scattering and the magnetic field ($\vec{B}_{dipole}$) of the dipole magnet. The regions corresponding to NH_3 cells, the vertex detector (FI35), the Aluminium (Al) thin target and the tungsten (W) plug are highlighted.

possible value, *DBL_MAX*. Once the event generator is triggered, its step length is changed into zero, ensuring the call. Note that the trigger of the event generator for a muon beam follows a different working principle compared to the hadron beam case, given the weak interactive nature of the muons. In both the cases, the four-momentum of the beam particle approaching the collision is used as input for the event generator, ensuring the energy conservation.

Among the broad spectrum of generators already available in TGEANT, LEPTO [184] and HEPGen++ [185] are suited for simulations involving the muon beam, like for DVCS and SIDIS processes. On the other hand, Pythia6 [186] and Pythia8 [187] generators have been successfully implemented to work with hadron beams. The implementation of these two generators took place during the development of the DY programme simulation in TGEANT.

Pythia6 and Pythia8 are based on FORTRAN and C++ respectively. Given the C++ nature of TGEANT, the *root* interface to Pythia6 was used to include the generator in the simulation. Choosing Pythia6, the generator can be tuned writing an XML settings file linked in the setup file. Concerning Pythia8, the tuning of the generator is done writing a text file. In both the cases, a default example is delivered with the software in the DY resources folders.

3.3.1 Simulation of p-n composition of the targets

An event generator simulates the collision between two particles. In a fixed target experiment like COMPASS, the reaction occurs between the beam and target particle. While the former is well defined, the second could be even proton or neutron, depending on the material where the inelastic interaction occurs and on the cross section of the process of interest. In the case of dimuon pairs production in $\pi^- + p$ collisions, the cross-section varies in function of the selected mass range. All the aforementioned factors must be taken into account while initializing the event generator. For this purpose, a *p-n* mixing algorithm has been implemented in TGEANT. It can be summarized as in the following:

1. The number of protons (Z) and the number of nucleons (A) of the material in which the primary vertex is generated are retrieved thanks to Geant4 internal tools.

2. The probabilities to scatter off a *p* or a *n* are computed as

$$P_p = \frac{Z}{A} \qquad P_n = \frac{A - Z}{A} \qquad (3.1)$$

In case of compounds the computation of P_p and P_n is done accounting for the different materials present and their relative fraction. For the NH_3 target, P_p and P_n can be expressed as

$$P_p = \frac{(p \cdot Z_{NH_3} + (1-p) \cdot Z_{LHe})}{(p \cdot Z_{NH_3} + (1-p) \cdot Z_{LHe}) + (p \cdot N_{NH_3} + (1-p) \cdot N_{LHe})}$$
$$P_n = \frac{(p \cdot N_{NH_3} + (1-p) \cdot N_{LHe})}{(p \cdot Z_{NH_3} + (1-p) \cdot Z_{LHe}) + (p \cdot N_{NH_3} + (1-p) \cdot N_{LHe})} \quad (3.2)$$

where p represents the packing factor (see Tab. 3.1 and Sec. 3.5 for more details.)

3. The probabilities of 3.1 are then renormalized for the ratio R between the cross-sections for proton and neutrons, σ_p and σ_n

$$R = \frac{\sigma_p}{\sigma_n} \quad \rightarrow \quad P'_n = \frac{P_n}{R} \quad \rightarrow \quad P^f_p = \frac{P_p}{P_p + P'_n} \qquad P^f_n = \frac{P'_n}{P_p + P'_n} \quad (3.3)$$

4. A random number $r \in [0,1]$ is drawn. If $r < P^f_p$, a p is initialized as target particle, otherwise a n is taken.

While writing the tuning file for the generator, the user can decide to enable or disable the *p-n* mixing. In the first instance, the only additional input needed is the cross-sections ratio R for the simulated process. Usually, it can be determined running the generator in a stand-alone mode for p and n and retrieving the information about the σ. The cross section depends significantly on the generated kinematics, thus the inclusion of a full cross section parametrisation to be automatically invoked by the software was not possible, since the specific kinematic characterisation of an event cannot be determined a priori.

The *p-n* mixing options is available for both Pythia6 and Pythia8 event generators. Accounting for the *p-n* mixture in function of the target material brings sizable differences respect to the pure p MC, as can be seen in Fig. 3.7

3.4 Pile-up

The COMPASS experiment makes use of high-intensity beams, both in the muon and in the hadron case. Especially for the DY measurements, the rate of beam particles is quite high ($\sim 10^8 \ \pi^-$/s), to compensate in luminosity for the low DY cross-section in the High Mass region. The elevate flux of beam particles can cause issues at the level of the beam reconstruction, as misassociations of beam
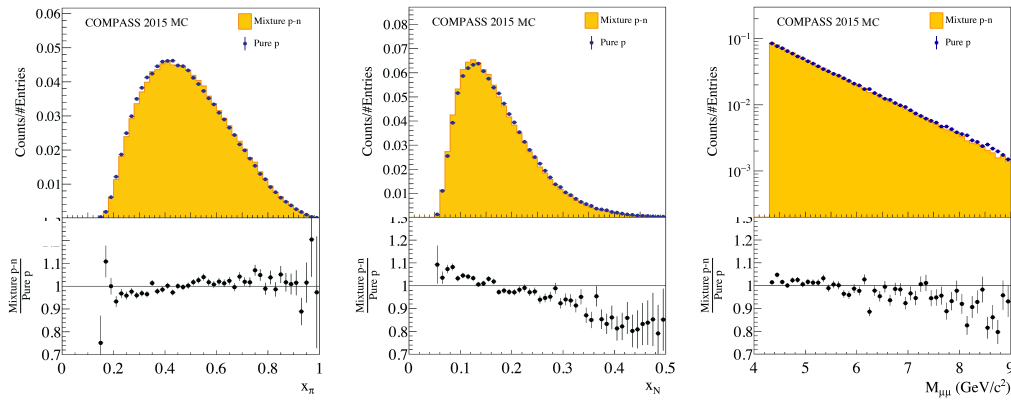
Fig. 3.7 Comparison of x_π (left), x_N (middle) and $M_{\mu\mu}$ (right) kinematic variables for two different MC samples. One is generated using the *p-n* mixing algorithm (orange histogram) and the other assuming pure *p* target (blue dots). Just events reconstructed in the NH$_3$ target and passing the standard cut flow (see 4.4) are selected.

trajectory to a reconstructed vertex. Furthermore, hits related to an underlying event particle can be associated to one of the tracks of interest, worsening the reconstruction and the vertexing procedure. All of these kinds of effects impact on the experimental resolution of kinematic and angular variables. Therefore, to include a realistic rate of beam particles at the level of the simulation is crucial to reproduce the experimental environment in the MC.

To emulate the beam flux on the target, the so-called pile-up beam particles are injected in the simulation together with the primary particle. The number of pile-ups depends on the desired beam flux Φ, usually set according to the real data conditions, and from the time window ΔT chosen for the pile-up simulation.

The beam flux is assumed to be constant in a finite time gap. By definition, the shooting of the primary beam particle defines the $t_0 = 0$. Given the half-width of the time window ΔT, set by the user in the setup file, a time window $[-\Delta T, \Delta T]$ is opened around the t_0 and within it a certain number of pile-up particles, determined according to the Poissonian distribution are shot. Once defined ΔT and Φ, the resulting N_{PileUp} particles is determined as

$$\hat{x} = \Phi \cdot 2\Delta T$$
$$N_{\text{PileUp}} = \text{RandPoisson}(\hat{x}) - 1 \tag{3.4}$$

where RandPoisson() function in Eq. 3.4 is a random number generator producing integers according to Poissonian probability distribution. The -1 appearing in the N_{PileUp} computation is due to the subtraction of the primary beam particle, accounted in the mean number of beam particles $\hat{x}$.

Also the pile-up particles are randomly extracted from the beam file. If halo particles are included in the beam file (as usually done in the muon beam case) they can also be injected as halo. For Drell-Yan the situation is more complicated, given the different nature of beam and halo particles. To allow the user to dress the DY event with both pile-up pions and halo muons, coming from the decay of the π^- while travelling in the M2 beam line, an additional pile-up was implemented in TGEANT.

3.5   New implementations for Drell-Yan

When the TGEANT for DY project started, the components of the experimental setup already implemented were the ones used for the DVCS 2012 run. Several detectors and structures were missing, namely:

- One scintillating fibres station (FI03);

- The DY polarised target system;

- The Vertex Detector (FI35);

- The Hadron Absorber;

- Three Pixel Micromega stations (PM01, PM02 and PM03);

- The Rich Wall;

- The new Drift Chamber (DC05);

so far, no technical drawings were anymore available for FI03, because the detector was built in the early stage of the COMPASS Phase I, quite some years ago. The bulk implementation in TGEANT has been done according to its description in the previous MC software, COMGEANT[7]. In addition many issues due to overlaps have been solved in TGEANT. The geometry of the detector was completed adding a full description of the support structure and of the light guides. Analysing the efficiencies of the detector, it was found that two over three projections, namely FI03X and FI03U, slipped down along the fibres direction of ~ 1.4 cm. Also this feature, characteristic of the runs 2014, 2015 and 2016, has been implemented in the MC and is automatically taken into account while choosing the trigger plugin. A sketch of the current implementation, obtained thanks to TGEANT interface visualization, is shown in Fig. 3.8.

---

[7]Considered trustable since it was done directly by the detector expert at time of the detector construction.

The polarised target system comprising the cryostat, the solenoid and the dipole magnet, the microwave cavity and the target holder, was implemented from scratch according to the information provided by the target group [188]. The material, filled in the two target cells immersed into a cylindrical liquid helium housing, had different composition depending on the cell and on the year of the run (2014 or 2015). These variations can be attributed to many causes, like for instance a leak of the polarised target material in the second cell during the 2014 pilot run or the peculiarities of the target filling procedure, done inclining upwards the target in a N_2 bath. All the features mentioned above must be taken into account to achieve a satisfactory description of the target system in the MC. The target material consists of a compound of NH_3 and liquid helium. The proportion of the two components are given by the so-called packing factor, which is measured while weighing the target material during the download procedure at the end of each year of run. A summary of the target cells composition for 2014 and 2015 DY runs can be found in Tab. 3.1.

The detailed composition of the cells is described in the MC on a yearly basis. For 2014, also the leak of material in the upstream part of the downstream cell
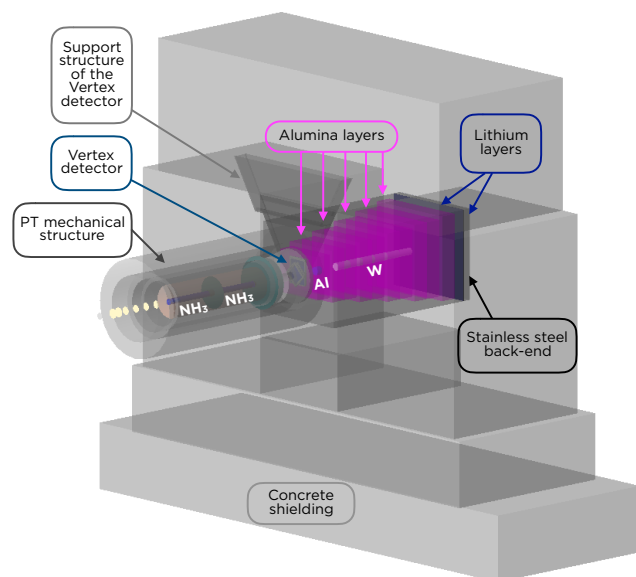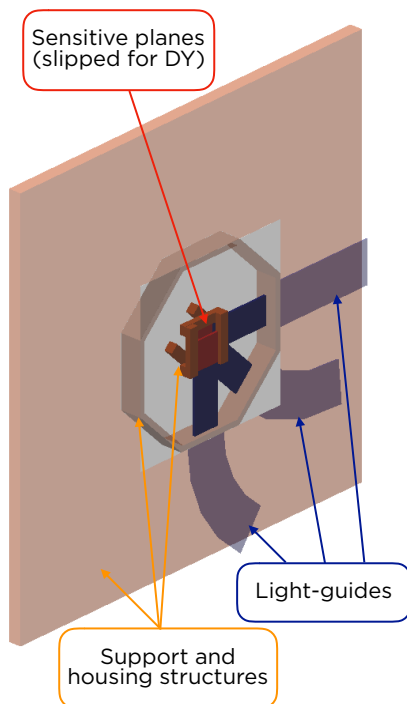
Fig. 3.8 Visualization of FI03 station implementation, in the specific case of Drell-Yan 2015 run.

Fig. 3.9 Visualization of the target area as implemented for the Drell-Yan run 2015.

NH$_3$ **Cell**	**2014**		**2015**	
	Upstream	Downstream	Upstream	Downstream
p	0.5212	0.4558	0.5657	0.4797
$\rho_{\mathbf{cell}}\,(g/cm^3)$	0.5141	0.4677	0.5456	0.4847

Table 3.1 The packing factor p for the two NH$_3$ cells measured at the end of 2014 and 2015 data takings. Each cell density is computed as $\rho_{cell} = p \cdot \rho_{NH_3} + (1-p) \cdot \rho_{LHe}$ where $\rho_{NH_3} = 0.853$ g/cm^3 and $\rho_{LHe} = 0.1485$ g/cm^3.

has been included in the description[8]. The year is selected via the trigger plugin (see Sec. 3.8). Each year of run is associated to a trigger plugin that, among its utilities, is also used to load specific features of the geometries included in the setup. A three-dimensional view of the 2015 target implementation in TGEANT is presented in Fig. 3.9.

Just downstream of the PT cryostat, the Vertex Detector was installed in the interspace between the absorber and its nose. The implementation of this detector was based on the technical drawings used for its design. Also the housing of the detector and the support that anchored it to the hadron absorber concrete shielding have been carefully described.

The hadron absorber description is crucial for both MC and real data. The material budget, parametrised in the geometry file created via MC, is used in the reconstruction of both MC and real data to account for the energy loss of the particles passing through the materials on their trajectories. The implementation has been done according to the CAD drawing. The aluminium target, located upstream of the tungsten plug, was placed according to the survey measurements performed while assembling the structure. Also the concrete blocks surrounding the structure, serving as radiation shield, have been implemented in the simulation for completeness. The additional lithium sheets introduced in 2015 (see Sec. 2.8.2) are also described in the geometry, together with their support layers. They are placed in the setup just in case the DY 2015 trigger plugin is selected. A visualization of the system formed by the polarised target, the hadron absorber and the FI35 detector is shown in Fig. 3.9.

Other sensitive detectors have been implemented in the spectrometer. The old Micromega stations, present in 2012 data taking, were replaced in 2015 by the new Pixel Micromegas. These three detectors have been implemented according to the COMGEANT, where the detector expert carried out the description. Further

---

[8]The possible geometry-scenario deriving from the leak has been studied by the COMPASS target group. The outcome of these studies [189] was used to implement a realistic geometry in the MC.

improvements have been done, as the inclusion of the front-end cards and the upgrade of the pixel core description.

The RichWall, already in use during the Phase I, was removed in 2012 setup to reduce the material budget upstream of ECAL1, with the aim of minimising the photon absorption. In the previous MC the simulation of this detector was very simplified, while in TGEANT all the peculiarities of its structure have been reproduced, as the inactive gap between each MDT module.

The new Drift Chamber DC05 built to replace the Straw Tube Detector ST02 station dowstream of SM2 was also added. Its implementation was easy, since its structure is very close to DC04. Anyhow the new features of the detector, like the higher number of wires covering also the corners of the chamber, have been implemented.

3.6   Detector response

After generating the physics event, Geant4 algorithms transport the products of the reaction through the experimental setup. While during the propagation the information about all the particles entering the simulation can be retrieved at any step, from the empirical point of view the trace left by an event is limited to the hits in detectors. Each charged particle passing through the sensitive volume of a detector gives an MC hit[9]. The response to a neutral particle passage depends on the specific settings of the detector.

The information for each sensitive detector is merged at the end of each event loop, in order to cluster stepping data belonging to the same particles. The whole stack of hits in the various tracking detectors is written in the output file at the end of the event loop, together with the energy deposits in the calorimeters modules and the optical photons detected by the RICH PDs. The three kinds of experimental observables just mentioned need different readout logic.

Specific restrictions for each sensitive detector, as the spatial and time resolutions, are not present in TGEANT. These constraints are included by the reconstruction software. Therefore, the whole stack of hits should be delivered to CORAL.

---

[9]A MC hit is defined as the combination of all particle steps inside a sensitive detector that belongs to one particle track that enters the detector.

3.7 Simulation of the detectors efficiency

To reproduce the real data, a realistic simulation of the detector response is mandatory. TGEANT produces MC hits in all the sensitive detectors, without caring about possible inefficiencies that may be present during the data taking. So far, the efficiency of the detector's response was taken into account by a single efficiency number, characteristic of each detector station. To make a step forward in the simulation, the inclusion of 2D efficiency maps has been implemented in the COMPASS TGEANT MC-chain in order to describe the spatial anisotropies in the detectors.

In principle, the simulation of each detector efficiency can be included at the level of transport code, but this choice would strongly constrain the flexibility, forcing the user to run the MC every time a change in detectors efficiency occurs. Also, one should consider that the time needed to produce an MC event simulating the full COMPASS setup is about 10 s, while to reconstruct it in CORAL requires just 1-2 s. Thus, it was decided to include the 2D efficiency maps at the reconstruction stage, *i.e.* in the TGEANT interface to CORAL.

The effects to be parametrised are empirical. Therefore they cannot be described by theory but must be extracted from the data. The procedure to obtain the efficiency map for a detector relies on the comparison of its illuminated map with its hits map. The term *illuminated maps* means 2D histograms containing *x-y* position of tracks that have been reconstructed picking up hits upstream and downstream of the examined plane and that are falling in the active area of the examined plane when extrapolating to its z coordinate. The efficiency in a specific bin is given by the ratio

$$\varepsilon(x_b, y_b) = \frac{N_{fav}(x_b, y_b)}{N_{fav}(x_b, y_b) + N_{unfav}(x_b, y_b)} \tag{3.5}$$

where x_b and y_b stands for the mean x and y coordinate of the bin b, $N_{fav}(x_b, y_b)$ is the counter of hits correlated in space and time to a track that illuminates the plane in the bin b and $N_{unfav}(x_b, y_b)$ account for the cases when no hits are found or when they are found to be uncorrelated with the track examined. A graphical representation is shown in Fig. 3.4. The bin-width adopted varies for different detectors, as rates differ substantially between VSATs, SATs and LATs, resulting in significant differences in statistical power per sensitive area. Furthermore, even in the same detector plane, sizable differences in statistics may be observed between inner and outer regions. In the best case scenario, the maps are fully populated with statistical significance in each bin. Unfortunately,
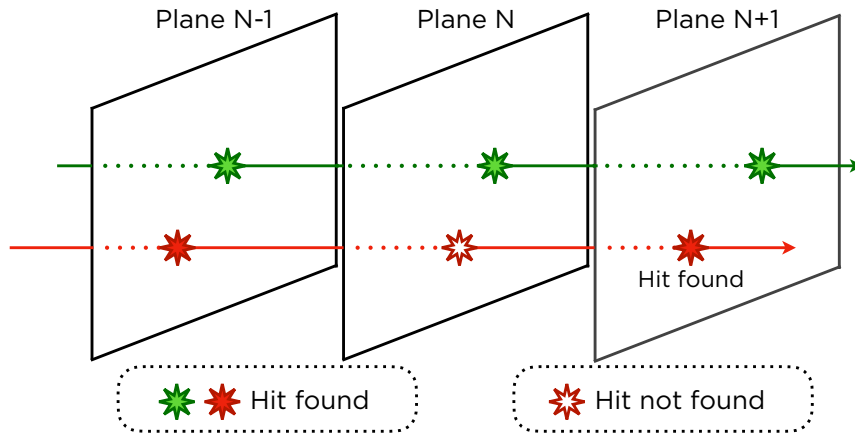
Fig. 3.10 Schematic drawing of the efficiency determination logic. The green track exemplifies a favourable tracks, contributing to $N_{fav}(x_b, y_b)$ in the bin b of the plane N. On the contrary, the red track is an example of track entering in $N_{unfav}(x_{b'}, y_{b'})$.

it is very hard to get such a situation for LATs, like Muon Wall 1 and Rich Wall. Several improving algorithms[10] are available in specific TGEANT binaries (efficienciesDB, efficConverter.py) to make up for these inconveniences.

To study the efficiency of a single detector plane, the data are reproduced excluding it from the tracking. Having COMPASS more than 300 detector planes, to extract detector efficiency for all of them is a huge task. In addition, significant fluctuations in the detector efficiency on a period and in particular sub-period basis, should be taken into account and reproduced. To include as better as possible these effects, a re-normalization of the efficiency maps based on the variations of the so-called pseudo-efficiencies is now being studied.

3.8   Simulation of the trigger system

Before TGEANT in the COMPASS MC the trigger bit was attributed a posteriori, checking if the combination of MC hits in the hodoscopes was satisfying the trigger logic. Such a method was forcing each user to re-implement the trigger logic at level of the MC. In TGEANT, this check takes place at the end of each event, storing a trigger bit already at level of MC truth. It is implemented in the *Trigger Plugin*, which must be customized for each physics program and year of measurement.

---

[10]*e.g.* geometric bridging of empty bins, cutting weighted mean to cut out extremely sharp fluctuations caused by low statistics bins, 2D maps editing by hand etc.

The TGEANT implementation represents a flexible and practical way for the analysis. Indeed, the user can decide to re-trigger at level of CORAL (to add trigger efficiencies, described in the next section, or to apply changes in the trigger logic, if needed). Even in the worst case scenario, in which the MC data would be produced with a wrong trigger bit assignment, a re-triggering at level of analysis can always be applied accessing MC hits information in the hodoscopes.

In a nutshell, the trigger simulation starts at the end of the event loop retrieving the information about the hits left in all the trigger slabs by the particles. Each hit in the upstream plane of the hodoscope system is combined with all hits in the downstream plane. A combination is accepted if fulfils the following criteria:

- The absolute difference in timing of the two hits must be within the coincidence time window $t_{w,i}$ for the corresponding hodoscope system

$$\left| t_u - t_d \right| < t_{w,i} \ i \in \left\{ LAST, OT, MT, LT, IT \right\} \tag{3.6}$$

  where the pedices u and d identifies the hit in the upstream and in the downstream hodoscope respectively.

- The paired hits should be geometrically correlated. This is tested via trigger matrices. Since the hodoscope planes in COMPASS are constructed with up to 32 channels, the trigger matrices M_i are quadratic with 32 rows and columns. The entries of the matrices are Booleans, whereby an accepted hit combination is encoded as 1 and a rejected combination as 0. The trigger logic checks for the entry $M_{i,u,d}$.

As far as the Dimuon trigger is concerned, an additional step is added, checking the possible coincidences of pairs of the triggered muons in a given time window, as discussed in Sec. 2.8.5. If the the event triggers, the corresponding trigger bit is stored. The trigger bits defined for the DY measurements and implemented in the MC are summarized in Tab. 3.2.

3.9   Simulation of the efficiency of the trigger system

Further improvements have been made to TGEANT to increase the agreement between MC and data. In particular, for the DY 2015 case a non-negligible impact of trigger efficiencies on the data has been identified [190]. As illustrated in sec. 2.21 the COMPASS dimuon trigger system consists of three sub-systems, each one covering a different kinematical region. Each station of hodoscopes is not redundant. Thus a specific inefficiency may easily provoke the loss of an event.

Trigger System	Trigger bit position
MTLAST	0
MT	1
OTLAST	2
OT	3
CALO Trigger	4
LAST2μ	8
LAST	9

Table 3.2 Trigger bits for the 2014 and 2015 DY runs implemented in TGEANT. The missing ones, Beam Trigger, Inner Veto Trigger and Halo Trigger, are not relevant for DY simulations.

Therefore, a realistic simulation of the trigger performance is crucial to better describe the data.

Inefficiencies in the trigger may have different sources. It could be related to an hardware-wise issue or a logic-wise one. TGEANT allows to reproduce the former in two different ways: via 2D-efficiency maps (see sec. 3.7) or to feed the value of efficiency slab by slab. Because of the high statistic needed for the 2D-efficiency maps and of the exceptional running condition to collect unbiased data to extract the trigger efficiency, the preferred method is the slab by slab one.

As well as the hardware efficiency, also the performances of the trigger logic need unbiased data. Every pixel of the trigger coincidence matrices is characterised by an efficiency value depending on several factors. More information on trigger efficiency extraction can be found in [191]. Analogously to the 2D-maps case the source code of the trigger simulation is part of the library libEvent, to be loaded while running the reconstruction via CORAL. All the efficiency values are loaded while initialising CORAL and are fed to it via special options in the CORAL setup file. Both the slabs efficiency and the coincidence matrix one are condensed in a single matrix, used afterwards to decide to accept or not the trigger of a single event. The working principles of the trigger efficiency implementation in the MC reconstruction are illustrated with an example in by Figs. 3.11 and 3.12.
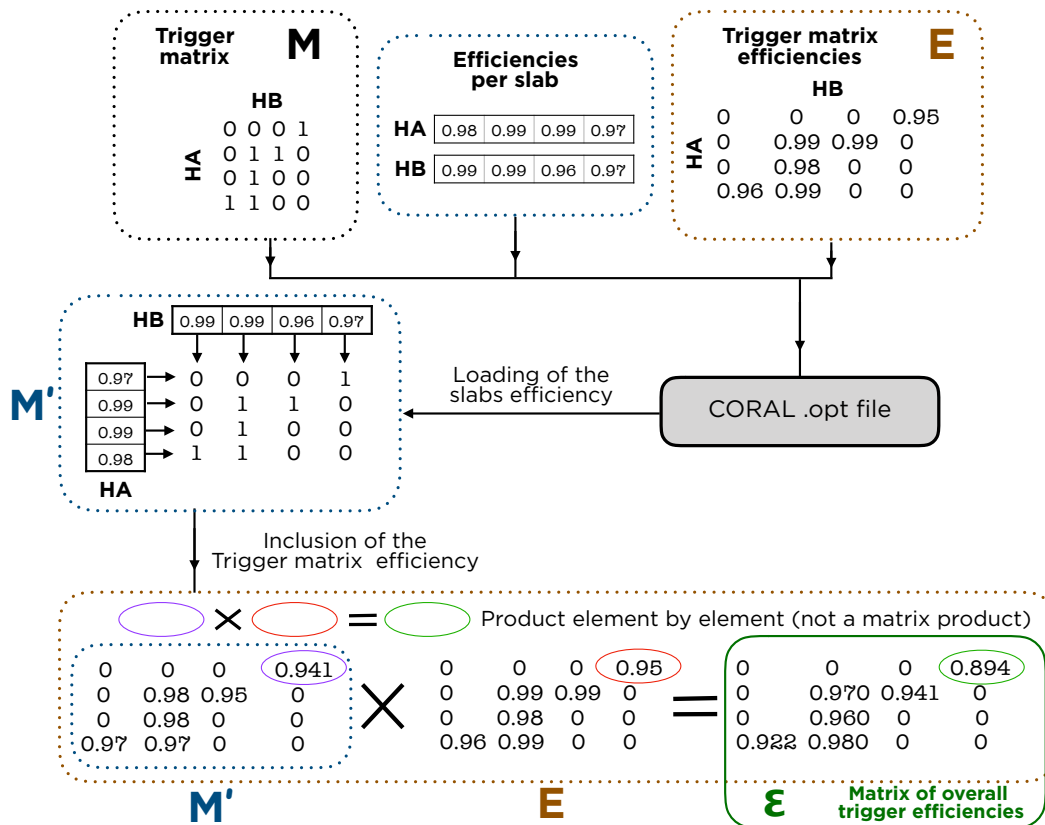
Fig. 3.11 Dummy example of the treatment of trigger efficiencies at level of CORAL. The generic COMPASS trigger system is simplified into a coincidence of two hodoscopes, HA and HB, with 4 slabs each. A random trigger matrix $\mathbf{M}$ is assumed for the example. The hardware-wise contribution, encoded in a slab by slab format, and th e efficiencies of the coincidence matrix, given in the matrix $\mathbf{E}$, are fed to CORAL in the setup file. Since each slab corresponds of HA (HB) corresponds to a row (column) in the matrix, the corresponding efficiency is multiplied for the boolean values in the associated row (column) to obtain the matrix $\mathbf{M'}$. Afterwards, each value $\mathbf{M'_{a,b}}$ is multiplied for the value $\mathbf{E_{a,b}}$, to build $\boldsymbol{\varepsilon}$, the matrix of the overall trigger efficiencies, reproducing both the effects of the hardware and the logic applied in the chain. The usage of $\boldsymbol{\varepsilon}$ is illustrated in Fig. 3.12. Notice that, if nothing is specified for slab efficiencies and/or trigger matrix efficiencies, TGEANT interface to CORAL assumes them to be 1.
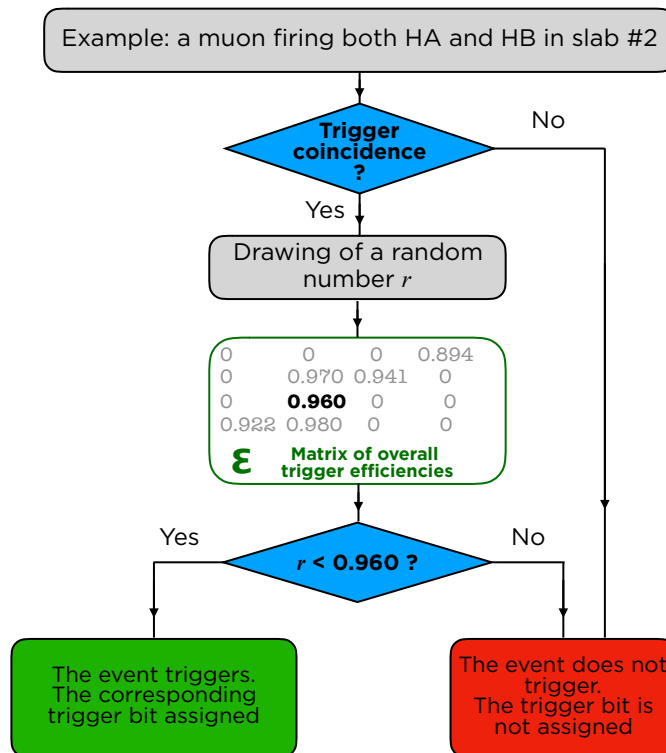
Fig. 3.12 Illustration of the usage of the matrix of overall trigger efficiencies $\boldsymbol{\varepsilon}$, computed while initialising CORAL according to the settings fed by the user. The event assumed for the example fires both HA and HB in the slabs number 2. If it satisfies the timing coincidence it passes to the trigger efficiency check. The value $\boldsymbol{\varepsilon}_{2,2}$ is retrieved and compared to a random value r drawn between 0 and 1. If r is greater than $\boldsymbol{\varepsilon}_{2,2}$, the event does not trigger because of a trigger inefficiency. Notice that, in this way, the trigger matrix check and the efficiency check are clusterized in just one step, since uncorrelated hits correspond to a 0 value in both $\mathbf{M}$ and $\boldsymbol{\varepsilon}$.

Chapter 4

Measurement of the Transverse Spin Dependent Azimuthal Asymmetries in the Drell-Yan process

After the three months long pilot-run taken in 2014, in mid 2015 COMPASS started polarised Drell-Yan measurements campaign. This chapter describes the analysis carried out for the extraction of Transverse-Spin-dependent azimuthal Asymmetries (TSA) that appear in the Drell-Yan cross-section (see Eq. 1.25).

The analysis is done for Drell-Yan dimuon events in the mass range 3.5 GeV/c^2 < $M_{\mu\mu}$ < 9.5 GeV/c^2 (High Mass (HM) range) produced with 190 GeV/c π^- beam and transversely polarised NH$_3$ target. The sample is sub-divided into nine periods (W07 - W15) of physics data, collected between 9 July and 16 November 2015. Various aspects of the data analysis will be reviewed in the following sections, namely the event selection tuning, the stability analysis, the analysis methods applied and the systematics checks performed. Technical details on the evaluation of the dilution factor, target polarisation and asymmetry extraction methods are discussed.

4.1   Overview of the measurement

For the 2015 polarised DY measurements a 190 GeV/c π^- beam delivered by the CERN SPS with an average intensity of 0.6×10^8 s^{-1} was scattered off the COMPASS transversely polarised NH$_3$ target. The average proton polarisation was measured to be $\langle P_T \rangle \approx 0.73$ and the mean dilution factor is $\langle f \rangle \approx 0.18$. The polarised target consisted of two longitudinally aligned cylindrical cells of 55 cm length and 2 cm in radius, divided by a 20 cm gap filled with liquid helium and was placed in a magnetic field of 0.6 T generated by the PT magnet. The non interacted beam was dumped into a 120 cm long tungsten (W) plug located

downstream of the PT and preceded by a 7 cm thick Aluminium (Al) target. Both Al and W are being used as nuclear targets for polarisation-independent studies, not discussed in this Thesis.

Outgoing charged particles are detected by the system of tracking detectors and their momenta are determined by means of two large-aperture dipole magnets. In each stage muon identification was accomplished by a system of muon filters. The trigger required the hit pattern of several hodoscope planes to be consistent with at least two muon candidates originating from the target region. For any pair of them, this implies that the laboratory polar angle θ_μ of each candidate is covered by the first stage ($25 < \theta_\mu < 160$ mrad), or one candidate is covered by the first stage and the other one by the second stage of the spectrometer ($8 < \theta_\mu < 45$ mrad). Detailed description of the setup used for DY measurements is given in Chapter 2.

The raw experimental data was processed in three production campaigns. The first two production-slots (t1, t2) were used mainly for the configuration of the reconstruction-software, iterative detector-alignment adjustments and various other tests. After these test-productions a mass production campaign (slot-t3) started in June 2016 and was accomplished by mid-November 2016.

To speed up the analysis procedures, the data stored in the mDSTs during the mass production (in total about 200 so-called *chunks* per run and about 100 000 chunks per period) were filtered into so-called μDST, containing only events with at least one dimuon candidate (a pair of oppositely charged muon tracks)[1] originating from a primary vertex[2].

4.2   Data sample

The data collected between July the 8th and November the 12th (~ 18 weeks) was acquired in relatively stable conditions and was considered to be good for physics analyses. The data from these 18 weeks was combined into 9 periods, coupling consecutive weeks with opposite target polarisation. Neighboring weeks with opposite polarisation of the NH_3 cells are labelled in the following as *sub-periods*. Details on the data-periods, as the polarisation states and run-number intervals defining each sub-period, are summarized in Table 4.1.

---

[1] at this early stage, muons were defined by tracks crossing more than 15 radiation lenghts.
[2] a primary vertex is defined as a vertex with a beam track associated.

Period	Sub-period	Polarisation	Run numbers	Begin date	End date
W07 (P1)	SP-1	$\downarrow\uparrow\,(+-)$	259363 - 259677	09 Jul	15 Jul
	SP-2	$\uparrow\downarrow\,(-+)$	259744 - 260016	16 Jul	22 Jul
W08 (P2)	SP-1	$\uparrow\downarrow\,(-+)$	260074 - 260264	23 Jul	29 Jul
	SP-2	$\downarrow\uparrow\,(+-)$	260317 - 260565	29 Jul	05 Aug
W09 (P3)	SP-1	$\downarrow\uparrow\,(+-)$	260627 - 260852	05 Aug	12 Aug
	SP-2	$\uparrow\downarrow\,(-+)$	260895 - 261496	12 Aug	26 Aug
W10 (P4)	SP-1	$\uparrow\downarrow\,(-+)$	261515 - 261761	26 Aug	01 Sep
	SP-2	$\downarrow\uparrow\,(+-)$	261970 - 262221	04 Sep	09 Sep
W11 (P5)	SP-1	$\downarrow\uparrow\,(+-)$	262370 - 262772	11 Sep	22 Sep
	SP-2	$\uparrow\downarrow\,(-+)$	262831 - 263090	23 Sep	30 Sep
W12 (P6)	SP-1	$\uparrow\downarrow\,(-+)$	263143 - 263347	30 Sep	07 Oct
	SP-2	$\downarrow\uparrow\,(+-)$	263386 - 263603	08 Oct	14 Oct
W13 (P7)	SP-1	$\downarrow\uparrow\,(+-)$	263655 - 263853	15 Oct	21 Oct
	SP-2	$\uparrow\downarrow\,(-+)$	263926 - 264134	22 Oct	28 Oct
W14 (P8)	SP-1	$\uparrow\downarrow\,(-+)$	264170 - 264330	28 Oct	02 Nov
	SP-2	$\downarrow\uparrow\,(+-)$	264429 - 264562	04 Nov	08 Nov
W15 (P9)	SP-1	$\downarrow\uparrow\,(+-)$	264619 - 264672	09 Nov	11 Nov
	SP-2	$\uparrow\downarrow\,(-+)$	264736 - 264857	12 Nov	16 Nov

Table 4.1 Partition of the DY 2015 data in periods. The polarisation-direction is indicated for the upstream and downstream cells, respectively. The sign of the transverse polarisation (+,-) is defined w.r.t. the dipole field. For Drell-Yan data taking the dipole field was oriented from up to down. Therefore measured positive value of the polarisation indicates that, in the laboratory reference frame, it was pointing down $\downarrow$ and vice-versa (negative polarisation - $\uparrow$ (up))

4.3   Stability checks

4.3.1   Bad-spill analysis

The quality of the data was carefully checked on spill-by-spill and run-by-run basis to discard data recorded in unstable conditions. Firstly, the quality of the spills was evaluated monitoring several averaged over spill *macro*-variables. The *macro*-variables were chosen to be sensitive to the general stability of the setup and its sub-systems (such as, the beam telescope, trigger-systems, muon-identification systems) and their role in further analysis. The spill by spill stability studies were performed using standardized COMPASS-framework defined previously for several COMPASS SIDIS analyses [192] [193]. Dedicated software-package was adapted to the DY case doing necessary modifications and redefining the set of *macro*-variables to be monitored. The list of DY *macro*-variables used in the spill stability analysis is the following one:

- # of beam particles divided by number of events

- # of beam particles divided by number of primary vertices

- \# of hits per beam track divided by number of beam particles

- \# of primary vertices divided by number of events

- \# of outgoing tracks divided by number of events

- \# of outgoing particles divided by number of events

- \# of outgoing particles from primary vertex divided by number of primary vertices

- \# of outgoing particles from primary vertex divided by number of events

- \# of hits in outgoing particles divided by number of outgoing particles

- \# of μ^+ tracks divided by number of events

- \# of μ^+ tracks from primary vertex divided by number of events

- \# of μ^- tracks divided by number of events

- \# of μ^- tracks from primary vertex divided by number of events

- $\sum \chi^2$ of outgoing particles divided by number of outgoing particles

- $\sum \chi^2$ of all vertices divided by number of all vertices

- Trigger rates (MTLAST, OTLAST, LAST2μ)

If the setup was stable during the given time window (period or sub-period), the aforementioned variables should stay constant along this interval. A spill was chosen as time unit for the stability checks. The average value of each variable in a given spill is compared to that in the neighbouring spills in the interval of 5000 spills (2500 before, and 2500 after the current one). If the value of spill passes the specific interval (*sigma box*) more than a certain number of times (*minimum number of neighbours*), the spill is marked as *good*. Otherwise it is marked as *bad* and tagged for rejection. The *sigma box* and *minimum number of neighbours* criteria are optimised for each variable and period of data taking. The spill is marked as *bad* if it fails the tests for at least one of the variables. In addition, runs with less than ten spills and those with more than 70% of bad spills were also rejected. An example of bad spill monitoring is shown in Fig. 4.1 where three *macro*-variables are analyzed along three data-taking periods. The spills classified as bad are marked in red. One can see that period W15 appears to be considerably more stable compared to the other two (W07 and W13).
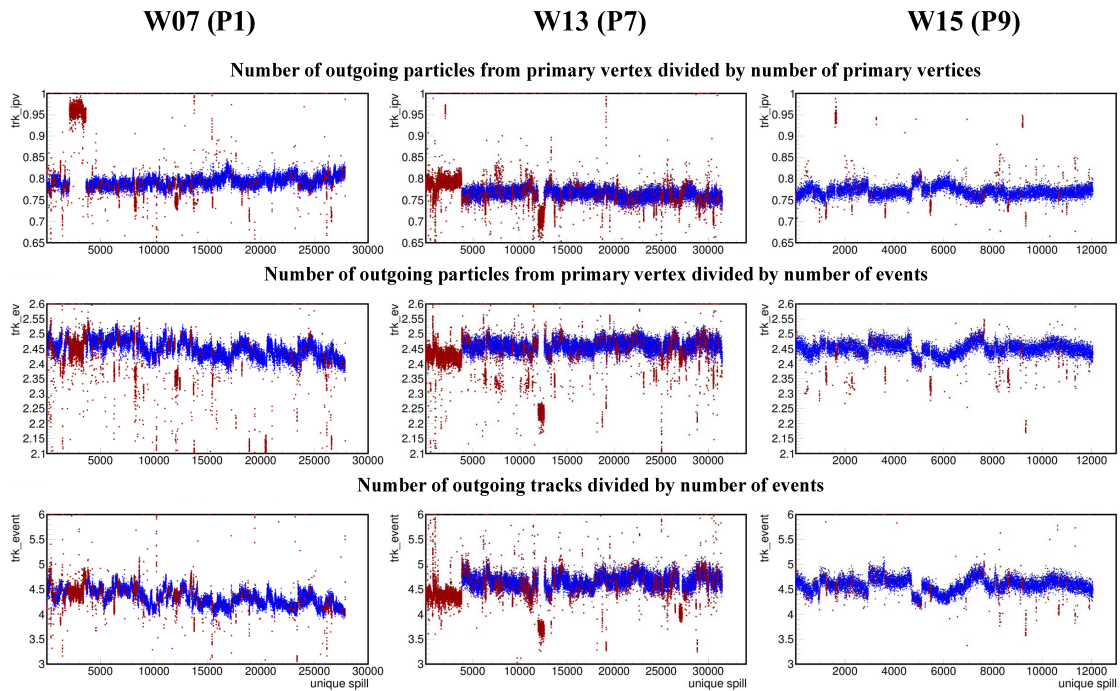
Fig. 4.1 Example of bad spill rejection for 3 periods of data taking. Spills classified as bad are marked in red.

4.3.2 Run-by-Run Stability Checks

The data stability is controlled also on a run-by-run basis. A set of relevant kinematical variables (x_N, x_π, x_F, q_T, $M_{\mu\mu}$, P_{μ^+}, P_{μ^-}, P_{γ^*} and P_{π^-}, X-, Y- and Z-position of the interaction vertices) was monitored run-by-run, checking for instabilities that could show up in the shapes and the means of the corresponding distributions. The comparison of the shapes is done for each pair of runs in a given period using an Unbinned-Kolmogorov Test (UKT) [194]. It is generally assumed that instabilities are occasional and most of the data is taken in stable conditions. The runs found to be incompatible with most of the runs in the given period are marked as bad.

The comparison of the means is done for the same set of variables applying different criteria to determine the quality of the run. In this case, a run is marked as bad if the average value of the given observable in this run is more than 5 standard deviations away from the overall average evaluated for the whole period. This information is then coupled with the results obtained from detector hit-profile monitoring using the histograms stored in COOOL, the online-monitoring software developed for the COMPASS experiment. Performed studies have shown that the spill-by-spill analysis removes most of the unstable data (about $\sim 4\%$ to $\sim 20\%$ of overall sample) and the run-by-run monitoring rejects a few percent more data

if applied afterwards ($\sim 1\%$ - $\sim 5\%$). The rejection rates for each of 9 periods of
2015 are summarized in Tab. 4.2.

Period	Bad spills rejection	Bad spills + runs rejection
W07 (P1)	11.79%	17.94%
W08 (P2)	18.00%	21.19%
W09 (P3)	14.76%	17.11%
W10 (P4)	15.88%	17.80%
W11 (P5)	22.49%	26.14%
W12 (P6)	12.71%	13.79%
W13 (P7)	22.32%	22.73%
W14 (P8)	8.91%	10.70%
W15 (P9)	3.94%	3.94%

Table 4.2 Percentage of rejected events by the only bad-spill lists and by the bad-spill list applied
together with the bad run list, for each period of data taking. The last two periods of 2015 data
taking appear to be the most stable ones.

4.4   Event selection

The event selection criteria relevant for the TSA-analysis have been adjusted on
the data of t1 and t2 test productions and verified on t3-slot data. Several aspects
were verified with full-chain MC simulations done with TGEANT. In this section
the final list of cuts adopted in various physics analyses presented in this Thesis is
reviewed.

The initial filtering done at the level of μDSTs selects pairs of oppositely-
charged muon tracks associated to primary vertices (PV). Muon-tracks are checked
to satisfy the muon hypothesis ensured by the requirement of 30 radiation lengths
to be crossed along the spectrometer ($x/X_0 > 30$), which is fulfilled by a passage
through one of the muon filter systems[3]. In case of more than one PV per pair, the
Best Primary Vertex tagged by CORAL is selected if existent[4], otherwise the PV
reconstructed with the smallest χ^2 is chosen. The sample obtained is then subject
to the following cuts:

1. **Dimuon trigger fired**. The dimuon trigger requires the hit pattern of several
   hodoscope planes to be consistent with two muons originating from the target
   region. This can be either double trigger in LAST hodoscopes, or one in
   LAST and another one in Outer or Middle hodoscopes, or both in Outer

---

[3]the distance crossed inside the hadron absorber is not taken in account in the calculation of the radiation lengths
[4]Accessed through PHAST method PaVertex::IsBestPrimary().

or Middle hodoscopes. In this analysis just LAST2μ and OTLAST (see Sec. 2.8.5) triggers were selected. The MTLAST trigger was removed from the analysis to reject the Beam Decay Muons (BDM) component. Remaining BDMs are removed by the 'Trigger Validation' cut presented below (see Fig. 4.4). In Fig 4.4 θ_{μ^-} vs θ_{μ^+} distributions for various trigger combinations are shown. The BDMs are clearly distinguished at low θ_{μ^-} and are associate mostly with the MTLAST trigger.

2. **Cut on the first and the last measured point of the tracks**. The tracks are asked to have the first measured point upstream of SM1 dipole magnet ($Z_{first} < 300$ cm) and the last downstream of the Muon Wall 1 ($Z_{last} > 1500$ cm). The first is to ensure the momentum measurement, while the second guarantees that the tracks were not stopped into Muon Filter 1.

3. $t_{\mu^\pm}$ **defined**. The time of the muon tracks with respect to the trigger time must be defined.

4. $|t_{\mu^+} - t_{\mu^-}| < 5$ **ns**. The absolute difference between the time of the two muons[5] must be lower than 5 ns. This requirement rejects uncorrelated pairs, in particular the ones formed picking up a BDM. Having other BDM-rejection criteria applied, the impact of this cut appears to be marginal, around 0.9 %.

5. $\chi^2_{\mu^\pm} < 10$. This cut represents a standard restriction on the quality of the muon tracks, usually applied also in COMPASS SIDIS analyses.

6. **Trigger validation or hodoscope-pointing cut.** This cut requires that extrapolated[6] muon tracks fall in the active area of the hodoscopes corresponding to the fired trigger(s). Since only LAST-LAST and OT-LAST triggers are selected in the analysis, just these combinations were considered. As mentioned above, this cut combined with the rejection of the MT-LAST events ensures BDM events to be removed.

7. **Bad Spill/Run selection**. Pairs belonging to spills and/or runs marked as bad by the stability checks described in Sec. 4.3 are removed from the data sample.

8. x_π, x_N **and** x_F **cuts**. Requirement on the variables to be within physical limits: x_N and $x_\pi \in [0; 1]$ and $x_F \in [-1; 1]$.

---

[5]Defined with respect to the trigger time.
[6]The extrapolation is performed using PHAST method PaTrack::Extrapolate().

9. **q_T cut**. $0.4 < q_T \ (\text{GeV}/c) < 5.0$ is requested for each pair entering the analysis. The lower limit is set to ensure a reasonable resolution in the azimuthal angles and was estimated via TGEANT MC simulation (see Sec. 4.6 and in particular Fig. 4.10 and Tab. 4.6). The upper limit has a negligible impact and removes the tail of high q_T events.

10. **Cut z-position of the primary vertex**. This cut was fixed according to the NH$_3$ target cells limits provided by the target group: $z_{PV} \in [-294.5, -239.3] \cup [-219.5, -164.3]$ cm.

11. **Radial cut** : a cut on $r_{PV} < 1.9$ cm was applied to minimize the contribution from the surrounding unpolarised material. The cells radius is 2 cm. The impact in statistics of selecting 2 cm or 1.9 cm is 1.7%. An illustration of the radial cut impact is shown in Fig 4.2.
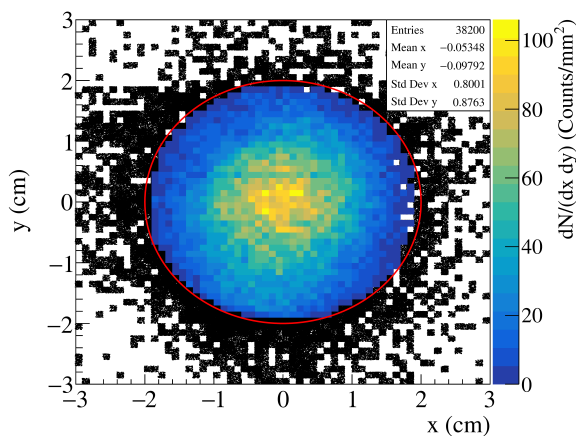
Fig. 4.2 Distribution of vertices reconstructed with $z \in ([-294.5 ; -239.3] \ \| \ [-219.5; -164.3])$ (**black**). The circle shows the geometrical cell size, while the color-scaled distribution represents the events selected in the final analysis ($r_{PV} < 1.9$).
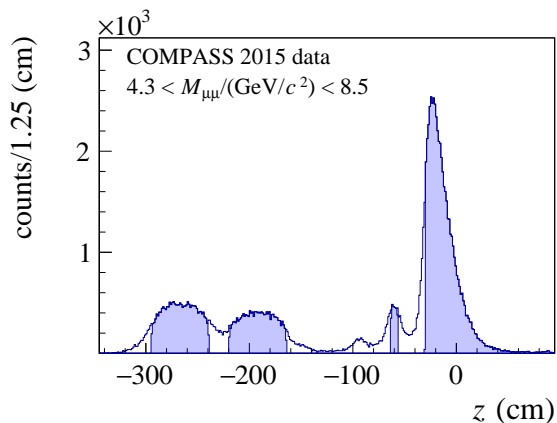
Fig. 4.3 z distribution of events passing the event selection criteria (except of r_{PV} and z_{PV} cut). The regions highlighted in corresponds to the two NH$_3$ cells, the aluminium target and the tungsten plug, respectively. The bump $\sim$ -100 cm corresponds to the dead region of the vertex detector.

In addition to these cuts, a **mass cut** was applied to select the High Mass range. It was adjusted evaluating the contamination of all competing processes (open charm, combinatorial background, $J/\psi, \psi'$ and Drell-Yan)[7] using full-chain MC-simulations and fitting all components simultaneously to the mass-spectra obtained from experimental data. The physics event generation for each process was done using Pythia8 generator, while the full simulation of the COMPASS

---

[7]the contribution from Υ meson is removed by an upper mass-cut at 8.5 GeV/c^2
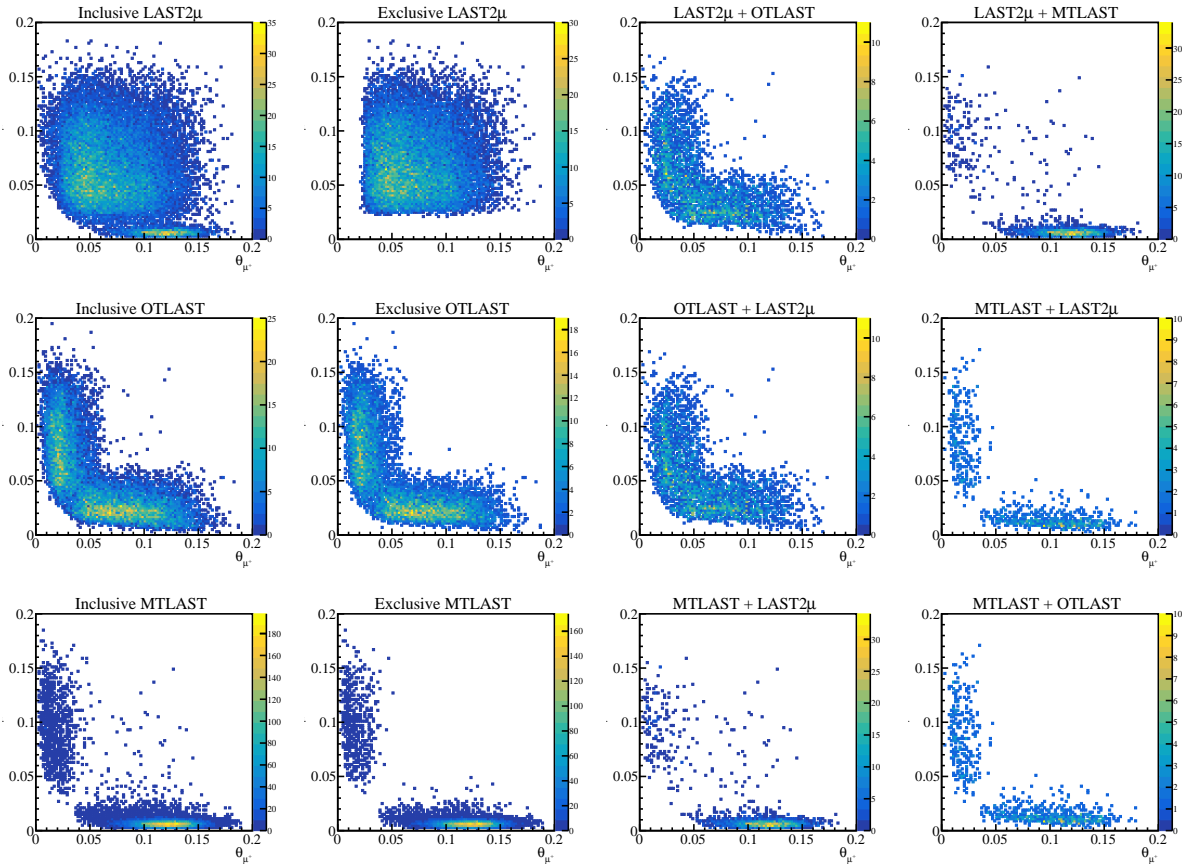
Fig. 4.4 θ_{μ^-} vs θ_{μ^+} obtained applying all the cuts described in Sec. 4.4 except of MTLAST rejection. Each plot is obtained selecting different combinations of trigger bits. The beam decay muons can be identified with island located at low θ_{μ^-}. From these distributions, it is clear that they come associated with the MTLAST trigger.

setup was carried out using TGEANT. The MC-data reconstruction was done using the same CORAL version used in the mass production. The combinatorial background (CB) is explicitly evaluated using dedicated parametrization obtained from experimental data (the details are given in Sec. 4.5), hence, CB-component is fixed in the fit. The fraction of DY process is also fixed in the fitting procedure. It is defined by a separate fit performed in mass range between 5.0 GeV/c^2 and 8.5 GeV/c^2 where no other process contributes. The weights of the other three components (open charm, $J/\psi, \psi'$) were defined as free-parameters and were determined by the fit to the mass-spectra.

The dimuon mass spectra obtained experimentally and evaluated components corresponding to aforementioned processes as well as the overall fit-curve are shown in Fig. 4.5. The resulting fit-curve reasonably well described the experimental data. The fraction of dimuons originating from different processes in different mass intervals is shown in Tab. 4.4. Based on these results, the final High Mass Range cut selecting the region of interest for DY analyses was defined by the

limits $4.3 < M_{\mu\mu}$ (GeV/c^2) < 8.5. The upper limit is set to avoid contamination for the Υ resonance. The applied cuts and their impact on the statistics for the mass range $M_{\mu\mu} > 2$ GeV/c^2 and for the high mass range, $4.3 < M_{\mu\mu} < 8.5$ GeV/c^2, used for the extraction of the asymmetries are summarized in Table 4.3. After all event-selection cuts about 35×10^3 dimuons remain for the analysis in HM-range.

Criteria	$M_{\mu\mu} > 2$ GeV/c^2	$4.3 < M_{\mu\mu} < 8.5$ GeV/c^2
PV: 2 opposite charge muon($x/X_0 > 30$) tracks	41008609	1159349
dimuon trigger bit (LAST, OT no MT)	32046393	868291
$Z_{first} < 300$ cm and $Z_{last} > 1500$ cm	30467114	784379
$t_\mu^\pm$ defined	30301533	776643
$\Delta t_\mu < 5$ ns	19059490	373081
$\chi^2_{tracks}/n.d.f. < 10$	18937973	370054
hodoscope pointing (LAST, OT)	14238292	169526
"bad" spill/run rejection	11629288	138255
x_N and $x_\pi \in [0; 1]$ and $x_F \in [-1; 1]$	11629087	138159
$0.4 < q_T/(GeV/c) < 5.0$	10107057	124848
$z_{PV} \in [-294.5, -239.3] \cup [-219.5, -164.3]$ cm	2917566	38200
$r_{PV} < 1.9$ cm	2554933	34904

Table 4.3 Impact of the event-selection criteria and final statistics.

The kinematic distributions of Bjorken variables x_N and x_π and the dimuon Feynman variable x_F are presented in Fig. 4.6. The dimuon mass, transverse momentum q_T distributions and two-dimensional distribution of the Bjorken scaling variables of pion and nucleon, x_π and x_N, for the selected mass range are presented in Fig. 4.7. The latter figure shows that the kinematic phase space explored by the COMPASS spectrometer matches the valence region in x_π and x_N. In this region, the DY cross section for a proton target is dominated by the contribution of nucleon u-quark and pion $\bar{u}$-quark TMD PDFs. The corresponding mean values of the kinematic variables are: $\langle x_N \rangle = 0.17$, $\langle x_\pi \rangle = 0.50$, $\langle x_F \rangle = 0.33$, $\langle q_T \rangle = 1.2$ GeV/c and $\langle M_{\mu\mu} \rangle = 5.3$ GeV/c^2.

The correlations between different kinematic variables are shown in Fig. 4.8.

4.5   Combinatorial Background

The combinatorial background, originated from uncorrelated pion and kaon decays into muons, is represented by the black dotted curve in Fig. 4.5. The CB

Mass (GeV/c^2)	Data	DY	J/ψ	ψ'	OC	CB	Background fraction
4.0 - 8.5	44245	40412	1054	1863	1679	319	10.8 %
4.1 - 8.5	39089	37186	608	722	1347	233	7.3 %
4.2 - 8.5	34986	34213	415	310	1106	176	5.5 %
4.3 - 8.5	31721	31448	242	139	814	126	**4.0 %**
4.4 - 8.5	28916	28907	164	65	656	91	3.3 %
4.5 - 8.5	26453	26583	120	33	557	75	2.9 %
4.6 - 8.5	24287	24434	94	17	440	60	2.4 %
4.7 - 8.5	22265	22451	64	9	332	45	2.0 %
4.8 - 8.5	20383	20593	53	8	274	28	1.7 %
4.9 - 8.5	18779	18871	41	3	199	17	1.4 %
5.0 - 8.5	17202	17320	39	3	149	15	1.2 %

Table 4.4 Estimated number of events from various physics processes in different mass intervals within the High Mass range. The background contamination is estimated as (J/ψ + ψ' + OC + CB)/All. The interval selected for the TSAs analysis and the corresponding contamination are highlighted in **green**.
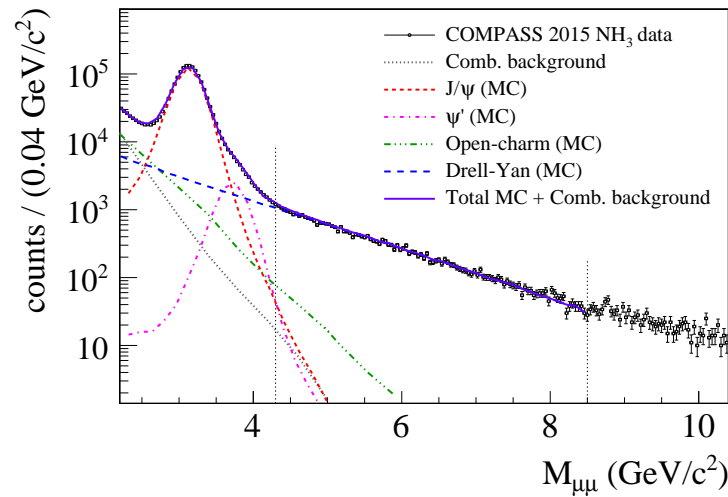
Fig. 4.5 Dimuon mass distribution. Global description using CB estimated from real data like-sign pairs, and physics contributions evaluated by MC.
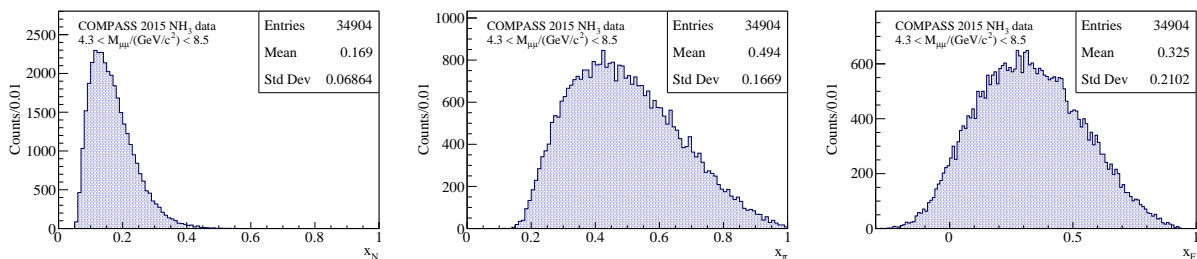
Fig. 4.6 Kinematic distribution of x_N (left panel), x_π (central panel) and x_F (right panel) passing all analysis requirements.
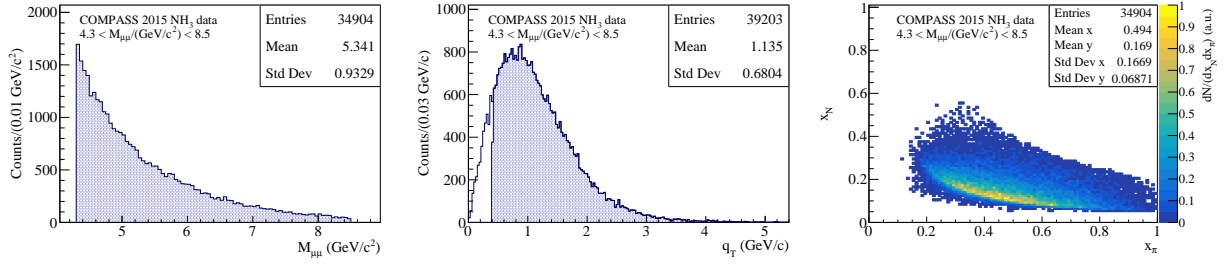
Fig. 4.7 Kinematic distribution of $M_{\mu\mu}$ (left panel) and q_T (central panel) and scatter plot x_N vs x_π (right panel) passing all analysis requirements. In the q_T distribution the part selected for the analysis is highlighted in blue.
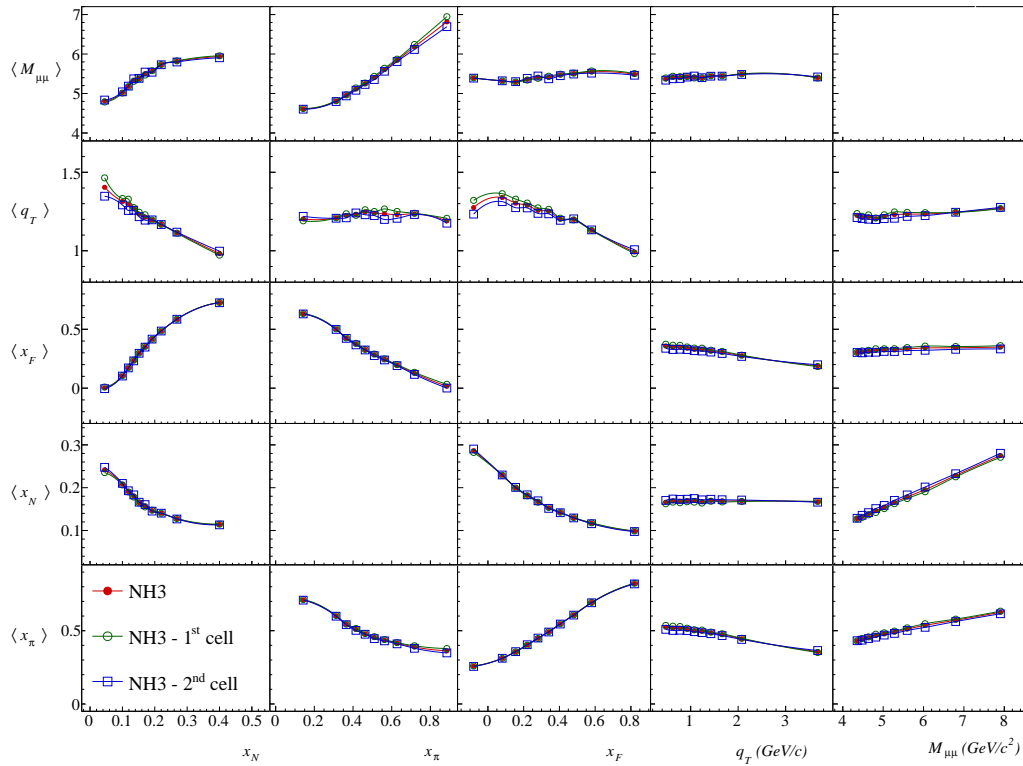
Fig. 4.8 Kinematic map: correlations between kinematic variables.

contribution in each bin was estimated using the so-called like-sign method:

$$N_{\mu^+\mu^-} = 2\sqrt{N_{\mu^-\mu^-} N_{\mu^+\mu^+}} \tag{4.1}$$

where $N_{\mu^-\mu^-}$ and $N_{\mu^+\mu^+}$ represents the negative and positive like-sign pairs respectively. The events entering the like-sign spectra are selected applying the same cut-flow used for the physics events, described in Sec 4.4. Since the formula in eq. 4.1 is valid only if the spectrometer is charge symmetric, the so-called **image cut** was applied to fulfil this requirement.. A muon pair passes the cut if

both muons would still be in the hodoscopes acceptance if each of them separately would have opposite charge. As one can see from Fig. 4.5, the combinatorial background is quite sizable in the low mass regions, and decreases moving towards higher masses. The CB contribution in the region above 4.3 GeV/c^2 is negligibly small.

4.6 Experimental resolutions and cell-to-cell event migration

A full-chain Monte-Carlo simulation was used to evaluate resolutions of kinematic and angular variables and to estimate cell-to-cell and "surrounding material"-to-cell event migrations. Simulations were performed using TGEANT COMPASS-MC tool (see Chap. 3). For MC-data reconstruction the same CORAL version was used as for the t3 mass production (revision r14146). Only the DY process yielding a dimuon pair in the final state ($q+\bar{q} \rightarrow \gamma^* \rightarrow \mu^+\mu^-$) in the extended mass-range 3.5 GeV/c^2 < $M_{\mu\mu}$ < 9.5 GeV/c^2 was generated using PYTHIA 6.428. Initial and final state radiations were turned off. As for the PDF-sets, the GRV98lo [195] and GRVPI0 [196] were used for nucleons and beam pions, respectively[8]. For nucleon and pion primordial k_T, the following gaussian parametrization was used:

$$\exp\left(\frac{-k_\perp^2}{\sigma^2}\right) k_\perp dk_\perp \tag{4.2}$$

with σ = 0.9 GeV/c and subsequently $< k_\perp >$= 0.81 GeV^2/c^2 and with an upper tail cut-off of 3 GeV/c. A summary of applied Pythia tunings is listed in Tab. 4.5.

A separate MC-sample was generated for each of the periods, placing the detectors according to the respective alignment and generating the beam tracks according to the parametrization extracted from the corresponding data-taking slot. The pile-up time window was set to $\pm$ 20 ns and corresponding intensity was set to $1 \cdot 10^8$ π^-/s. The MC sub-samples generated for each period entered in the final sample with a corresponding weight equivalent to the contribution of the corresponding data-taking period into the overall real data sample. In Fig. 4.9 real data versus Monte-Carlo comparisons for kinematic distributions x_N, x_π, q_T and $M_{\mu\mu}$ obtained after all analysis cuts (see Sec 4.4) are shown. In general, the agreement is good and some deviations observed mostly at the edge of the accessed kinematic phase-space are at acceptable level (beside edge-effects, maximal deviations are at the level of 10-20%). The sizable discrepancies at high

---

[8]both nucleon and pion PDF-sets are loaded via LHAPDF interface

q_T can be explained by the peculiarities of primordial k_T tuning in Pythia event generator.

General settings	
Nucleon PDF	GRV98lo
Pion PDF	GRVPI0
MSTP(61) - Initial State Radiation Switch	0 (off)
MSTP(71) - Final State Radiation Switch	0 (off)
CKIN(1) - Lower Invariant Mass Limit	3.5 GeV/c^2
CKIN(2) - Upper Invariant Mass Limit	9.5 GeV/c^2
CKIN(3) - Lower p_T Limit	0.1 GeV/c
CKIN(4) - Upper p_T Limit	10 GeV/c
k_T **tuning**	
MSTP(91) - Primordial k_T shape	91 (Gaussian)
PARP(91) - Width of the k_T distribution	0.9 GeV/c
PARP(93) - Upper cut-off to k_T distribution	3.0 GeV/c

Table 4.5 Main part of the Pythia6 tuning used in the MC discussed in Sec. 4.6

.
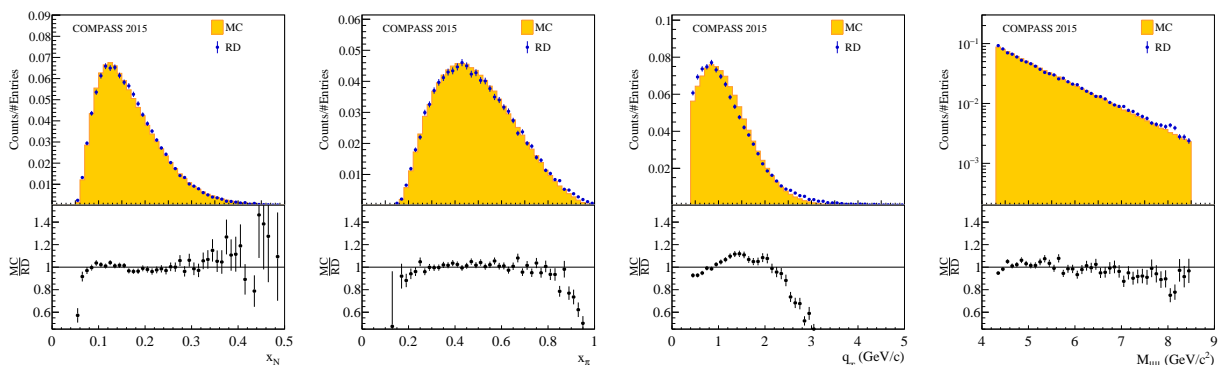
Fig. 4.9 Real data vs MC comparison for (from left to right) x_N, x_π, q_T and $M_{\mu\mu}$. All the distributions are normalized to their integrals.

The MC sample described above was used to evaluate experimental resolutions of different kinematic and angular variables. The results of these studies are summarized in Tab. 4.6. The two columns represent results obtained applying two different estimators. The first is the RMS of the residuals[9] while the second is obtained from a two-gaussian fit (leading signal + tails) and corresponds to the σ of the leading gaussian distribution. The latter estimate doesn't take into account the tails of the residual-distribution and thus gives an optimistic estimate, while the former one is sensitive to the selected range of the residual-distribution. In

---

[9]The *residual* represents the difference between the generated value and the reconstructed one evaluated event-by-event.

Fig. 4.10, the q_T dependences of ϕ_{CS} and ϕ_S angular resolutions, evaluated using the RMS estimator, are presented.

Variable	RMS	Leading Gaussian σ
Xv (cm)	0.0404	0.0279
Yv (cm)	0.0382	0.0240
Zv (cm)	10.97	8.22
$M_{\mu\mu}$ (GeV/c^2)	0.1907	0.1815
x_N	0.0186	0.0110
x_π	0.0131	0.0090
x_F	0.0195	0.0139
q_T (GeV/c)	0.1487	0.1070
ϕ_S (rad)	0.1933	0.0900
ϕ_{CS} (rad)	0.1976	0.0946
θ_{CS} (rad)	0.0264	0.0172

Table 4.6 Resolutions for main kinematic and angular variables.
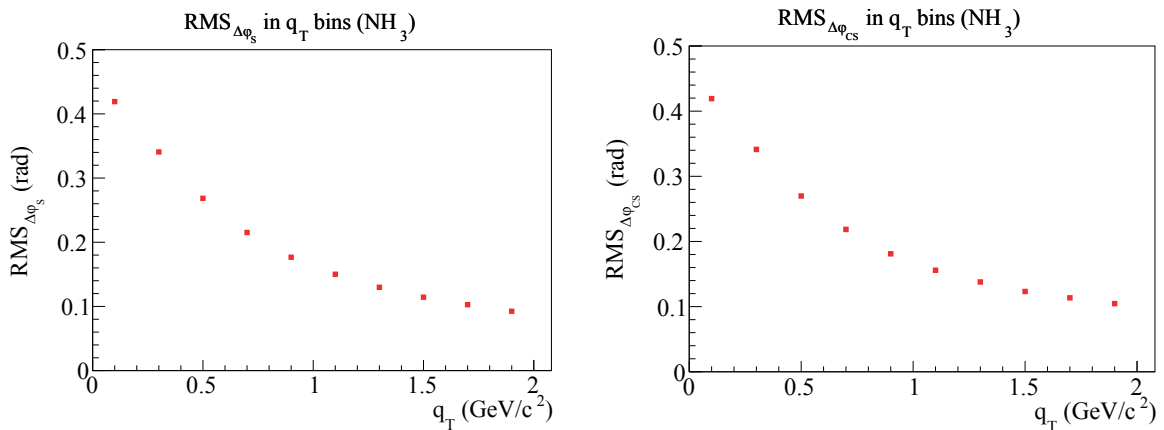
Fig. 4.10 The q_T dependence of the ϕ_S (left) and ϕ_{CS} (right) angular resolutions.

Using reconstructed and MC-truth information the event migration from one NH$_3$ cell to the other and from the surrounding unpolarised material to each of the cells was also estimated. This migration was taken into account as additional dilution effect (see Sec. 4.8). The estimated composition of the events reconstructed in the NH$_3$ cells is presented in Tab. 4.7 and illustrated in Fig. 4.11.

4.7   Target Polarisation measurement

A description of the polarised target system can be found in Sec. 2.8.3. The measured polarisation resulted to be non-uniform along each cell. This behaviour was attributed to several factors, mainly:

Events generated in	%		Events generated in	%
1st cell	94.94		2nd cell	92.92
LHe gap	1.57		LHe gap	3.88
LHe upstream the cell	2.37		LHe downstream the cell	0.60
2nd cell	0.15		1st cell	1.49
Other materials (R < 2)	0.29		Other materials (R < 2)	0.26
Other materials (R > 2)	0.69		Other materials (R > 2)	0.85

Table 4.7 Composition of the events reconstructed in the polarised target cells.
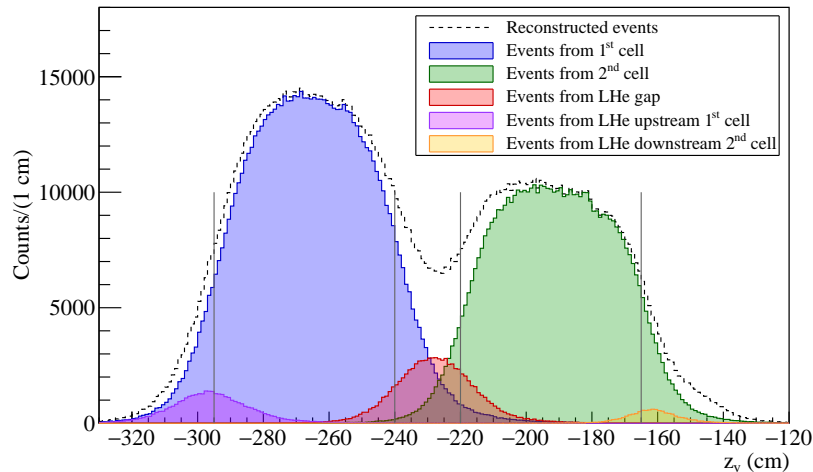
Fig. 4.11 Z-vertex distribution of the events originating from different materials in the NH_3 target region.

- The heating due to the high intensity beam and the high rate of secondary hadrons, originated in the $\pi^- + N$ collisions.

- The change of optimum frequency of microwave for DNP (dynamic nuclear polarisation).

- The non-uniform supply of the liquid ^{3}He along the target cells.

- The tuning of the trim coils.

All these factors led to differences in the measurements done by different coils of the same target cell going from 4 to 13%. In the past, e.g. for the muon programme with transversely polarised target, this difference was measured to be sizably smaller (less than few percent). Therefore, a simple average of the measurements done by different coils was applied to compute the polarisation value for each cell (which eventually enters the asymmetry-analysis procedure). This simple algorithm could not be applied for the DY case because of much larger dispersion compared to previous runs, so that a simple average would not characterise realistically the polarisation in a cell.

Finally it was decided to determine the polarisation as a function of the z-coordinate (along the beam axis) using a linear interpolation method. The method assumes that the change of the polarisation along z (from coil to coil) in a given cell is not an artifact of the systematic error attributed to the measurement, but is due to actual non-uniformity of the polarisation as a function of z.

The COMPASS PT system was optimised to perform the polarisation measurement with the very homogeneous solenoid magnetic field for a precise longitudinal polarisation measurement at 2.5 T. Therefore, the polarisation measurements were performed while polarising the target and then interpolated during the data-taking period using an exponential decrease law

$$P(t) = P_0 \cdot e^{(-t/\tau)} + P_{TE} \tag{4.3}$$

where τ represents the relaxation time, characterising the polarisation loss rate, and P_{TE} is the polarisation at the thermal equilibrium. Similar to the polarisation, also the τ varies from one coil to another, mainly because of inhomogeneities in the dipole magnetic field and of the different rate of secondary hadrons originated along the target. Fig. 4.12 shows the polarisation values along the data-taking year, per each coil. The average values of the polarisation calculated for each period for
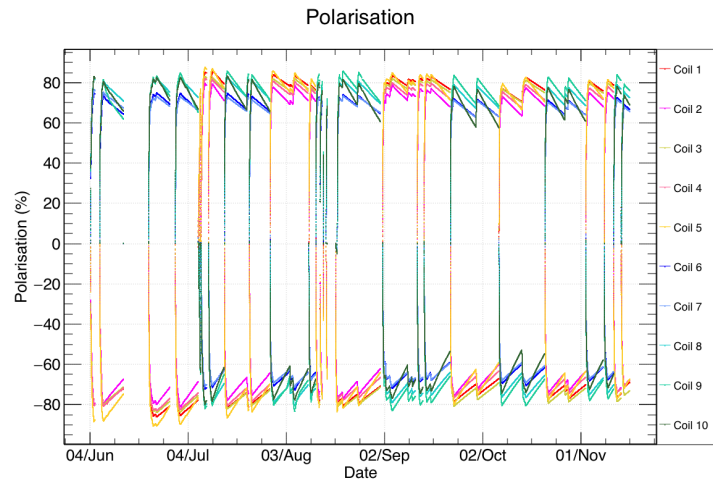
Fig. 4.12 Polarisation values during the 2015 DY run, for each coil.

the events selected for the analysis are shown in Table 4.8. The overall average is about 73%.

Period	W07	W08	W09	W10	W11	W12	W13	W14	W15
Polarisation	0.752	0.738	0.746	0.731	0.718	0.695	0.720	0.716	0.730

Table 4.8 Average polarisations (absolute value) for each period.

4.8 Dilution factor

The dilution factor accounts for the fraction of the polarisable material in the target volume. It depends on the composition of the target material and on the physics process of interest. In the case of pion induced DY, it can be written as

$$f = \frac{n_H \sigma^{DY}_{\pi-H}}{n_H \sigma^{DY}_{\pi-H} + \Sigma_A n_A \sigma^{DY}_{\pi-A}}. \tag{4.4}$$

In this equation n_H, n_A represent the amount of polarisable protons (H_3) and nuclei in the target respectively[10] and σ^{DY} the pion-induced Drell-Yan cross-section. Measurement of the differential Drell-Yan cross section is one of the objectives of the COMPASS DY programme. For the calculation of f the DY cross-section was evaluated using a dedicated parton-level Monte-Carlo program, MCFM [198]. Both NLO and NNLO calculations were performed, while for final evaluation only the NLO results were used. The accounting for nuclear effects is done via PDF correcting factors extracted by EKS [199]. It was checked that at LO the MC reasonably describes the nuclear effects measured by E772 [200].

Large samples were generated to estimate the cross-section with a relative statistical uncertainty of the order of few percents in the main kinematic domain populated by the data. In the simulation, fluctuations may arise in the regions where the cross-section is small. These are removed applying a smoothing procedure. In any case, these regions correspond to the unpopulated edges of the COMPASS acceptance.

Different kinematical dependencies of f were evaluated on different levels of complexity. The one-dimensional kinematic representations are shown in Fig. 4.13. The increase of f with x_N is mainly due to the faster u-quark suppression in n with
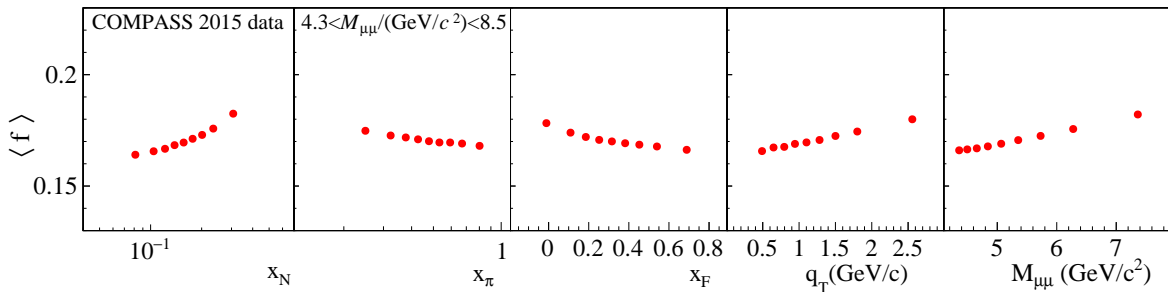
Fig. 4.13 Average dilution factor a function of kinematic variables.

respect to p. The increase with $M_{\mu\mu}$ can also be explained by the faster growth of u-quark in the p compared to the one in the n.

---

[10]these data was provided by the COMPASS PT group [197].

The mean dilution factor is found to be 10% smaller compared to the projected value estimated in the COMPASS-II proposal [136]. This difference could be mainly attributed to the actual amount of polarisable material measured in the target cells. In addition, the amount of material is not the same for two target cells and f varies of about 4% from one cell to another. The migrations of events from one cell to another and from surrounding unpolarised material to the cells are accounted as additional suppression factors (0.95 for the upstream and 0.91 for the downstream cell). In the analysis the dilution factor for given event-kinematics is accessed using PHAST method PaEvent()::GetDilutionFactor().

4.9 Depolarisation factors

In Fig 4.14 the depolarisation factors introduced in Eq. 1.25 are shown as extracted from the data. In the analysis in the evaluation of the depolarisation factors, the approximation $\lambda = 1$ is used. As shown in Fig. 4.14, known deviations from this assumption with λ ranging between 0.5 and 1 decrease the normalization factor by at most 10% and about 5% for bins selected for the analysis. The latter estimate of possible variations is taken into account at the level of systematic scale uncertainties.
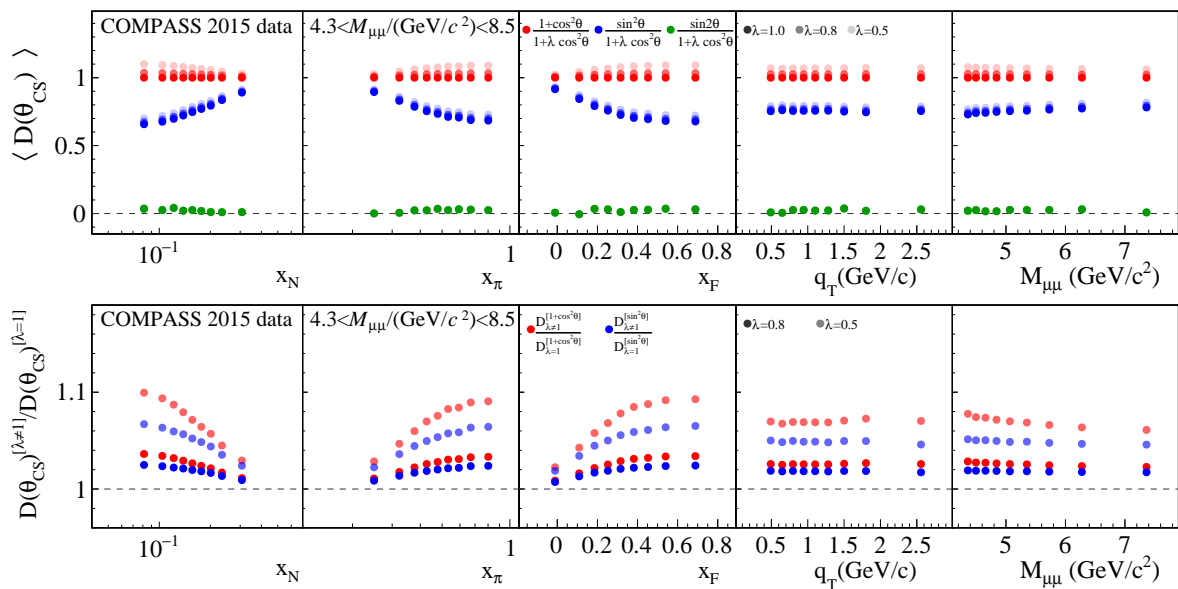
Fig. 4.14 Depolarisation factors shown as function of kinematic variables. Top plot: impact of different "λ-value" hypotheses. Bottom plot: relative impact of different "λ-value" hypotheses with respect to the $\lambda = 1.0$ case.

4.10 Extraction of the asymmetries

4.10.1 Extraction using the Weighted Extended Unbinned Likelihood method

All target spin (in)dependent azimuthal asymmetries arising in the Eq. 1.25 are extracted simultaneously together with their correlation matrices using Event-Weighted extended Unbinned Maximum Likelihood method [201], hereafter referred to as EWUML. Here event-weighting refers to the fD-corrections accounted on event-by-event basis. Several other methods such as the One-Dimensional Double Ratio method (1DDR or simply 1D) and the standard[11] extended Unbinned Maximum Likelihood (UML) method were also tested, and used too for x-checks and systematics studies.

The likelihood fit-function $\mathscr{L}$ used for the extraction of DY-asymmetries is defined as follows:

$$\mathscr{L} = \prod_{c=1}^{n_{cell}} \left\{ \left(e^{-I_c^+} \prod_{n=1}^{N_c^+} P^+(\varphi_{CSn}, \varphi_{Sn}; a_c^+, \vec{A}) \right)^{\frac{\bar{N}}{N_c^+}} \right. \tag{4.5}$$

$$\left. \times \left(e^{-I_c^-} \prod_{m=1}^{N_c^-} P^-(\varphi_{CSm}, \varphi_{Sm}; a_c^-, \vec{A}) \right)^{\frac{\bar{N}}{N_c^-}} \right\}$$

The probability density functions, $P^{\pm}(\varphi_{CS}, \varphi_S; a_c^{\pm}, \vec{A})$, are given by the products

$$P^{\pm}(\varphi_{CS}, \varphi_S; a_c^{\pm}, \vec{A}) = \sigma^{\pm}(\varphi_{CS}, \varphi_S; \vec{A}) \cdot a_c^{\pm}(\varphi_{CS}, \varphi_S) \tag{4.6}$$

The first multiplier denotes the DY cross section as a function of the azimuthal physics angles and the vector of the asymmetries, $\vec{A}$:

$$\sigma^{\pm}(\varphi_{CS}, \varphi_S; \vec{A}) = 1 + A_U^{cos\varphi_{CS}} + A_U^{cos2\varphi_{CS}} \pm \sum_{i=1}^{5} \langle P_T \rangle fD(\theta_{CS})^{w_i(\varphi_{CS}, \varphi_S)} A_T^{w_i(\varphi_{CS}, \varphi_S)}$$

$$\tag{4.7}$$

The second term of the product, $a_c^{\pm}(\varphi_{CS}, \varphi_S)$, accounts for different factors such as: the unpolarised cross section, the luminosity and the acceptance of the experimental apparatus corresponding to the given cell.

The fitting function presented in Eq. 4.5 invokes $2 \times n_{cell}$ products corresponding to dimuon samples coming from two NH$_3$ cells acquired with two opposite (up and down) target spin orientations. In order to reduce possible false asymmetries

---

[11]fD-correction is not done using event-by-event fD-weighting within the fit, but is applied as averaged correction.

and acceptance effects, which could be induced in case of unbalanced statistics in two cells, each of these four multipliers is weighted with powers of $\bar{N}/N_c^{\pm}$, where $N_c^{\pm}$ gives the number of dimuons in the target cell c with spin up or down respectively, while $\bar{N}$ is the average number of muon pairs in the given kinematic bin[12]. The terms, $I_c^{\pm}$, are the probability density normalisation coefficients given by the integrals of the probability density functions over φ_{CS} and φ_S:

$$I_c^{\pm} = \int \int d\varphi_{CS} \, d\varphi_S P^{\pm}(\varphi_{CS}, \varphi_S; a_c^{\pm}, \vec{A}) \qquad (4.8)$$

and can be interpreted as an expected number of dimuons for the given cell and polarisation.

Analogously to COMPASS SIDIS analyses [201], the coefficients $a_c^{\pm}$ are left as free fit-parameters, to account for unpolarised part of the cross-section and the different beam fluxes in the two sub-periods. Note that, similar to the SIDIS case, EWUML method doesn't include corrections for spectrometer azimuthal acceptance. Hence, extracted spin-independent azimuthal amplitudes are not deconvoluted for possible acceptance components and have no clear physics meaning. At the same time, in stable data-taking conditions with no azimuthal acceptance variations, in the EWUML estimator the spectrometer induced azimuthal effects factor out in the polarisation dependent part and in the minimization the spin-dependent terms remain unaffected. The minimization was carried out using TMinuit class in ROOT.

The dilution factor f and the depolarisation factors D are calculated for each event and enter in the fit as asymmetry weighting factors (see Eq. 4.7). In contrast to this, the average target polarisation is evaluated per each period separately and doesn't enter on event-by-event basis in order not to introduce systematic biases, see [201] and references therein.

The asymmetries were evaluated in kinematic bins of x_N, x_π, x_F, q_T and $M_{\mu\mu}$, while always integrating over all the other variables. The kinematic bins listed in Tab. 4.9 were chosen to contain nearly the same number of events.

Variable	Bin Limits			
x_N	0.0	0.13	0.19	1.0
x_π	0.0	0.40	0.56	1.0
x_F	-1.0	0.21	0.41	1.0
q_T (GeV/c)	0.4	0.9	1.4	5.0
$M_{\mu\mu}$ (GeV/c^2)	4.3	4.75	5.5	8.5

Table 4.9 Kinematic bin limits used in the TSA analysis.

---

[12]the index c runs over the two NH_3 cells, $c \in \{1, 2\}$

The correlations between different asymmetries have been studied using co-variance matrix coefficients determined within the fit-procedure.

4.10.2 Comparison of the results from different methods

As a general consistency check the asymmetries extracted using different fit-methods were compared one to another. The comparison between asymmetries extracted using classical UML and EWUML is presented in Fig. 4.15. The difference between the two methods is that in EWUML $f \cdot D(\theta_{CS})$-correction is done on an event-by-event basis and is included in the fit, while in classical UML the correction is done afterwards and asymmetries are corrected for average $f \cdot D(\theta_{CS})$ in the given kinematic bin.

The smallest deviations are observed for the Sivers asymmetries, $A_T^{sin\varphi_S}$, since corresponding term enters in Eq. 1.25 with a depolarisation factor equal to 1 and asymmetry is corrected only for f. In general the event-by-event weighting
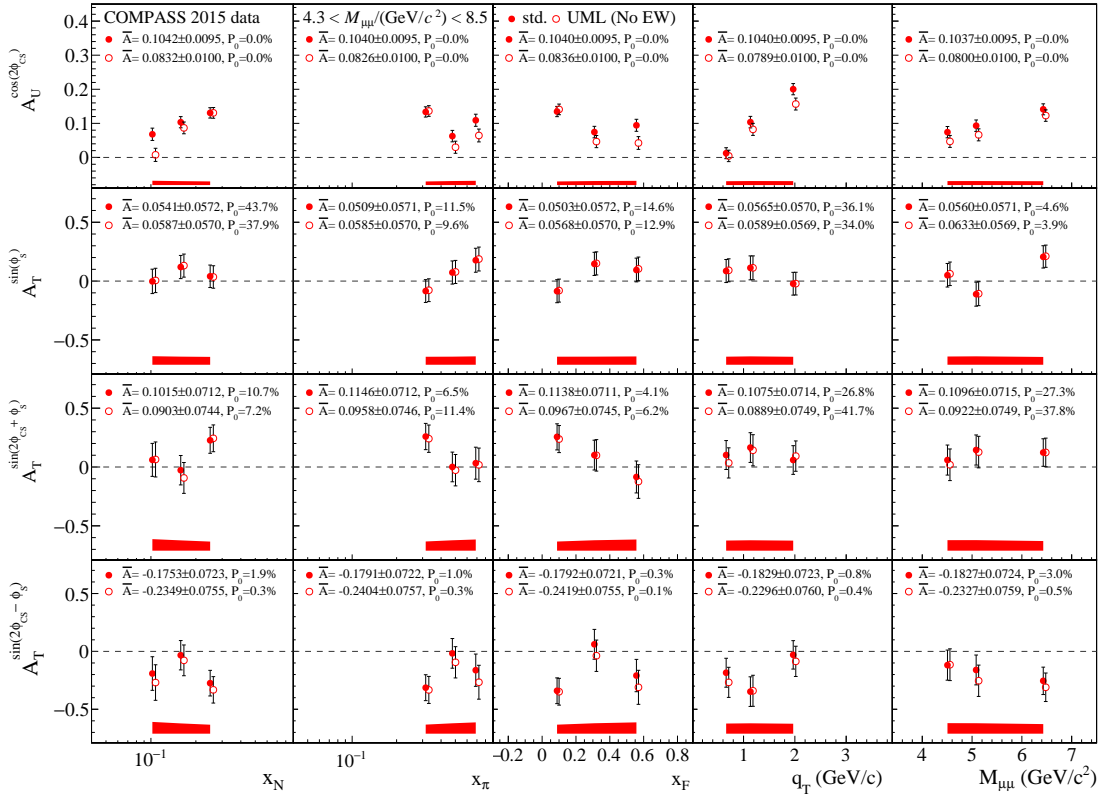
Fig. 4.15 Comparison of the asymmetries extracted with EWUML and UML methods.)

is expected to reduce statistical uncertainties of the asymmetries, see [201] and references therein. Indeed, this is the case for Pretzelosity and Transversity-related TSAs, $(D_{[sin^2 \theta_{CS}]} = sin^2 \theta_{CS}/(1 + cos^2 \theta_{CS}))$ for which the statistical errors from EWUML are by $\sim 4-5\%$ smaller compared to UML ones.

Average $A_T^{sin(2\varphi_S+\varphi_{CS})}$ and $A_T^{sin(2\varphi_S-\varphi_{CS})}$ TSAs extracted with two methods dif-fer by about ~0.2 and ~0.8 standard deviations, correspondingly, while for unpolarised Boer Mulders $A_U^{cos2\varphi_{CS}}$ asymmetry the difference is at the level of two standard deviations. This behaviour is related to the three higher twist asymmetries (one UA and two TSAs) and corresponding depolarisation factor, $D_{[\sin 2\theta_{CS}]} = \sin 2\theta_{CS}/(1+\cos^2\theta_{CS})$. The distributions of both aforementioned depolarisation factors are shown in Fig. 4.16. The $D_{[\sin^2\theta_{CS}]}$ in average is close to 1 while $D_{[\sin 2\theta_{CS}]}$ ranges between ±0.7 and in average is very small (~ 0.02). Therefore, in UML fit higher twist asymmetries are strongly suppressed, when corrected for averaged $f \cdot D(\theta_{CS})$. In the EWUML case, event-by-event accounting for $D_{[\sin^2\theta_{CS}]}$ allows to extract higher twist amplitudes correctly. As a consequence, possible correlations affect other amplitudes entering in the fit which explains differences between EWUML and UML results.
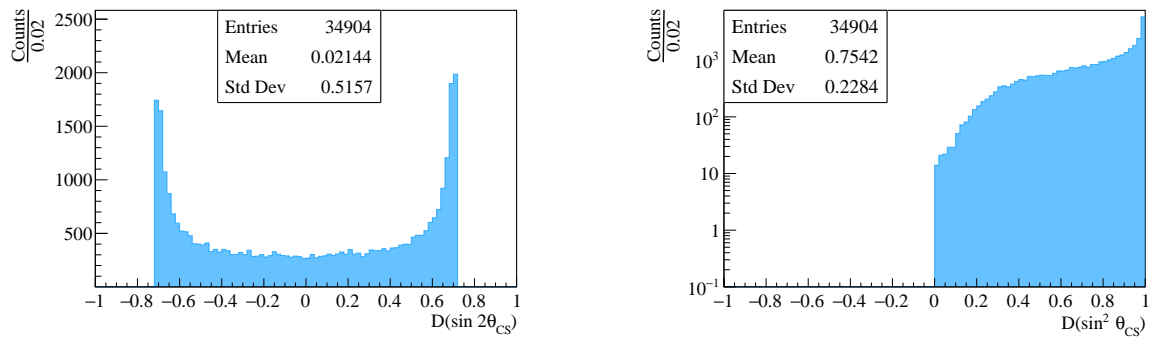
Fig. 4.16 $D(\sin 2\theta_{CS})$ (left) and $D(\sin^2\theta_{CS})$ (right) distributions for events selected in TSAs analysis. $D(\sin^2\theta_{CS})$ is presented in logarithmic scale for better visibility.

Since it is difficult to disentangle expected differences between asymmetries obtained by EWUML and UML from the unexpected ones the deviations between the two methods are not taken into account in the evaluation of the systematic uncertainties.

4.11 Systematic studies

In this section main systematic studies carried out for TSA-analysis are reviewed. Some of the tests belong to the set of standard checks performed for SIDIS TSAs analysis at COMPASS, while others were introduced specifically for DY TSAs analysis.

4.11.1 Compatibility of the periods.

Possible discrepancies between the asymmetries extracted from the nine periods of the data taking have been tested. The pull-distributions were built to compare the asymmetries from each period with the asymmetries averaged over the whole data taking (see Fig. 4.17). The differences between values of weekly asymmetry A_i, where i indicates the number of the week, and corresponding mean asymmetry $\langle A \rangle$ normalized as $pull = A_i - \langle A \rangle / \sqrt{\sigma_{A_i}^2 - \sigma_{\langle A \rangle}^2}$, define the entries of the pull distribution. In case week to week deviations are caused just by statistical fluctuations, the pull distributions should be represented by normal distributions centred at 0 with a gaussian width σ_{Pull} (or RMS) close 1. Apart from the $A_T^{sin(2\varphi_S - \varphi_{CS})}$ asymmetry, the pulls are well compatible with a standard normal distribution. This is an indication of the compatibility of the results and proves the statistical origin of the deviations from period to period. In case of $A_T^{sin(2\varphi_S - \varphi_{CS})}$ TSA the distribution appears to be narrower than expected. This could point to overestimated statistical uncertainties. Nevertheless, extending the mass range to lower masses (increasing the statistics and the number of the bins) restores the canonic shape of the pull-distribution. The asymmetries averaged over each period are demonstrated in Fig. 4.18. The
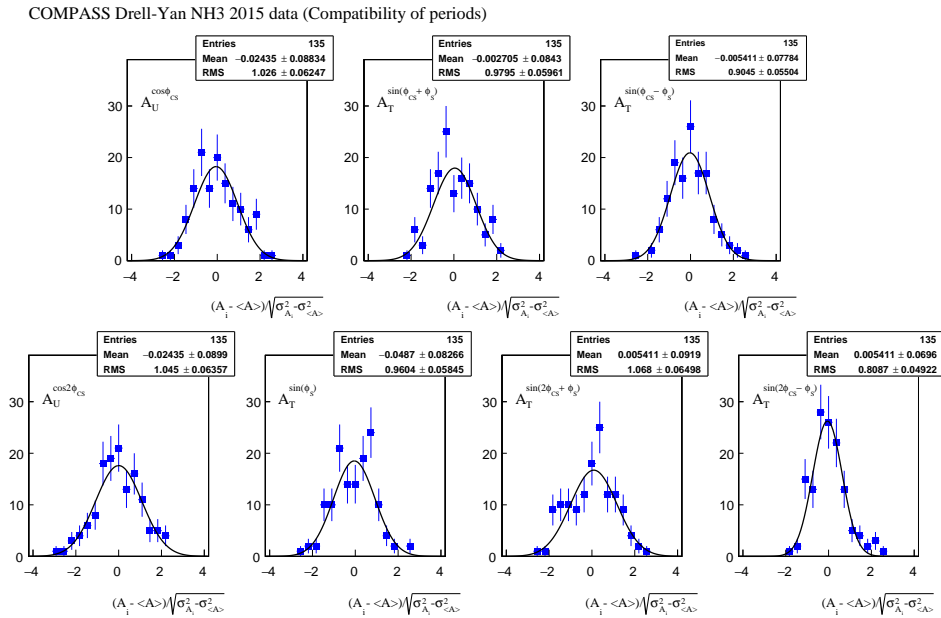
Fig. 4.17 Pulls distributions showing the compatibility of the periods. Each histogram has 135 entries, which corresponds to 5(kinematic variables)×3(number of the bins)×9(number of periods).

line drawn in each plot represents a fit with a constant function. Values from different periods appear to be compatible. Asymmetries as extracted from each period separately are shown in Fig. 4.19. Since there are no evidences of possible

problems, the results of this test do not enter in the final estimate of the systematic uncertainty.

4.11.2 Impact of the data quality cuts.

The stability of the asymmetries with respect to different *bad* spill/run quality tests was studied. The impact of different strictness levels of the quality criteria has been evaluated, varying from soft requirements (up to $\sim$10%) to very strong ones ($>$20% rejection). In general, the average asymmetries seem to grow when the *bad* spills/runs are rejected, but the differences are not statistically clear. The impact of the quality tests is shown in Figs. 4.20, 4.21. In Fig. 4.20, asymmetries from "all spills/runs" are compared with the ones coming from the filtered sample. It can be noted that for the $A_T^{sin(2\varphi_S-\varphi_{CS})}$ and $A_T^{sin(2\varphi_S+\varphi_{CS})}$ TSAs rejection of *bad* spills and runs increases the magnitude of the asymmetries. This is an expected behaviour since *bad* spill/run sample can be considered as a noise which would dilute the physics signal. Nevertheless, data-filtering doesn't seem to affect $A_U^{cos2\varphi_{CS}}$ and $A_T^{sin\varphi_S}$ amplitudes.

In Fig. 4.21, the 'pseudo'-pull histograms filled by bin-by-bin differences normalized to statistical uncertainty are built. The RMS of the distributions is at the level of 0.4-0.5 in units of statistical error, while the mean values are below 0.1, which means that average deviations are below 10% of the statistical uncertainty.

4.11.3 Statistical equalization of the sub-periods

Numbers of events in two sub-periods of a given period can differ by up to 50% (which is the case for P1(W07) and P9(W15) periods) and such imbalance may potentially bias the results. This situation was observed in former SIDIS analysis when the results of simple one-dimensional extraction methods were getting distorted. Unbinned maximum likelihood methods do not suffer from such deviations, unless one of the sub-periods is not affected by strong azimuthal instabilities.

In order to test this conjecture the number of dimuons pairs in two sub-periods of each period have been forcibly equalized rejecting runs from the largest sub-period. The rejection was done in a way that the final sample consists of runs that are close in time (runs were cut from the beginning of the first sub-period or the end of the second one). A particular aim of this test was to improve the flux-cancellation in each period. The rejection of the events is at the level of $\sim$10%. Asymmetries were found to be stable and no biases were observed, see
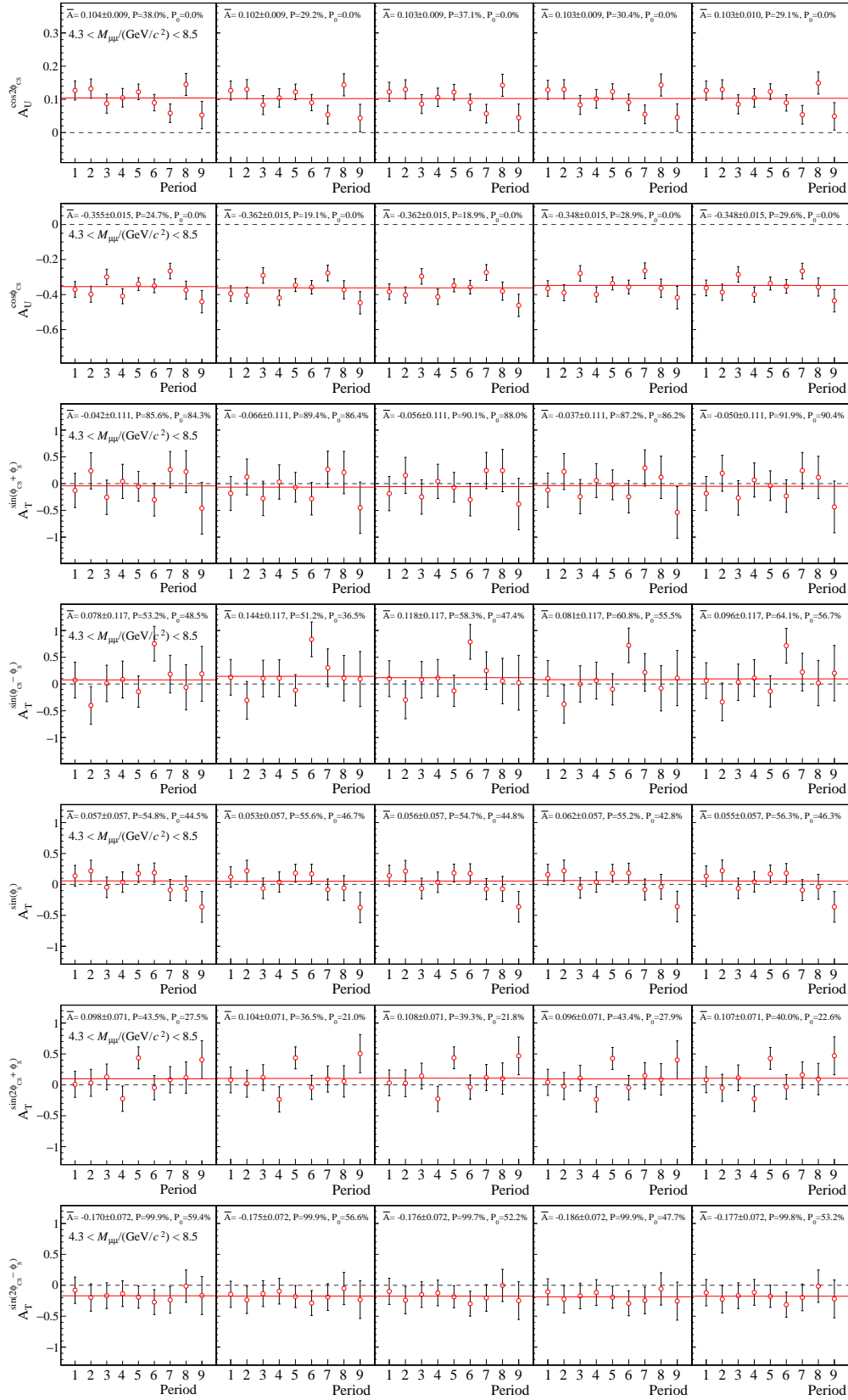
Fig. 4.18 Asymmetries averaged per period
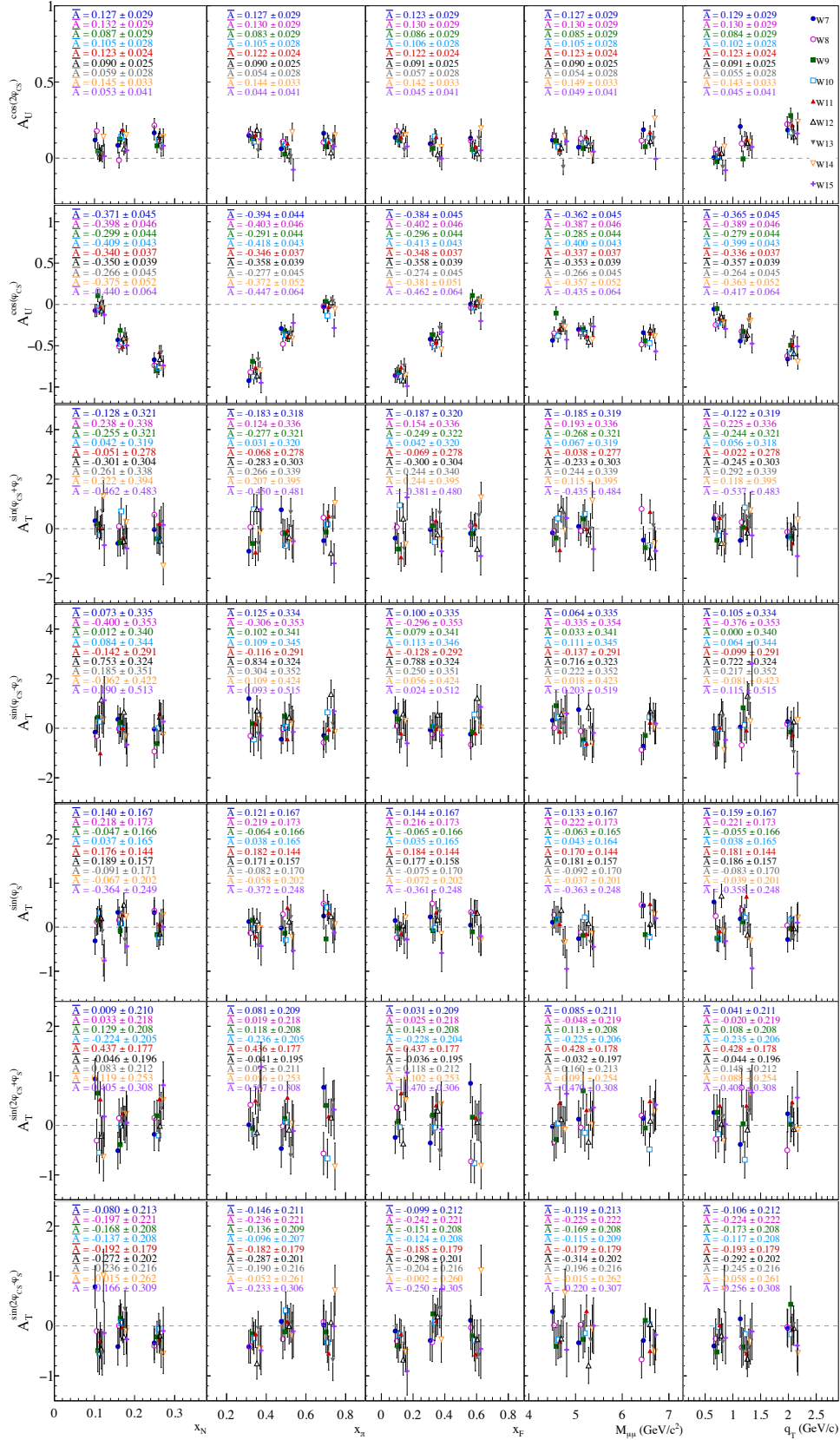
Fig. 4.19 Asymmetries period by period
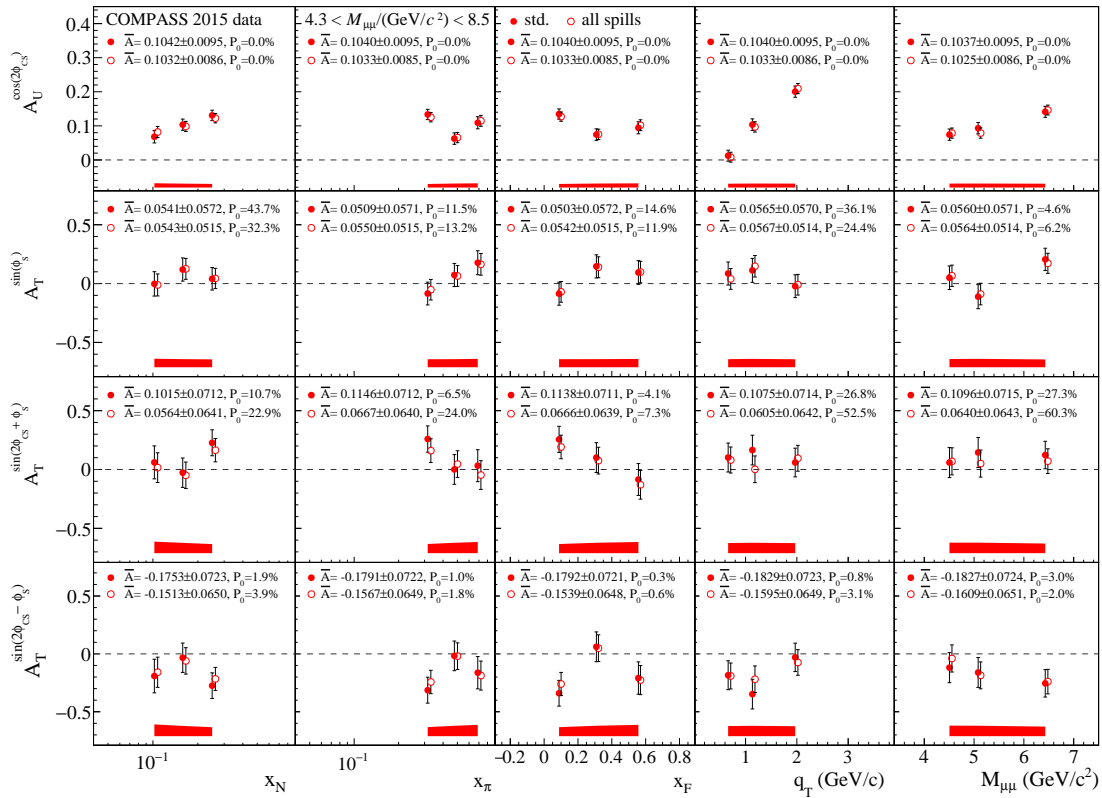
Fig. 4.20 LO asymmetries: impact of the *bad* spill/run rejection.
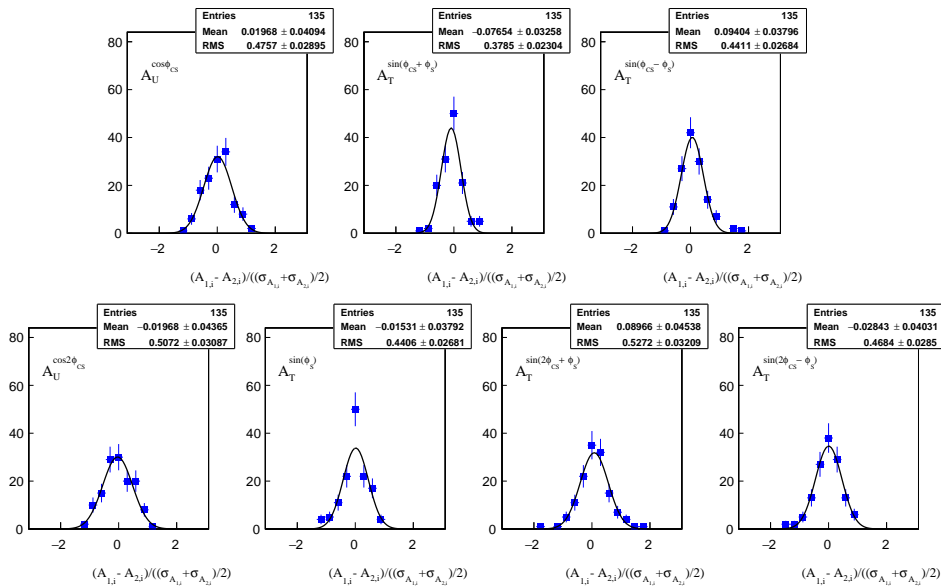
Fig. 4.21 Pseudo 'pulls' for this comparison, consisting in the differences normalized to the statistical error.

Fig. 4.22 (top panel). The 'pseudo' pulls shown in the bottom figure are centered at zero and have an RMS about 0.4-0.5 in units of the statistical error.
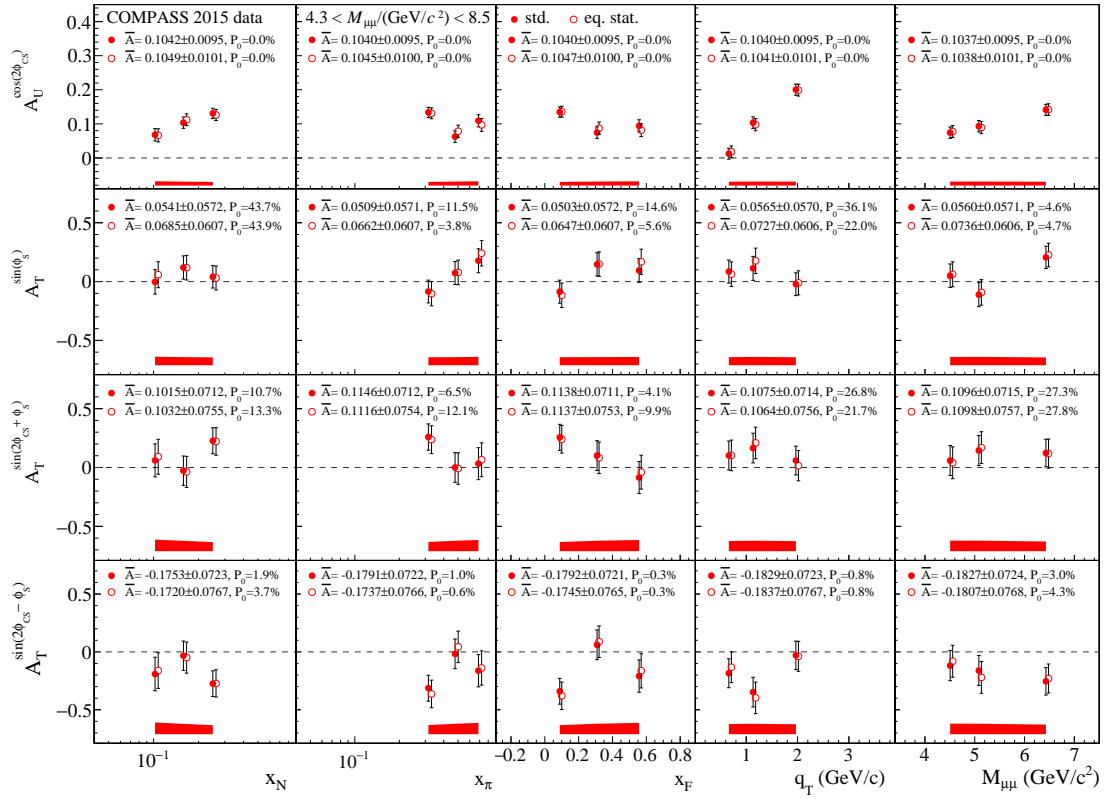
Fig. 4.22 Comparison of standard asymmetries with the ones extracted from "equipopulated" sub-periods.

4.11.4 Stability with respect to target-cuts and other selections.

The possible impact of various selection criteria on the asymmetries was examined. In particular, enhanced target-cuts (shrinking the cells by 10 cm, 5 per each edge) were tested, see Fig. 4.23 (top panel). At the level of statistics, this rejection lead to a decrease by about 20%. The impact at the level of asymmetries is not clear (one would expect a slight increase of the magnitudes of the asymmetries due to reduced dilution, but the statistical precision may not be sufficient to see these effect). The RMS of the corresponding 'pseudo'-pulls for TSAs is about 0.4 σ_{stat}.

Another test was dedicated to study of angular resolution impact. The asymmetries were extracted with enhanced (relaxed) lower q_T-cut which corresponds to improved (worsened) angular resolution. The result is shown in Fig. 4.23 (bottom panel). Following the expectations, in the first bin of q_T the asymmetry goes down to zero (and so does the average asymmetry) at least in case of $A_U^{cos2\varphi_{CS}}$ asymmetry and $A_T^{sin(2\varphi_S-\varphi_{CS})}$ and $A_T^{sin(2\varphi_S+\varphi_{CS})}$ TSAs. The Sivers effect remains unchanged, which could be a statistical effect. The RMS of 'pseudo' pulls is about 0.3 in terms of the statistical error.
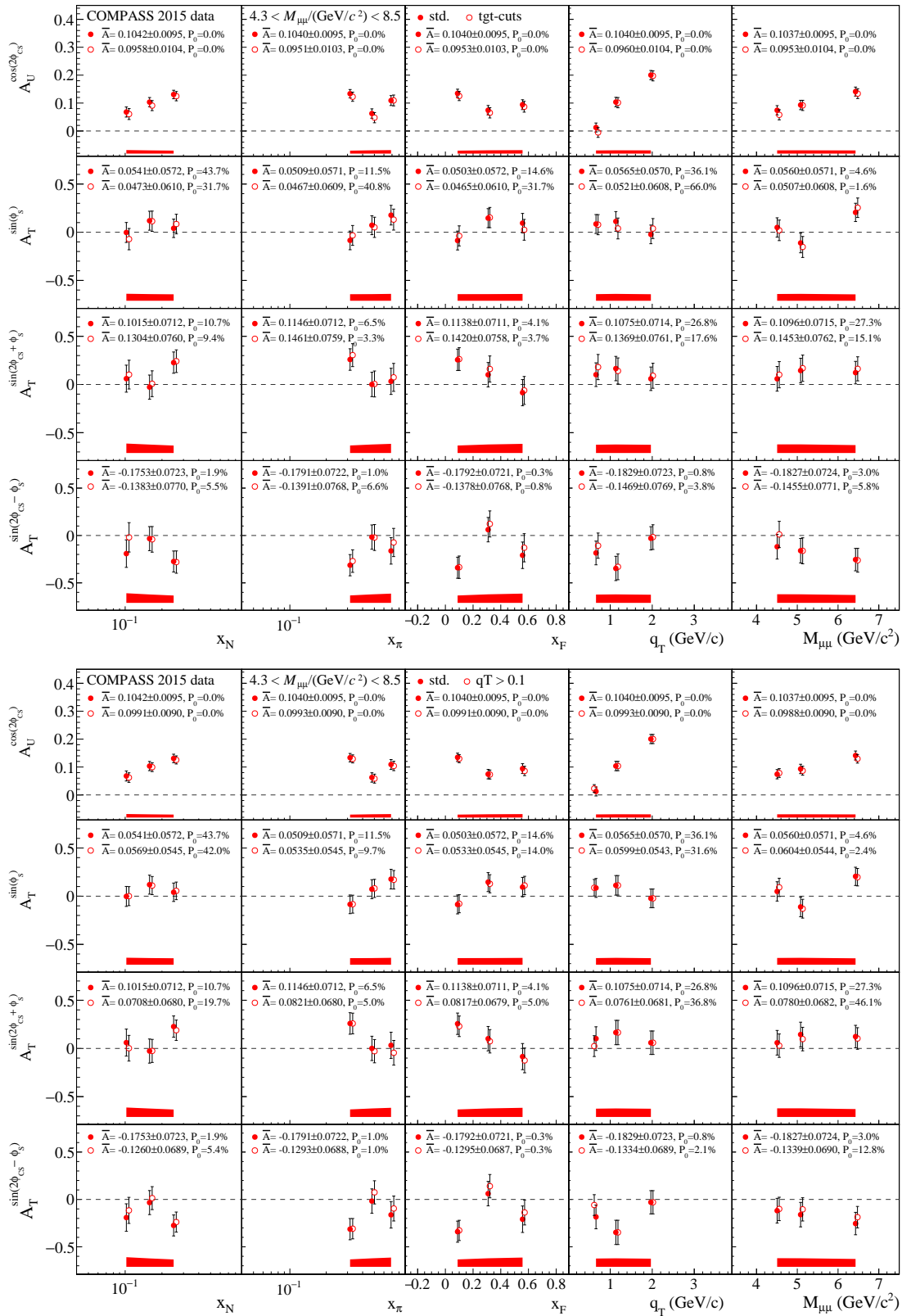
Fig. 4.23 Top panel: impact of enhanced target cuts (-5 cm from each side of both NH$_3$ cells. Bottom panel: impact of the relaxation of the q_T-cut.

Several other tests and comparisons were performed studying the dependence of the asymmetries on various event-selection criteria (track-timing, track-quality, radial-cuts, trigger-selection, angular and kinematic acceptances, etc.). Performed studies did not reveal any critical problems or significant systematic biases. Based on the analysis of all these tests, an upper limit for the systematic uncertainty of $0.4 \times \sigma_{stat}$, which corresponds to the average RMS of corresponding "pseudo-pull" distributions, was assigned to all TSAs.

4.11.5   Right (R), Left (L), Top (T), Bottom (B) - RLTB test.

As another possible source of systematic biases the dependence of TSAs on the dimuon angular variables defined in the spectrometer frame was studied. Such an approach is supposed to be directly sensitive to the possible instabilities of the spectrometer and related acceptance variations. In particular, the studies were performed for the azimuthal angle ϕ_{μ^+} of the antimuon in the laboratory frame[13].

To perform the test, the spectrometer phase space over ϕ_{μ^+} is divided into four segments corresponding to the top, bottom, left and right hemispheres. The asymmetries are extracted separately from each of the four data-samples. Even if there might be non-trivial correlations between different angles and kinematic variables, the asymmetries extracted with adopted methods are not expected to change from one segment to another. In the top panel of Fig. 4.24 the 'twist-2' asymmetries for top, bottom, left and right segments are shown as a function of kinematic variables. In the bottom panels the differences between the left/right and top/bottom asymmetries are shown. In general, the TSAs from different segments are in agreement and differences are compatible with zero. Some systematic deviations are evident for 'R-L' case for the $A_U^{cos2\varphi_{CS}}$ polarisation independent asymmetry, which might be related to possible left-right non-uniformity of the φ_{CS}-acceptance since in EWUML acceptance-corrections are not preformed.

To have an estimation of the systematic errors, absolute values of the left-right and top-bottom asymmetry-differences have been computed for each TSA in each kinematic bin and period and normalized to corresponding statistical errors:

$$A_{left-right} = \frac{|A_{left} - A_{right}|}{\sqrt{\sigma_{left}^2 + \sigma_{right}^2}} \quad , \quad A_{top-bottom} = \frac{|A_{top} - A_{bottom}|}{\sqrt{\sigma_{top}^2 + \sigma_{bottom}^2}}. \quad (4.9)$$

Afterwards, the statistically expected value ~ 0.68 has been subtracted in quadrature from each of them determining a set of $\alpha = \sqrt{A^2 - 0.68^2}$ values for left-right

---

[13]since muon and antimuon angles are strongly correlated, the results do not change if ϕ_{μ^-}-angle is selected instead.
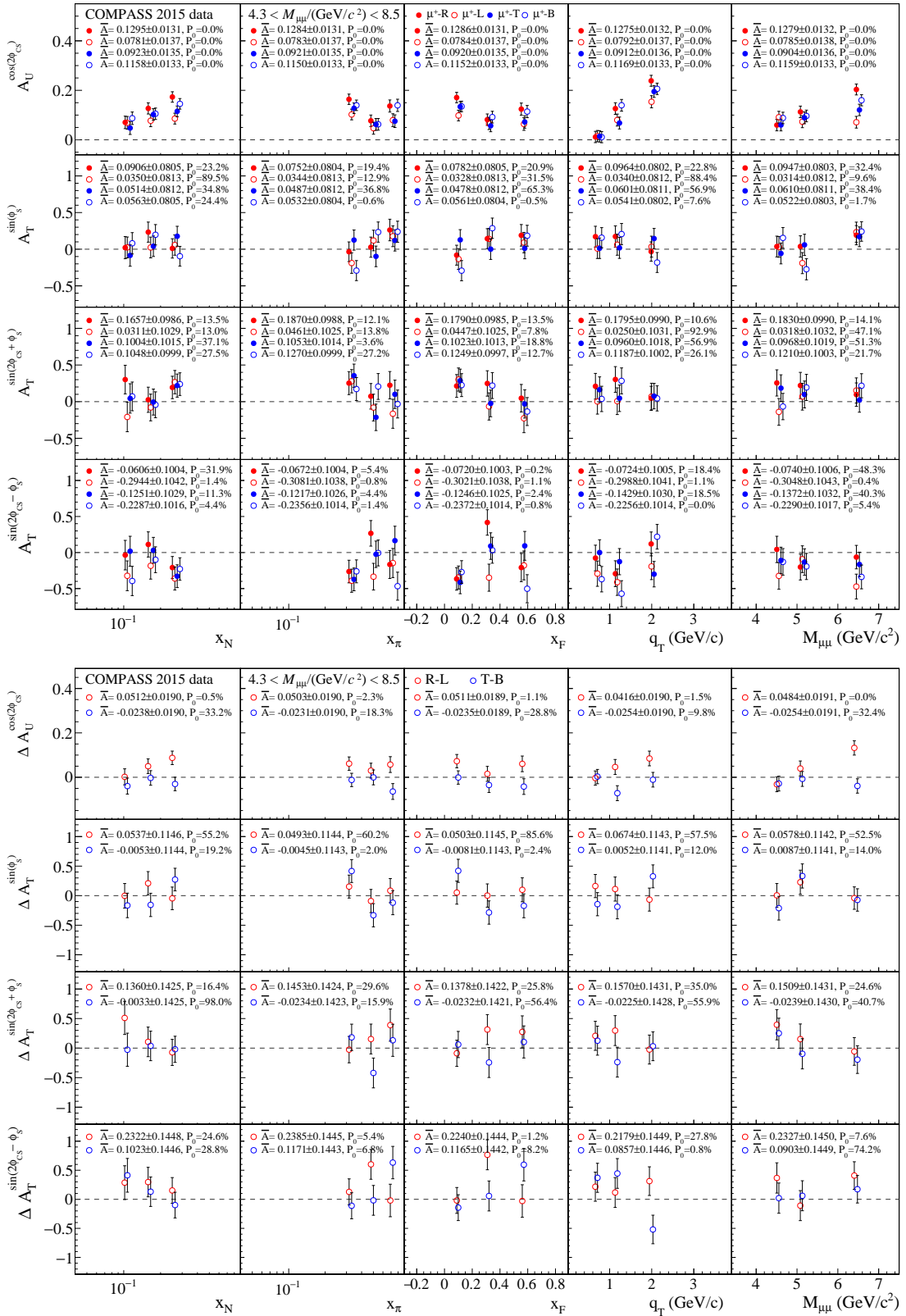
Fig. 4.24 **R**ight, **L**eft, **T**op, **B**ottom (RLTB) test. Top plot: Asymmetries extracted in the RLTB segments. Bottom plot: R-L and T-B asymmetries.

and top-bottom configurations. The systematic errors have been calculated separately for the 'R-L' and 'T-B' configurations as a statistical weighted means of the corresponding α-values over the 9 periods. Obtained estimates of systematic uncertainties are expressed in units of statistical errors. The results are shown in Fig. 4.25.
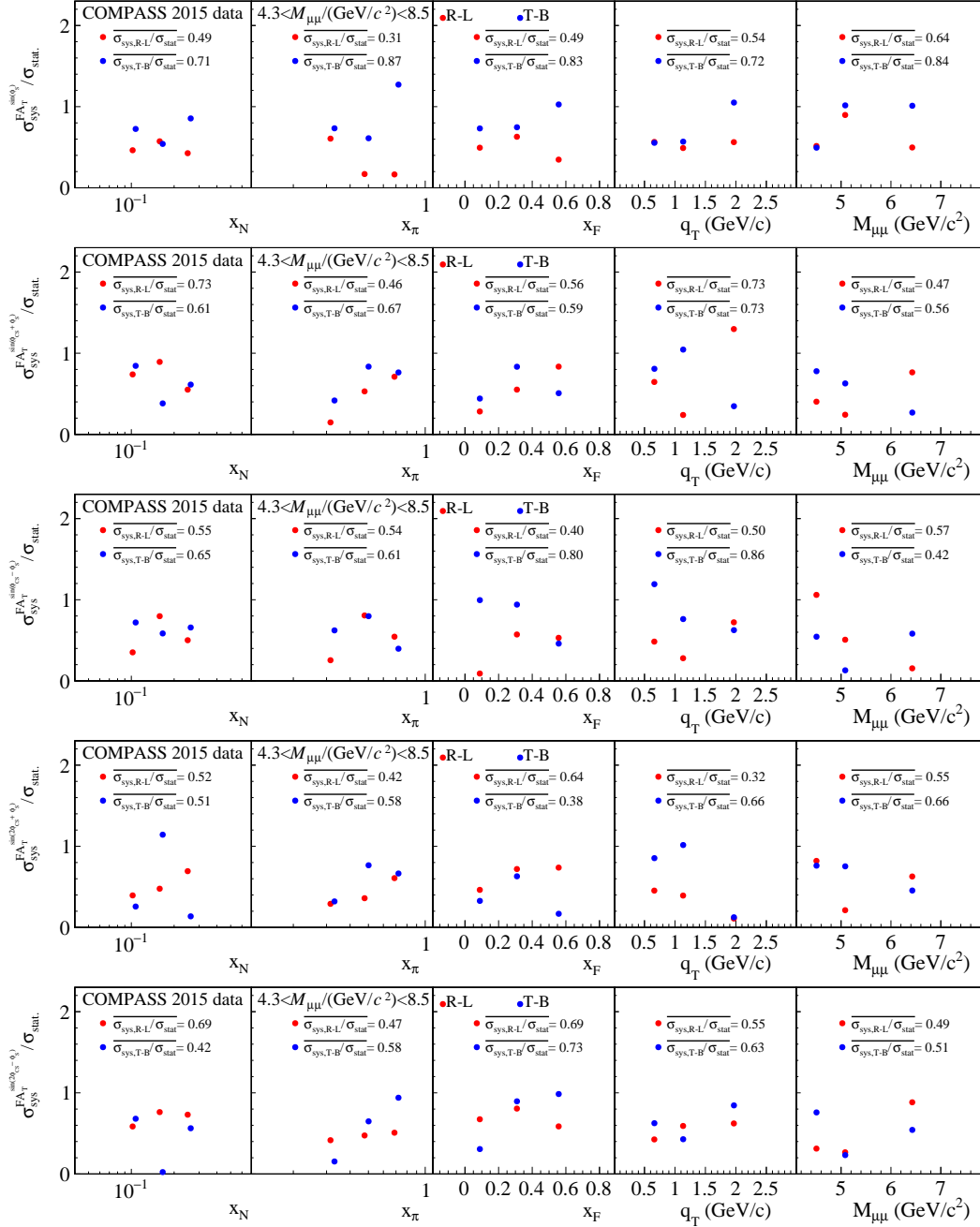
Fig. 4.25 RLTB-test: Systematic uncertainties in terms of the statistical ones.

Since the final asymmetries are built on overall sample and not the segmented one (each segment contributes in overall asymmetry with reduced statistical strength), as estimate for the overall 'RLTB' systematic error the average be-

tween 'R-L' and 'T-B' is taken. The 'RLTB' systematic errors are listed in the following table in the units of the statistical uncertainties:

Segment	$A_T^{sin\varphi_S}$	$A_T^{sin(\varphi_S+\varphi_{CS})}$	$A_T^{sin(\varphi_S-\varphi_{CS})}$	$A_T^{sin(2\varphi_S+\varphi_{CS})}$	$A_T^{sin(2\varphi_S-\varphi_{CS})}$
R-L	0.49	0.59	0.51	0.49	0.58
T-B	0.79	0.63	0.67	0.56	0.57
RLTB	0.6	0.6	0.6	0.5	0.6

Table 4.10 Systematic uncertainties, in terms of $\sigma_{sys}/\sigma_{stat}$, estimated from the RLTB-test.

4.11.6   Estimation of False Asymmetries

The estimation of the systematic uncertainties originated by the residual acceptance variations in each period was performed evaluating the magnitude of various "false asymmetries" (FA). To reduce the statistical fluctuations and increase the precision of the estimations, false asymmetries have been studied on larger samples obtained applying different selections e.g. relaxed target cuts (+10 cm from each edge and relaxed radial cut $R > 2.5\,cm$), relaxed q_T- and mass-cuts, relaxed BDM-cuts etc.

For all tests only UML-estimators have been adopted to guarantee the reliability of the results also for the case of low-statistical samples. Different types of false asymmetries were considered and evaluated, namely:

I) FAs arising even when the Log-Likelihood estimator is defined in a way that physical amplitudes from the two sub-periods cancel out (sign of polarisation is flipped for one of the cells).

II) FAs arising while considering a sample polarised in just one direction. Both cells are sub-divided into two fake sub-cells assigning fake polarisation values and forming two fake sub-periods with polarisation reversal. The asymmetry is extracted for each of the cells using these fake-sub-period configurations. The asymmetries are expected to be equal to zero since the physics cancels out. Possible non-zero effects can be attributed to acceptance variations per cell.

III) FAs appearing while data of each given period has been randomized into two sub-periods. Again two fake-sub-periods have been formed and asymmetries have been extracted treating the data as a normal sample.

IV) In addition, false asymmetries and physics asymmetries have been extracted as functions of laboratory variables such as the z-position of the vertex, target radius R, azimuthal angles of beam and muons, etc.

Results for type-*I* FAs are shown in Fig. 4.26. The approach to compute the final estimate for the systematic uncertainties due to I, II, III and IV is similar to the one adopted for 'RLTB'-case. In units of statistical uncertainties, the systematic uncertainties due to FAs were found to be below 0.6 for all the TSAs.
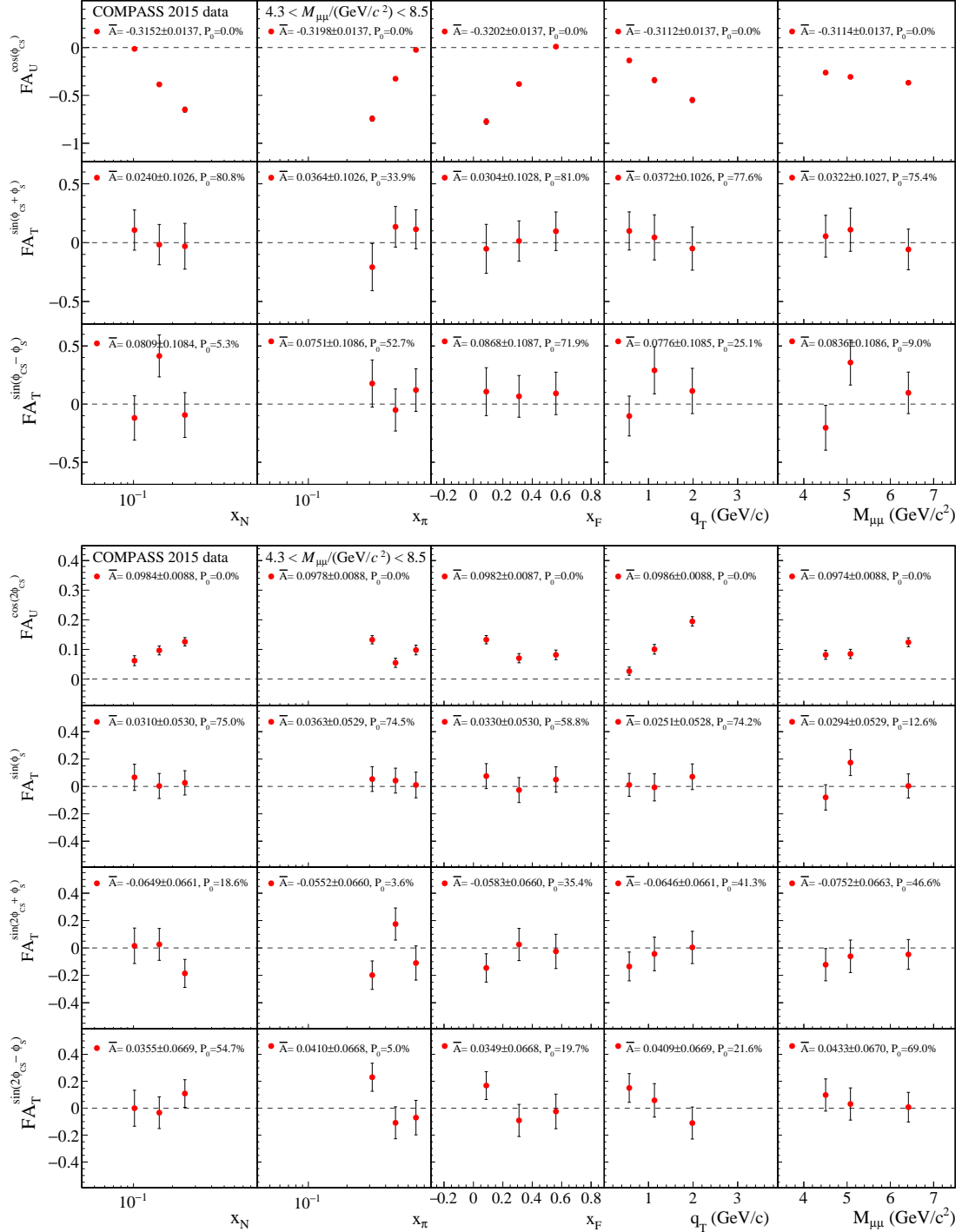
Fig. 4.26 Results for *a*-type FAs. Note that unpolarised asymmetries are not supposed to be affected.
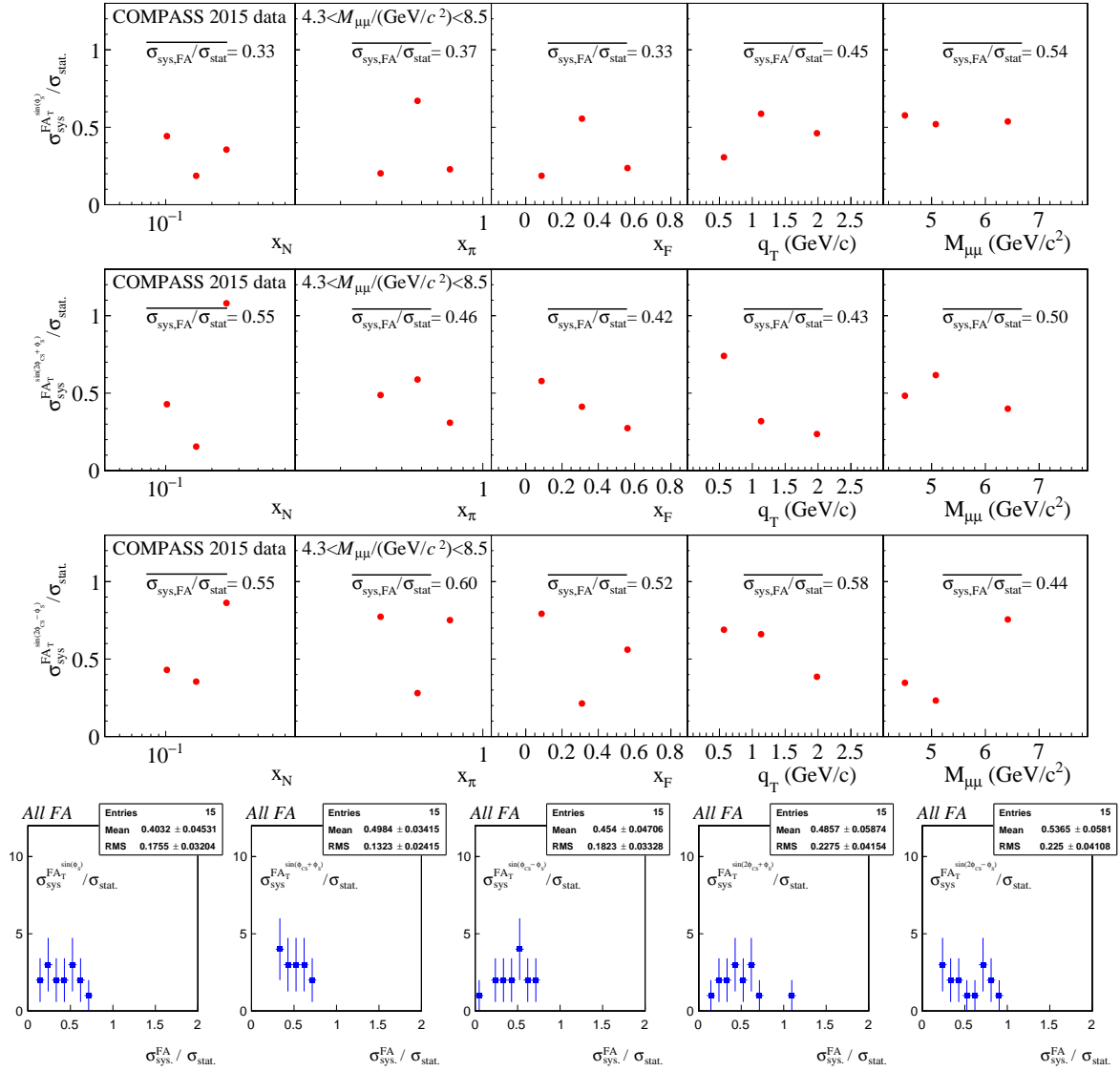
Fig. 4.27 Averaged systematic uncertainties estimated from studies of false asymmetries.

The upper limits for systematics uncertainties estimated from 'RLTB'-test (0.6-0.5 in units of σ_{stat}) and from study of false asymmetries ($0.6 \times \sigma_{stat}$) can be correlated and treating them equally would lead to a double-counting, thus the largest of the two is kept. All uncorrelated systematic uncertainties, that were estimated in the aforementioned systematic studies, are taken into account for the evaluation of the final systematic uncertainty of a certain azimuthal asymmetry. This includes the additive systematic errors of $0.6 \times \sigma_{stat}$ from joined RLTB and FA tests and $0.4 \times \sigma_{stat}$ from other tests, all summed up in quadrature to total uncertainty of $0.7 \times \sigma_{stat}$.

4.12   Results

In this section the final results for transverse-spin-dependent asymmetries are presented. The resulting systematic point-to-point uncertainties are found to be ~0.7 times the statistical error and are shown in the plots in a form of bands. The normalization uncertainties deriving from the uncertainties on the target polarisation (5%), the dilution factor (5%) and the assumption $A_U^1 = 1$ (5%) are not accounted in the systematic bands shown in the figures.

The results for all the asymmetries extracted in the EWUML fit, integrated over the whole phase space, are shown in Fig. 4.28. The average $A_T^{sin\varphi_S}$ is found to be above zero at about one standard deviation of the total uncertainty. The transversity related TSA, $A_T^{sin(\varphi_S-\varphi_{CS})}$, is found to be below zero with a significance $\sim$ two standard deviations. The $A_T^{sin(\varphi_S+\varphi_{CS})}$ asymmetry, related to the nucleon pretzelosity TMD, is measured to be positive with a significance of about one standard deviation. The higher-twist TSAs have relatively larger statistical uncertainties and are found to be compatible with zero.

The LO Asymmetries are shown in Fig. 4.29 (top 4 panels) as a function of x_N, x_π, x_F, q_T and $M_{\mu\mu}$ kinematic variables. Because of large statistical uncertainties, no clear trend can be observed for any of the TSAs. For completeness, also the higher twist asymmetries extracted in the fit are shown if Fig. 4.29 (bottom 3 panels). The presented unpolarised asymmetries cannot be interpreted as physics results, since no acceptance correction was applied in this analysis. Within the EWUML method, the correlations coefficients between different TSAs are also extracted. The correlations for *twist-two* asymmetries are found to be small (below 0.2) and are shown in Fig. 4.30.
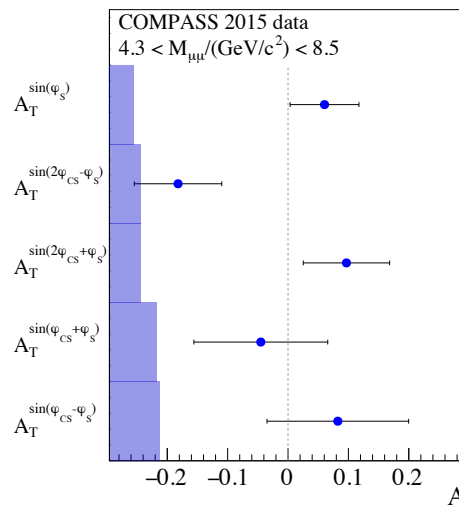
Fig. 4.28 All the extracted TSAs averaged over the whole kinematic range.
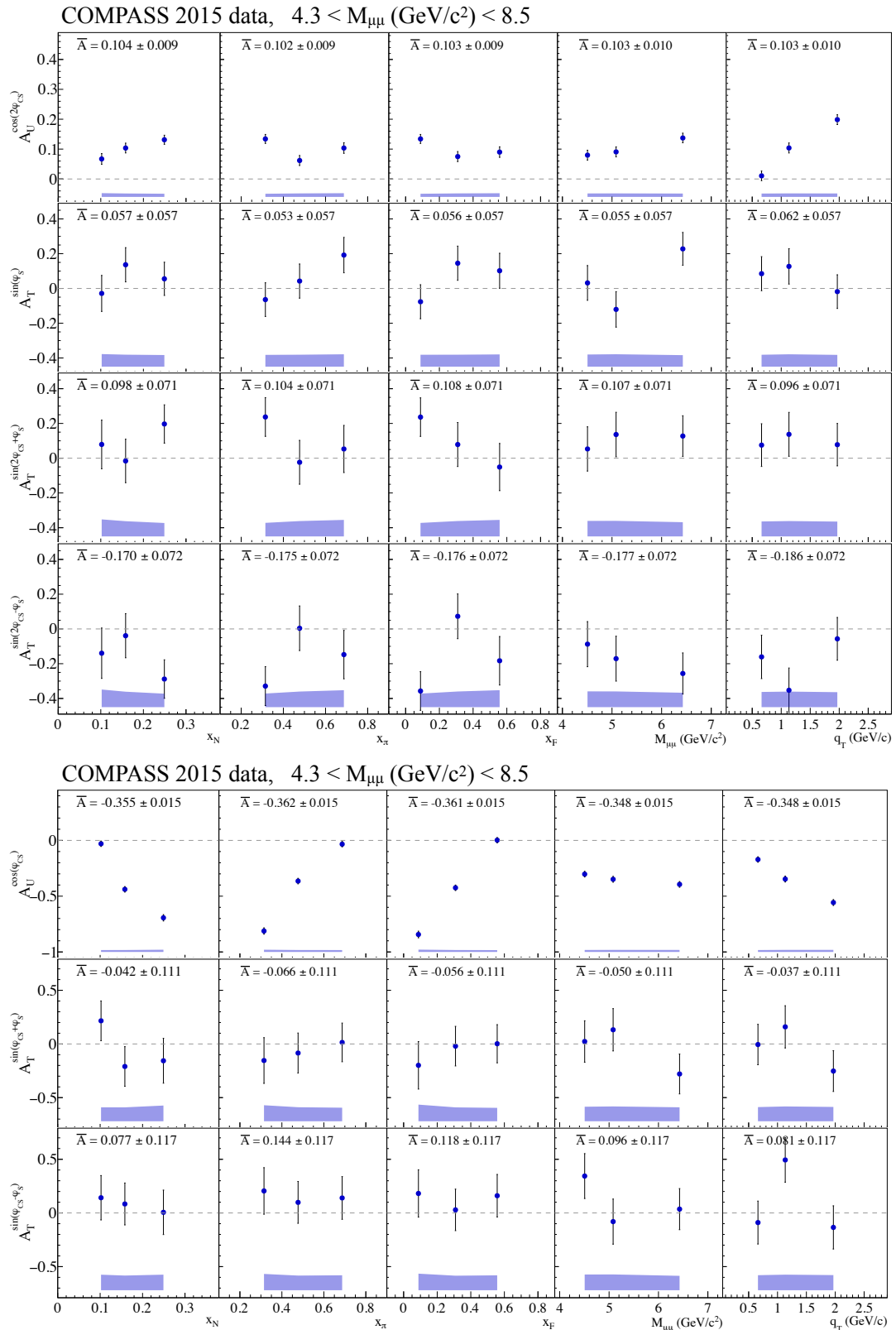
Fig. 4.29 The LO (top 4 panels) and higher twist (bottom 3 panels) TSAs as a function of x_N, x_π, x_F, q_T and $M_{\mu\mu}$ kinematic variables. The bands represent the systematic uncertainties. The results for $A_U^{cos2\varphi_{CS}}$ and $A_U^{cos\varphi_{CS}}$ are not deconvoluted for acceptance contribution and thus cannot be interpreted as a physics result.
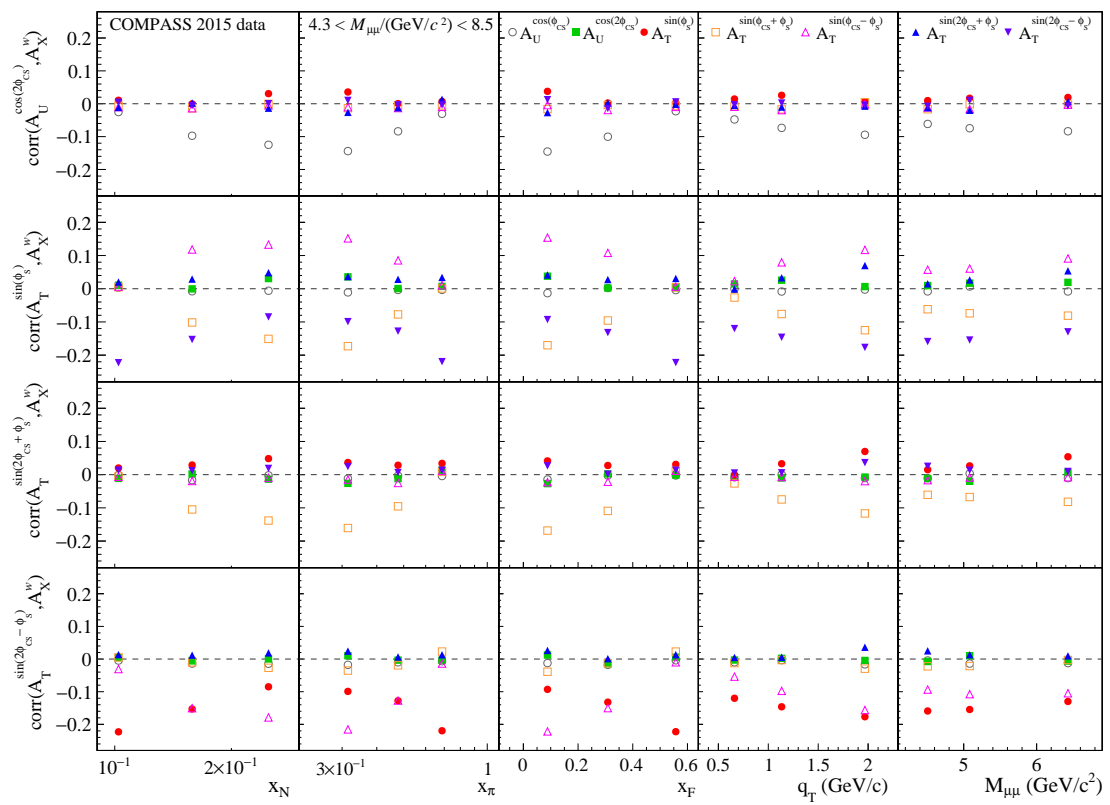
Fig. 4.30 Correlation coefficients for LO asymmetries, extracted while applying the EWUML method.

Chapter 5

Measurement of the q_T-weighted Transverse Spin Dependent Azimuthal Asymmetries in the Drell-Yan process

In this chapter, the analysis of q_T-weighted transverse-spin-dependent asymmetries in the Drell-Yan process is presented. As defined in Chapter 1 (Sec.1.11.1), q_T is the transverse component of the total dilepton momentum q in target rest frame and measurement of the q_T-weighted TSAs (wTSAs) is an alternative and promising way to access nucleon TMD PDFs.

The asymmetries are extracted from the polarised Drell-Yan data collected by COMPASS during the 2015 run. For details on the spectrometer and Drell-Yan data-taking, the reader is referred to the Secs. 4.1,4.2. In the following sections the data selection procedure, the asymmetry extraction method and various systematic studies are presented. The last section is dedicated to the review and discussion of the obtained results. Many aspects of the q_T-weighted TSA analysis were carried out in analogy to the non-weighted case. In order to avoid repetitions, those details will be presented in abbreviated form, concentrating on the specificities of the wTSA studies.

5.1   Event selection

The event selection applied to define the final data sample is identical to the one adopted for the non-weighted TSAs extraction, described in Sec. 4.4 and the only differences are related to the q_T-cuts. In the non-weighted TSA analysis the q_T was required to be between 0.4 and 5 GeV/c, excluding the region with poor azimuthal resolution and the large q_T tail. This cut could not be applied in the case of the q_T-weighted TSAs, where it is essential to perform the integration over the

full q_T range. Nevertheless, it will be demonstrated that the impact on the results is marginal.

The q_T distribution after removing the q_T cuts applied in the non-weighted TSA analysis is shown in Fig. 5.1. A long and partially unphysical tail extending above 5 GeV/c was not reproduced by MC-simulations. This sample contains only 124 events and the impact of this range on the asymmetries is expected to be relatively small, probably with an exception for the $\sin(\varphi_S + \varphi_{CS})$-related asymmetry which is weighted by q_T^3.

While investigating the nature of the very-high q_T events, it was found that they might be affected by specific event-reconstruction issues not reproduced in MC and for some of them even general energy conservation considerations could potentially be violated. A requirement on the sum of the magnitudes of the momenta of the two muons, $P_{\mu^+} + P_{\mu^-} < 190$ GeV/c, was added to the original cut-flow in order to reject part of the tail. The cut imposes the energy conservation considerations[1], requiring the sum of the energy of the two muons to be smaller than the energy available in the initial state. In this way, the q_T spectrum tails are reduced to 20 GeV/c, as it can be seen in Fig. 5.1.
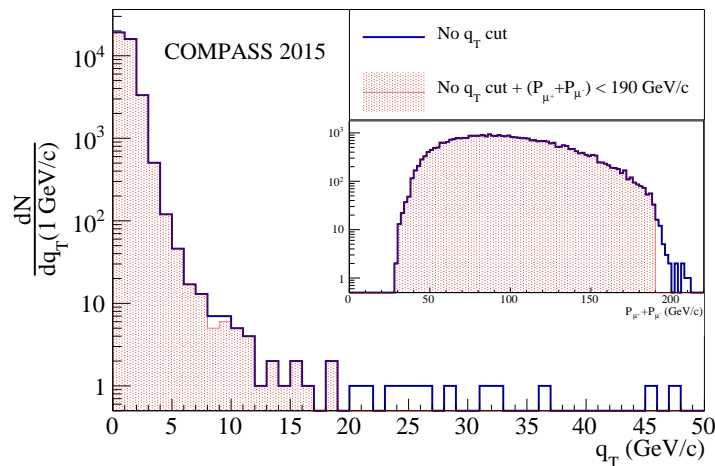
Fig. 5.1 In blue the q_T distribution obtained using the TSAs event selection without the q_T cuts. In red the same distribution obtained requiring in addition $P_{\mu^+} + P_{\mu^-} < 190$ GeV/c. The insert shows the corresponding $P_{\mu^+} + P_{\mu^-}$ distribution.

After this cut, even if more reasonable, the q_T distribution still reaches rather high values. Inspecting various kinematic distributions of these events, they were found to be concentrated mostly at the edges of the two NH_3 cells. Neither this artifact could be reproduced in MC and the events were considered to be not genuine and to be removed from the analysis.

---

[1]Neglecting masses of the particles and the beam momentum spread, not measured

Among the different tests performed, a cut on the transverse momentum of each muon in the laboratory frame $P_{T,\mu^\pm} < 7$ GeV/c was found to be the best option to remove the nonphysical tails. Figs. 5.2,5.3,5.4,5.5 show the correlations between $P_{T,\mu^\pm}$ and q_T in real data and in MC, illustrating the impact of the $P_{T,\mu^\pm}$ cut.
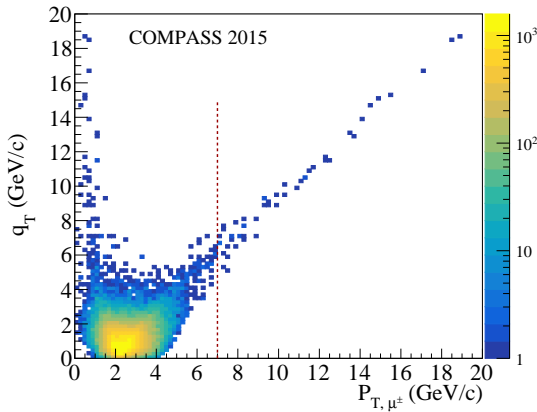
Fig. 5.2 Distribution of q_T vs $P_{T,\mu^\pm}$ for 2015 RD before applying the $P_{T,\mu^\pm} < 7$ GeV/c cut (red dashed line). In this plot each dimuon pair contributes twice, ones for μ^+ and ones for μ^-. The events at high q_T look to be strongly correlated with $P_{T,\mu^\pm}$. This behaviour is not observed in MC (Figs. 5.4,5.5).
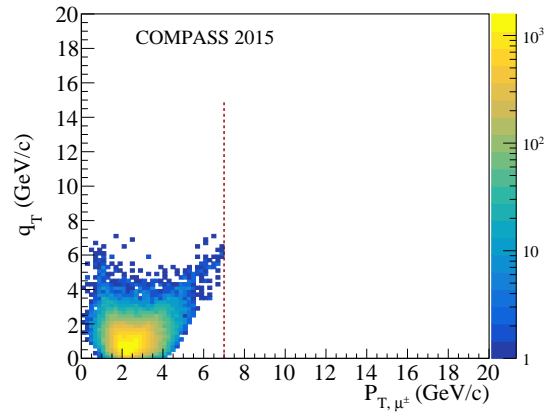
Fig. 5.3 Distribution of q_T vs $P_{T,\mu^\pm}$ for 2015 RD after applying the $P_{T,\mu^\pm} < 7$ GeV/c cut. In this plot each dimuon pair contributes twice, ones for μ^+ and ones for μ^-.The correlated events at high q_T are removed.
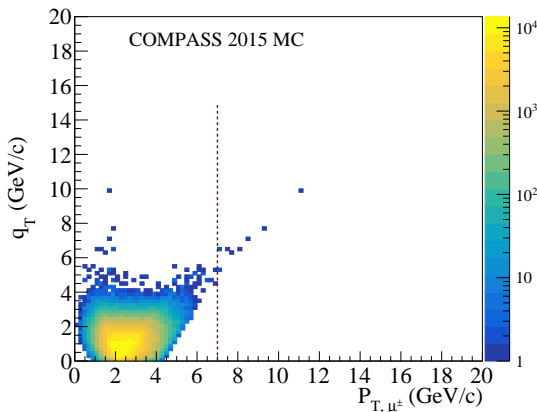
Fig. 5.4 Distribution of q_T vs $P_{T,\mu^\pm}$ for 2015 MC before applying the $P_{T,\mu^\pm} < 7$ GeV/c cut (red dashed line). The k_T tuning adopted for the generation is the same described in Sec. 4.6 and hereafter referred as 'realistic'. In this plot each dimuon enters twice, ones for μ^+ and ones for μ^-.
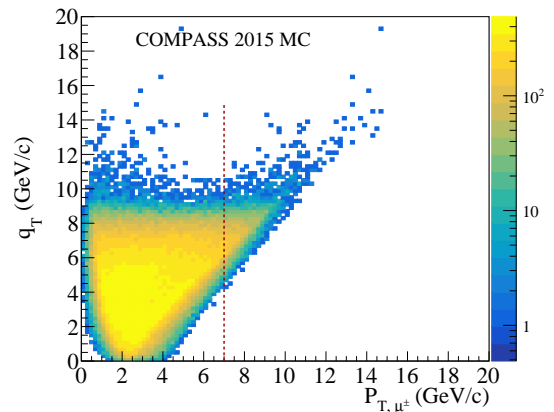
Fig. 5.5 Distribution of q_T vs $P_{T,\mu^\pm}$ for 2015 MC before applying the $P_{T,\mu^\pm} < 7$ GeV/c cut (red dashed line). The k_T tuning adopted for the generation consists in a unrealistically wide distribution, generated for dedicated MC-studies. In this plot each dimuon enters twice, ones for μ^+ and ones for μ^-.

For large q_T one of the muons always has low and the other has large P_T. A similar but less pronounced trend can be observed in the MC simulations presented in Figs. 5.4, 5.5 obtained with 'realistic' and unrealistically wide k_T tunings, respectively. For the former tuning the generated q_T extends up to 4 GeV/c and for the latter up to 8 GeV/c. Both MC and experimental distributions have similar "triangular" shapes. The upper edge of the "triangle" indicates the upper limit of generated q_T. Despite much higher statistics (MC-sample contains factor of 10 more events), the tails in MC-simulation do not extend beyond 5 GeV/c from the highest generated value which, while in real data the tails extend much further from the upper edge of the hypothetical "triangle". These kind of peculiarities are interpreted as another hint towards event-reconstruction problems.

Summarizing, the event selection for the wTSA analysis comprises all the cuts already used for TSAs, except for the q_T cut which was substituted by the requirements, $P_{\mu^+} + P_{\mu^-} < 190$ GeV/c and $P_{T,\mu^\pm} < 7$ GeV/c. The impact of the cut flow on the overall data sample of 2015 is illustrated in Tab. 5.1.

Cut	Events
Dimuon Pairs, $X/X_0 > 30$	1 905 927 808
$M_{\mu\mu} \in [4.3; 8.5]$ GeV/c	1 970 147
Tracks of opposite sign	1 159 349
(LAST2μ ‖ OTLAST) & !MTLAST	868 291
$Z_{\text{first}} < 300$ cm and $Z_{\text{last}} > 1500$ cm	784 379
$t_{\mu^\pm}$ defined	776 643
$\|t_{\mu^+} - t_{\mu^-}\| < 5$ ns	373 081
$\chi^2_{\mu^\pm}/n_{\text{dof}} < 10$	370 054
$P_{\mu^-} + P_{\mu^+} < 190$ GeV/c	219 304
$P_{T,\mu^\pm} < 7$ GeV/c	219 014
Trigger validation	168 939
Bad spills list	137 812
$x_\pi \in [0,1]$ and $x_N \in [0,1]$ and $x_F \in [-1,1]$	137 802
$Z_{PV} \in [-294.5, -239.3] \cup [-219.5, -164.3]$ cm	42 646
$r_{PV} < 1.9$ cm	39 088

Table 5.1 Impact of the event selection criteria on the overall 2015 data sample.

5.2   Binning

The asymmetries have been extracted as a function of four different kinematic variables (x_N, x_π, x_F and $M_{\mu\mu}$) dividing corresponding ranges into three bins. The bin-limits are the same as for non-weighted TSAs and can be found in Tab. 4.9. In

addition, the TSAs were extracted from the entire sample without applying any binning (hereafter referred to as "integrated" wTSAs). Note that the extraction in q_T bins was avoided because the q_T-weighted TSAs require the integration over the whole q_T range.

5.3 Extraction of the q_T weighted asymmetries

The wTSAs are extracted making use of the modified double ratio method [202]. The extraction is carried out separately in each of the nine data-taking periods and then the statistical weighted average TSA is built.

In adopted notations, $N_{cp} = N_{cp}(\Phi)$ represents the yield of DY events in a given cell $c = U, D$, sub-period $p = 1, 2$ (corresponding to spin configuration of the cells $\uparrow\downarrow, \downarrow\uparrow$) and Φ bin[2]. To apply the double ratio method the range of the azimuthal angle Φ was divided into 8 bins. In other COMPASS SIDIS analyses 16 bins were usually adopted but, given the low statistics of the DY measurements with respect to the SIDIS case, a lower number of bins was chosen to minimise the impact of statistical fluctuations on the number of entries $N_{cp}(\Phi)$ and to justify the usage of gaussian errors. Looking at the values of $N_{cp}(\Phi)$ obtained using different binnings for Φ, the configuration with 8 bins was found to have $N_{cp}(\Phi) > 5$ and in most cases $N_{cp}(\Phi) > 20$.

$N_{cp}^W = N_{cp}^W(\Phi)$ stands for the weighted event count, i.e. the sum of event weights $W = W_\Phi$ in the given bin. Within this formalism, the modified double ratio is defined as

$$R_{DM}^W(\Phi) = \frac{N_{U1}^W N_{D2}^W - N_{U2}^W N_{D1}^W}{\sqrt{(N_{U1}^W N_{D2}^W + N_{U2}^W N_{D1}^W)(N_{U1}N_{D2} + N_{U2}N_{D1})}}. \tag{5.1}$$

Using the so-called *reasonable assumption* defined for the ratio of the acceptances $a_{U1}(\Phi)/a_{D1}(\Phi) = a_{U2}(\Phi)/a_{D2}(\Phi)$ and assuming that the asymmetries are small (the size of raw TSAs in average is about 0.01), one can derive the following approximation:

$$R_{DM}^{W_\Phi}(\Phi) \approx 2\tilde{D}_\Phi \langle f_D \rangle \langle P_T \rangle A_T^{\sin\Phi W_\Phi} \sin\Phi, \tag{5.2}$$

where the average target polarisation $\langle P_T \rangle$ and dilution factor $\langle f_D \rangle$ are computed over the two cells and sub-periods. All the details on the evaluation of the target polarisation P_T and the dilution factor f can be found in Sec. 4.8 and Sec. 4.7

---

[2]In this case, Φ represents the generic physics angle analysed using the double ratio. For the specific case of DY, $\Phi \in \{\varphi_S, \varphi_S - \varphi_{CS}, \varphi_S + \varphi_{CS}\}$.

respectively. As in the non-weighted analysis, the dilution factor of the events originating from the upstream cell is multiplied by a correction factor 0.95, which is

$$c_U = r_{U \to U} - r_{D \to U}, \tag{5.3}$$

where $r_{c_1 \to c_2}$ is the fraction of events originating from one cell and being reconstructed in the other. The analogous correction factor for the downstream cell is 0.91. The factor $\tilde{D}_\Phi$ results from the integration of the depolarisation factors in the cross-section

$$\tilde{D}_{\varphi_S} = 1, \qquad \tilde{D}_{(2\phi \pm \varphi_S)} = \frac{\int d \cos \theta \, a(\theta) \sin^2 \theta}{\int d \cos \theta \, a(\theta) (1 + \cos^2 \theta)} = \frac{1 - \langle \cos^2 \theta \rangle}{1 + \langle \cos^2 \theta \rangle}, \tag{5.4}$$

where $a(\theta)$ is the acceptance[3] in θ and the averaging runs again over the two cells and sub-periods. The uncertainty associated to the modified double ratio can be expressed as

$$\sigma_{R_{\mathrm{DM}}^W}^2 = \frac{\sum_{c,p} \sigma_{N_{cp}^W}^2}{\sum_{c,p} N_{cp}} \frac{4 \left(N_{U1} N_{D2} N_{U2} N_{D1} \right)^2}{\left(N_{U1} N_{D2} + N_{U2} N_{D1} \right)^4} \sum_{c,p} \frac{1}{N_{cp}}, \tag{5.5}$$

where $\sigma_{N_{cp}^W}^2 = \sum_j W_{cpj}^2$ is the sum of squared weights of the events in the given angular bin.

Each q_T-weighted TSA is extracted by fitting the modified double ratios, calculated in the 8 Φ-bins, with the mean value of the Eq. 5.2 over each Φ-bin (to take into account the finite bin width $\Delta\Phi = 2\pi/8$)

$$\langle R_{\mathrm{DM}}^{W_\Phi} \rangle (\Phi_i) = \frac{1}{\Delta\Phi} \int_{\Phi_i - \frac{\Delta\Phi}{2}}^{\Phi_i + \frac{\Delta\Phi}{2}} d\varphi \, R_{\mathrm{DM}}^{W_\Phi}(\varphi) = \frac{2}{\Delta\Phi} \sin \frac{\Delta\Phi}{2} R_{\mathrm{DM}}^{W_\Phi}(\Phi_i). \tag{5.6}$$

The mean value over the bin is equal to the value at the bin centre times a correction factor, which is close to 1.

5.4 Systematic studies

General conclusions of data quality and stability tests as well as results of systematic studies performed for non-weighted TSA analysis (see Secs. 4.3, 4.11) stay valid also for wTSA case. In particular, for q_T-weighted asymmetries no additional data quality checks were done. Several tests to estimate the systematic uncertainties specific for wTSAs were performed. These include the study of

---

[3]The factorisation of the acceptance $a_{cp}(\Phi, \theta) = a_{cp}(\Phi) a(\theta)$ is assumed implicitly.

statistical compatibility of asymmetries measured in the nine periods, the estimation of false asymmetries and the estimation of possible biasses introduced by the q_T-event-migration. The contributions found to be significant were added in quadrature to get the final systematic uncertainty. The details and results of the aforementioned tests are reviewed in the following. For tests that are common between TSA and wTSA analyses, the reader is referred to the previous Chapter. 4 and Secs. 4.3,4.11.

5.4.1 Compatibility of the periods

The compatibility between the periods was checked using two methods. The first is analogous to the TSA-case and is based on the analysis of the pull-distributions ΔA_i built for each asymmetry (see Sec. 4.11 for details). The evaluated pulls are defined as

$$\Delta A_i = \frac{A_i - A}{\sqrt{\sigma_i^2 - \sigma^2}}. \tag{5.7}$$

Fitting the pulls with a gaussian function (see Fig. 5.6) all the distributions were found to have gaussian widths close to 1, as expected. The pulls are somewhat narrower for the nucleon transversity TMD PDF related wTSA, $A_T^{sin(2\varphi_S - \varphi_{CS})\frac{q_T}{M_\pi}}$, which was the case also for the corresponding TSA (see Sec. 4.11).
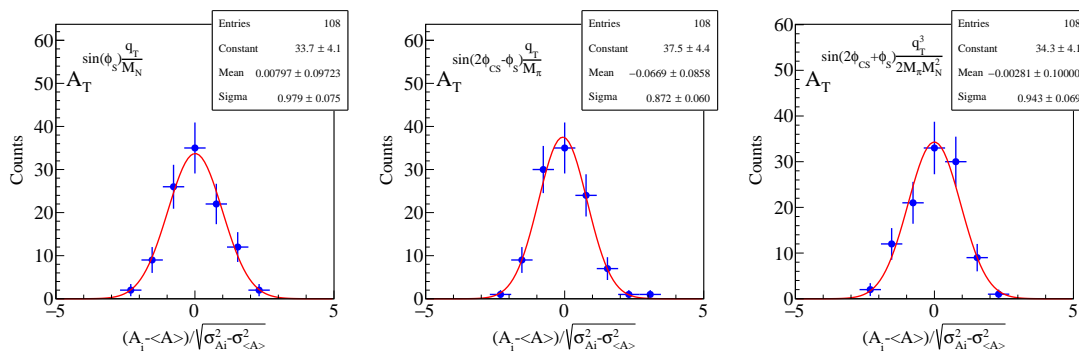
Fig. 5.6 Pulls for the q_T-weighted TSAs in the nine periods of 2015, fitted with normal distributions. Each histogram has 9 (periods) × 4 (kinematic variable) × 3 (kinematic bins) = 108 entries. All the σ of the gaussian fits are smaller than 0.98.

Further to the pull histograms, the asymmetries extracted separately from each of the nine data-taking periods are shown in Fig. 5.7.
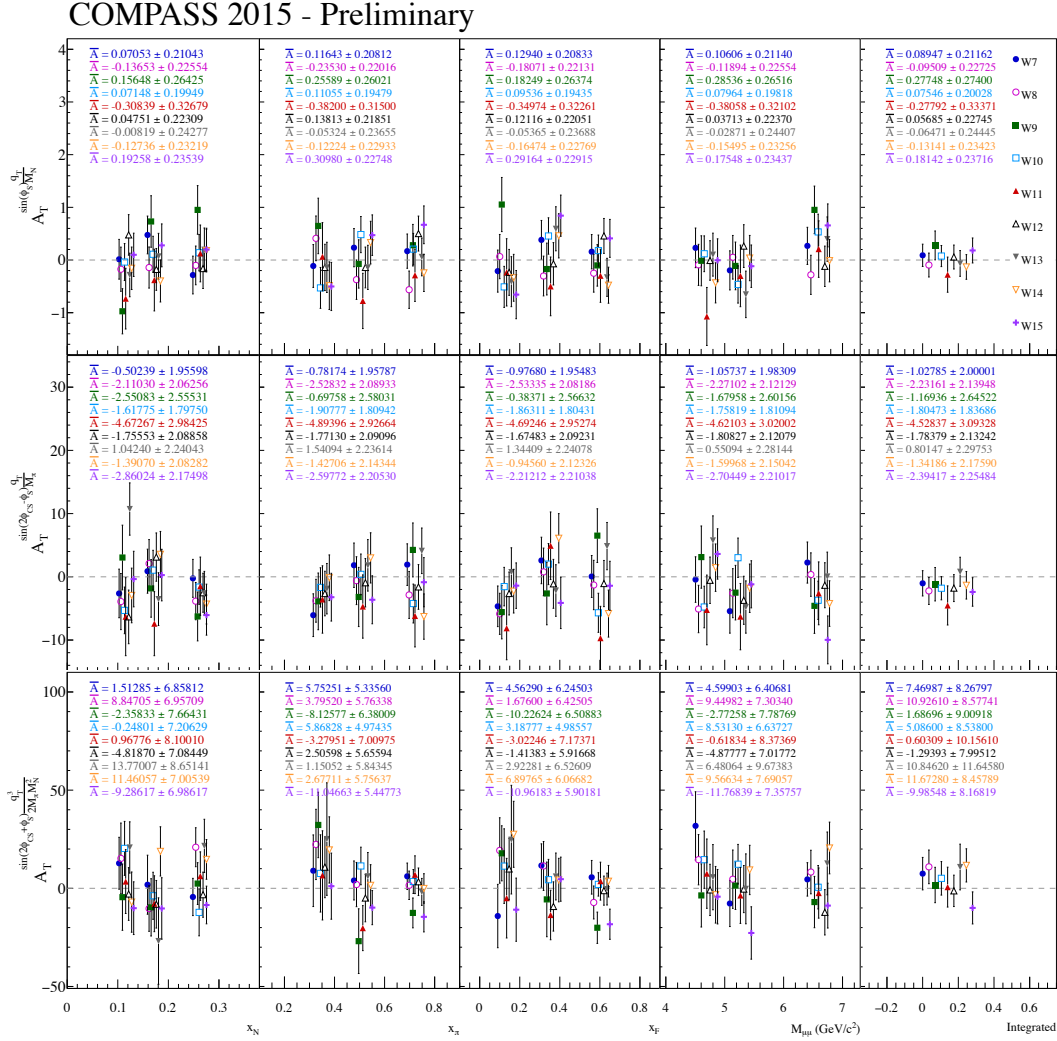
Fig. 5.7 The wTSAs extracted in each of the nine periods of 2015 data taking. From top to bottom, the q_T weighted Sivers, Transversity and Pretzelosity related asymmetries. The points are staggered in abscissa for a better readability.

The second period-compatibility method is based on the calculation of the reduced χ^2 of the weighted averages of the asymmetries

$$\frac{\chi^2}{n_{\text{df}}} = \frac{1}{n_{\text{per}} - 1} \sum_i \frac{(A_i - A)^2}{\sigma_i}. \tag{5.8}$$

The results of this test are shown in Fig. 5.8. One can see that obtained values are mostly around 1 or slightly below. There are three exceptions that reach value of about 1.6 (such χ^2 occurs with a probability $\sim 20\%$).

The conclusion driven from these two tests was that, similar to the TSA-case, the asymmetries extracted from each week are well compatible. Thus the

contribution to the total systematic uncertainty from this source was assumed to be zero.
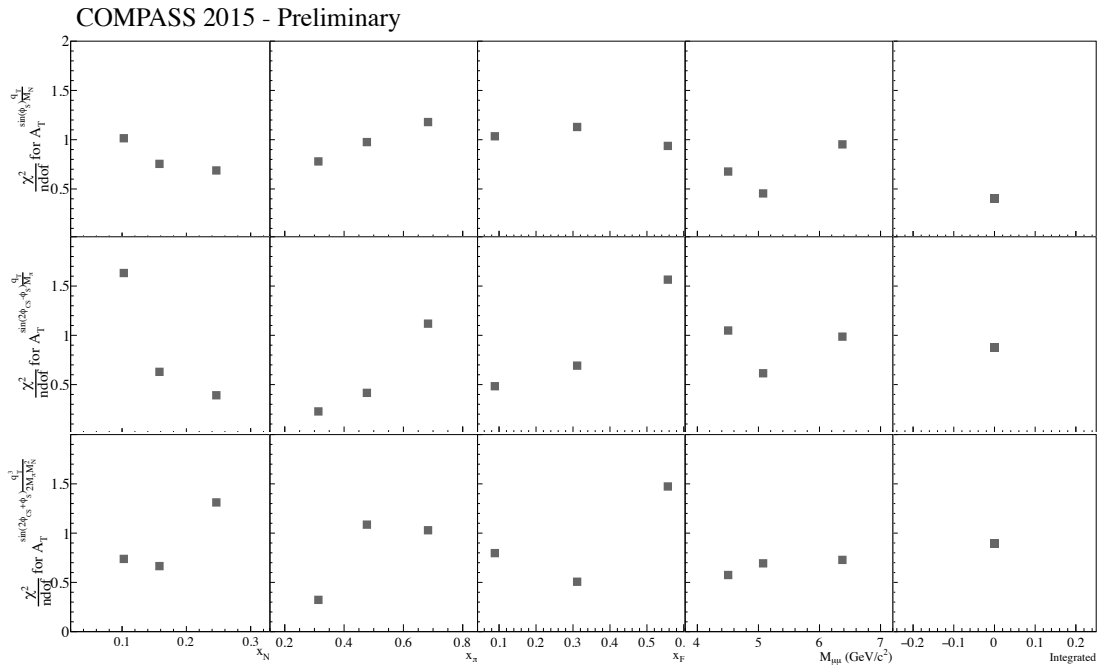
Fig. 5.8 The reduced χ^2 of the error-weighted averages of the asymmetries over the nine periods.

5.4.2   False asymmetries (FA)

This study is dedicated to the estimation of the impact of possible residual azimuthal acceptance variations that can potentially occur in the spectrometer during the data-taking. The method is based on the study of the false asymmetries used to monitor the acceptance cancellation in the modified double ratio (defined in Eq. 5.1). Similarly to the non-weighted TSAs case, data with different polarisations were mixed-up in a way that physics asymmetries are supposed to cancel. Possible non-zero azimuthal modulations would then indicate residual acceptance variations between the cells that lead to a failure of the *reasonable assumption.*

   Two different mixing techniques were used. The first consisted in randomly reshuffling the events between the two sub-periods in each data-taking period. After such mixing, if the statistics is reasonably balanced between the sub-periods, the average polarisation in each sub-period and target cell must be very small. Hence, the physics TSA are expected to be close to zero and non-zero modulations can be attributed to the acceptance instabilities and are called "False Asymmetries" (FAs).

The event distribution in sub-periods is shown in Fig. 5.9 while the event mixing from different sub-periods is illustrated by Fig. 5.10. The event selection is applied on the randomised data and, afterwards, the asymmetries are extracted using the same extraction method as in case of physics wTSAs. The resulting false asymmetries are shown in Fig. 5.13. They are found to be compatible with zero within the statistical accuracy.

The second type of the mixing is done within the two target cells. Each of them is divided into two halves, which are then combined forming fake "inner" and "outer" cells as illustrated in Figs. 5.11 and 5.12). The average polarisation in each cell is not exactly zero in this case, but it is expected to cancel out in the modified double ratio. Also in this case, the modified data is treated in the same way as the usual physics sample and the asymmetries are extracted using the standard method. Resulting false asymmetries are shown in Fig. 5.13. Also in this case they are found to be compatible with zero within the uncertainties.
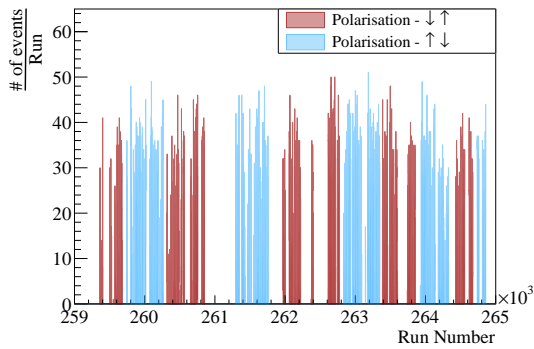
Fig. 5.9 Illustration of the swap of polarisation configurations of the two NH$_3$ cells ($\downarrow\uparrow$ or $\uparrow\downarrow$) along the year.
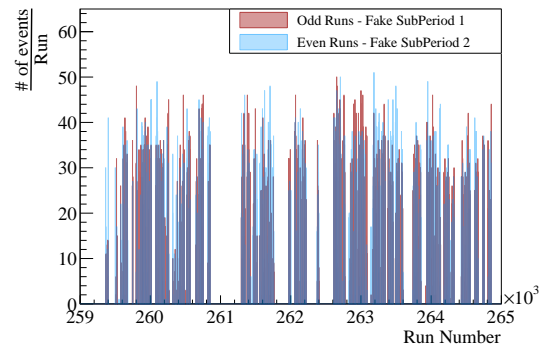
Fig. 5.10 Division of 2015 runs into *fake* sub-periods used for the study of the false asymmetries. All odd runs were packed into $\downarrow\uparrow$ sub-period and the even ones into another ($\uparrow\downarrow$).

After extracting the FAs arising in the weighted analysis, the question to be addressed is to what extent their non-zero values can be attributed on one hand to statistical fluctuations and on the other hand to real systematic effects. The approach adopted was similar to the one already used for the non-weighted TSA analyses see Sec. 4.11), calculating for each false asymmetry FA, each bin, and data-taking period i:

$$
\begin{aligned}
\left(\frac{\sigma_{\text{syst}}}{\sigma_{\text{stat}}}\right)_i &= 0 & \text{if } |\text{FA}_i| < 0.68\,\sigma_{\text{stat},i}, \\
\left(\frac{\sigma_{\text{syst}}}{\sigma_{\text{stat}}}\right)_i &= \sqrt{(\text{FA}_i)^2/\sigma_{\text{stat},i}^2 - 0.68^2} & \text{otherwise.}
\end{aligned}
\tag{5.9}
$$
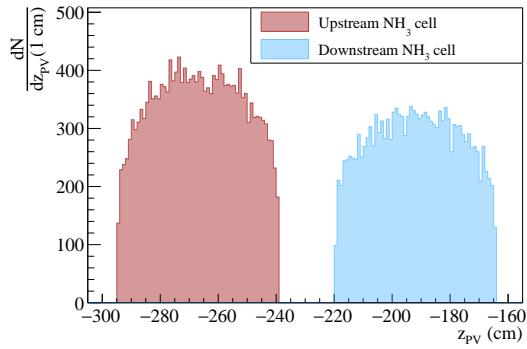
Fig. 5.11 Distribution of the events in the *true* target cells.
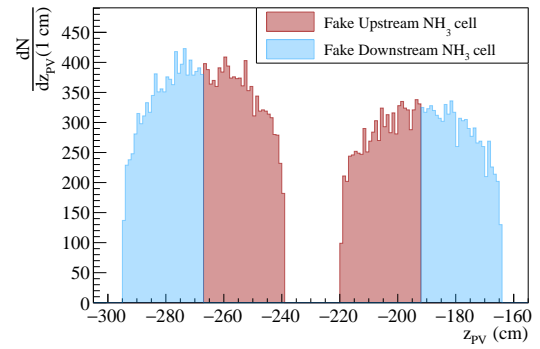
Fig. 5.12 Distribution of the events in the *fake* target cells defined for the study of the false asymmetries.
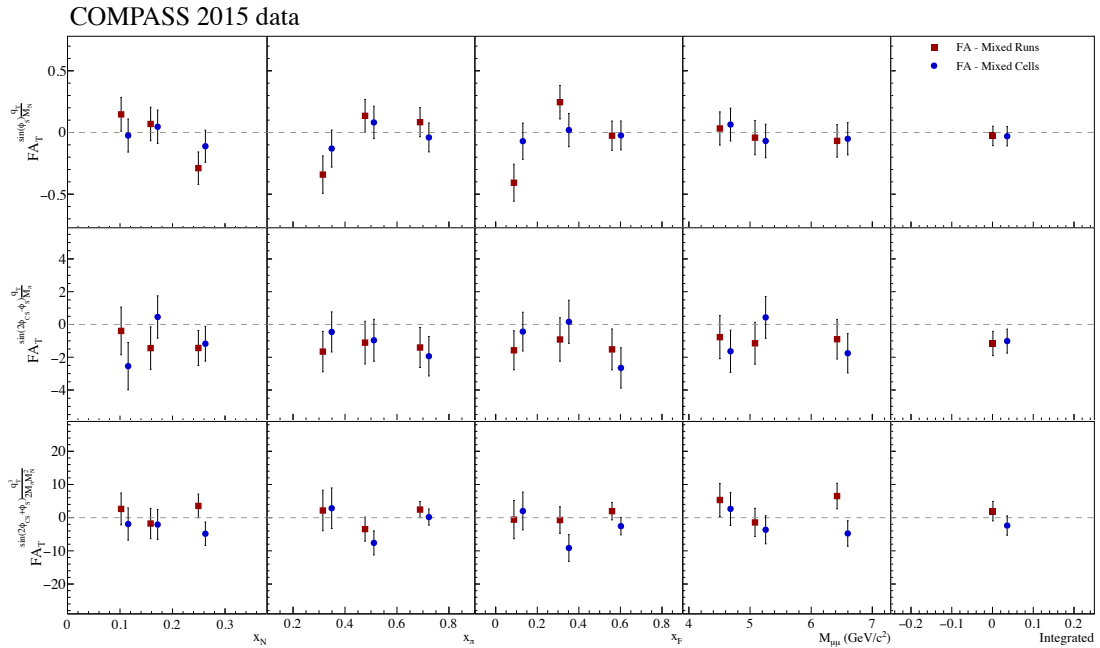
Fig. 5.13 Extracted false asymmetries.

If the only source of FA_i are the statistical fluctuations, the variable should be normally distributed around zero with width $\sigma_{\text{stat},i}$. The probability that $|FA_i| > 0.68\,\sigma_{\text{stat},i}$ is then 50%. Using Eq. 5.9, it was decided to conservatively assume that such a case is an indication of a possible systematic effect. The systematic error of the statistically weighted average of the asymmetries over the data-taking periods is obtained taking the statistically weighted average of the systematic

errors over the periods

$$\frac{\sigma_{\text{syst}}}{\sigma_{\text{stat}}} = \frac{\sum_i \left(\frac{\sigma_{\text{syst}}}{\sigma_{\text{stat}}}\right)_i \sigma_{\text{stat},i}^{-2}}{\sum_i \sigma_{\text{stat},i}^{-2}}. \tag{5.10}$$

The ratios of systematic and statistical errors evaluated for each kinematical bin using Eq. 5.10 are plotted for both false asymmetries in Fig. 5.14. For each point the greater of the two values is taken. Afterwards, an average over kinematic bins is made. The two contributions are not added in quadrature, since the two FAs are not completely independent.
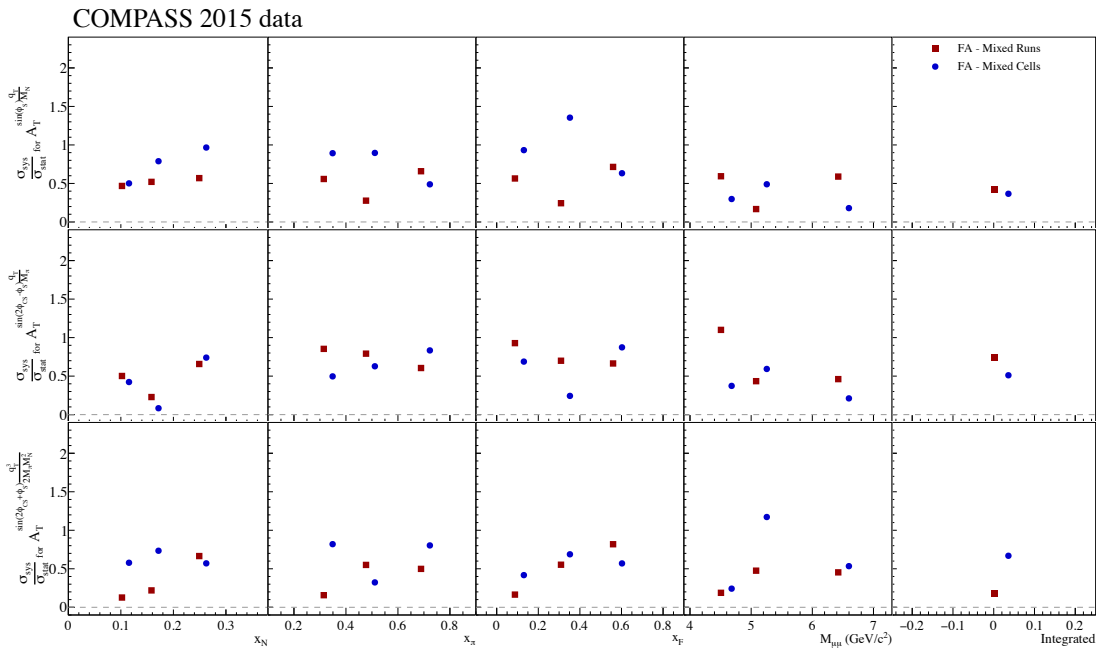
Fig. 5.14 The systematic uncertainty arising from the false asymmetries. For each point, the larger value is taken.

5.4.3 Event-migration in the q_T distribution

While extracting from generated MC-sample the kinematic and azimuthal acceptance distibutions[4] for the COMPASS 2015 DY setup, it was observed that q_T-acceptance grows towards higher values of q_T as shown on Fig. 5.15. Such behaviour was explained by the finite resolution of the experimental setup which results in smearing of the observables. This effects become more evident for non-flat distributions. Indeed, generated q_T distribution rapidly decreases going

---

[4]using the same MC settings described in Sec. 4.6.

towards higher values and only a small fraction of the events populate the distribution in the region of $q_T > 2.5$ GeV/c. However, while looking at the events after the reconstruction, this range will receive additional contribution from the events generated in lower q_T regions which would migrate towards larger values because of smeared q_T in the reconstruction. Due to the slope of the q_T distribution, there will be not enough events to compensate this migration in the opposite direction. Two test have been performed to illustrate this explanation. The first consisted of building the acceptance using the true value of generated q_T associated with the given reconstructed event, to disentangle the geometrical acceptance from the experimental smearing. The results of this test are shown in Fig. 5.17. The second test required a production of MC-sample with special k_T tuning allowing to produce nearly flat q_T distribution in a wider range $[0, 9]$ GeV/c (see Fig. 5.18). Acceptance distribution obtained for this sample is shown in Fig 5.16. It looks rather flat and smearing related growth can be noticed only at the upper edge of the distribution.
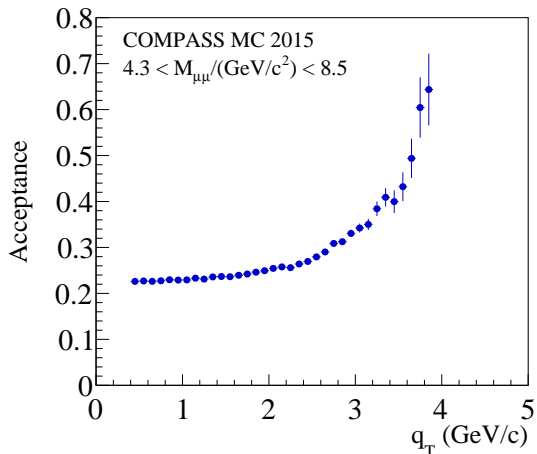
Fig. 5.15 The acceptance as function of q_T evaluated using MC-data generated with the settings presented in Sec. 4.6
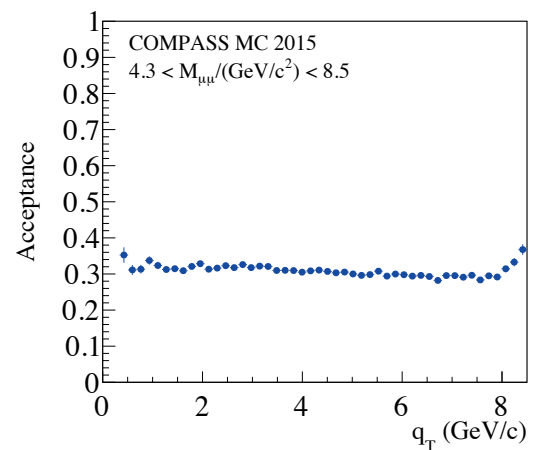
Fig. 5.16 The acceptance as function of q_T evaluated using MC-data generated with a wider k_T tuning, covering the range $[0, 9]$ GeV/c.

The migration effects observed so far in the q_T distributions required further checks on the q_T-weighted asymmetries, since a migration towards higher q_T results in a systematic shift of the weight defined in the analysis. To recover the true distribution, a histogram unfolding method based on a Bayesian approach was implemented [203]. The next section is devoted to the detailed description of this procedure.
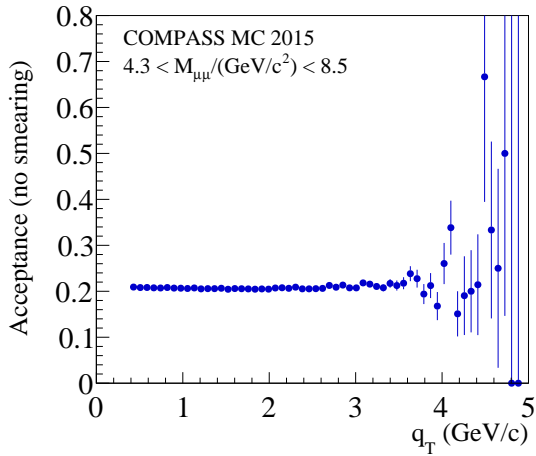
Fig. 5.17 The acceptance as function of q_T evaluated using MC-data generated with the settings presented in Sec. 4.6. The difference w.r.t. Fig. 5.15 is that to accepted events generated q_T values are assigned instead of reconstructed (smeared) ones.
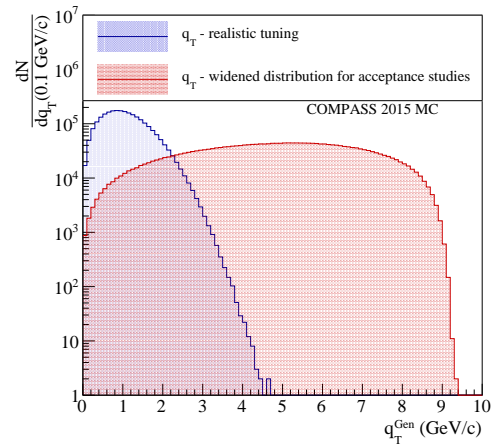
Fig. 5.18 The two generated q_T distributions for systematic studies: realistic k_T tuning and widened k_T tuning for acceptance studies.

5.5 Unfolding of the q_T distribution

5.5.1 Bayesian unfolding method

In this study the approach described in Ref. [203] was adopted. It is suitable for multi-dimensional distributions and arbitrary binning of both generated and reconstructed quantities, which are called causes and effects, respectively. The final goal of the exercise is to obtain the n_{true}-binned distribution of $q_{\text{T,true}}$. In the chosen notation scheme, the cause C_i represents the occurrence of an event in the bin $i = 1, 2, ..., n_{\text{true}}$. In addition to the physics causes also the background is accounted as a special cause C_0. The result of the measurement is a $n_{\text{rec.}}$-binned $q_{\text{T,rec.}}$ distribution. Under the assumption that initial probabilities of the causes $P(C_i)$ (i.e. the true q_T distribution) and the conditional probability of the ith cause to produce the jth effect $P(E_j|C_i)$ are known, one can use the Bayes formula

$$P(C_i|E_j) = \frac{P(E_j|C_i)P(C_i)}{\sum_{k=0}^{n_{\text{true}}} P(E_j|C_k)P(C_k)} \tag{5.11}$$

to quantify the improvement of knowledge on $P(C_i)$ having the observation of E_j. Knowing $P(C_i|E_j)$ and having observed $n(E_j)$ events for each effect E_j (in each $q_{\text{T,rec.}}$ bin), the expected number of events for the causes (in the $q_{\text{T,true}}$ bins)

is given by:

$$\hat{n}(C_i)|_{\text{obs.}} = \frac{1}{\varepsilon_i} \sum_{j=1}^{n_{\text{rec.}}} n(E_j)P(C_i|E_j). \qquad\qquad \varepsilon_i = \sum_{k=1}^{n_{\text{rec.}}} P(E_k|C_i), \qquad (5.12)$$

where ε_i is the overall efficiency of detection of the cause C_i. The estimated numbers of events can be used to calculate the probability of the causes

$$\hat{P}(C_i) = P(C_i|n(E)) = \frac{\hat{n}(C_i)}{\sum_{i=1}^{n_{\text{true}}} \hat{n}(C_i)}. \qquad (5.13)$$

This expression is then inserted into Eq. 5.11 instead of the initial probabilities $P(C_i)$ and the whole process is iterated until the χ^2 comparison of $n(C_i) = P(C_i)N_{\text{obs}}$ and $\hat{n}(C_i)$

$$\frac{\chi^2}{n_{\text{true}}} = \frac{2}{n_{\text{true}}} \sum_{i=0}^{n_{\text{true}}} \frac{[n(C_i) - \hat{n}(C_i)]^2}{n(C_i) + \hat{n}(C_i)} \qquad \text{for } n(C_i) + \hat{n}(C_i) > 0 \qquad (5.14)$$

becomes lower then a desired threshold or simply a maximum number of iterations is reached. Both these ending conditions should be adjusted depending on the distributions, the size of the sample and other specific factors.

The initial distribution $P(C_i)$ used in the first iteration does not influence the unfolded distribution, but it affects the convergence rate of the method. A uniform distribution was selected for simplicity. The $P(E_j|C_i)$ probabilities were evaluated using MC-simulation. Since each $P(E_j|C_i)$ is independent on the shape of the true distribution[5], in order to cover wider range of potential causes, an artificially wide distribution of generated q_T was adopted, instead of a realistic distribution of the physics process under study.

As suggested in [203], to cope with statistical fluctuations in the high q_T tail, which tend to amplify in the iterations, a smoothing algorithm was applied to the $P(C_i)$ distribution at each step.

5.5.2 Event-by-event unfolding

In the previous section, unfolding method applicable for distributions was described. Although the method is powerful, it cannot be used for the extraction of the weighted asymmetries, since the unfolded q_T information is needed on an event-by-event basis. However, for a given $q_{T,\text{rec.}} \in E_j$ the aforementioned method provides the probabilities $P(C_i|E_j)$, which can be used to evaluate which $q_{T,\text{true}}$

---

[5]The $P(E_j|C_i)$ describes the impact of factors as response of the experimental apparatus, reconstruction effects, and selection cuts on a given input C_i

are more probable. The strongest effect on the asymmetries is expected to come from the changed values of the weights.

To get the apparatus response $P(E_j|C_i)$ a mix of the two Monte Carlo samples shown in Fig. 5.18 was used. The reconstructed MC data was selected according to the same criteria used for the real data (see Sec. 5.1). The unfolding procedure was firstly validated on MC data. Both approaches (with and without the additional smoothing) were tested separately giving compatible results apart from some statistical fluctuations in the high q_T region.

5.5.3 Unfolding of the real data

To minimise the statistical uncertainties, all the data was merged together to determine the unfolded distribution and the unfolding matrix $P(C_i|E_j)$. The overall effect of the q_T migration observed while extracting the weighted asymmetries from the unfolded data was found to be rather small. For the weighted Sivers asymmetry it is compatible with zero. In the case of the weighted transversity-related asymmetry ($A^{\sin 2\phi_{CS} - \phi_S}$) there is a hint of a systematic positive shift, but it is well below 10% of the statistical uncertainty. The strongest effect is naturally observed on the q_T^3-weighted $A^{\sin 2\phi_{CS} + \phi_S}$ asymmetry. A difference up to 30% of the statistical uncertainty is observed and is most pronounced in the first bins of x_π and x_F, which correspond to relatively large q_T values due to kinematic correlations.

5.6   Final systematic uncertainty

Among the different sources of possible systematic uncertainties mentioned above, the most significant contribution comes from the false asymmetries. The systematic biases introduced by the q_T event migration were estimated using the unfolding procedure. Apart from distortions observed for q_T^3-weighted $A^{\sin 2\phi_{CS} + \phi_S}$ asymmetry in few kinematic bins correlated with high-q_T events, the impact was found to be marginal.

The uncertainty estimated from the false asymmetries was averaged over kinematic bins first and then combined with the q_T event-migration contribution. Systematic uncertainties originated from FAs and from the q_T migration were added in quadrature and the final systematic uncertainty was estimated to be about $0.7\,\sigma_{\text{stat.}}$. The other sources of systematic biases were found to have a negligible contribution.

The normalisation uncertainties of about 5% originating from the target polarisation measurements and dilution factor estimation were discussed in Secs. 4.7, 4.8 for the standard TSA analysis. These corrections are also to be considered in case of wTSAs.

5.7 Results

The results for the q_T-weighted TSAs extracted from the 2015 polarised Drell-Yan data are presented in Fig. 5.19. The bands represent the systematic uncertainties associated to the experimental points. The asymmetries integrated over the entire kinematic range are shown in the last column. The weighted Sivers asymmetry is measured to be ~ 0.3 standard deviations above zero. The effect results to be suppressed if compared to the standard TSA. The explanation for this trend can be given looking to standard Sivers TSA as a function of q_T (Fig. 4.29). There the effect is found to be smaller in the last bin, which corresponds to events characterised by high q_T. These events dominate in the q_T weighted analysis. The pretzelosity related q_T-weighted TSA is found to be above zero of about ~ 1.2 standard deviations. This asymmetry is affected by large statistical uncertainty due to the weight used in the extraction, $q_T^3/(2M_\pi M_N^2)$. The uncertainty is particularly large in the first bin of x_π and x_F, since these variables are anti-correlated with q_T. The transversity-related asymmetry is measured to be ~ 2 standard deviations below zero.
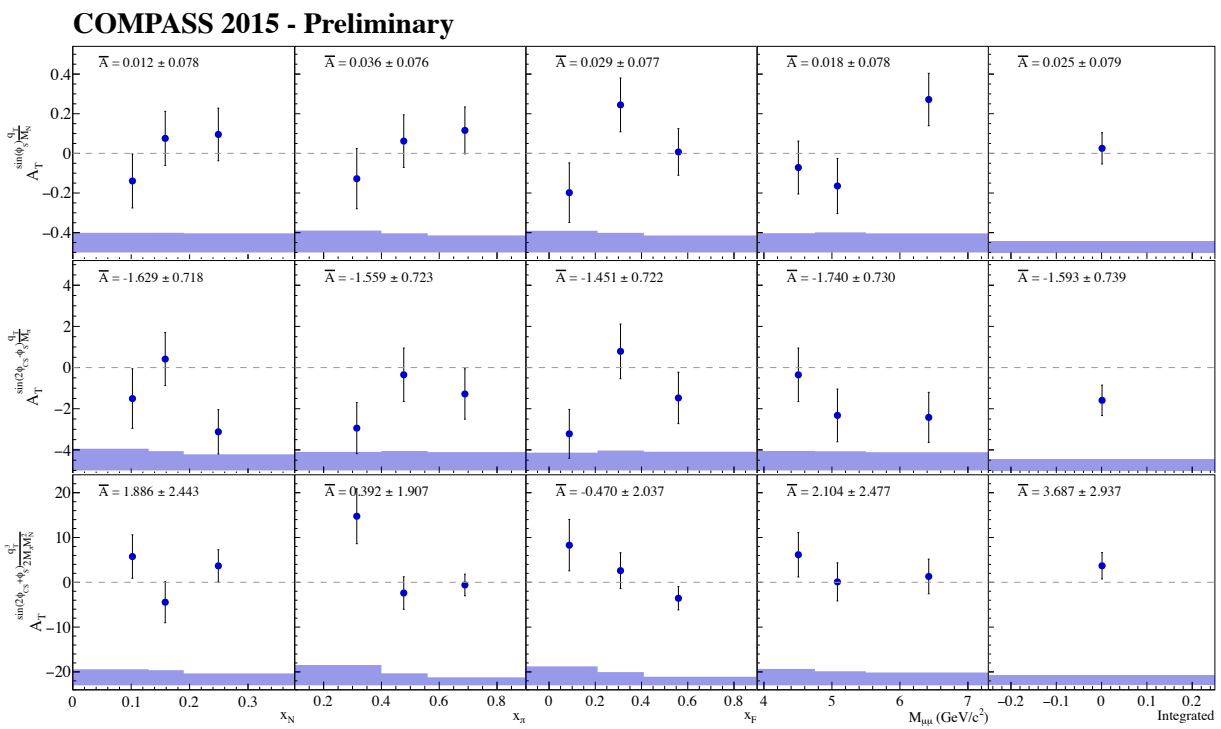
Fig. 5.19 The q_T-weighted TSAs from the 2015 Drell-Yan run, extracted in the High Mass range. The overall systematic uncertainty of $0.7\,\sigma_{\text{stat.}}$ is represented by the blue bands.

Chapter 6

Measurement of the Unpolarised Azimuthal Asymmetries in the Drell-Yan process

In this chapter the results on Drell-Yan unpolarised asymmetries (UAs) λ, μ and ν, extracted from the nine periods of 2015 COMPASS NH_3 data, are presented. The details on data stability analyses and the event selection procedure are discussed in Chap. 4. Polarisation effects were cancelled out by combining data with opposite polarisation orientations.

For the extraction of TSAs the data collected with different polarisations from both target cells can be combined in a specific way to cancel out the acceptance of the experimental setup (see Chap. 4). Study of the unpolarised asymmetries requires a different approach. The acceptance of the spectrometer is evaluated using a detailed Monte-Carlo (MC) description of the setup and detector responses. Obtained information is then used to correct measured azimuthal distributions for the acceptance component.

In contrast with the TSAs and wTSAs analyses presented in this Thesis, the results of UA asymmetries discussed in this Chapter are not yet final and still need to be accomplished and released by the COMPASS collaboration. The reason for this is that by the time of this work, the analysis of detector-responses (2D efficiency maps) and trigger-efficiency studies were not yet fully evaluated and could not be included in the simulation of the setup. Nevertheless, presented analysis framework is complete and foreseen future improvements are not expected to change the results dramatically. The impact of possible acceptance variations due to insufficient description of detector-efficiencies is taken into account at the level of systematic uncertainties.

In the following sections, the MC-evaluation of the spectrometer acceptance is discussed, together with the extraction methods and various studies carried out

for estimation of systematic uncertainties. The analysis was performed on the COMPASS 2015 NH_3 data (t3 mass production). As for the TSAs and wTSAs cases, only the High Mass range ($4.3 < M_{\mu\mu}$ GeV/$c^2 < 8.5$) is considered.

6.1   Full-chain Monte Carlo simulations

The extraction of the unpolarised azimuthal asymmetries and evaluation of related systematic uncertainties require extensive full-chain Monte-Carlo simulations. In particular, a careful Monte-Carlo description of the experimental apparatus and detector responses is mandatory to disentangle the physics asymmetries from those induced by the acceptance of the setup. For technical details of the COMPASS TGEANT MC chain the reader is referred to the Chap. 3. In the analysis of UAs in the pion-induced DY the simulations are done using TGEANT configuration for hadronic beams (Sec. 3.2.1).

The description of the beam-tracks in MC is based on the parametrization extracted from the experimental data collected with random- and beam-triggers[1]. In MC the spatial characteristics of the π^- beam-tracks are defined by four parameters (θ_x, θ_y, x_{beam} and y_{beam}), while the beam momenta is simulated according to the distribution extracted from low intensity data collected during a short run taken in 2014 with COMPASS beam momentum stations activated. For each simulated event a pile up with a rate of 10^8 π^-/s is considered in a time window of $\Delta T = \pm$ 20 ns.

In the simulations done for this analysis, the DY process is simulated using Pythia6.428 physics event generator [186]. Only pure $q + \bar{q} \rightarrow \gamma^* \rightarrow \mu^+\mu^-$ DY interactions were simulated in the wide mass-range of $3.5 < M_{\mu\mu}$ (GeV/c^2) < 10.5. As for the nucleon and pion PDFs the GRV98lo[195] and GRVPI0[196] parameterizations were used. The PDFs were delivered to Pythia6.428 via LHAPDF[2] interface (revision 5.9.1). Both initial and final state radiations were turned-off in the generator. The *p-n* mixture in different targets was simulated assuming σ_p/σ_n of 1.96 [204]. The k_T tuning applied in the simulations is defined by the settings described in Sec. 4.6 (see Tab. 4.5).

The CORAL revision used to process the mDSTs generated by TGEANT corresponds to the version used in the t3 mass production. This includes various specific settings for each detector station (e.g. beam telescope time window). The detector.dat comprising the information on the position of each detector

---

[1]The random trigger events being unbiased are supposed to serve as the most appropriate input, but they are few. In order to increase the statistics also the beam trigger events are used. It was demonstrated that beam profiles obtained with random- and beam-trigger events are in agreement [166]

[2]**L**es **H**ouches **A**ccord **P**arton **D**istribution **F**unction.

station used by CORAL in the reconstruction was produced in TGEANT and was modified to reproduce particular features specific for the t3 mass production (*e.g.* FI03 slip of X-U planes).

6.1.1   Experimental resolutions

Values of reconstructed physical quantities (particle momenta, kinematic and angular variables) are affected by the uncertainties due to the finite resolution of the detectors, by the tracking algorithms and procedures, by the experimental conditions and other factors. This in particular leads to a smearing of azimuthal angles and can possibly bias some of the observables. The natural way to study these effects is to use a full chain Monte-Carlo simulation comparing generated distributions and observables (the so-called *MC-truth* input from the physics generator) with the reconstructed ones. The realistic description of the apparatus and usage of the same reconstruction framework is a key-point for these studies.

In this work, the effects on all main angular and kinematic variables have been studied using the full COMPASS-DY MC-chain and storing both generated and reconstructed events. The differences between the *MC-truth* values of x_{PV}, y_{PV}, z_{PV}, $M_{\mu\mu}$, x_π, x_N, x_F, q_T, φ_S, φ_{CS} and θ_{CS} and those calculated using the reconstructed quantities (vertex position, momenta of the particles) have been computed for every reconstructed event in the MC mDSTs passing the event selection criteria described in Sec. 4.4. To evaluate the resolution for each variable X, the RMS of $\Delta_X = V^{\text{Rec}} - V^{\text{Gen}}$ distribution has been chosen as an estimator. The Δ_X dependence on various kinematic variables has also been inspected. The angular (φ_S, φ_{CS}, θ_{CS}) resolutions for events generated in the NH$_3$ cells are presented as functions of the *MC-truth* values of x_π, x_N, x_F, q_T and $M_{\mu\mu}$ in Fig. 6.1.

The φ_S and φ_{CS} resolutions look similar and follow the same trends. In particular it is evident that resolution degrades at lower values of q_T. This was the motivation to apply a cut on lower values of q_T in the analysis of TSAs and UAs (see Sec. 4.4). The average resolution for these angles (the RMS of integrated Δ_ϕ distribution) is about 0.15 radians.

Similar exercise was done for kinematic resolutions. In Fig. 6.2 the resolutions for different kinematic variables are plotted in bins of the same generated (*MC-truth*) variables. This information was used to estimate the impact of the resolution effects and related event-migrations in case of wTSAs as discussed in Sec. 5.4.3. Correct reproduction of experimental resolutions in MC is crucial for MC-based
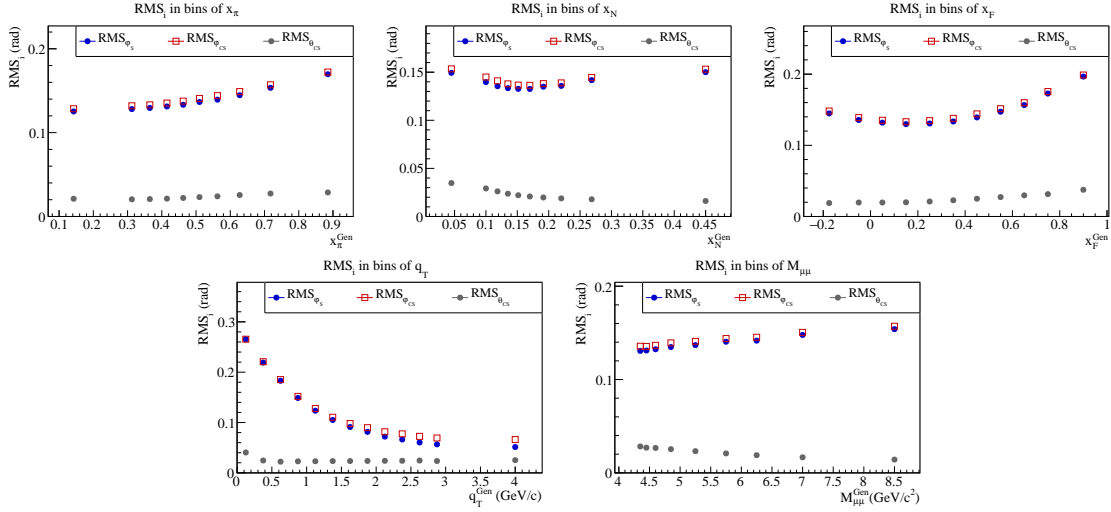
Fig. 6.1 RMS of Δ_X distributions for φ_S, φ_{CS}, θ_{CS} in bins of generated x_π, x_N, x_F, q_T and $M_{\mu\mu}$. The points are drawn in the geometrical center of each bin. The bin widths were chosen in a way to ensure enough precision.

physics analyses and it requires proper and detailed simulation of the setup and detector-efficiencies.
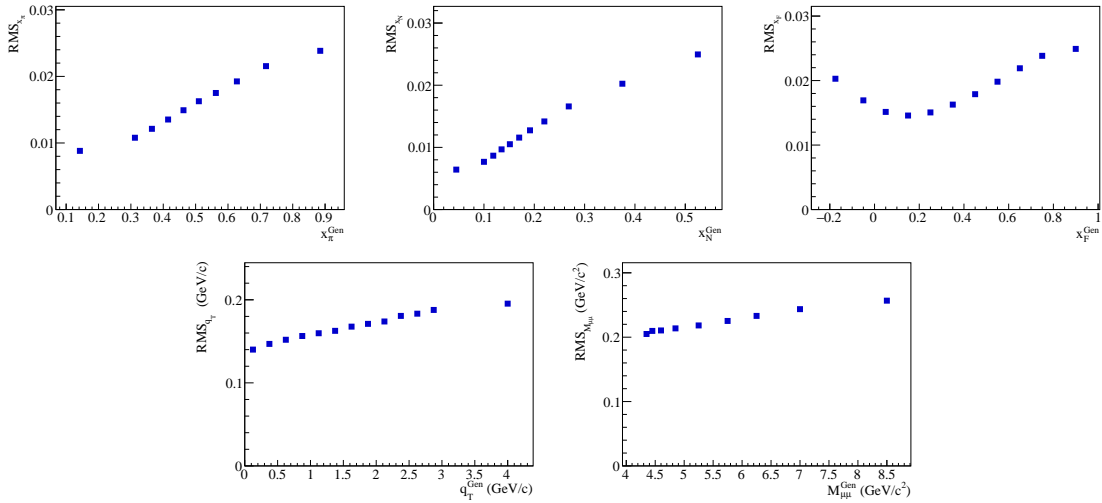
Fig. 6.2 RMS of Δ_X distributions for x_π, x_N, x_F, q_T and $M_{\mu\mu}$ in bins of the respective generated variable. The points are drawn in the geometrical center of each bin. The bin widths are the same as in Fig. 6.1.

6.1.2   Comparison of MC-experimental data and evaluation of the acceptances

In Fig. 6.3 a comparison between the aforementioned simulated MC-data and COMPASS experimental DY data (mass production, t3 slot) for the main DY kinematic variables is presented. In most of the cases the agreement is satisfactory
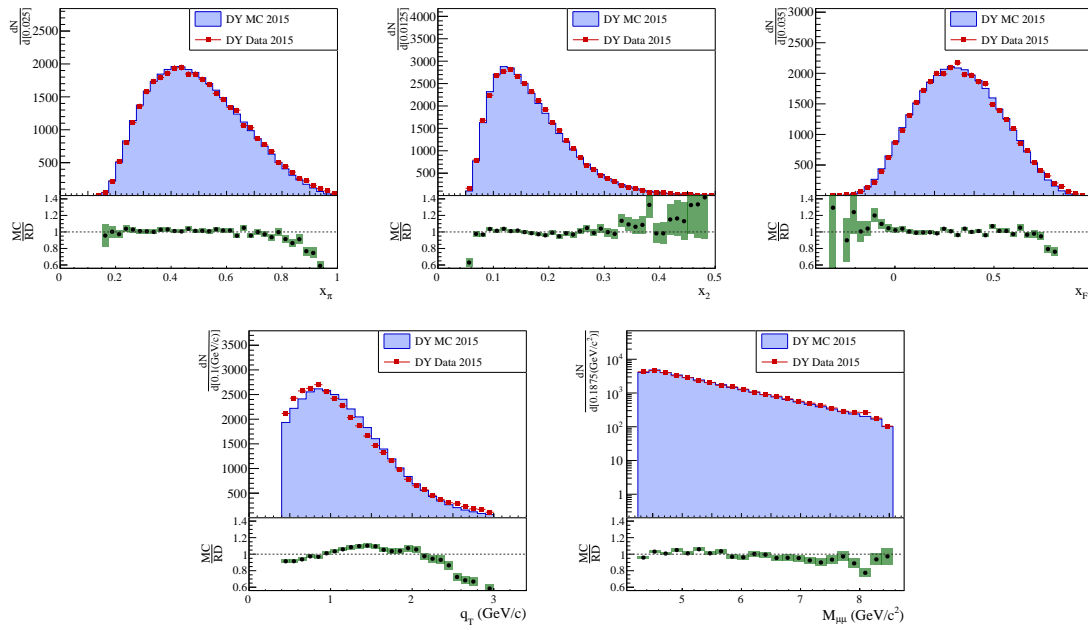
Fig. 6.3 Comparison between DY MC and 2015 real data (t3 slot) for x_π, x_N, x_F, q_T and $M_{\mu\mu}$. The green bars represent the statistical error associated to the ratio. The width of each bar represents the bin-width.

and shows deviations exceeding a 10% tolerance level only at the edges of the kinematic phase-spaces, *e.g.* at high x_π and x_F. The rapidly increasing disagreement in q_T starting from 2.5 GeV/c is due to the features of the k_T tuning selected in the generator (see Fig. 5.18), and corresponding discussion in Sec. 4.6. In Pythia6, selecting the Gaussian assumption to generate k_T (see Eq. 4.2), it is difficult to describe q_T higher than 2.5-3.0 GeV/c. The region above 3.0 GeV/c was thus excluded from the UA analysis.

Despite the satisfactory reproduction of the kinematic distributions by MC, some significant discrepancies can be observed while comparing simulated and experimentally measured *laboratory* variables. In Fig. 6.4 the comparison between MC and data for momentum, azimuthal and polar angles of μ^- is shown. Whereas P_{μ^-} and θ_{μ^-} description is still satisfactory, with disagreements arising only at the edges of the distributions, sizable differences can be observed for ϕ_{μ^-}. Looking at the two-dimensional distribution of θ_{μ^-} vs ϕ_{μ^-}, some well-defined structures can be observed in real data (Fig. 6.5, left panel) while they are missing in the MC (Fig. 6.5, central panel). Possible trigger-inefficiencies were identified as a potential source for such discrepancies.

The trigger system of COMPASS is carefully maintained during the data-taking since hardware or trigger-logic inefficiencies can easily cause the loss of an event. Still some inefficiencies happen and must be taken into account in the simulations. A rough estimation of possible trigger inefficiencies that would lead
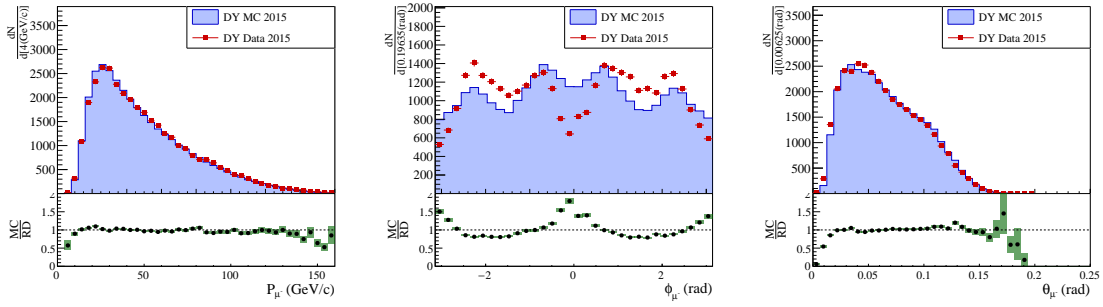
Fig. 6.4 As Fig. 6.3 but for μ^--related variables in the laboratory frame (P_{μ^-}, ϕ_{μ^-} and θ_{μ^-}).
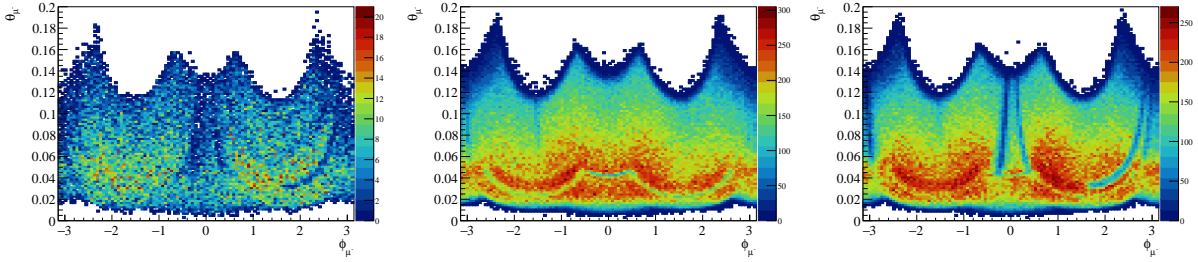
Fig. 6.5 Scatter plot θ_{μ^-} vs ϕ_{μ^-} for 2015 real data (left), MC (center) and MC with *imitated* trigger efficiency (right).

to the distributions observed in the data has been done. Preliminary extractions of trigger hardware efficiencies has shown that, except for a couple of slabs, the overall performances of the trigger hardware was quite high in 2015 ($\geq 98\%$) and the problem should originate from trigger-matrix instabilities. The extraction of the trigger-matrix efficiencies was not yet ready by the time of this Thesis, however preliminary evaluations have already unveiled some problems. For the sake of simplicity, the imitation of trigger-related issues was reproduced only via hardware efficiencies trying to reproduce the structures seen in the data. The results are shown in 6.5, (right panel). Qualitatively one can see that problematic slabs have been identified. The comparison data-MC with *imitated* trigger efficiencies is shown in Fig. 6.6. The agreement in ϕ_{μ^-} improves significantly.
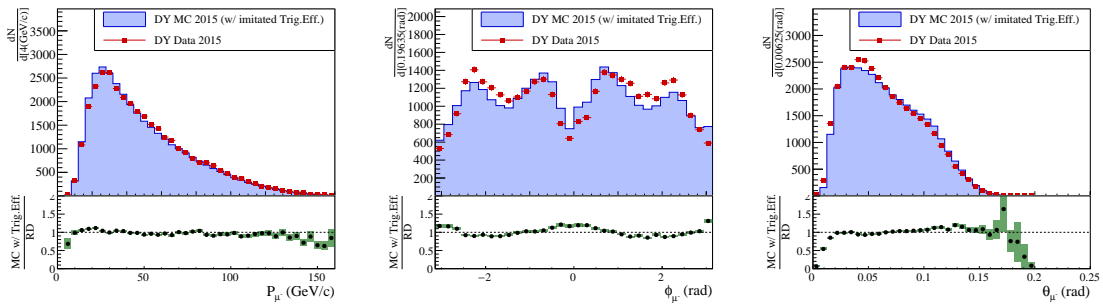
Fig. 6.6 As Fig. 6.4 but for MC with *imitated* trigger efficiency.

The generated MC sample is reconstructed using the same CORAL configuration (same revision and reconstruction options) as for the experimental data production. The *MC truth* information, which is necessary to evaluate the acceptance, is also stored for each generated event. The acceptance $A(X)$, where X represents a generic kinematic or angular variable, is calculated as the ratio

$$A(X) = \frac{N_{MC}^{Rec}}{N_{MC}^{Gen}} \tag{6.1}$$

where N_{MC}^{Gen} and N_{MC}^{Rec} are correspondingly the distributions of all generated and reconstructed events belonging to the same sample and passing the event selection criteria. Note that N_{MC}^{Rec} is defined not only by the geometrical acceptance of the spectrometer, but it is affected also by the reconstruction efficiency, tracking performances, experimental smearing and etc. An example of generated, reconstructed and acceptance distributions is shown in Fig. 6.7.
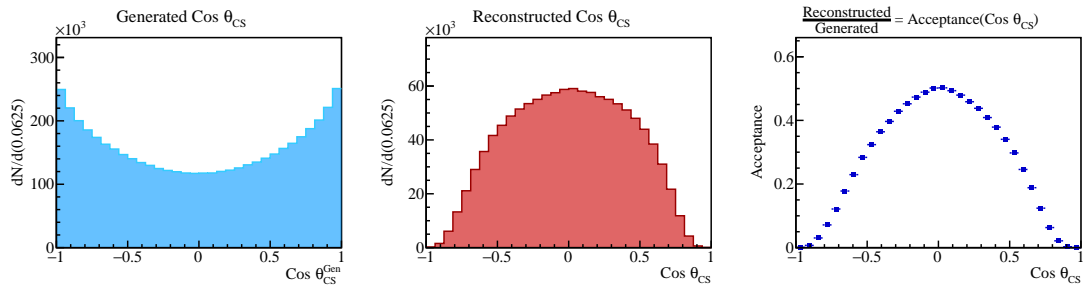
Fig. 6.7 Example of acceptance ingredients and computation. Left panel: generated distribution of $\cos\theta_{CS}$. Central panel: $\cos\theta_{CS}$ distribution of reconstructed events passing the event selection. Right panel: acceptance for $\cos\theta_{CS}$, computed as a ratio of reconstructed to generated distributions.

The single-variable (often referred to as *one-dimensional*) acceptances for main kinematic and angular DY variables are shown in Fig. 6.8. Similarly to the q_T-case (see Sec. 5.4 for details), the increasing trend observed for x_π and x_F can be explained in terms of experimental smearing. The acceptance in φ_S is mostly flat, whereas φ_{CS} shows a clear $\cos 2\varphi_{CS}$ modulation (with an amplitude of about 2%). The acceptance in $\cos\theta_{CS}$ rapidly drops at the edges of the distribution $|\cos\theta_{CS}| \sim 1$. Such a behaviour needs to be studied carefully since polar angle asymmetry, λ, is very sensitive[3] to variation of the acceptance on the edges of $\cos\theta_{CS}$. As far as the kinematics is concerned, compared to past DY experiments, COMPASS is characterised by overall higher acceptance. In particular it provides an opportunity to explore a wide range of x_F, going from $\sim$ -0.2 till mostly 1.

---

[3]in Eq. 1.39 λ is the amplitude of the $\cos^2\theta_{CS}$ modulation

However, as shown in Fig. 6.8, the acceptance in negative x_F range is relatively small.
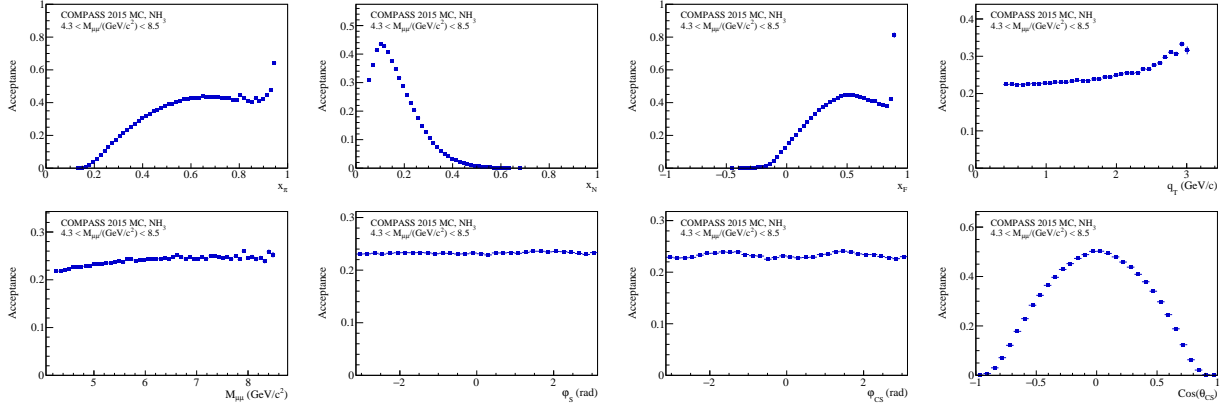
Fig. 6.8 One-dimensional acceptances for COMPASS 2015 setup. Top row (from left to right): x_π, x_N, x_F, q_T. Bottom row (from left to right): $M_{\mu\mu}$, φ_S, φ_{CS}, $\cos\theta_{CS}$. The rapid increase of acceptance at the upper edge of x_π and x_F can be explained in terms of the experimental smearing, as done for q_T in Sec. 5.4.3.

6.2   Event selection and binning

The event selection applied to the filtered data stored in μ-DST is similar to that used for TSAs analysis (see Sec. 4.4). Only one modification has been implemented. The upper-cut on q_T has been lowered from 5 to 3 GeV/c, since in the range $3 < q_T$ (GeV/c) < 5 the MC shows a rapidly increasing disagreement with the experimental data. The reason for this discrepancy comes from the event generation level, where the generated q_T distribution rapidly decrease because of a cut-off at 3 GeV/c applied on primordial k_T (see Sec. 4.6). On the other hand, in the unpolarised analysis, a finer binning can be adopted (5 bins instead of 3 in TSA and wTSA analyses), since the data are summed over polarisation states and not divided in sub-periods. This allows to retrieve more detailed information about eventual kinematic dependences. The impact of the event selection criteria on the dimuon sample and the final statistics after all cuts is given in Tab. 6.1.

The UAs have been determined in the High Mass region as functions of the variables x_N, x_π, x_F, q_T and $M_{\mu\mu}$. In contrast to the TSA analysis, the acceptance effects are removed making use of the Monte Carlo. The limits of the kinematic bins used in the analysis are listed in Tab. 6.2. They were chosen in a way that bins contain approximately the same number of events.

Cut	Events
Dimuon Pairs, $X/X_0 > 30$	1 905 927 808
$M_{\mu\mu} \in [4.3; 8.5]$ GeV/c	1 970 147
PV: 2 opposite charge muon($x/X_0 > 30$) tracks	1 159 349
Dimuon trigger bit (LAST ∥ OT, no MT)	868 291
$Z_{\text{first}} < 300$ cm and $Z_{\text{last}} > 1500$ cm	784 379
$t_{\mu^\pm}$ defined	776 643
$|t_{\mu^+} - t_{\mu^-}| < 5$ ns	373 081
$\chi^2_{\mu^\pm}/n_{\text{dof}} < 10$	370 054
Trigger validation	169 526
Bad spills list	138 255
$x_\pi \in [0,1]$ and $x_N \in [0,1]$ and $x_F \in [-1,1]$	138 159
$q_T \in [0.4, 3]$ (GeV/c)	121 839
$Z_{PV} \in [-294.5, -239.3] \cup [-219.5, -164.3]$ cm	37 448
$r_{PV} < 1.9$ cm	34 279

Table 6.1 Impact of the event selection criteria for UA analysis on the overall 2015 data sample.

Variable	Bin Limits					
x_N	0	0.11	0.14	0.18	0.23	1.0
x_π	0	0.34	0.44	0.53	0.65	1.0
x_F	-1.	0.13	0.26	0.38	0.53	1.0
q_T (GeV/c)	0.4	0.68	0.95	1.25	1.7	3.0
$M_{\mu\mu}$ (GeV/c^2)	4.3	4.53	4.87	5.35	6.15	8.5

Table 6.2 Kinematic bin limits chosen for the UA analysis

6.3 Extraction of the asymmetries

Acceptance corrections, if properly parametrised, allow to cancel out effects introduced in the experimental or *real* data (RD) by different factors such as the geometrical acceptance of the spectrometer, experimental smearing, reconstruction efficiency and event selection criteria. The MC simulations are used to parametrise the acceptance of the apparatus. Two different methods that have been considered and tested to extract the unpolarised asymmetries of the DY-cross section are described in this section.

6.3.1 Two dimensional ratio method

The first method is the one used for unpolarised SIDIS analysis [97], hereafter referred to as two dimensional ratio (2DR). In this method the data is filled into a two-dimensional ($\varphi_{CS}, \cos\theta_{CS}$) histogram, which is later on corrected for

acceptance dividing by the acceptance-histogram extracted from MC. Obtained ratio-histogram is then fitted using the χ^2 minimization.

In each kinematic bin the two-dimensional RD angular distributions are presented in a from of two-dimensional 8×8-binned histograms ranging between [-π, π] for φ_{CS} and [-1,1] for $\cos \theta_{CS}$ [4], with the angular bin content, $N(\varphi_{CS}, \cos \theta_{CS})$. In this configuration, the resulting bin widths were sufficiently larger than the experimental resolutions estimated from MC simulations (see Fig. 6.1). The acceptance[5] $A(\varphi_{CS}, \cos \theta_{CS})$ is calculated from Monte Carlo simulations for each angular $(\varphi_{CS}, \cos \theta_{CS})$-bin and for each kinematic bin, as described in Sec. 6.1.2. The $N_{RD}(\varphi_{CS}, \cos \theta_{CS})$ counts corrected for the acceptance are defined as

$$N_{RD}^{Corr}(\varphi_{CS}, \cos \theta_{CS}) = \frac{N_{RD}(\varphi_{CS}, \cos \theta_{CS})}{A(\varphi_{CS}, \cos \theta_{CS})} \qquad (6.2)$$

The associated statistical error, σ_{corr}, is calculated in each $(\varphi_{CS}, \cos \theta_{CS})$ bin as the sum in quadrature of two contributions. The first one is given by the statistical error associated to $N_{RD}^{Corr}(\varphi_{CS}, \cos \theta_{CS})$ in each angular bin, computed as[6]

$$\sigma_{stat} = \sqrt{\sum_{i=1}^{N_{RD}} \omega_i^2} \qquad (6.3)$$

where $\omega_i = 1/A$. The second contribution comes from the uncertainty on the acceptance evaluation and is calculated taking into account that the acceptance is a binomial quantity. The acceptance related contribution to the uncertainty is then given by the expression:

$$\sigma_A = \frac{\sqrt{N_{MC}^{Gen} \cdot A \cdot (1 - A)}}{N_{MC}^{Gen}} \qquad (6.4)$$

It is evident that, for large enough MC-sample, the σ_A will become negligibly small. For a given angular bin the final expression of the statistical error assigned to N_{RD}^{Corr} can be written as follows:

$$\sigma_{RD}^{Corr} = N_{RD}^{Corr} \sqrt{\left(\frac{\sigma_{stat}}{N_{RD}^{Corr}} \right)^2 + \left(\frac{\sigma_A}{A} \right)^2} \qquad (6.5)$$

---

[4]In SIDIS a finer binning was chosen due to a higher statistics (factor of $\sim 10^3$ more) compared to the DY case

[5]acceptance includes apparatus acceptance, reconstruction efficiency, tracking performances, experimental smearing and etc.

[6]to simplify the notations, the angular dependence $(\varphi_{CS}, \cos \theta_{CS})$ is omitted in the computation of the errors

The resulting $N_{RD}^{Corr}(\varphi_{CS}, \cos\theta_{CS})$-histograms are then fitted with a four parameter function corresponding to the Eq. 1.39

$$F(\varphi_{CS}, \cos\theta_{CS}) = p_0 \cdot \left(1 + p_\lambda \cdot \cos^2\theta_{CS} + p_\mu \cdot \cos\theta_{CS} \cdot \sqrt{1 - \cos^2\theta_{CS}} \cdot \cos\varphi_{CS} \right.$$

$$\left. + \frac{p_\nu}{2} \cdot (1 - \cos^2\theta_{CS}) \cdot \cos 2\varphi_{CS} \right)$$

$$(6.6)$$

where p_0 is a normalisation parameter and p_λ, p_μ and p_ν represent the unpolarised azimuthal asymmetries λ, μ and ν, respectively.

It should be mentioned that derivation of uncertainties in the 2DR method is based on the assumption of Gaussian errors requiring that there is enough statistics in each given bin. However, the low acceptance at the edges of $\cos\theta_{CS}$ distribution (see Fig. 6.7) leads to a very low statistical population in these regions, that would be more properly described by Poissonian errors. Nevertheless, using Poissonian errors together with introduced weights would complicate the usage of both MINUIT-standard χ^2 and likelihood minimization algorithms requiring a more sophisticated approach. These aspects are discussed in more details in Sec. 6.4, where the results of testing the different extraction methods are presented.

6.3.2 Histogram binned likelihood fit method

Similarly to the 2DR case, in the so-called Histogram Binned Likelihood fit (HBL) method the angular distributions in each kinematic bin are presented in a form of two-dimensional histograms (eight by eight bins over [-π, π] for φ_{CS} and [-1,1] for $\cos\theta_{CS}$ angular ranges). In case of HBL the errors assigned to each $(\varphi_{CS}, \cos\theta_{CS})$-bin content ($N_{RD}$) are Poissonian. The acceptance is also computed on 8×8 $(\varphi_{CS}, \cos\theta_{CS})$ grids using a sufficiently large MC sample[7], so that the acceptance uncertainties given by the Eq. 6.3 can be neglected in each bin. The RD histogram is then fitted using the function given by Eq. 6.6 with acceptance entering as a scale-factor without any uncertainties assigned. The minimization is done using the MINUIT-likelihood option.

6.4 MC-tests of the extraction methods

Both aforementioned extraction methods were tested and validated on MC data. At first, a large sample of Monte Carlo events generated according to an isotropic two-

---

[7]At least 10 times more reconstructed events compared to the real data.

dimensional angular distribution (($\varphi_{CS}, \cos\theta_{CS}$)) was prepared. The isotropic MC sample was generated with a modified version of Pythia8. The part of the Pythia8 source code (the *src/SigmaEW.cc* file) introducing the re-weighting of the Drell-Yan angular distributions was edited to cancel the modulations. Resulting uniform φ_{CS} and $\cos\theta_{CS}$ distributions are shown in Fig. 6.9. Afterwards, using the so-called *Hit and Miss* event-sampling technique, generated uniform angular distribution was modulated according to an azimuth-dependent function, $\Lambda(\vec{A}, \varphi_{CS}, \cos\theta_{CS})$, representing the unpolarised part of the Drell-Yan cross-section from Eq. 1.39:

$$\Lambda(\vec{A}, \varphi_{CS}, \cos\theta_{CS}) = \frac{3}{4\pi}\frac{1}{\lambda+3}\left[1 + \lambda\cos^2\theta_{CS} + \mu\sin 2\theta_{CS}\cos\varphi_{CS}\right.$$
$$\left. + \frac{\nu}{2}\sin^2\theta_{CS}\cos 2\varphi_{CS}\right] \tag{6.7}$$

where $\vec{A}$ is a vector of fixed parameters λ, μ, ν defined as:

$$\vec{A} = (\lambda = 0.9, \mu = -0.05, \nu = 0.2) \tag{6.8}$$

Resulting $\vec{A}$-modulated angular distributions are shown in Fig. 6.10. It was checked that the λ, μ and ν amplitudes introduced by the *Hit and Miss* event-sampling indeed correspond to the selected set (Eq. 6.8).
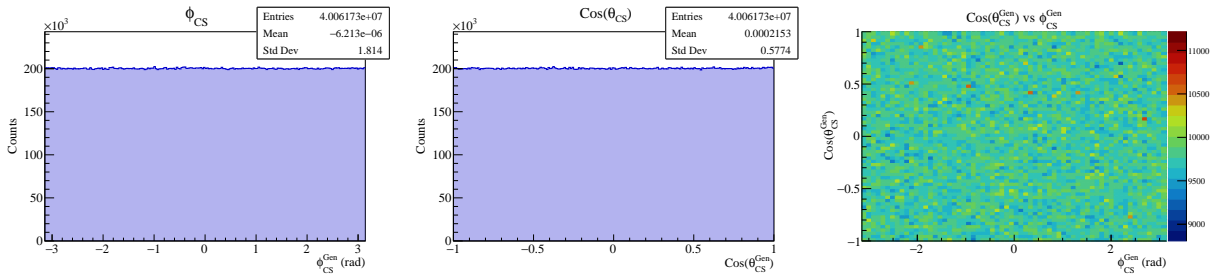
Fig. 6.9 Isotropic distribution of φ_{CS}, $\cos\theta_{CS}$ and φ_{CS} vs $\cos\theta_{CS}$ generated using the modified Pythia8.

Obtained sample of events was then reconstructed in the same way as the experimental data. The initial *MC-truth* information was also stored in the produced mDSTs.

Two different data-sets of $q + \bar{q} \rightarrow \gamma^* \rightarrow \mu^+ + \mu^-$ events generated in the mass range $3.5 < M_{\mu\mu}/(\text{GeV}/c) < 10.5$, have been produced:

i) 60 samples containing ~ 35000 High Mass DY events each (same statistics as the whole 2015 data taking for UA analysis);
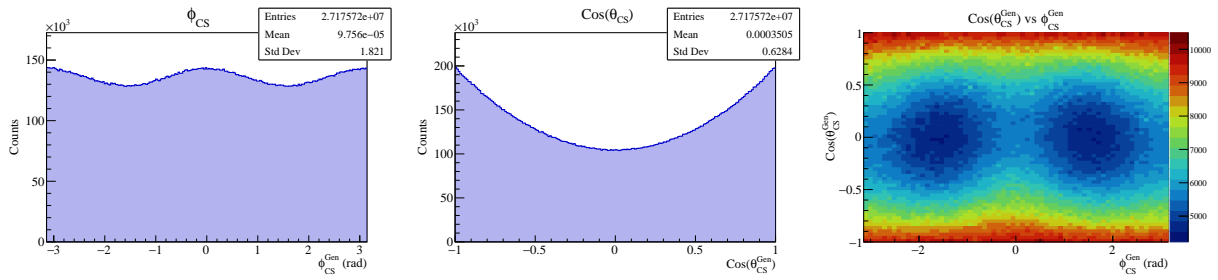
Fig. 6.10 Distribution of generated φ_{CS}, $\cos\theta_{CS}$ and φ_{CS} vs $\cos\theta_{CS}$ obtained after applying the modified Pythia8.

ii) 200 samples containing ~ 4000 High Mass DY events each (average of the statistics per period in 2015);

In both cases the number of events refers to the reconstructed events passing the event selection procedure. Both asymmetry extraction methods introduced in previous sections have been used to extract the injected amplitudes. For the acceptance-evaluation a separate statistically independent MC-sample was produced.

The outcome of test i) is presented in Fig. 6.11. The extraction using the
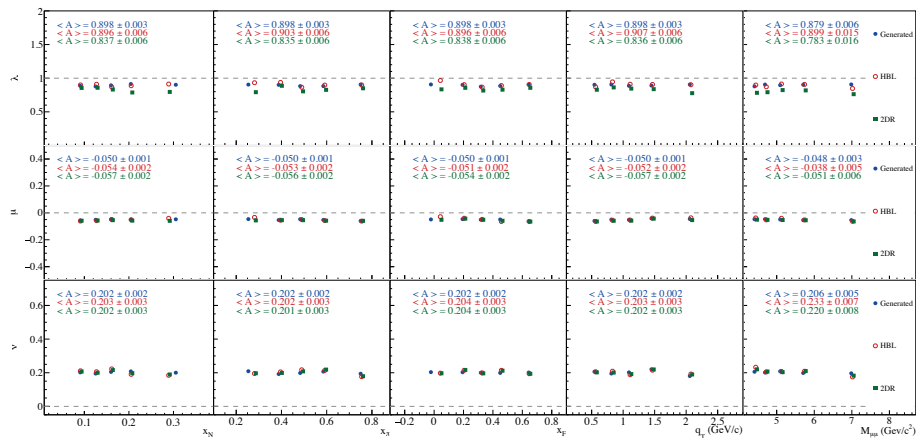
Fig. 6.11 The outcome of HBL and 2DR methods for the eaxtraction of the asymmetries from MC data samples containing roughly the statistics entering the whole 2015 analysis
.

HBL method shows a rather satisfactory agreement with the values injected in the generated sample. On the other hand, the 2DR is found to be biased in specific kinematic regions, even with such high number of entries. These biases can be explained in terms of error treatment at the edges of $\cos\theta_{CS}$, as described in previous sections. Comparing with the 2D-acceptance distributions shown in Fig. 6.12, it can be noticed that the biases arise in the bins where the acceptance shape becomes steeper in terms of $\cos\theta_{CS}$. There HBL works well, thanks to the

Poissonian treatment of the errors, while the Gaussian error assumption used in 2DR leads to a bias in these conditions.
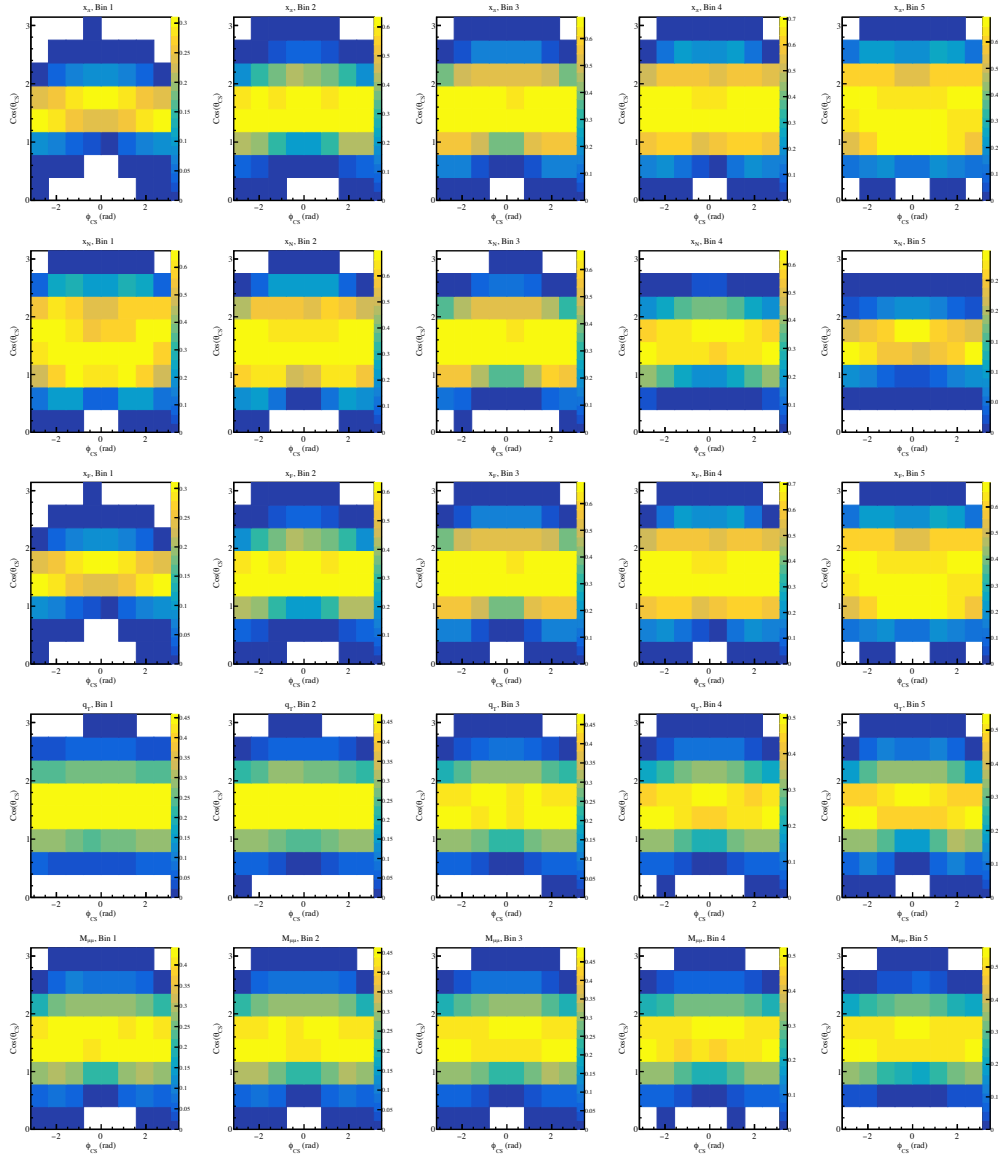
Fig. 6.12 $A(\varphi_{CS}, \cos\theta_{CS})$ in the kinematic bins defined for the analysis. From top to bottom: x_π, x_N, x_F, q_T, $M_{\mu\mu}$.

The results of test ii) are shown in Fig. 6.13. The 2DR is found to be strongly biased in the case of λ extraction, while the HBL performances are still satisfactory, with small biases appearing for λ that are taken into account at level of systematic uncertainties.

Based on these tests, the HBL method has been chosen for the analysis.
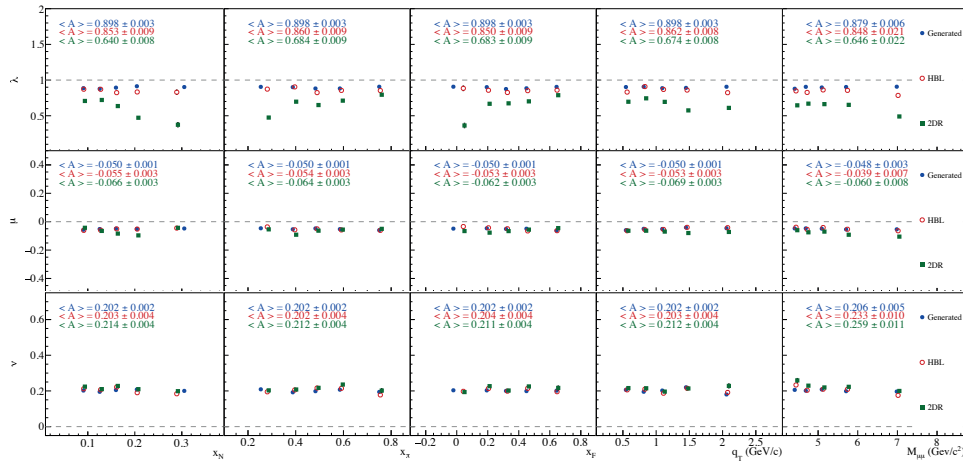
Fig. 6.13 The outcome of HBL and 2DR methods for the eaxtraction of the asymmetries from MC data samples containing roughly the average statistics contained in one of the 2015 data-taking periods.

6.5 Systematic studies

Several tests were performed to estimate the systematic uncertainties of unpolarised Drell-Yan asymmetries. These include the study of the statistical compatibility of asymmetries measured in the nine periods, the estimation of possible biases introduced by the extraction method, the evaluation of the differences introduced by variation of MC generator options. In addition, the impact of the detailed simulation of detector and trigger inefficiencies was evaluated and compared to the results obtained with uniform efficiency assumption. All significant uncorrelated contributions to the systematic uncertainties were combined to estimate the overall systematic uncertainty. The details and results of the aforementioned tests are reviewed in the following.

6.5.1 Compatibility of the periods

The asymmetries extracted from nine data taking periods have been tested for possible discrepancies. In Fig. 6.14 the asymmetries extracted from each period are superimposed. In general, within statistical uncertainties, they appear to follow similar trends. This is confirmed by studying the standard pull-distributions (see Sec. 4.11 for the definition) built to compare the asymmetries from each period with the asymmetries averaged over the full year. They are shown in Fig. 6.15. The 225 entries in each histogram correspond to 5(number of kinematic variables) $\times$ 5(number of bins) $\times$ 9(number of periods). If the results from nine periods are statistically compatible with each other, the resulting pull distribution is expected

to be a Gaussian with *mean* $= 0$ and with $\sigma = 1$. In general all three (λ, μ and ν) pull-distributions are satisfactorily compatible with this "normal distribution"-hypothesis. Nevertheless, to account for small deviations, the differences of mean M_{pull,A_i} and width σ_{pull,A_i} from the expectation values are used to estimate the systematic uncertainties as follows:

$$\left(\frac{\sigma_{syst}^{stab}}{\sigma_{stat}}\right)_{A_i} = \sqrt{|\sigma_{pull,A_i}^2 - 1|} + \frac{|M_{pull,A_i}|}{2} \qquad A_i \in \lambda, \mu, \nu \qquad (6.9)$$

This results in a systematic uncertainty of $\sim 0.75\ \sigma_{stat}$ for λ and $\sim 0.55\ \sigma_{stat}$ for ν.
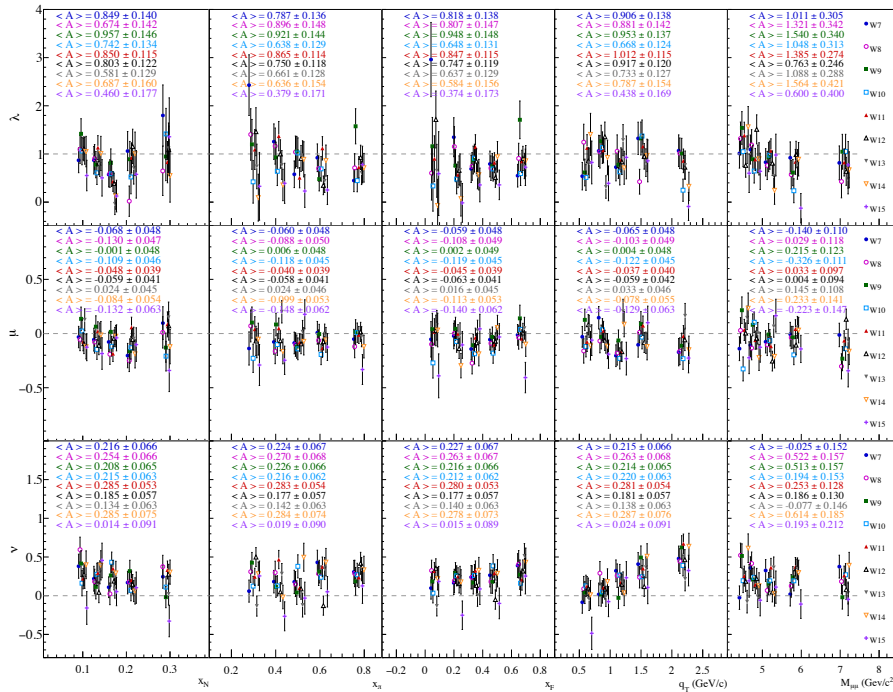
Fig. 6.14 The UAs extracted in each of the nine periods of 2015 data taking. From top to bottom: λ, μ, ν. Dependences on x_N, x_π, x_F, q_T and $M_{\mu\mu}$ are shown from left to right.
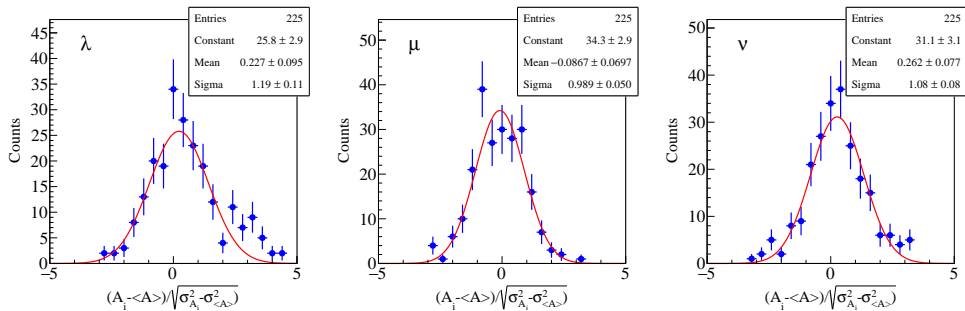
Fig. 6.15 Pulls illustrating the compatibility of UAs between different 2015 periods.

6.5.2 Compatibility of results from different cells

Providing that the experimental apparatus is satisfactorily well described in MC and assuming that acceptance corrections are done properly, the asymmetries extracted separately for the upstream and downstream cells are expected to be the same. Thus, comparing these asymmetries allows to determine if there are biases due to an improper description of the acceptance of the spectrometer in the MC. The pulls used for this test are defined as

$$\text{Pull}_{A_i} = \frac{A_{i,Upstr.} - A_{i,Down.}}{\sqrt{\sigma_{i,Upstr.}^2 + \sigma_{i,Down.}^2}} \qquad (6.10)$$

Since the physics asymmetries are supposed to be independent of the target cell, the pulls distributions are expected to be centred at zero with RMS equal to one. The results are shown in Fig. 6.16. The pull-distribution for ν is in agreement with
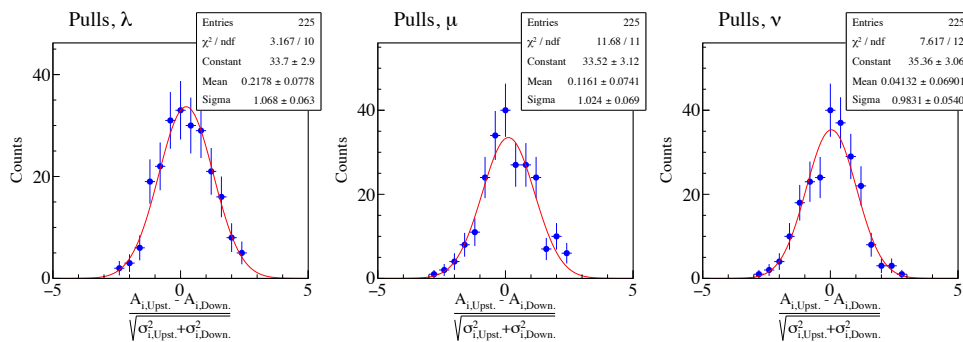
Fig. 6.16 Pulls illustrating the compatibility of the results extracted from each target cell separately.

a standard normal distribution (mean centred at zero and RMS ~ 1), while for λ and μ some deviation in the mean is observed. This is taken into account at level of systematics using Eq. 6.9, resulting in $\sim 0.1\sigma_{stat}$ for λ and $\sim 0.05\sigma_{stat}$ for μ.

6.5.3 Systematics biases introduced by the extraction method

As shown in Sec. 6.4, while extracting the asymmetries on a period basis some bias can be introduced due to low statistics. This bias was evaluated computing

$$\Delta_i^{Meth} = \frac{A_i^{Gen} - \bar{A}_i^{Rec}}{A_i^{Gen}} \qquad (6.11)$$

for each bin. $\bar{A}_i^{Rec}$ represents the weighted average of the results of 300 tests with single-period reconstructed entries in each bin. Obtained precision was enough to neglect the statistical uncertainties of the amplitudes. The resulting

scale systematic uncertainties evaluated in each kinematic bin for each of the asymmetries are shown in Fig. 6.17.
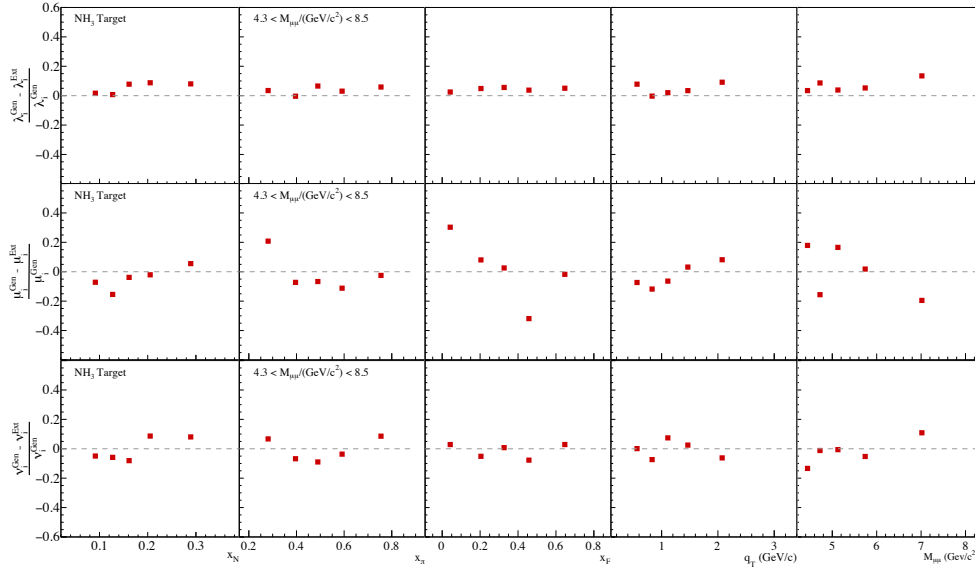
Fig. 6.17 Bin-by-bin estimation of the bias of the HBL method while extracting the asymmetries from a sample with a statistic similar to 1 period of 2015 data taking.

6.5.4 Impact of different MC-generator settings

In first approximation, extracted asymmetries should not depend on the shape of the generated kinematic and angular distributions[8], since generator information cancels out in the definition of the acceptance. Nevertheless, possible acceptance and phase-space edge effects can be convoluted in a complicated manner with the experimental resolutions and may introduce some correlations between the properties of generated distributions and evaluated azimuthal acceptances. Different MC samples were generated to study eventual correlations between evaluated azimuthal acceptance distributions and event generator options and settings. A series of MC datasets have been produced applying different changes each time at the level of generation but keeping the same description of the apparatus and of the beam, as well as the same reconstruction settings. Compared to the event generator configuration described in 6.1, labelled in the following as *Reference*, four cases have been studied:

1. Different proton PDFs, switching from GRV98lo [195] to MSTW2008lo90cl [205] (sample labelled as *MSTW*).

---

[8]Assuming that generated distributions cover the same phase space as the experimental data.

2. Different pion PDFs, switching from GRVPI0 [196] to GRVPI1[9] [195] (sample labelled as *GRVPI1*).

3. Next to leading order (NLO) scheme for the generation of the Drell-Yan process, obtained enabling in Pythia6 both initial and final state radiations, and using NLO PDFs for p (MSTW2008nlo90cl) and π^- (GRVPI1) (sample labelled as *NLO*)).

4. Different event generator, using Pythia8 instead of Pythia6 (sample labelled as *PY8*).

As for the last case, a separate study was carried out to determine the best k_T tuning to be used in Pythia8. In Pythia8 the intrinsic k_T distribution is generated according to Gaussian distributions in p_x and p_y separately. The widths of these distributions depend on the hard scale of the physics process and on the mass of the whole subsystem. The dependence is fixed by the relation

$$\sigma = \frac{\sigma_{soft} \cdot Q_{half} + \sigma_{hard} \cdot Q}{(Q_{half} + Q)} \cdot \frac{m}{m_{half} + m} \qquad (6.12)$$

where Q is the hard-process re-normalisation scale for the hardest process, m is the mass of the system and σ_{soft}, σ_{hard}, Q_{half} and m_{half} are parameters to be tuned by the user. Their meaning is explained in Tab. 6.3, where also the values chosen to generate the MC for the test are reported.

Parameter	Description	Setting
σ_{soft}	Gaussian width, assigned as primordial k_T in the soft-interaction limit	1.28
σ_{hard}	Gaussian width, assigned as primordial k_T in the hard-interaction limit	1.86
Q_{half}	Half-way point between hard and soft interactions	1.92
m_{half}	Half-way point between low-mass and high-mass subsystems.	3.7

Table 6.3 Description of the parameters entering Eq. 6.12 and values chosen to generate the Pythia8 MC for the test.

An empirical tuning of the parameters was done, trying to maximally reproduce the experimental distributions and to achieve a satisfactory description of q_T distribution. Inline with the standard Pythia6 configuration used for the analysis, both initial and final state radiations were turned off. Moreover, the same PDFs have been chosen for both p (GRV98lo) and π^- (GRVPI0).

---

[9]There are few PDFs available for pions. At LO, the only set apart from GRVPI was extracted more than thirty years ago [206]. This work was based on the Drell-Yan data available at this time, that were not covering $x_N < 0.2$, generating large ambiguities in the PDF extraction in this region. Thus, it was preferred to use a more recent PDF, although it refers to a NLO extraction.

Large number of events was generated for all fours test-samples (~ 1.2 million of reconstructed events passing the event selection.). In Fig. 6.18 reconstructed kinematic distributions for the reference sample and for test-samples are compared with corresponding distributions obtained with experimental data. The agreement is enough satisfactory for all five cases.
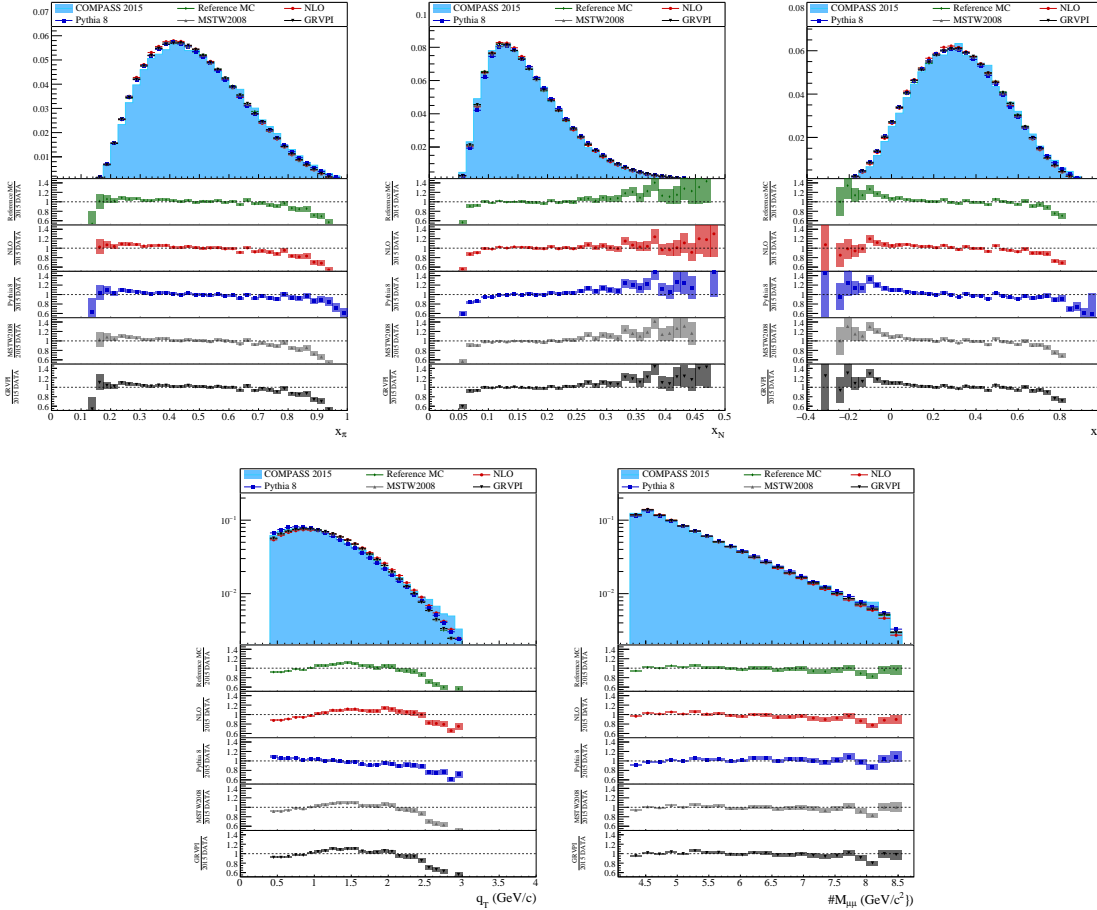
Fig. 6.18 Comparison between different MCs used for systematic checks and 2015 real data. The coloured bars represent the statistical error associated to the ratio. The width of each bar represents the bin-width. Each sample shows good agreement with the real data, with deviations only at kinematic edges. The disagreement observed for $q_T > 2.5$ was explained in Sec. 5.4.3.

In Fig. 6.19 are shown the asymmetries extracted using corresponding MC-samples for the azimuthal acceptance evaluations. Overall, the observed differences are relatively small (within 1 standard deviation in most of the cases), except for q_T and $M_{\mu\mu}$ dependences for λ and μ which are sizably distorted for Pythia8 case. Shown in Fig. 6.20 kinematical correlations obtained for tested MC-samples also underline Pythia6 - Pyhtia8 differences especially for q_T and $M_{\mu\mu}$.

To have a better visualization of these variations, the q_T vs $M_{\mu\mu}$ distributions obtained from the two generators are shown in Fig. 6.21. The ratio between the two distributions is shown in the right panel. Combining this information with
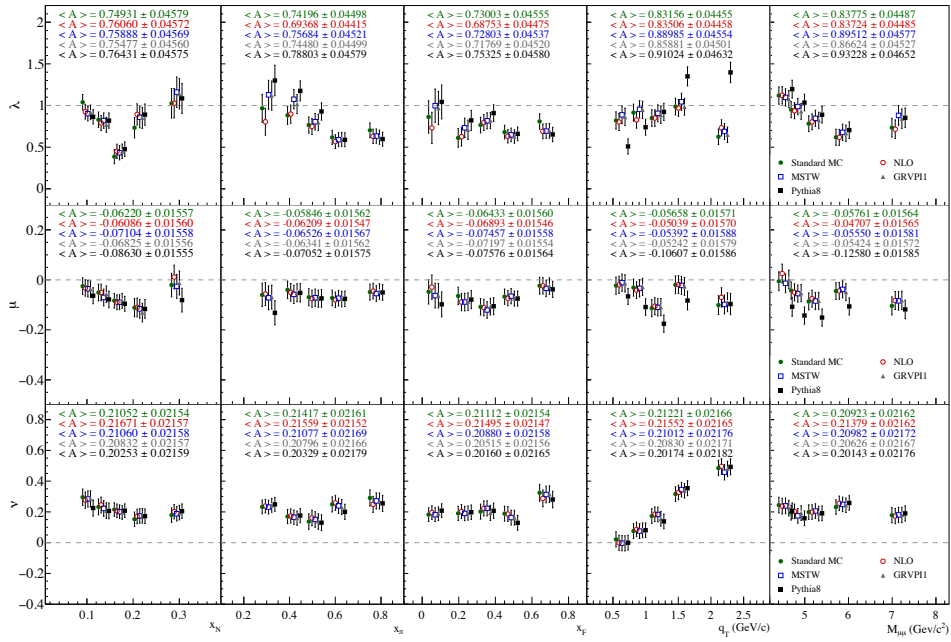
Fig. 6.19 UAs extracted using five MC samples: Reference, NLO, MSTW, GRVPI1 and **Pythia8**.
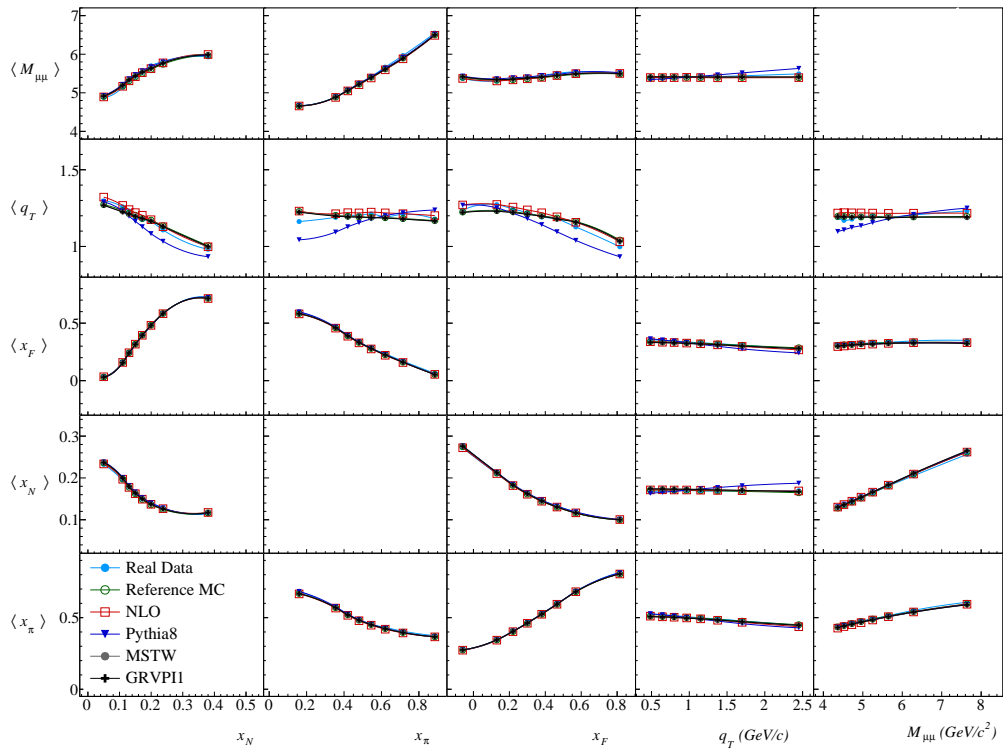
Fig. 6.20 Kinematic map for Real data and five MC samples: Reference, NLO, MSTW, GRVPI1 and **Pythia8**.

the angular resolutions presented in Fig. 6.22 as a function of q_T and $M_{\mu\mu}$, it can be noticed that, compared to Pythia6, Pythia8 favours the events with large q_T at large $M_{\mu\mu}$. These events are characterised by better angular resolutions. On the other hand, in Pythia6 there are more events at large q_T but lower invariant mass. In this region, the angular resolution is worse with respect to the previous case. All these differences translate into different migrations between bins in the reconstructed MC sample, which is the used for the evaluation of the azimuthal acceptance. A careful unfolding of the distributions should fix the difference. In addition, it becomes clear that acceptance corrections should preferably be done in a multidimensional basis.
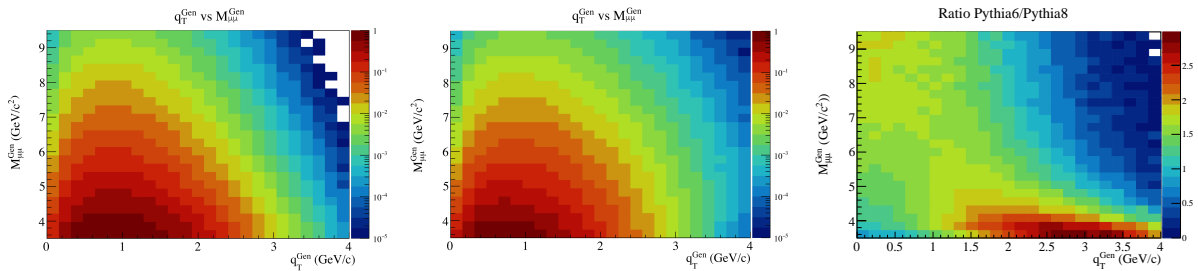
Fig. 6.21 q_T vs $M_{\mu\mu}$ correlations as generated in Pythia6 (left panel) and Pythia8 (central panel). The right panel displays the ratio between Pythia6 and Pythia8.
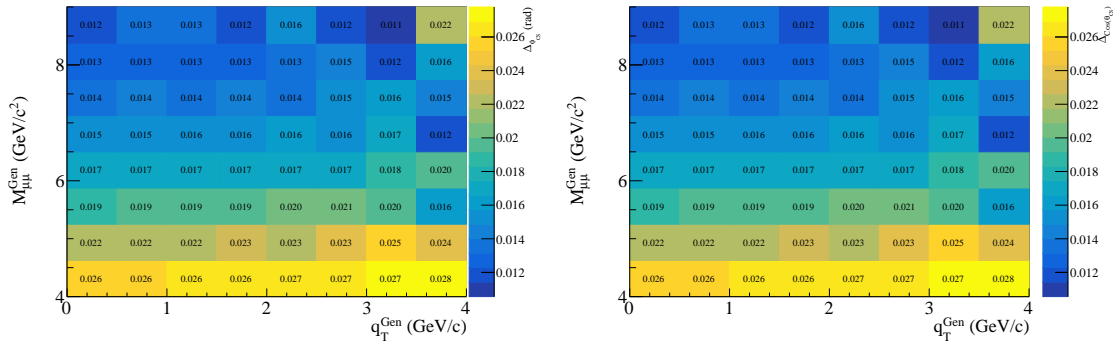
Fig. 6.22 Two dimensional resolutions. Left: $\Delta_{\phi_{CS}}$ as a function of q_T and $M_{\mu\mu}$. Right: $\Delta_{Cos(\theta_{CS})}$ as a function of q_T and $M_{\mu\mu}$. In both the cases, the *Reference* MC was used to extract the values.

In this work no unfolding of the distributions was done and the differences between the amplitudes extracted from the data corrected using aforementioned test MC-samples were used to evaluate the systematic biases. The quantities

$$\sigma_{syst,A_i}^{MC,T} = \frac{|A_i^{Ref} - A_i^{MC,T}|}{2}, \qquad T \in \left[\text{MSTW, GRVPI, NLO, PY8}\right]. \quad (6.13)$$

have been calculated for the 3 amplitudes $A = \lambda, \mu, \nu$ and for each kinematic bin i, taking the largest value as an estimation of σ_{syst}^{MC}. The results, shown in Fig. 6.23
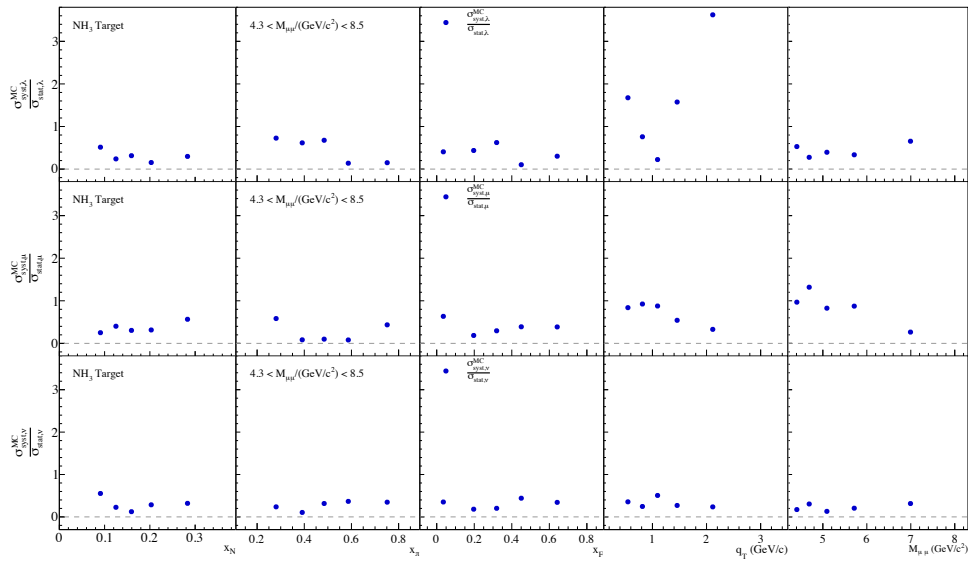
Fig. 6.23 Final estimation of the systematic uncertainty due to the settings chosen at level of MC event generator ($\sigma_{syst}^{MC}/\sigma_{stat}$).

in units of the statistical errors of the corresponding amplitudes, are used in the calculation of the final systematic errors.

6.5.5 Impact of non-uniform detector efficiencies

Since by the time of this Thesis the preliminary 2D efficiency maps with detailed description of instabilities (missing channels, inefficiencies) were produced only for selected detector planes and limited statistics[10], the MC-configuration with uniform detector-efficiencies was used for evaluation of the acceptances. Nevertheless, possible systematic effects arising because of the 2D structure of detectors efficiencies have been carefully studied. The set of two dimensional efficiency maps available at the time of this work were plugged into CORAL and used to process (reconstruct) the aforementioned *Reference* MC-sample. Obtained sample, hereafter referred to as *EFF2D* MC, was used to extract the acceptance distributions which was used to correct the experimental data and extract UAs. The results are illustrated in Fig. 6.24. The contribution of this test to the systematic uncertainty was estimated building quantities analogous to Eq. 6.13 in each kinematic bin. The corresponding systematic uncertainties, σ_{syst}^{EFF2D}, are shown in Fig. 6.25 in units of statistical error.

---

[10]A massive "detector 2D efficiency maps extraction campaign" was already ongoing by the time of this work, but not yet accomplished.
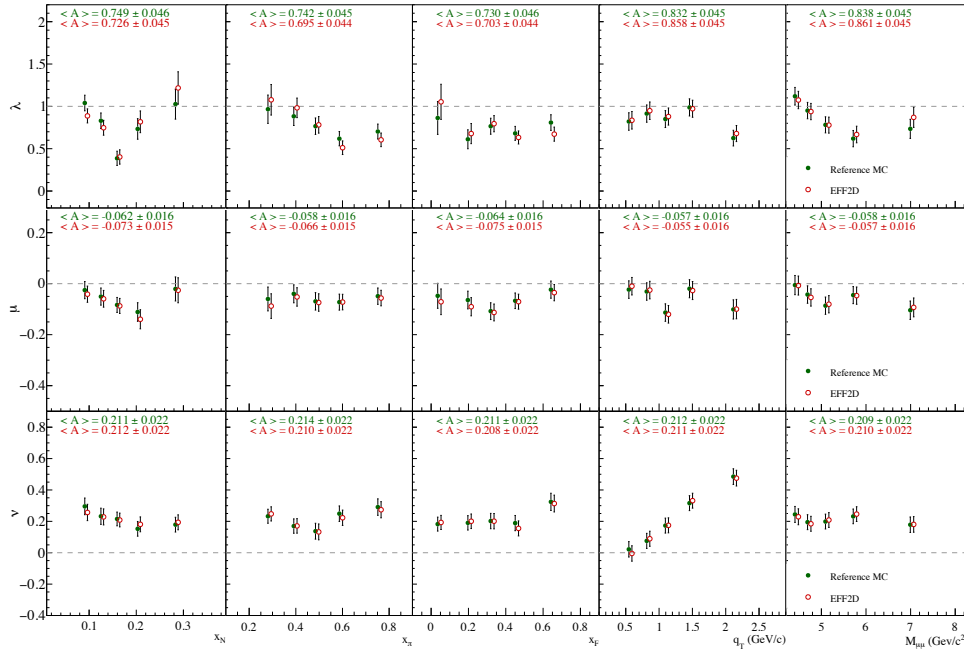
Fig. 6.24 Comparison between λ, μ and ν extracted using the Reference MC and a EFF2D MC.
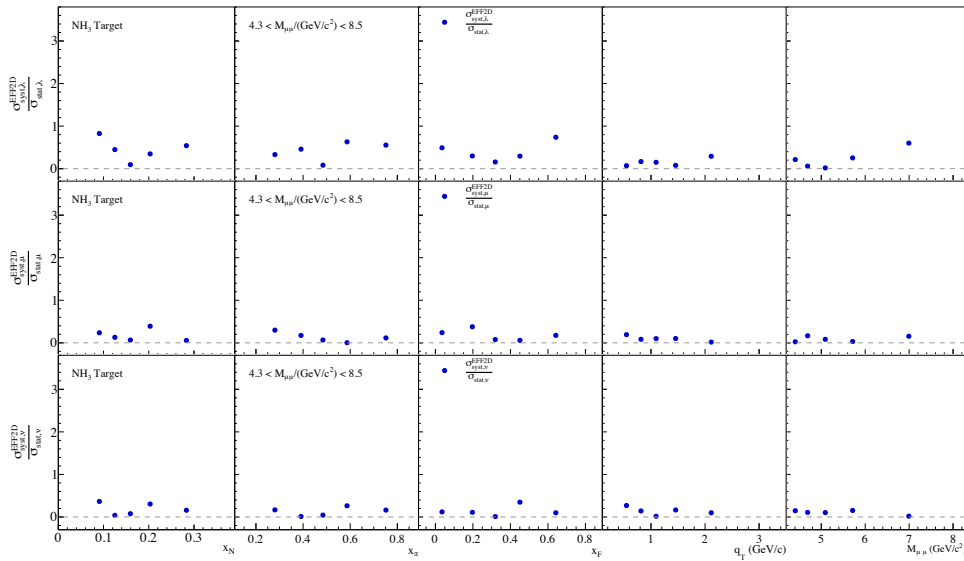
Fig. 6.25 σ_{syst}^{EFF2D} corresponding to the systematic test illustrated in Fig. 6.24.

6.5.6 Impact of non-uniform trigger efficiencies

As mentioned in Sec. 6.1.2, the implementation of trigger efficiencies is crucial to achieve a reasonable description of the laboratory azimuthal distributions. Therefore, it should be checked to what extent the acceptance, and thus the extracted asymmetries, are affected when inefficiencies of the trigger system are reproduced in the MC. By the time of this Thesis the determination of the

trigger efficiency of 2015 was not over. The "imitated" efficiencies used to demonstrate the importance of this ingredient in the description of the real data contain only hardware (trigger-slab) efficiencies, while it was found that the major problems in 2015 could be attributed to the trigger coincidence matrix inefficiencies. Nevertheless, lacking a better input, only the impact on asymmetries of aforementioned simplified imitation of trigger inefficiency was checked and accounted at the level of systematic uncertainties. The test was carried out with large number of generated MC-events in order to minimize statistical fluctuations. The same *Reference* MC-sample was reproduced with and without applying the "imitated" trigger efficiencies and used then to extract the UAs. The two sets of results have been compared and the contribution of this test to the systematic uncertainties was estimated building quantities analogous to Eq. 6.13 in each kinematic bin. The corresponding $\sigma_{syst}^{Trig}/\sigma_{stat}$ in each kinematic bin are shown in Fig. 6.26.
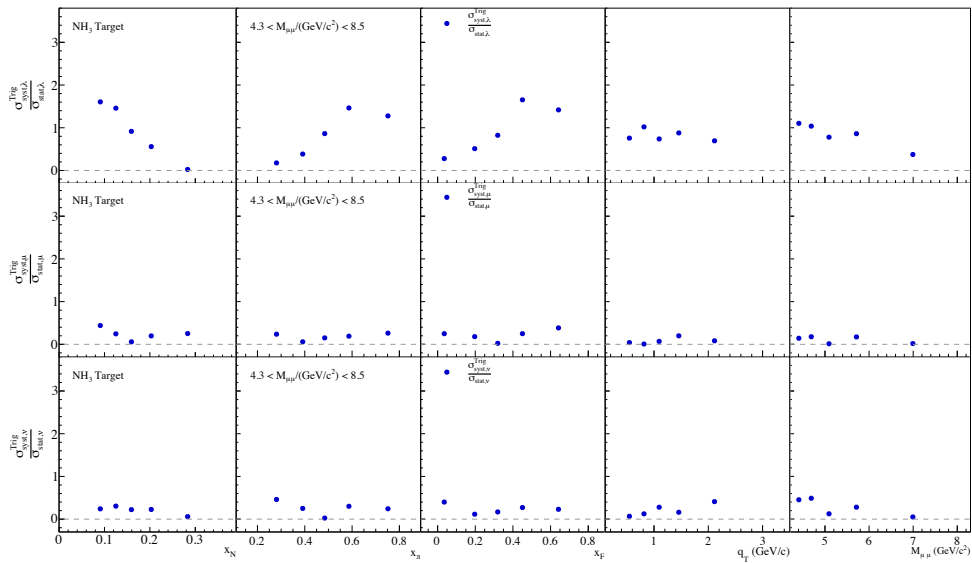
Fig. 6.26 σ_{syst}^{Trig} corresponding to the systematic test related to trigger efficiency implementation in the MC.

6.6   Final systematic uncertainties

The uncorrelated systematic uncertainties estimated in the studies discussed in previous sections are taken into account for the evaluation of the final systematic uncertainty of the azimuthal amplitudes in each kinematic bin i. This includes the additive systematic errors estimated from: **i)** the test of compatibility of the periods (σ_{syst}^{stab}), **ii)** the study of compatibility of results extracted from two target cells

(σ_{syst}^{cells}), **iii)** the probing of different settings of the MC generator (σ_{syst}^{MC}), **iv)** the detector response (2D efficiency maps) simulation (σ_{Syst}^{EFF2D}) and **v)** to the trigger efficiency simulation (σ_{syst}^{Trig}). The multiplicative systematic error estimated for the extraction method was also included in the evaluation of the overall uncertainties. The additive systematic errors are summed up in quadrature in each bin i, to compute

$$\sigma_{syst,i}^{add} = \sqrt{(\sigma_{syst}^{stab})^2 + (\sigma_{syst}^{cells})^2 + (\sigma_{syst,i}^{MC})^2 + (\sigma_{syst,i}^{EFF2D})^2 + (\sigma_{syst,i}^{Trig})^2} \quad (6.14)$$

Notice that the first two contributions, σ_{syst}^{stab} and σ_{syst}^{cells}, are estimated globally for all kinematic bins and not bin-by-bin, so they contribute to each kinematic bin i in the same way. The final systematic uncertainty in a kinematic bin i is then calculated for each asymmetry combining additive and multiplicative systematic uncertainties as follows

$$\sigma_{syst,i} = \sqrt{\left(\sigma_{syst,i}^{add} \cdot \sigma_{stat,i}\right)^2 + \left(\Delta_i^{Meth} \cdot A_i\right)^2} \quad (6.15)$$

6.7   Results

The final results of the UA analysis are presented in Fig. 6.27. The error bars correspond to the statistical error, while the systematic uncertainties are represented by the full horizontal bands on the bottom side of each panel.

The polar angle asymmetry, λ, is primarily determined by large values of $\cos\theta_{CS}$ (the edges of the distribution). The acceptance of the COMPASS experiment is wider compared to past Drell-Yan experiments, nevertheless the edges of $\cos\theta_{CS}$ distribution are still affected by low acceptance (and are poorly populated), which causes general instabilities. The extraction of λ presented in this work is affected by relatively large systematic uncertainties mostly due to these edge-effects. On the other hand, the coefficient ν comes multiplied with $\sin^2\theta$ in the DY angular distribution. Therefore, it is sensitive to $\cos\theta_{CS}$ values around zero, where the acceptance is largest and a major part of the population is concentrated. For this reason, this amplitude is more stably determined compared to the λ. The strong dependence of ν on q_T was already observed by past experiments, and it is confirmed by these results. As far as μ asymmetry is concerned, the effect is found to be relatively small and negative.

The extracted values of λ and ν have been used to test the Lam-Tung [146] relation 1.42. The relation was evaluated using the λ and ν amplitudes and corresponding total uncertainties evaluated in each kinematic bin. The results
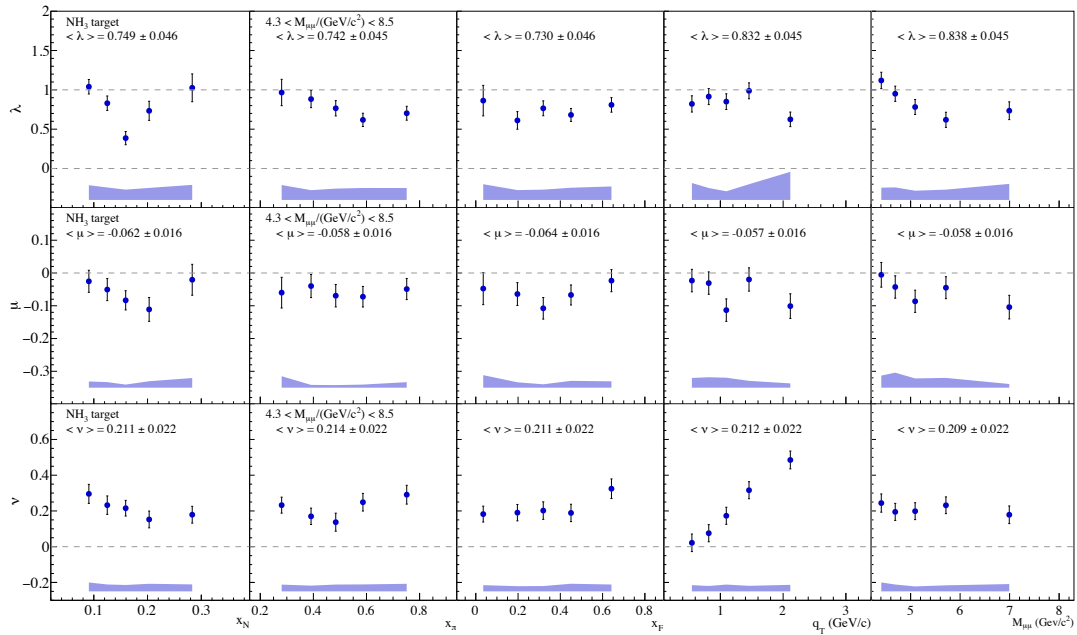
Fig. 6.27 The unpolarised asymmetries from the 2015 Drell-Yan run, extracted in the High Mass range. The overall systematic uncertainty is represented by the blue bands, and was estimated bin by bin.

are presented in Fig. 6.28. The results tend to agree with NA10 observations, but relatively large uncertainties do not allow to make conclusive remarks on the validity of the Lam-Tung relation.
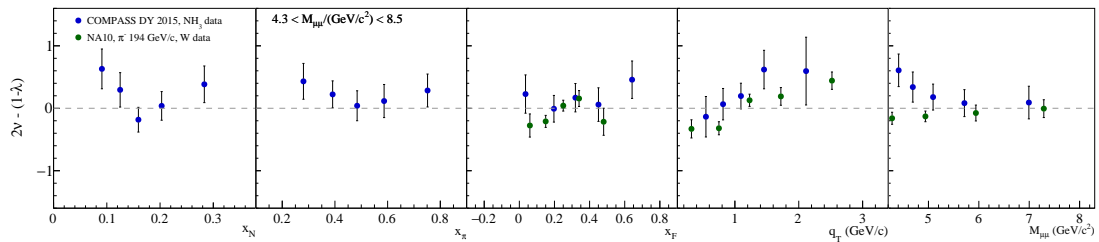
Fig. 6.28 Test of the Lam-Tung sum rule using the λ and ν values extracted from COMPASS 2015 data. The error bars are resulting from the propagation of both statistic and systematic errors.

Chapter 7

Conclusions

An important part of the physics programme of the COMPASS experiment at CERN is dedicated to the exploration of the transverse spin structure of the nucleon via measurements of spin (in)dependent azimuthal asymmetries in SIDIS and, recently, also in Drell-Yan processes. Study of the azimuthal effects induced by various spin-correlations in these two reactions is a complementary way to access the structure of the nucleon spin expressed in terms of transverse momentum dependent parton distribution functions (TMD PDFs). The test of the sign change of the Sivers and Boer-Mulders naive-time-reversal-odd TMDs PDFs measured in SIDIS on the one hand, and in Drell-Yan or W and Z-boson production on the other, represents a fundamental step in the validation of the TMD framework of QCD. Furthermore, also the genuine universality and process-independence of T-even TMD PDFs (*e.g.* the transversity and pretzelosity TMD PDFs) is to be proved yet. Non-zero quark Sivers TMD PDFs have been extracted from SIDIS single-differential results of HERMES [96], COMPASS [87, 88, 91, 95] and JLab [94] using both collinear [138, 139] and TMD evolution approaches [120, 140, 207–209]. The first measurement of the Sivers effect in the W and Z-boson production in collisions of transversely polarised protons at RHIC was reported by the STAR collaboration [210]. These measurements have been performed at corresponding hard scales defined by the mass of a given boson ($Q \approx 80$ GeV/c and 90 GeV/c). This regime is quite different from the one explored in fixed-target experiments where Q ranges approximately between 1 GeV/c and 9 GeV/c. Thus it is not excluded that TMD evolution effects may play a key role when describing the STAR results using the Sivers TMD PDFs extracted from fixed-target SIDIS results.

The COMPASS, high-energy fixed-target experiment located at CERN [15, 136], has the unique capability to explore the transverse-spin structure of the nucleon by the two alternative experimental approaches (SIDIS and DY), using mostly the same setup and accessing a similar kinematic region. In 2010, COM-

PASS collected SIDIS data using a 160 GeV/c polarised μ^+ beam scattering off a transversely polarised proton (NH$_3$) target. A few years later, in 2015, the experiment collected first ever polarised Drell-Yan data, making use of a 190 GeV/c π^- beam impinging on a transversely polarised NH$_3$ target. In this way COMPASS became the only experiment exploring the transverse spin structure of the nucleon via measurement of spin effects arising in these two alternative processes. COMPASS data offers the unprecedented opportunity to test the opposite-sign prediction by QCD for the T-odd TMD PDFs at practically the same hard scale, thereby minimising possible bias introduced by the TMD evolution.

In 2016 COMPASS has published the first multi-differential results for the Sivers asymmetry extracted from SIDIS data at four different hard scales [18] similar to the ones used in the COMPASS Drell-Yan analyses. In particular, the analysis was done for the range 4 GeV/c $< Q <$ 9 GeV/c, where the hard scale is very similar to the high mass range defined for Drell-Yan analyses. In this range, the Sivers asymmetry for positive hadrons was found to be above zero by 3.2 standard deviations of the total experimental accuracy. The COMPASS analysis presented in [18] is not limited only to the Sivers asymmetry but to all the SIDIS TSAs. The results, reported in Fig. 7.1, show a clear signal for the transversity-related asymmetry, $A_{UT}^{\sin(\phi_h - \phi_S - \pi)}$, for both positive and negative hadrons, whereas $A_{UT}^{\sin(3\phi_h - \phi_S)}$ effect, related to pretzelosity TMD PDF, is found to be quite small and compatible with zero.

In this thesis, the analysis of the 2015 Drell-Yan data has been presented. The simultaneous extraction of all the TSA asymmetries arising in the Drell-Yan cross-section (Eq. 1.25) was carried out using dimuon events with invariant mass between 4.3 GeV/c^2 and 8.5 GeV/c^2. The obtained TSAs are shown in Fig. 7.4 as a function of the variables x_N, x_π, x_F, $M_{\mu\mu}$ and q_T. Because of the relatively large statistical uncertainties, no clear trend is observed for any of the TSAs. The results for the extracted TSAs averaged over the entire kinematic range are presented in Fig. 7.2.

The average Sivers asymmetry $A_T^{\sin\varphi_S} = 0.060 \pm 0.057(\text{stat.}) \pm 0.040(\text{sys.})$ is found to be above zero at about one standard deviation of the total uncertainty. In Fig. 7.3 the result is compared with recent theoretical predictions from Refs. [207–209] that are based on standard DGLAP and two different TMD evolution approaches[1]. The positive sign of these theoretical predictions for the DY Sivers asymmetry was obtained by using the sign-change hypothesis for the Sivers TMD PDFs. These predictions were based on fits performed on the available

---

[1]Note that the kinematic constraints used in Refs. [207–209] differ from one to another and also from those used in the analysis presented in this work.
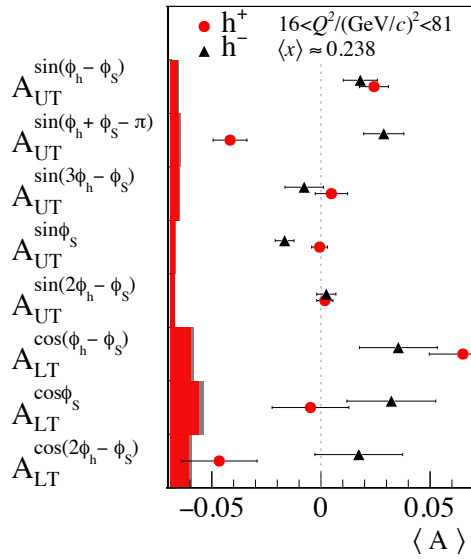
Fig. 7.1 Mean SIDIS TSAs measured by COMPASS at hard scale 4 GeV/c < Q < 9 GeV/c. The error bars represent statistical uncertainties. Systematic uncertainties are shown by the full bands next to the vertical axis. Plot from Ref. [18].
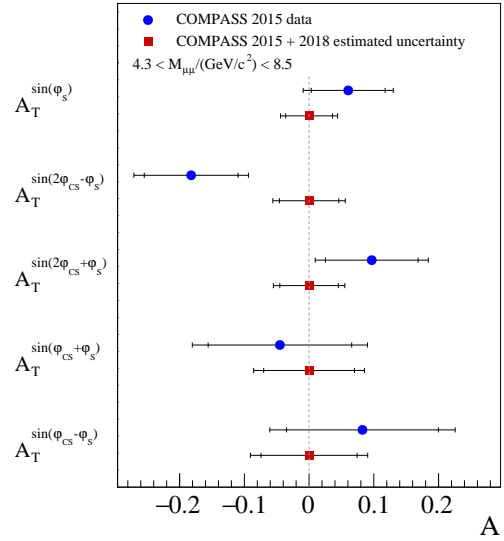
Fig. 7.2 In blue, DY TSAs averaged over the whole kinematic range. In red, estimated uncertainties on the TSAs obtained combining 2015 and 2018 data samples. The internal (external) error bars represent statistical (full experimental) uncertainties.

COMPASS SIDIS data for the Sivers TSA [88, 95]. The predictions evaluated without the sign-change hypothesis are also shown for the comparison (light-shaded curves and bands mirrored with respect to the main predictions). The figure shows that this first measurement of the DY Sivers asymmetry is consistent with the predicted change of sign for the Sivers function.

The results obtained for the other DY TSAs also look interesting. The transversity related TSA, $A_T^{sin(2\varphi_S-\varphi_{CS})}$, has been found to be negative with a significance of about two standard deviations. The value is compatible with the model calculations presented in Ref. [212] and serves as a valuable input to test the universality of the transversity TMD PDF. The $A_T^{sin(2\varphi_S+\varphi_{CS})}$ asymmetry, related to the nucleon pretzelosity TMD PDF, is measured to be positive with a significance of about one standard deviation. Since $A_T^{sin(2\varphi_S-\varphi_{CS})}$ and $A_T^{sin(\varphi_S-\varphi_{CS})}$ are related also to the Boer-Mulders TMD PDF of the pion, the extracted asymmetries may be also used to further study this function and to possibly determine its sign.

An alternative way to access nucleon TMD PDFs and address the sign-change issue is represented by the measurement of transverse momentum weighted asymmetries in SIDIS or Drell-Yan (wTSAs). This method allows to solve the convolution integrals over transverse momenta without making assumptions on the transverse momentum dependence of TMDs and FFs. Recently, COMPASS has
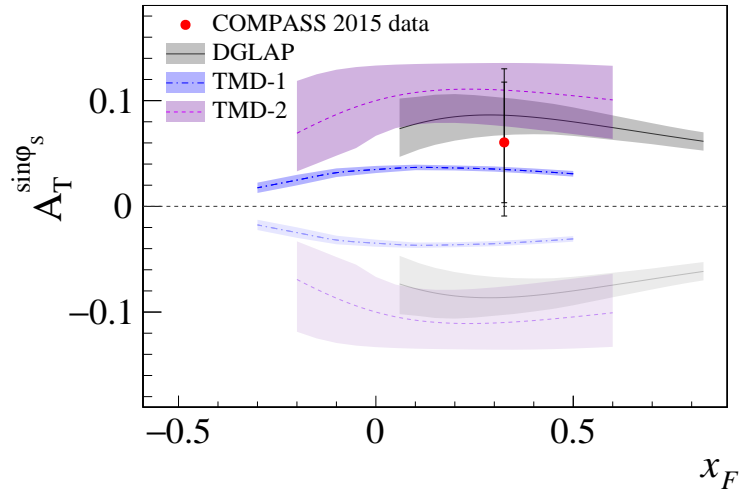
Fig. 7.3 The measured mean Sivers asymmetry and the theoretical predictions for different Q^2 evolution schemes from Refs.[211] (DGLAP), [208] (TMD1) and [209] (TMD2). The dark-shaded (light-shaded) predictions are evaluated with (without) the sign-change hypothesis. The error bar represents the total experimental uncertainty

evaluated the transverse momentum weighted Sivers asymmetries using the SIDIS data collected in 2010 [132]. In Fig. 7.6 the results for both positive and negative hadron TSAs weighted by $P_T/(zM)$ are shown as a function of x. The first extraction of q_T-weighted TSAs in Drell-Yan reactions has been presented in this thesis. The weighted TSAs are shown in Fig. 7.5 as a function of the variables x_N, x_π, x_F, and $M_{\mu\mu}$. The last column in Fig. 7.5 shows the results for the three extracted weighted TSAs integrated over the entire kinematic range. The weighted Sivers asymmetry is found to be ~ 0.3 standard deviations away from zero. The suppression of the effect compared to the standard TSA can be explained by the fact that the non-weighted Sivers TSA in last bin of q_T is small and compatible with zero (see Fig. 7.4). In the q_T-weighted case this range is strongly favoured (TSAs get larger weight) and so the overall asymmetry decreases. The pretzelosity related weighted TSA is found to be above zero of about ~ 1.2 standard deviations. This asymmetry is affected by large statistical uncertainties which is conditioned by the corresponding weight, $q_T^3/(2M_\pi M_N^2)$. This is visible in particular in the first bin of x_π and x_F (since these variables are anti-correlated with q_T). The transversity-related wTSA is measured to be ~ 2 standard deviations below zero.

The last section of the Thesis was dedicated to the measurement of the unpolarised Drell-Yan azimuthal asymmetries, λ, μ and ν. In the naive DY model (within the collinear perturbative QCD approach), the parton intrinsic transverse momentum and QCD radiative corrections are neglected, and unpolarized amplitudes follow the equalities $\lambda = 1$ and $\mu = \nu = 0$, which satisfies the Lam-Tung relation [146]. Possible deviations of the angular coefficients from these naive
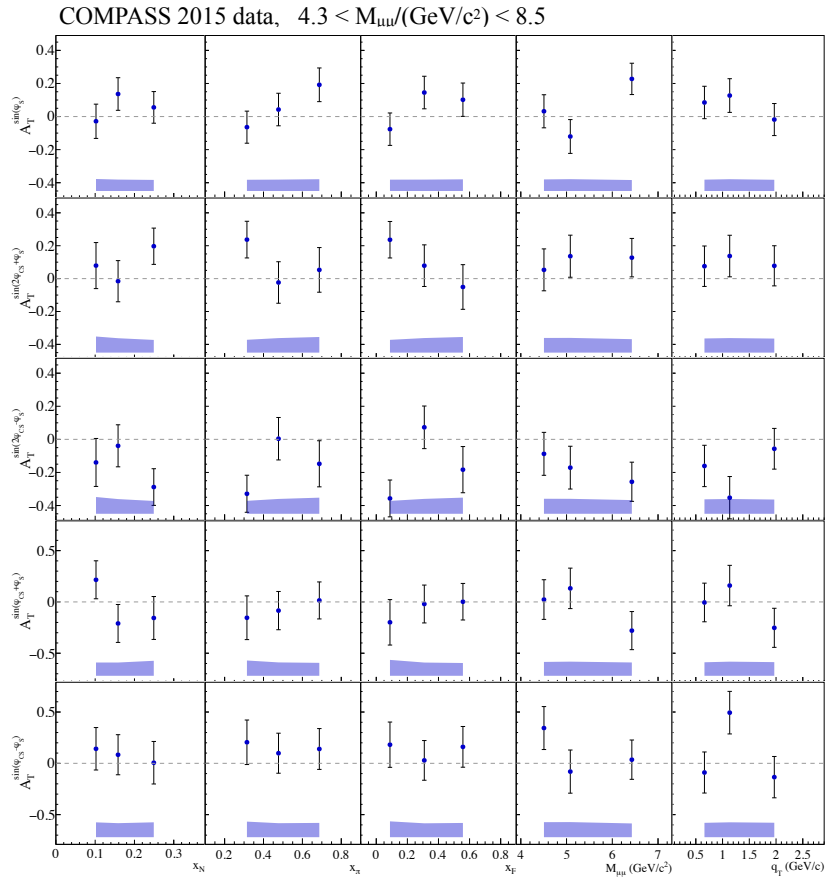
Fig. 7.4 Extracted Drell-Yan TSAs related to Sivers, pretzelosity and transversity TMD PDFs (top to bottom). In the last two rows the results obtained for two *subleading-twist* TSAs are shown. The error bars represent the statistical uncertainties. The horizontal error-bands indicate the systematic uncertainties.
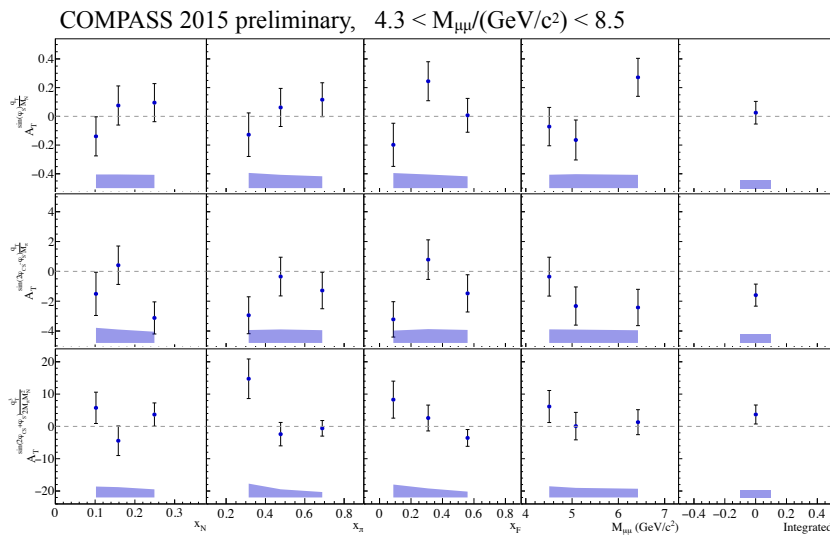
Fig. 7.5 The q_T-weighted TSAs extracted from COMPASS 2015 Drell-Yan data. The horizontal error-bands indicate the systematic uncertainties.
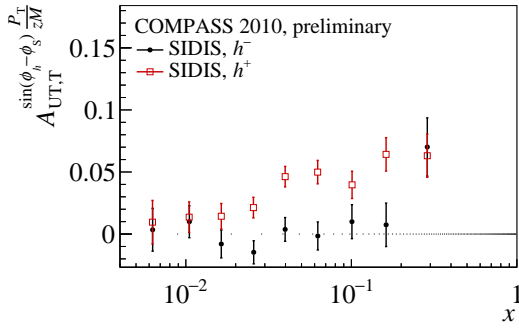
Fig. 7.6 Weighted Sivers asymmetry extracted by COMPASS from SIDIS 2010 data [132] for positive and **negative** hadrons. The error bars represent only the statistical uncertainties.
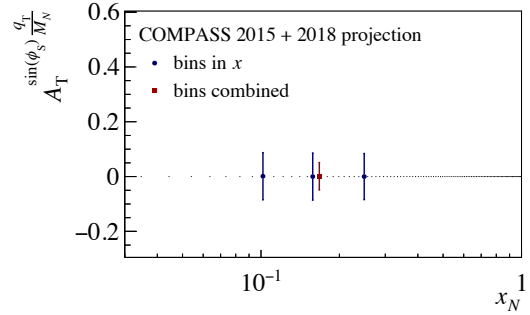
Fig. 7.7 Projected statistical uncertainties for the q_T-weighted Sivers TSA after 2018 Drell-Yan data taking.

predictions can be attributed to the non-vanishing transverse momentum of the partons inside the nucleon or to next to leading order contributions.

The coefficient ν, which corresponds to the amplitude of $\cos 2\varphi_{CS}$ modulation in the azimuthal angle φ_{CS}, triggers a lot of attention since within TMD-formalism it probes the Boer-Mulders TMD PDF [80] of the nucleon. In the last decades, the target polarization independent angular asymmetries in the Drell-Yan process were measured at different fixed-target experiments [151, 153, 156, 200]. This wide spectra of obtained results could not be described using only predictions based on TMD or pQCD approach. Recent results coming from experiments at Tevatron [162] and LHC [163] brought again the focus on these observables. Different theoretical groups tried to estimate the role of the QCD next-to-leading order corrections and to interpret the results obtained at both fixed-target and colliders regimes [144, 145, 164] and to match them.

Even if the analysis of Drell-Yan unpolarised azimuthal asymmetries presented in this Thesis is enough comprehensive, since by the time of this work the detailed MC-description of the detector and trigger efficiencies was not fully accomplished, the obtained results have not been released yet and should be considered as preliminary. Nevertheless, the impact of the efficiency-maps was estimated and taken into account at the level of the systematic uncertainties, as well as that one of trigger efficiencies. Applying the final detector and trigger the efficiency-maps in the simulation is a mandatory phase, but it is not expected to change dramatically the results presented in this Thesis. In Fig. 7.8 extracted λ, μ and ν asymmetries (NH_3 target, high mass range) are shown together with the NA10 results from Refs. [151, 153], demonstrating the potential of COMPASS data in this field.

The ν amplitude shows clear non-zero effect increasing with q_T, confirming the observations made by previous Drell-Yan experiments [151, 153, 200]. In-
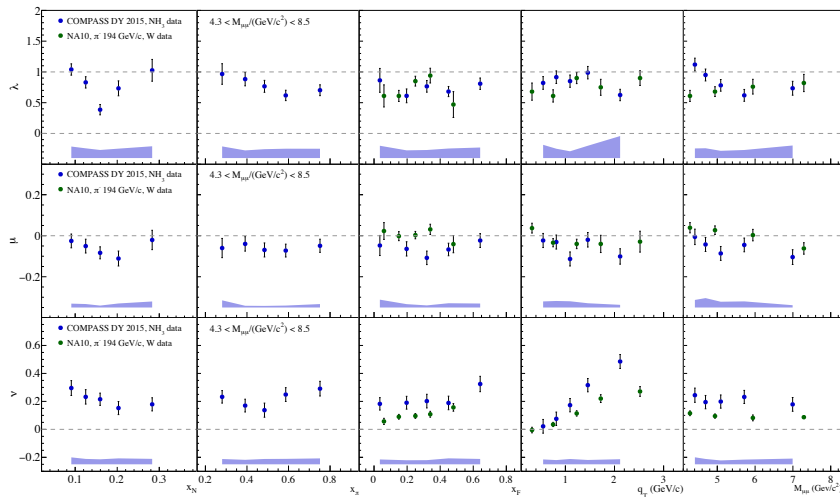
Fig. 7.8 Preliminary results on the Drell-Yan unpolarised asymmetries in the Collins-Soper frame from COMPASS 2015 Drell-Yan data (NH_3 target). The horizontal full bands indicate the systematic uncertainties. The green dots represent the results obtained by NA10 [151] with π^- beam (194 GeV/c) impinging on W target.

triguingly, the asymmetry measured at COMPASS is found to be significantly larger than the one measured by NA10, as can be seen in Fig. 7.8. This interesting observation has still to be clarified. In particular, one has to take into account that the two experiments have different kinematic acceptances and their phase-space coverage is not the same. The μ asymmetry at COMPASS is found to be negative and relatively small compared to ν UA, while for NA10 the effect was found to be compatible with zero within uncertainties. The results obtained for polar angle asymmetry λ, at this stage of the analysis are affected by large systematic uncertainties, mainly driven by the low acceptance of the experiment in the edges of $\cos\theta_{CS}$ distribution. In average, the data-points obtained for λ appear to be comparable with the NA10 results.

The extracted values of λ and ν were also used to test the Lam-Tung relation [146], corresponding results are presented in Fig. 7.9. Relatively large uncertainties do not allow to make conclusive remarks on the validity of the Lam-Tung relation. Nevertheless, the comparison with NA10 did not reveal strong inconsistencies within available accuracy.

Finally, even if not included in this work, it is worth to mention that the unpolarised Drell-Yan studies are being performed at COMPASS also for the nuclear targets (W and Al).

In May 2018, COMPASS will continue the measurements of the polarized Drell-Yan process for another full data-taking year. The goal is to considerably improve the statistical precision of the Sivers and other azimuthal asymmetries measured in the Drell-Yan process. Compared to the 2015 run, the number of
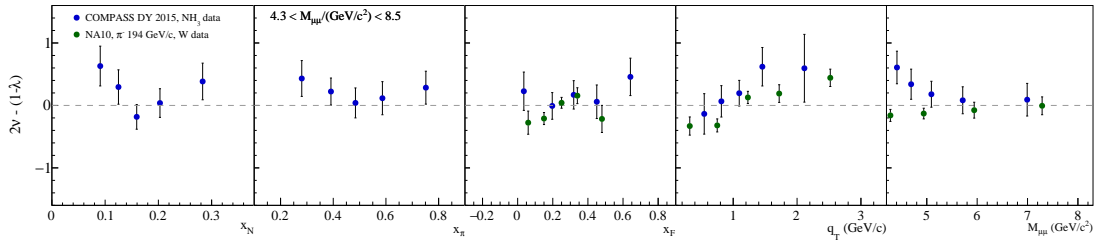
Fig. 7.9 Test of the Lam-Tung sum rule performed using the preliminary angular coefficients λ and μ extracted in this work and shown in Fig. 7.8. The error bars include both systematic and statistical uncertainties. The green dots represent the results obtained by NA10 [151] with π^- beam (194 GeV/c) on W target.

events to be accumulated is expected to increase by a factor 1.5. For the combined 2015 + 2018 data samples this would correspond to ~ 87500 dimuon pairs in the high mass range entering the analysis. This expectation is mainly based on the longer data-taking period (106 effective physics-data collection days in 2015 against 140 days in 2018) and on some additional gain that can be achieved in 2018 *e.g.* due to increased efficiency of the beam telescope and expected stability of the polarised target equipment in high-radiation environment.

The projected uncertainties for all the Drell-Yan TSAs after 2018 data-taking are demonstrated in red in Fig 7.2, together with the results of the 2015 run. The systematic uncertainty was assumed to be 0.7 times the statistical uncertainly, as it was estimated in 2015 analysis. The uncertainty on the Sivers asymmetry would decrease down to $\sim 4\%$. The projected statistical uncertainty that will be achieved after 2018 data taking for the averaged q_T-weighted Sivers TSA is illustrated in Fig. 7.7. As far as the Drell-Yan UAs are concerned, the projected statistical uncertainties for λ, μ and ν are shown in Fig. 7.10
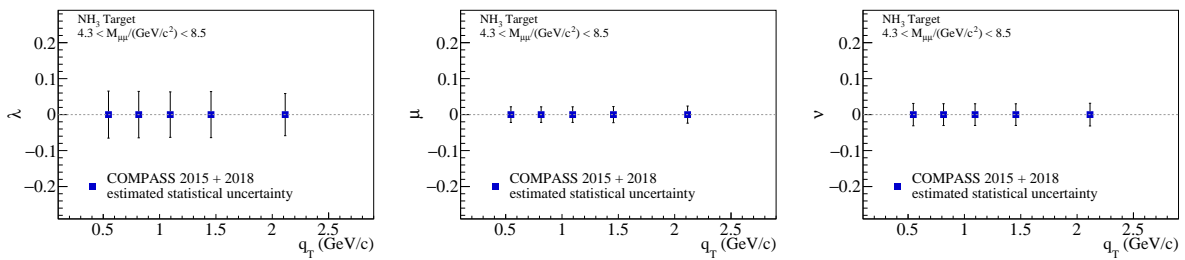
Fig. 7.10 Projected statistical uncertainties for the Drell-Yan unpolarised asymmetries after 2018 data-taking. From left to right: λ, μ and ν. All the uncertainties are presented in q_T bins.

Combined with COMPASS SIDIS results provided Drell-Yan data will serve as a crucial input for the QCD universality studies of TMD PDFs. Obtained results will be used to constrain various TMD evolution based theoretical models for

Sivers and other Drell-Yan azimuthal asymmetries and will play a unique role in our general understanding of spin structure of the nucleon.

List of figures

List of tables

References

[1] M. Gell-Mann. A schematic model of baryons and mesons. *Physics Letters*, 8(3):214 – 215, 1964.

[2] G. Zweig. An SU(3) model for strong interaction symmetry and its breaking. Version 2. In D.B. Lichtenberg and Simon Peter Rosen, editors, *DEVELOPMENTS IN THE QUARK THEORY OF HADRONS. VOL. 1. 1964 - 1978*, pages 22–101. 1964.

[3] Richard P. Feynman. Very high-energy collisions of hadrons. *Phys. Rev. Lett.*, 23:1415–1417, Dec 1969.

[4] John R. Ellis and Robert L. Jaffe. A Sum Rule for Deep Inelastic Electroproduction from Polarized Protons. *Phys. Rev.*, D9:1444, 1974. [Erratum: Phys. Rev.D10,1669(1974)].

[5] J. Ashman et al. A measurement of the spin asymmetry and determination of the structure function g1 in deep inelastic muon-proton scattering. *Physics Letters B*, 206(2):364 – 370, 1988.

[6] C. Adolph et al. Final COMPASS results on the deuteron spin-dependent structure function g_1^d and the Bjorken sum rule. *Phys. Lett.*, B769:34–41, 2017.

[7] C. Adolph et al. Leading and next-to-leading order gluon polarization in the nucleon and longitudinal double spin asymmetries from open charm muoproduction. *Phys. Rev. D*, 87:052018, Mar 2013.

[8] L. Dick et al. Spin Effects in the Inclusive Reactions pi+- Polarized p –> pi+- Anything at 8-GeV/c. *Phys. Lett.*, 57B:93–96, 1975.

[9] R. P. Feynman, R. D. Field, and G. C. Fox. Correlations Among Particles and Jets Produced with Large Transverse Momenta. *Nucl. Phys.*, B128:1–65, 1977.

[10] Robert N. Cahn. Azimuthal Dependence in Leptoproduction: A Simple Parton Model Calculation. *Phys. Lett.*, 78B:269–273, 1978.

[11] John C. Collins and Davison E. Soper. Angular distribution of dileptons in high-energy hadron collisions. *Phys. Rev. D*, 16:2219–2225, Oct 1977.

[12] John C. Collins and Davison E. Soper. Back-to-back jets in qcd. *Nuclear Physics B*, 193(2):381 – 443, 1981.

[13] Aram Kotzinian. New quark distributions and semi-inclusive electroproduction on polarized nucleons. *Nuclear Physics B*, 441(1):234 – 256, 1995.

[14] P. J. Mulders and R. D. Tangerman. The Complete tree level result up to order 1/Q for polarized deep inelastic leptoproduction. *Nucl. Phys.*, B461:197–237, 1996. [Erratum: Nucl. Phys.B484,538(1997)].

[15] P. Abbon et al. The COMPASS experiment at CERN. *Nucl. Instrum. Meth.*, A577:455–518, 2007.

[16] P. Abbon et al. The compass setup for physics with hadron beams. *Nuclear Instruments and Methods in Physics Research Section A: Accelerators, Spectrometers, Detectors and Associated Equipment*, 779:69 – 115, 2015.

[17] John C. Collins. Leading twist single transverse-spin asymmetries: Drell-Yan and deep inelastic scattering. *Phys. Lett.*, B536:43–48, 2002.

[18] C Adolph et al. Sivers asymmetry extracted in SIDIS at the hard scales of the Drell–Yan process at COMPASS. *Phys. Lett.*, B770:138–145, 2017.

[19] C. S. Lam and Wu-Ki Tung. A Parton Model Relation Sans QCD Modifications in Lepton Pair Productions. *Phys. Rev.*, D21:2712, 1980.

[20] C.R. Regali. *Exclusive event generation for the COMPASS-II experiment at CERN and improvements for the Monte-Carlo chain*. PhD thesis, Albert-Ludwigs-Universität Freiburg, 2016.

[21] T. Szameitat. *New Geant4-based Monte Carlo Software for the COMPASS-II Experiment at CERN*. PhD thesis, Albert-Ludwigs-Universität Freiburg, 2017.

[22] M. Anselmino, A. Efremov, and E. Leader. The Theory and phenomenology of polarized deep inelastic scattering. *Phys. Rept.*, 261:1–124, 1995. [Erratum: Phys. Rept.281,399(1997)].

[23] J. D. Bjorken. Asymptotic Sum Rules at Infinite Momentum. *Phys. Rev.*, 179:1547–1553, 1969.

[24] M. Breidenbach, J. I. Friedman, H. W. Kendall, E. D. Bloom, D. H. Coward, H. DeStaebler, J. Drees, L. W. Mo, and R. E. Taylor. Observed behavior of highly inelastic electron-proton scattering. *Phys. Rev. Lett.*, 23:935–939, Oct 1969.

[25] D. H. Coward, H. DeStaebler, R. A. Early, J. Litt, A. Minten, L. W. Mo, W. K. H. Panofsky, R. E. Taylor, M. Breidenbach, J. I. Friedman, H. W. Kendall, P. N. Kirk, B. C. Barish, J. Mar, and J. Pine. Electron-proton elastic scattering at high momentum transfers. *Phys. Rev. Lett.*, 20:292–295, Feb 1968.

[26] J. S. Poucher, M. Breidenbach, R. Ditzler, J. I. Friedman, H. W. Kendall, E. D. Bloom, R. L. A. Cottrell, D. H. Coward, H. DeStaebler, C. L. Jordan, H. Piel, and R. E. Taylor. High-energy single-arm inelastic $e - p$ and $e - d$ scattering at 6 and 10°. *Phys. Rev. Lett.*, 32:118–121, Jan 1974.

[27] J. D. Bjorken and Emmanuel A. Paschos. Inelastic Electron Proton and gamma Proton Scattering, and the Structure of the Nucleon. *Phys. Rev.*, 185:1975–1982, 1969.

[28] Curtis G. Callan, Jr. and David J. Gross. High-energy electroproduction and the constitution of the electric current. *Phys. Rev. Lett.*, 22:156–159, 1969.

[29] S. Wandzura and F. Wilczek. Sum rules for spin-dependent electroproduction- test of relativistic constituent quarks. *Physics Letters B*, 72(2):195 – 198, 1977.

[30] L. W. Whitlow, E. M. Riordan, S. Dasu, Stephen Rock, and A. Bodek. Precise measurements of the proton and deuteron structure functions from a global analysis of the SLAC deep inelastic electron scattering cross-sections. *Phys. Lett.*, B282:475–482, 1992.

[31] A. C. Benvenuti et al. A High Statistics Measurement of the Proton Structure Functions F(2) (x, Q**2) and R from Deep Inelastic Muon Scattering at High Q**2. *Phys. Lett.*, B223:485–489, 1989.

[32] M. R. Adams et al. Proton and deuteron structure functions in muon scattering at 470-GeV. *Phys. Rev.*, D54:3006–3056, 1996.

[33] M. Arneodo et al. Measurement of the proton and deuteron structure functions, F2(p) and F2(d), and of the ratio sigma-L / sigma-T. *Nucl. Phys.*, B483:3–43, 1997.

[34] H. Abramowicz et al. Combination of measurements of inclusive deep inelastic $e^{\pm}p$ scattering cross sections and QCD analysis of HERA data. *Eur. Phys. J.*, C75(12):580, 2015.

[35] K. A. Olive et al. Review of Particle Physics. *Chin. Phys.*, C38:090001, 2014.

[36] Guido Altarelli. Partons in Quantum Chromodynamics. *Phys. Rept.*, 81:1, 1982.

[37] Yuri L. Dokshitzer. Calculation of the Structure Functions for Deep Inelastic Scattering and e+ e- Annihilation by Perturbation Theory in Quantum Chromodynamics. *Sov. Phys. JETP*, 46:641–653, 1977. [Zh. Eksp. Teor. Fiz.73,1216(1977)].

[38] V. N. Gribov and L. N. Lipatov. Deep inelastic e p scattering in perturbation theory. *Sov. J. Nucl. Phys.*, 15:438–450, 1972. [Yad. Fiz.15,781(1972)].

[39] G. Altarelli and G. Parisi. Asymptotic freedom in parton language. *Nuclear Physics B*, 126(2):298 – 318, 1977.

[40] R. D. Klem, J. E. Bowers, H. W. Courant, H. Kagan, M. L. Marshak, E. A. Peterson, K. Ruddick, W. H. Dragoset, and J. B. Roberts. Measurement of Asymmetries of Inclusive Pion Production in Proton Proton Interactions at 6-GeV/c and 11.8-GeV/c. *Phys. Rev. Lett.*, 36:929–931, 1976.

[41] W. H. Dragoset, J. B. Roberts, J. E. Bowers, H. W. Courant, H. Kagan, M. L. Marshak, E. A. Peterson, K. Ruddick, and R. D. Klem. Asymmetries in Inclusive Proton-Nucleon Scattering at 11.75-GeV/c. *Phys. Rev.*, D18:3939–3954, 1978.

[42] M. J. Alguard et al. Deep-inelastic $e - p$ asymmetry measurements and comparison with the bjorken sum rule and models of proton spin structure. *Phys. Rev. Lett.*, 41:70–73, Jul 1978.

[43] M. J. Alguard et al. Deep inelastic scattering of polarized electrons by polarized protons. *Phys. Rev. Lett.*, 37:1261–1265, Nov 1976.

[44] G. Baum et al. Measurement of asymmetry in spin-dependent $e - p$ resonance-region scattering. *Phys. Rev. Lett.*, 45:2000–2003, Dec 1980.

[45] G. Baum et al. New measurement of deep-inelastic $e - p$ asymmetries. *Phys. Rev. Lett.*, 51:1135–1138, Sep 1983.

[46] P. L. Anthony et al. Deep inelastic scattering of polarized electrons by polarized [3]he and the study of the neutron spin structure. *Phys. Rev. D*, 54:6620–6650, Dec 1996.

[47] K. Abe et al. Measurements of the proton and deuteron spin structure functions g_1 and g_2. *Phys. Rev. D*, 58:112003, Oct 1998.

[48] P.L. Anthony et al. Measurement of the deuteron spin structure function g1d(x) for 1 (gev/c)2<q2<40 (gev/c)2. *Physics Letters B*, 463(2):339 – 345, 1999.

[49] J. Ashman et al. An Investigation of the Spin Structure of the Proton in Deep Inelastic Scattering of Polarized Muons on Polarized Protons. *Nucl. Phys.*, B328:1, 1989.

[50] V.Yu. Alexakhin et al. The deuteron spin-dependent structure function g1d and its first moment. *Physics Letters B*, 647(1):8 – 17, 2007.

[51] M.G. Alekseev et al. The spin-dependent structure function of the proton g1p and a test of the bjorken sum rule. *Physics Letters B*, 690(5):466 – 472, 2010.

[52] M.G. Alekseev et al. Quark helicity distributions from longitudinal spin asymmetries in muon–proton and muon–deuteron scattering. *Physics Letters B*, 693(3):227 – 235, 2010.

[53] X. Zheng et al. Precision measurement of the neutron spin asymmetry A1**N and spin flavor decomposition in the valence quark region. *Phys. Rev. Lett.*, 92:012004, 2004.

[54] K.V. Dharmawardane et al. Measurement of the x- and q2-dependence of the asymmetry a1 on the nucleon. *Physics Letters B*, 641(1):11 – 17, 2006.

[55] B. Adeva et al. Spin asymmetries A_1 and structure functions g_1 of the proton and the deuteron from polarized high energy muon scattering. *Phys. Rev. D*, 58:112001, Oct 1998.

[56] P.L Anthony et al. Measurements of the q2-dependence of the proton and neutron spin structure functions g1p and g1n. *Physics Letters B*, 493(1):19 – 28, 2000.

[57] A. Airapetian et al. Precise determination of the spin structure function g_1 of the proton, deuteron, and neutron. *Phys. Rev. D*, 75:012007, Jan 2007.

[58] C. Adolph et al. The spin structure function g_1^{p} of the proton and a test of the Bjorken sum rule. *Phys. Lett.*, B753:18–28, 2016.

[59] Daniel de Florian, Rodolfo Sassot, and Marco Stratmann. Global analysis of fragmentation functions for pions and kaons and their uncertainties. *Phys. Rev.*, D75:114010, 2007.

[60] B. Adeva et al. Polarisation of valence and non-strange sea quarks in the nucleon from semi-inclusive spin asymmetries. *Physics Letters B*, 369(1):93 – 100, 1996.

[61] B. Adeva et al. Polarised quark distributions in the nucleon from semi-inclusive spin asymmetries. *Physics Letters B*, 420(1):180 – 190, 1998.

[62] K. Ackerstaff et al. Flavor decomposition of the polarized quark distributions in the nucleon from inclusive and semi-inclusive deep-inelastic scattering. *Physics Letters B*, 464(1):123 – 134, 1999.

[63] A. Airapetian et al. Flavor decomposition of the sea-quark helicity distributions in the nucleon from semiinclusive deep inelastic scattering. *Phys. Rev. Lett.*, 92:012005, Jan 2004.

[64] A. Airapetian et al. Quark helicity distributions in the nucleon for up, down, and strange quarks from semi-inclusive deep-inelastic scattering. *Phys. Rev. D*, 71:012003, Jan 2005.

[65] A. Airapetian et al. Measurement of parton distributions of strange quarks in the nucleon from charged-kaon production in deep-inelastic scattering on the deuteron. *Physics Letters B*, 666(5):446 – 450, 2008.

[66] A. Adare et al. Measurement of parity-violating spin asymmetries in $W^{\pm}$ production at midrapidity in longitudinally polarized $p+p$ collisions. *Phys. Rev.*, D93(5):051103, 2016.

[67] Qinghua Xu. Measurement of Longitudinal Single-Spin Asymmetry for $W^{\pm}$ Production in Polarized Proton+Proton Collisions at STAR. *PoS*, DIS2017:226, 2018.

[68] D.L. Adams et al. Measurement of the double-spin asymmetry all for inclusive multi-γ pair production with 200 gev/c polarized proton beam and polarized proton target. *Physics Letters B*, 336(2):269 – 274, 1994.

[69] B. Adeva et al. Spin asymmetries for events with high p_T hadrons in dis and an evaluation of the gluon polarization. *Phys. Rev. D*, 70:012002, Jul 2004.

[70] A. Airapetian et al. Measurement of the spin asymmetry in the photoproduction of pairs of high- p_T hadrons at hermes. *Phys. Rev. Lett.*, 84:2584–2588, Mar 2000.

[71] E. S. Ageev et al. Gluon polarization in the nucleon from quasi-real photoproduction of high-p(T) hadron pairs. *Phys. Lett.*, B633:25–32, 2006.

[72] M. Alekseev et al. Direct Measurement of the Gluon Polarisation in the Nucleon via Charmed Meson Production. 2008.

[73] A. Airapetian et al. Leading-order determination of the gluon polarization from high-p t hadron electroproduction. *Journal of High Energy Physics*, 2010(8):130, Aug 2010.

[74] C. Adolph et al. Leading order determination of the gluon polarisation from DIS events with high-p_T hadron pairs. *Phys. Lett.*, B718:922–930, 2013.

[75] C. Adolph et al. Leading and Next-to-Leading Order Gluon Polarization in the Nucleon and Longitudinal Double Spin Asymmetries from Open Charm Muoproduction. *Phys. Rev.*, D87(5):052018, 2013.

[76] Daniel de Florian, Rodolfo Sassot, Marco Stratmann, and Werner Vogelsang. Extraction of spin-dependent parton densities and their uncertainties. *Phys. Rev. D*, 80:034030, Aug 2009.

[77] Elliot Leader, Aleksander V. Sidorov, and Dimiter B. Stamenov. Determination of polarized parton densities from a qcd analysis of inclusive and semi-inclusive deep inelastic scattering data. *Phys. Rev. D*, 82:114018, Dec 2010.

[78] M. Burkardt and B. Pasquini. Modelling the nucleon structure. *Eur. Phys. J.*, A52(6):161, 2016.

[79] Alessandro Bacchetta, Markus Diehl, Klaus Goeke, Andreas Metz, Piet J. Mulders, and Marc Schlegel. Semi-inclusive deep inelastic scattering at small transverse momentum. *JHEP*, 02:093, 2007.

[80] Daniel Boer and P. J. Mulders. Time reversal odd distribution functions in leptoproduction. *Phys. Rev.*, D57:5780–5786, 1998.

[81] Stanley J. Brodsky, Dae Sung Hwang, and Ivan Schmidt. Final-state interactions and single-spin asymmetries in semi-inclusive deep inelastic scattering. *Physics Letters B*, 530(1):99 – 107, 2002.

[82] Stanley J. Brodsky, Dae Sung Hwang, and Ivan Schmidt. Initial-state interactions and single-spin asymmetries in drell–yan processes. *Nuclear Physics B*, 642(1):344 – 356, 2002.

[83] S. D. Drell and Tung-Mow Yan. Partons and their Applications at High-Energies. *Annals Phys.*, 66:578, 1971. [Annals Phys.281,450(2000)].

[84] Aram Kotzinian. New quark distributions and semiinclusive electroproduction on the polarized nucleons. *Nucl. Phys.*, B441:234–248, 1995.

[85] Alessandro Bacchetta, Markus Diehl, Klaus Goeke, Andreas Metz, Piet J. Mulders, and Marc Schlegel. Semi-inclusive deep inelastic scattering at small transverse momentum. *Journal of High Energy Physics*, 2007(02):093, 2007.

[86] S. Wandzura and Frank Wilczek. Sum Rules for Spin Dependent Electroproduction: Test of Relativistic Constituent Quarks. *Phys. Lett.*, 72B:195–198, 1977.

[87] E. S. Ageev et al. A New measurement of the Collins and Sivers asymmetries on a transversely polarised deuteron target. *Nucl. Phys.*, B765:31–70, 2007.

[88] M. Alekseev et al. Collins and Sivers asymmetries for pions and kaons in muon-deuteron DIS. *Phys. Lett.*, B673:127–135, 2009.

[89] C. Adolph et al. Experimental investigation of transverse spin asymmetries in muon-p SIDIS processes: Collins asymmetries. *Phys. Lett.*, B717:376–382, 2012.

[90] M. G. Alekseev et al. Measurement of the Collins and Sivers asymmetries on transversely polarised protons. *Phys. Lett.*, B692:240–246, 2010.

[91] C. Adolph et al. Collins and Sivers asymmetries in muonproduction of pions and kaons off transversely polarised protons. *Phys. Lett.*, B744:250–259, 2015.

[92] A. Airapetian et al. Single-spin asymmetries in semi-inclusive deep-inelastic scattering on a transversely polarized hydrogen target. *Phys. Rev. Lett.*, 94:012002, 2005.

[93] A. Airapetian et al. Effects of transversity in deep-inelastic scattering by polarized protons. *Physics Letters B*, 693(1):11 – 16, 2010.

[94] X. Qian et al. Single spin asymmetries in charged pion production from semi-inclusive deep inelastic scattering on a transversely polarized ^{3}he target at $Q^2 = 1.4{\sim}2.7$ gev^2. *Phys. Rev. Lett.*, 107:072003, Aug 2011.

[95] C. Adolph et al. II – Experimental investigation of transverse spin asymmetries in μ-p SIDIS processes: Sivers asymmetries. *Phys. Lett.*, B717:383–389, 2012.

[96] A. Airapetian et al. Observation of the naive-t-odd sivers effect in deep-inelastic scattering. *Phys. Rev. Lett.*, 103:152002, Oct 2009.

[97] C. Adolph et al. Measurement of azimuthal hadron asymmetries in semi-inclusive deep inelastic scattering off unpolarised nucleons. *Nucl. Phys.*, B886:1046–1077, 2014.

[98] A. Airapetian et al. Azimuthal distributions of charged hadrons, pions, and kaons produced in deep-inelastic scattering off unpolarized protons and deuterons. *Phys. Rev. D*, 87:012010, Jan 2013.

[99] Aram Kotzinian. Beyond Collins and Sivers: Further measurements of the target transverse spin-dependent azimuthal asymmetries in semi-inclusive DIS from COMPASS. In *Proceedings, 15th International Workshop on*

Deep-inelastic scattering and related subjects (DIS 2007). Vol. 1 and 2: Munich, Germany, April 16-20, 2007, pages 647–650, 2007.

[100] B. Parsamyan. Six "beyond collins and sivers" transverse spin asymmetries at compass. *Physics of Particles and Nuclei*, 45(1):158, 2014.

[101] L. L. Pappalardo. Transverse spin phenomena in semi-inclusive deep-inelastic scattering of electrons and positrons off polarized hydrogen. *Nuovo Cim.*, B125N1:51–70, 2010.

[102] Y. Zhang et al. Measurement of pretzelosity asymmetry of charged pion production in Semi-Inclusive Deep Inelastic Scattering on a polarized ^{3}He target. *Phys. Rev.*, C90(5):055209, 2014.

[103] L. L. Pappalardo and M. Diefenthaler. Measurements of Double-Spin Asymmetries in SIDIS of Longitudinally Polarized Leptons off Transversely Polarized Protons. 2011.

[104] J. Huang et al. Beam-target double-spin asymmetry A_{lt} in charged pion production from deep inelastic scattering on a transversely polarized ^{3}he target at $1.4 < Q^2 < 2.7$ gev^2. *Phys. Rev. Lett.*, 108:052001, Jan 2012.

[105] M. Osipenko et al. Measurement of semi-inclusive π^+ electroproduction off the proton. *Phys. Rev. D*, 80:032004, Aug 2009.

[106] M. Anselmino, A. Efremov, A. Kotzinian, and B. Parsamyan. Transverse momentum dependence of the quark helicity distributions and the Cahn effect in double-spin asymmetry A(LL) in Semi Inclusive DIS. *Phys. Rev.*, D74:074015, 2006.

[107] Vincenzo Barone, Stefano Melis, and Alexei Prokudin. The Boer-Mulders effect in unpolarized SIDIS: An Analysis of the COMPASS and HERMES data on the cos 2 phi asymmetry. *Phys. Rev.*, D81:114026, 2010.

[108] Christopher Lefky and Alexei Prokudin. Extraction of the distribution function $h_{1T}^\perp$ from experimental data. *Phys. Rev.*, D91(3):034010, 2015.

[109] John P. Ralston and Davison E. Soper. Production of Dimuons from High-Energy Polarized Proton Proton Collisions. *Nucl. Phys.*, B152:109, 1979.

[110] M. Anselmino, M. Boglione, U. D'Alesio, J. O. Gonzalez Hernandez, S. Melis, F. Murgia, and A. Prokudin. Collins functions for pions from SIDIS and new e^+e^- data: a first glance at their transverse momentum dependence. *Phys. Rev.*, D92(11):114023, 2015.

[111] R. Seidl et al. Measurement of azimuthal asymmetries in inclusive production of hadron pairs in e^+e^- annihilation at belle. *Phys. Rev. Lett.*, 96:232002, Jun 2006.

[112] R. Seidl et al. Measurement of Azimuthal Asymmetries in Inclusive Production of Hadron Pairs in e+e- Annihilation at s**(1/2) = 10.58-GeV. *Phys. Rev.*, D78:032011, 2008. [Erratum: Phys. Rev.D86,039905(2012)].

[113] Dennis W. Sivers. Single Spin Production Asymmetries from the Hard Scattering of Point-Like Constituents. *Phys. Rev.*, D41:83, 1990.

[114] J. Antille, L. Dick, L. Madansky, D. Perret-Gallix, M. Werlen, A. Gonidec, K. Kuroda, and P. Kyberd. Spin Dependence of the Inclusive Reaction pp (Polarized) $\to \pi^0 X$ at 24-GeV/c for High $p_T \pi^0$ Produced in the Central Region. *Phys. Lett.*, 94B:523–526, 1980.

[115] John C. Collins, Davison E. Soper, and George F. Sterman. Factorization of Hard Processes in QCD. *Adv. Ser. Direct. High Energy Phys.*, 5:1–91, 1989.

[116] Alessandro Bacchetta, Daniel Boer, Markus Diehl, and Piet J. Mulders. Matches and mismatches in the descriptions of semi-inclusive processes at low and high transverse momentum. *JHEP*, 08:023, 2008.

[117] John C. Collins, Davison E. Soper, and George F. Sterman. Transverse Momentum Distribution in Drell-Yan Pair and W and Z Boson Production. *Nucl. Phys.*, B250:199–224, 1985.

[118] John Collins. *Foundations of perturbative QCD*. Cambridge University Press, 2013.

[119] S. Mert Aybat and Ted C. Rogers. TMD Parton Distribution and Fragmentation Functions with QCD Evolution. *Phys. Rev.*, D83:114042, 2011.

[120] S. Mert Aybat, Alexei Prokudin, and Ted C. Rogers. Calculation of TMD Evolution for Transverse Single Spin Asymmetry Measurements. *Phys. Rev. Lett.*, 108:242003, 2012.

[121] Miguel G. Echevarría, Ahmad Idilbi, and Ignazio Scimemi. Soft and Collinear Factorization and Transverse Momentum Dependent Parton Distribution Functions. *Phys. Lett.*, B726:795–801, 2013.

[122] Miguel G. Echevarria, Ahmad Idilbi, Andreas Schäfer, and Ignazio Scimemi. Model-Independent Evolution of Transverse Momentum Dependent Distribution Functions (TMDs) at NNLL. *Eur. Phys. J.*, C73(12):2636, 2013.

[123] Peng Sun and Feng Yuan. Energy Evolution for the Sivers Asymmetries in Hard Processes. *Phys. Rev.*, D88:034016, 2013.

[124] M. Anselmino, M. Boglione, U. D'Alesio, S. Melis, F. Murgia, and A. Prokudin. Sivers Distribution Functions and the Latest SIDIS Data. In *19th International Workshop on Deep-Inelastic Scattering and Related Subjects (DIS 2011) Newport News, Virginia, April 11-15, 2011*, 2011.

[125] M. Anselmino, M. Boglione, U. D'Alesio, S. Melis, F. Murgia, E. R. Nocera, and A. Prokudin. General Helicity Formalism for Polarized Semi-Inclusive Deep Inelastic Scattering. *Phys. Rev.*, D83:114019, 2011.

[126] P. Schweitzer and A. Bacchetta. Azimuthal single spin asymmetries in SIDIS in the light of chiral symmetry breaking. *Nucl. Phys.*, A732:106–124, 2004.

[127] John R. Ellis, Dae Sung Hwang, and Aram Kotzinian. Sivers Asymmetries for Inclusive Pion and Kaon Production in Deep-Inelastic Scattering. *Phys. Rev.*, D80:074033, 2009.

[128] A. M. Kotzinian and P. J. Mulders. Longitudinal quark polarization in transversely polarized nucleons. *Phys. Rev.*, D54:1229–1232, 1996.

[129] A. M. Kotzinian and P. J. Mulders. Probing transverse quark polarization via azimuthal asymmetries in leptoproduction. *Phys. Lett.*, B406:373–380, 1997.

[130] I. M. Gregor. Transverse spin physics at HERMES. *Acta Phys. Polon.*, B36:209–215, 2005.

[131] A. V. Efremov, K. Goeke, S. Menzel, A. Metz, and P. Schweitzer. Sivers effect in semi-inclusive DIS and in the Drell-Yan process. *Phys. Lett.*, B612:233–244, 2005.

[132] Franco Bradamante. Recent COMPASS results on Transverse Spin Asymmetries in SIDIS. *J. Phys. Conf. Ser.*, 938(1):012004, 2017.

[133] V. A. Matveev, R. M. Muradian, and A. N. Tavkhelidze. MUON PAIR PRODUCTION IN STRONG INTERACTIONS AND THE ASYMPTOTIC SUM RULES. 1969.

[134] J. H. Christenson, G. S. Hicks, L. M. Lederman, P. J. Limon, B. G. Pope, and E. Zavattini. Observation of massive muon pairs in hadron collisions. *Phys. Rev. Lett.*, 25:1523–1526, 1970.

[135] S. Arnold, A. Metz, and M. Schlegel. Dilepton production from polarized hadron hadron collisions. *Phys. Rev.*, D79:034005, 2009.

[136] F Gautheron et al. COMPASS-II Proposal. 2010.

[137] M. Anselmino, V. Barone, and M. Boglione. The Sivers asymmetry in Drell–Yan production at the J/Ψ peak at COMPASS. *Phys. Lett.*, B770:302–306, 2017.

[138] M. Anselmino, M. Boglione, U. D'Alesio, A. Kotzinian, F. Murgia, and A. Prokudin. Extracting the Sivers function from polarized SIDIS data and making predictions. *Phys. Rev.*, D72:094007, 2005. [Erratum: Phys. Rev.D72,099903(2005)].

[139] M. Anselmino, M. Boglione, U. D'Alesio, A. Kotzinian, S. Melis, F. Murgia, A. Prokudin, and C. Turk. Sivers Effect for Pion and Kaon Production in Semi-Inclusive Deep Inelastic Scattering. *Eur. Phys. J.*, A39:89–100, 2009.

[140] M. Anselmino, M. Boglione, and S. Melis. A Strategy towards the extraction of the Sivers function with TMD evolution. *Phys. Rev.*, D86:014028, 2012.

[141] M. Boglione, private communications. 2016.

[142] A. N. Sissakian, O. Yu. Shevchenko, A. P. Nagaytsev, and O. N. Ivanov. Direct extraction of transversity and its accompanying t-odd distribution from the unpolarized and single-polarized drell-yan processes. *Phys. Rev. D*, 72:054027, Sep 2005.

[143] A. Sissakian, O. Shevchenko, A. Nagaytsev, O. Denisov, and O. Ivanov. Transversity and its accompanying t-odd distribution from drell–yan processes with pion-proton collisions. *The European Physical Journal C - Particles and Fields*, 46(1):147–150, Apr 2006.

[144] Martin Lambertsen and Werner Vogelsang. Drell-Yan lepton angular distributions in perturbative QCD. *Phys. Rev.*, D93(11):114013, 2016.

[145] Jen-Chieh Peng, Wen-Chen Chang, Randall Evan McClellan, and Oleg Teryaev. Interpretation of Angular Distributions of Z-boson Production at Colliders. *Phys. Lett.*, B758:384–388, 2016.

[146] C. S. Lam and Wu-Ki Tung. A Systematic Approach to Inclusive Lepton Pair Production in Hadronic Collisions. *Phys. Rev.*, D18:2447, 1978.

[147] E. Mirkes. Angular decay distribution of leptons from W bosons at NLO in hadronic collisions. *Nucl. Phys.*, B387:3–85, 1992.

[148] E. Mirkes and J. Ohnemus. Angular distributions of Drell-Yan lepton pairs at the Tevatron: Order $\alpha - s^2$ corrections and Monte Carlo studies. *Phys. Rev.*, D51:4891–4904, 1995.

[149] L. Anderson et al. A High Resolution Spectrometer for the Study of High Mass Muon Pairs Produced by Intense Hadron Beams. *Nucl. Instrum. Meth.*, A223:26, 1984.

[150] J. Badier et al. Angular distributions in the dimuon hadronic production at 150 gev/c. *Zeitschrift für Physik C Particles and Fields*, 11(3):195–202, Sep 1981.

[151] S. Falciano et al. Angular distributions of muon pairs produced by 194 gev/c negative pions. *Zeitschrift für Physik C Particles and Fields*, 31(4):513–526, Dec 1986.

[152] M. Guanziroli et al. Angular distributions of muon pairs produced by negative pions on deuterium and tungsten. *Zeitschrift für Physik C Particles and Fields*, 37(4):545–556, Dec 1988.

[153] J. S. Conway et al. Experimental study of muon pairs produced by 252-gev pions on tungsten. *Phys. Rev. D*, 39:92–122, Jan 1989.

[154] K. Gottfried and John David Jackson. On the Connection between production mechanism and decay of resonances at high-energies. *Nuovo Cim.*, 33:309–330, 1964.

[155] Pietro Faccioli, Carlos Lourenco, Joao Seixas, and Hermine K. Wohri. Towards the experimental clarification of quarkonium polarization. *Eur. Phys. J.*, C69:657–673, 2010.

[156] J. C. Peng et al. Measurement of decay angular distributions of Drell-Yan events for p d interaction at 800-GeV/c. *AIP Conf. Proc.*, 870:681–684, 2006. [,681(2006)].

[157] A. Brandenburg, S. J. Brodsky, Valentin V. Khoze, and Dieter Mueller. Angular distributions in the Drell-Yan process: A Closer look at higher twist effects. *Phys. Rev. Lett.*, 73:939–942, 1994.

[158] K. J. Eskola, P. Hoyer, M. Vanttinen, and R. Vogt. Higher twist effects in the Drell-Yan angular distribution. *Phys. Lett.*, B333:526–530, 1994.

[159] A. Brandenburg, O. Nachtmann, and E. Mirkes. Spin effects and factorization in the Drell-Yan process. *Z. Phys.*, C60:697–710, 1993.

[160] Bing Zhang, Zhun Lu, Bo-Qiang Ma, and Ivan Schmidt. Extracting Boer-Mulders functions from p+D Drell-Yan processes. *Phys. Rev.*, D77:054011, 2008.

[161] L. Y. Zhu et al. Measurement of Angular Distributions of Drell-Yan Dimuons in p + p Interactions at 800-GeV/c. *Phys. Rev. Lett.*, 102:182001, 2009.

[162] T. Aaltonen et al. First Measurement of the Angular Coefficients of Drell-Yan e^+e^- pairs in the Z Mass Region from $p\bar{p}$ Collisions at $\sqrt{s} = 1.96$ TeV. *Phys. Rev. Lett.*, 106:241801, 2011.

[163] Vardan Khachatryan et al. Angular coefficients of Z bosons produced in pp collisions at $\sqrt{s} = 8$ TeV and decaying to $\mu^+\mu^-$ as a function of transverse momentum and rapidity. *Phys. Lett.*, B750:154–175, 2015.

[164] Wen-Chen Chang, Randall Evan McClellan, Jen-Chieh Peng, and Oleg Teryaev. Dependencies of lepton angular distribution coefficients on the transverse momentum and rapidity of Z bosons produced in pp collisions at the LHC. *Phys. Rev.*, D96(5):054020, 2017.

[165] H. W. Atherton, C. Bovet, N. Doble, G. von Holtey, L. Piemontese, A. Placci, M. Placidi, David E. Plane, M. Reinharz, and E. Rossa. Precise Measurements of Particle Production by 400-GeV/c Protons on Beryllium Targets. 1980.

[166] A.Ivanov R.Longo, B.Parsamyan. Beam properties from 2014 BMS-runs. https://twiki.cern.ch/twiki/pub/Compass/Drell_Yan/Subgroupmeeting/Longo_Beam2014.pdf, January 2016.

[167] A. Abragam. *The Principles of Nuclear Magnetism*. The Clarendon Press, Oxford, 1961.

[168] F. Sauli. GEM: A new concept for electron amplification in gas detectors. *Nucl. Instrum. Meth.*, A386:531–534, 1997.

[169] M. C. Altunbas et al. Construction, test and commissioning of the triple-GEM tracking detector for COMPASS. *Nucl. Instrum. Meth.*, A490:177–203, 2002.

[170] E. Albrecht et al. COMPASS RICH-1. *Nucl. Instrum. Meth.*, A502(1):112–116, 2003.

[171] P. Abbon et al. Design and construction of the fast photon detection system for COMPASS RICH-1. *Nucl. Instrum. Meth.*, A616:21–37, 2010.

[172] M. Alexeev et al. Status of COMPASS RICH-1 Upgrade with MPGD-based Photon Detectors. In *4th International Conference on Micro Pattern Gaseous Detectors (MPGD2015) Trieste, Italy, October 12-15, 2015*, 2017.

[173] F. G. Binon et al. HODOSCOPE MULTI - PHOTON SPECTROMETER GAMS-2000. *Nucl. Instrum. Meth.*, A248:86, 1986.

[174] M. Adamovich et al. WA92: A Fixed target experiment to trigger on and identify beauty particle decays. *Nucl. Instrum. Meth.*, A379:252–270, 1996.

[175] P. Astbury et al. Measurement of Deep Inelastic Compton Scattering of High-energy Photons. *Phys. Lett.*, 152B:419–427, 1985.

[176] N. Anfimov et al. Tests of the module array of the ECAL0 electromagnetic calorimeter for the COMPASS experiment with the electron beam at ELSA. *Phys. Part. Nucl. Lett.*, 12(4):566–569, 2015.

[177] T. Baumann et al. The GANDALF 128-channel time-to-digital converter. *JINST*, 8:C01016, 2013.

[178] M Bodlak, V Frolov, V Jary, S Huber, I Konorov, D Levit, J Novy, R Salac, and M Virius. Fpga based data acquisition system for compass experiment. *Journal of Physics: Conference Series*, 513(1):012029, 2014.

[179] M Bodlak, V Frolov, V Jary, S Huber, I Konorov, D Levit, A Mann, J Novy, S Paul, and M Virius. New data acquisition system for the compass experiment. *Journal of Instrumentation*, 8(02):C02009, 2013.

[180] R. Fruhwirth. Application of Kalman filtering to track and vertex fitting. *Nucl. Instrum. Meth.*, A262:444–450, 1987.

[181] S. Agostinelli et al. Geant4—a simulation toolkit. *Nuclear Instruments and Methods in Physics Research Section A: Accelerators, Spectrometers, Detectors and Associated Equipment*, 506(3):250 – 303, 2003.

[182] John Allison et al. Geant4 developments and applications. *IEEE Trans. Nucl. Sci.*, 53:270, 2006.

[183] A. S. Carroll et al. Total Cross-Sections of pi+-, K+-, p and anti-p on Protons and Deuterons Between 200-GeV/c and 370-GeV/c. *Phys. Lett.*, 80B:423–427, 1979.

[184] G. Ingelman, A. Edin, and J. Rathsman. LEPTO 6.5: A Monte Carlo generator for deep inelastic lepton - nucleon scattering. *Comput. Phys. Commun.*, 101:108–134, 1997.

[185] A. Sandacz and P. Sznajder. HEPGEN - generator for hard exclusive leptoproduction. 2012.

[186] Torbjorn Sjostrand, Stephen Mrenna, and Peter Z. Skands. PYTHIA 6.4 Physics and Manual. *JHEP*, 05:026, 2006.

[187] Torbjorn Sjostrand, Stephen Mrenna, and Peter Z. Skands. A Brief Introduction to PYTHIA 8.1. *Comput. Phys. Commun.*, 178:852–867, 2008.

[188] J. Koivuniemi et al. Drawings for drell-yan polarized target. https://twiki.cern.ch/twiki/bin/view/Compass/Drell_Yan/DyPtDrawings, 2014.

[189] G.Nukazuka. Preliminary estimation of the lost part of nh$_3$ in 2014 dy run. https://twiki.cern.ch/twiki/pub/Compass/Drell_Yan/WeeklyDYmeeting/20160714_Getnki_lost_material.pdf, January 2016.

[190] R.Longo. Tgeant mc for dy: impact of trigger efficiencies and other updates. http://wwwcompass.cern.ch/compass/software/analysis/transparencies/2017/am_170207/talks/Riccardo_Longo_AM_07022017.pdf, February 2017.

[191] B.M.Veit. Qualitative analysis of compass triggers, 2017.

[192] Susanne Koblitz. *Determination of the gluon polarisation from open charm production at COMPASS*. PhD thesis, Mainz U., 2009.

[193] Heiner Wollny. *Measuring azimuthal asymmetries in semi-inclusive deep-inelastic scattering off transversely polarized protons*. PhD thesis, Freiburg U., 2010.

[194] B.Parsamyan. Drell-yan 2015: status of the analysis. http://wwwcompass.cern.ch/compass/software/analysis/transparencies/2016/am_161122/talks/Parsamyan_161123-AM.pdf, November 2017.

[195] M. Glück, E. Reya, and A. Vogt. Dynamical parton distributions revisited. *Eur. Phys. J.*, C5:461–470, 1998.

[196] M. Gluck, E. Reya, and A. Vogt. Pionic parton distributions. *Z. Phys.*, C53:651–656, 1992.

[197] J. Koivuniemi. Preliminary result from target material weighing 2015. https://compassvm03.cern.ch/elog/target_polar/215, elog entry 215 2015.

[198] Radja Boughezal, John M. Campbell, R. Keith Ellis, Christfried Focke, Walter Giele, Xiaohui Liu, Frank Petriello, and Ciaran Williams. Color singlet production at NNLO in MCFM. *Eur. Phys. J.*, C77(1):7, 2017.

[199] K.J. Eskola, V.J. Kolhinen, and C.A. Salgado. The scale dependent nuclear effects in parton distributions for practical applications. *The European Physical Journal C - Particles and Fields*, 9(1):61–68, Jun 1999.

[200] D. M. Alde, H. W. Baer, T. A. Carey, G. T. Garvey, A. Klein, C. Lee, M. J. Leitch, J. W. Lillberg, P. L. McGaughey, C. S. Mishra, J. M. Moss, J. C. Peng, C. N. Brown, W. E. Cooper, Y. B. Hsiung, M. R. Adams, R. Guo, D. M. Kaplan, R. L. McCarthy, G. Danner, M. J. Wang, M. L. Barlett, and G. W. Hoffmann. Nuclear dependence of dimuon production at 800 gev. *Phys. Rev. Lett.*, 64:2479–2482, May 1990.

[201] C. Adolph et al. Transverse spin effects in hadron-pair production from semi-inclusive deep inelastic scattering. *Phys. Lett.*, B713:10–16, 2012.

[202] F. Bradamante et al. Measurement of the P_T^h weighted asymmetries in SIDIS at COMPASS. *COMPASS Release note*, 2016.

[203] G. D'Agostini. A Multidimensional unfolding method based on Bayes' theorem. *Nucl. Instrum. Meth.*, A362:487–498, 1995.

[204] C.Marques Quintans M.Chiosso, I.Gnesi. Estimation of the drell-yan process cross-section and of some important parameters for luminosity calculation for the future drell-yan measurements at compass.

[205] R. S. Thorne, A. D. Martin, W. J. Stirling, and G. Watt. Parton distributions for the LHC. In *Proceedings, 15th International Workshop on Deep-inelastic scattering and related subjects (DIS 2007). Vol. 1 and 2: Munich, Germany, April 16-20, 2007*, pages 305–308, 2007.

[206] J. F. Owens. Q**2 Dependent Parametrizations of Pion Parton Distribution Functions. *Phys. Rev.*, D30:943, 1984.

[207] M. Anselmino, M. Boglione, U. D'Alesio, F. Murgia, and A. Prokudin. Study of the sign change of the Sivers function from STAR Collaboration W/Z production data. *JHEP*, 04:046, 2017.

[208] Miguel G. Echevarria, Ahmad Idilbi, Zhong-Bo Kang, and Ivan Vitev. QCD Evolution of the Sivers Asymmetry. *Phys. Rev.*, D89:074013, 2014.

[209] Peng Sun and Feng Yuan. Transverse momentum dependent evolution: Matching semi-inclusive deep inelastic scattering processes to Drell-Yan and W/Z boson production. *Phys. Rev.*, D88(11):114012, 2013.

[210] L. Adamczyk et al. Measurement of the transverse single-spin asymmetry in $p^\uparrow + p \to W^\pm/Z^0$ at RHIC. *Phys. Rev. Lett.*, 116(13):132301, 2016.

[211] M. Anselmino, M. Boglione, U. D'Alesio, F. Murgia, and A. Prokudin. Study of the sign change of the sivers function from star collaboration w/z production data. *Journal of High Energy Physics*, 2017(4):46, Apr 2017.

[212] A. N. Sissakian, O. Yu. Shevchenko, A. P. Nagaitsev, and O. N. Ivanov. Polarization effects in Drell-Yan processes. *Phys. Part. Nucl.*, 41:64–100, 2010.